Precision Measurement of the Parity Violating Asymmetry in Elastic Electron Scattering of ^{208}Pb

A Dissertation presented

by

Tao Ye

to

The Graduate School

in Partial Fulfillment of the

Requirements

for the Degree of

Doctor of Philosophy

in

Physics

Stony Brook University

August 2021

Stony Brook University

The Graduate School

Tao Ye

We, the dissertation committee for the above candidate for the

Doctor of Philosophy degree, hereby recommend

acceptance of this dissertation

Krishna Kumar - Dissertation Advisor
Professor, Department of Physics and Astronomy

Abhay Deshpande - Chairperson of Defense
Professor, Department of Physics and Astronomy

James Lattimer
Distinguished Professor, Department of Physics and Astronomy

Paul Souder
Professor, Department of Physics
Syracuse University

This dissertation is accepted by the Graduate School

Eric Wertheimer

Dean of the Graduate School

Abstract of the Dissertation

Precision Measurement of the Parity Violating Asymmetry in Elastic Electron Scattering of ^{208}Pb

by

Tao Ye

Doctor of Philosophy

in

Physics

Stony Brook University

2021

The Lead Radius Experiment (PREX) measures the parity violating asymmetry $A_{\rm PV}$ in the elastic scattering of longitudinally polarized electrons from ^{208}Pb nuclei. $A_{\rm PV}$ provides a model independent measure of the neutron skin thickness, the difference between the point neutron radius R_n and the point proton radius R_p. In the summer of 2019, the PREX-2 collaboration completed data collection utilizing the electron beam from the Continuous Electron Beam Accelerator Facility (CEBAF) in Jefferson Lab. The instrumentation and the experimental technique for systematic control of $A_{\rm PV}$ measurement are introduced in Chapter 2 and Chapter 3. Chapter 4 introduces an event cut strategy taking target conditions into account to guarantee data quality. The discussion of the statistical properties of the data will be followed by the discussion on the correction for beam fluctuations. An accurate and precise beam correction method based on Lagrange multiplier regression and eigenvector analysis is developed in Chapter 5. After completion of data analysis, the PREX-2 result is $A_{\rm PV} = 550 \pm 16$ (stat) ± 8 (syst) parts-per-billion. Combined with the PREX-1 data, the result leads to the extracted neutron skin thickness $R_n - R_p = 0.283 \pm 0.071$ fm in ^{208}Pb. Implications of the PREX-2 results are discussed in Chapter 6.

To my parents
Ronglong Ye and Yueyun Cai

Contents

List of Figures

List of Tables

Acknowledgements

First of all, I would like to express my gratitude to my advisor, Prof. Krishna S. Kumar. KK provides me opportunities to work on different great projects in my PhD study. I benefit a lot from his guidance. KK's ability to explain complicated concepts to students is very impressive. KK not only taught me the skills and thoughts in experimental research but also offered me advice for career and life. I sincerely appreciate the time he spent on guiding my dissertation writing.

In the first few years after I joined KK's group in 2015, I worked with Seamus Riordan, Yuxiang Zhao, Michal Tarka and Oumarou Njoya on various projects. I appreciate their patience and guidance to a newbie from the other side of the Pacific Ocean. Beyond experimental techniques, I also learned how to think of a problem and how to examine a result from them. The experience from working with these senior researchers in the early stage of my PhD has a profound impact on my research methodology.

The SBU experimental nuclear physics group has been a large team. First I would like to thank Prof. Abhay Deshpande, Socorro Delquaglio and Marlene Vera-Viteri. Abhay has seen the progress I made step by step in this group. We also had several wonderful discussions in our group meeting. Socoro and Marlene have been helping me a lot in processing reimbursement for research and traveling costs. I would also like to thank Chandan Ghosh, Jinlong Zhang, Tyler Kutz, Ryan Richards, Cameron Clarke, Weibin Zhang, Marisa Petrusky and Catherine Feldman. I was getting to know how to collaborate with different types of researchers from the projects we worked on together.

I would like to thank Prof. Kent Paschke, Prof. Paul Souder, Ye Tian, Caryn Palatchi and Victoria Owen. My work on beam correction in this thesis would not have been possible without their support.

It is Caryn who introduced me to the instrumentation and the beam correction studies for parity experiments during my first trip to JLab in 2016. From 2016 to 2017, a year-long discussion with KK, Kent and Caryn on the regression analysis for SAMs established a solid foundation for my later work in PREX-2 at JLab.

Prof. Kent Paschke is one of the spokespeople for PREX-2 and he is also the group leader

during the PREX-2 data taking run. Kent has a strong intuition and logic in analyzing problems and making decisions. One of the most important experimental practices I learned from Kent is: a conclusion should be examined from different aspects and be consistent within analysis approaches. The suggestions, encouragement and support I received from Kent guided me to overcome challenges in the PREX-2 data analysis to get this far.

It was a wonderful experience to work with Prof. Paul Souder on the PREX-2 data analysis. Paul always has illuminating ideas to handle hard problems and insightful points of view to make a shortcut to the heart of intricate problems. The idea of beam correction with Lagrange Multiplier was first raised by Paul when we were examining the first few runs of the PREX-2 data late at night in the Counting House. What happened in the next two or three days was amazing: we developed the algorithm, built a prototype analysis software and proved the idea with the PREX-2 data.

The careful studies on the beam modulation control and analysis done by Ye and Victoria are the important inputs for the Lagrange Multiplier analysis in this work. Ye also organized the weekly meeting for the PREX-2 beam correction.

I would like to express my appreciation to Bob Michaels, Paul King, Ciprian Gal and Sanghwa Park for their guidance and advice while I was working in JLab. Bob introduced me to the hardware and the DAQ system for PREX-2. I learned a lot from Paul King in ROOT coding and software system design. The support and suggestions from Ciprian and Sanghwa in all of my works for PREX-2 are also invaluable.

Also, I sincerely acknowledge contributions from students, post-docs and JLab staff who signed up shifts, took the responsibility as a Run Coordinator or provided technical support for the PREX-2 run at JLab. Those days I was working together with the PREX students in Virginia are memorable. I am grateful to Eric King, Devi Adhikari and Siyu Jian for clarifying several technical details from their expertise.

I would like to offer my special thanks to friends I met at Stony Brook: Pengzhan Zhou, Yao Ma, Tutu Wan, Fanglida Yan, Ru Wang, Nan Hu, Xuanhua Wang, Tianqi Zhao and Ruoxi Wang to name a few. Special thanks should also go to folks in the SBU Friday Soccer Club: Rasmus Larsen, Dhananjay Ravikumar, Yuta Kikuchi, Gongjun Choi and Yusong Liu.

Last but not least, I am deeply indebted to my parents for their endless love and unconditional support during my PhD study abroad.

Chapter 1

Introduction

This chapter mainly discusses the physics motivation and the theoretical context of the parity violating asymmetry in ^{208}Pb. Section 1.1 introduces the definitions of symmetry energy parameters in the nuclear Equation of State (EOS) and reviews our current knowledges on the symmetry energy parameters. The neutron skin thickness in the neutron rich heavy nuclei is believed to be sensitive to the density dependence of the symmetry energy at saturation density. A model independent approach for the neutron skin thickness measurement using parity-violating electron scattering is introduced in Section 1.2. The connection between the parity-violating asymmetry and the point neutron radius in ^{208}Pb is discussed in Section 1.3. To optimize the sensitivity of the parity-violating asymmetry to the neutron radius and the statistical efficiency, the optimal experiment kinematics are chosen based on the metric named Figure of Merit (FOM) discussed in Section 1.4.

1.1 Nuclear Equation of State and the Neutron Skin

The energy per baryon of hadronic matter near saturation density n_s is traditionally expressed as a double Taylor series expansion in density $(n - n_s)$ and neutron excess $(1 - 2x)$,

$$e(u, x) = -B + \frac{K_0}{18}(u-1)^2 + \frac{K_0'}{162}(u-1)^3 + S_2(u)(1-2x)^2 + e_l + \ldots, \tag{1.1}$$

where B is the bulk binding energy of symmetry matter at saturation density, K_0 and K_0' are the standard incompressibility and skewness parameters, e_l is the lepton energy and u and x are dimensionless parameters:

$$u = \frac{n}{n_s}, \quad 1 - 2x = \frac{N - Z}{N + Z}. \tag{1.2}$$

The symmetry energy $S(u)$ is the energy difference between pure neutron matter and symmetric matter and is approximately $S_2(u)$

$$S(u) = e(u,0) - e(u,1/2) \approx S_2(u). \tag{1.3}$$

The Taylor series expansion of the symmetry energy near saturation density n_s (u=1) is

$$S(u) = S_v + \frac{L}{3}(u-1) + \frac{K_{\rm sym}}{18}(u-1)^2 + \ldots, \tag{1.4}$$

where the symmetry energy parameters are defined as below

$$S_v = S_2(1), \tag{1.5}$$

$$L = 3u\Big(\frac{\partial S_2}{\partial u}\Big)_{u=1}, \tag{1.6}$$

$$K_{\rm sym} = 9u^2\Big(\frac{\partial^2 S_2}{\partial u^2}\Big)_{u=1}. \tag{1.7}$$

L is known as the density dependence of the symmetry energy at saturation density and is closely related to the pressure of pure neutron matter at saturation density $p(1,0)$

$$p(u,x) = u^2 n_s\Big(\frac{\partial e}{\partial u}\Big)_x \approx u^2 n_s\Big[\frac{K_0}{9}(u-1) + \frac{K_0'}{54}(u-1)^2 + \frac{\partial S_2}{\partial u}(1-2x)^2\Big] + p_l, \tag{1.8}$$

$$p(1,0) \approx \frac{1}{3}n_s L, \tag{1.9}$$

where p_l is the lepton pressure. The density dependence of the symmetry energy governs the nuclear structure of nuclei, the radii of neutron stars and the thickness of their crusts, the cooling process of neutron stars and etc. Our knowledge of the density dependence of the symmetry energy L is still limited. One promising experimental portal to L is the neutron skin thickness, the difference between the RMS radius of the point neutron and the point proton distributions

$$\Delta r_{np} = R_n - R_p, \tag{1.10}$$

where the RMS radii R_n and R_p can be calculated with known of the point neutron distribution $\rho_n(r)$ and the point proton distribution $\rho_p(r)$

$$R_t^2 = \frac{\int {\rm d}^3 r r^2 \rho_t(r)}{\int {\rm d}^3 r \rho_t(r)}, \quad \text{for } t = n, p. \tag{1.11}$$

For a nucleus with a significant neutron excess, the formation of the neutron skin, to a large extend, is a consequence of the competition between the symmetry energy and the surface tension. The symmetry energy in the dense core is expected to be larger than that in the dilute surface region. On the one hand, placing the excess neutrons in the dense core region

is favored by the surface tension but disfavored by the symmetry energy. On the other hand, pushing the excess neutrons out reduces the symmetry energy at the cost of the surface tension. For a stiff symmetry energy, namely a large slope of the symmetry energy $L(u)$, a thick neutron skin is expected.

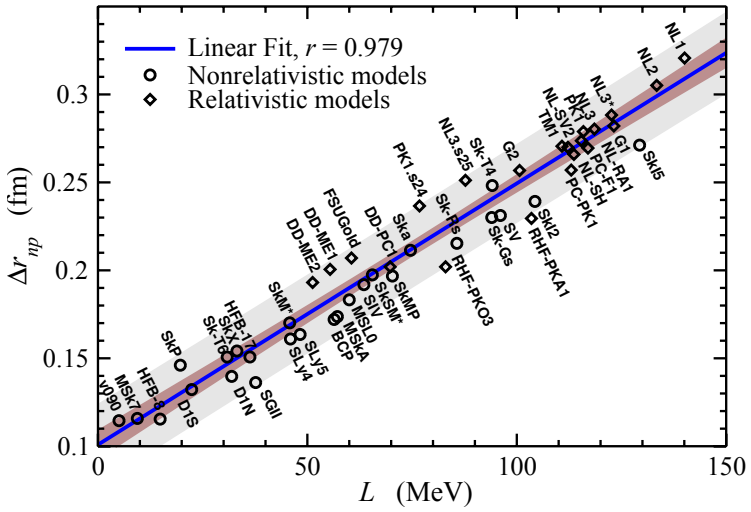

Figure 1.1: Neutron skin thickness of ^{208} Pb vs L. The linear fit is $\Delta r_{np} = 0.101 + 0.00147L$. This figure is adapted from [1].

Stable and doubly-magic nuclei with significant neutron excess are ideal candidates for the neutron skin thickness measurement. ^{208}Pb shows its advantage for having the largest known splitting to the first excited state (2.6 MeV) of any heavy nucleus. The neutron skin thickness of ^{208}Pb Δr_{np} is valuable for its sensitivity to the slope parameter of the symmetry energy L. The collective behavior of different mean field models in Figure 1.1 shows a strong correlation between Δr_{np} and L. A detailed discussion on the model dependence of the correlation between Δr_{np} and L will be given in Section 6.2.

Most of the existing measurements for the neutron skin rely on hadronic probes, such as pions, nucleons, α-particles and antiprotons. Though the hadronic probe generates a large scattering cross-section from its strong interaction nature, the interpretation of the data from hadronic probes is built on the model assumptions associated with the reaction mechanism, multiple scattering effects and the medium modification to the elementary interaction and etc. The inconsistency between the neutron radius extracted from π^+ and π^- beam [38], the broad and dramatic energy-dependency of the neutron skin thickness of ^{208}Pb using proton-nucleus scattering [39] and the potentially underestimated theoretical uncertainties in the antiprotonic atoms observables indicate a robust control over the theoretical uncertainties is needed.

The Sn isotopes neutron skin thickness has been measured with proton elastic scattering [40, 41], α-scattering [42], spin-dipole resonance [43], antiprotonic atom observables [44], pygmy dipole resonance [45]. A constraint in the $S_v - L$ plane was given from the χ^2-analysis of these Sn neutron skin data [6]. The 1-σ confidence band from the Sn neutron skin is shown as the light blue band in Figure 1.2 and is orthogonally intercepted with the yellow confidence ellipse given by the nuclear masses fit [5], therefore the neutron skin thickness is considered as a valuable constraint in S_v and L.

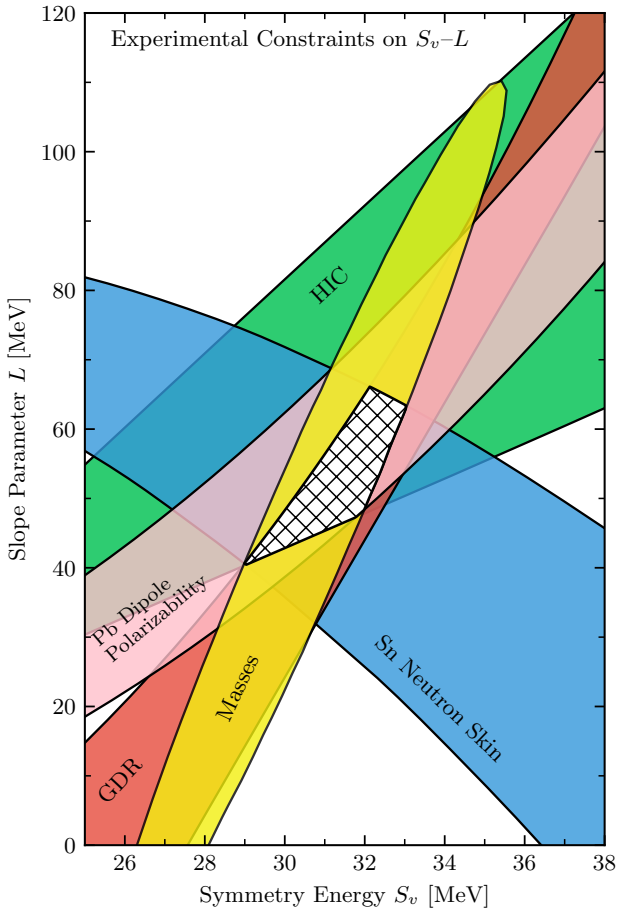

Figure 1.2: Experimental Constraints on the symmetry energy parameters adapted from [2, 3, 4]. a) Nuclear masses fit [5]; b) Sn isotopes neutron skin [6]; c) Giant Dipole Resonance (GDR) [7]; d) Heavy Ion Collision (HIC) [8]; e) Pb Dipole Polarizability [9, 10]. The hatched region is the common part of the 1-σ bands of all these measurements.

Existing constraints on S_v and L from laboratory observables have been reviewed in [2, 46, 3] and the illustration of these constraints are shown in Figure 1.2 adapted from [2, 46, 3, 4]. The density dependence of the symmetry energy is experimentally constrained within 40 MeV $< L <$ 68 MeV.

In contrast to the hardronic probes, the promising electroweak probe using the parity violating elastic scattering is model independent though challenging for high precision, and the path from the parity violating asymmetry to the neutron skin thickness will be given in the next section. Limited by the statistical uncertainty, the PREX-1 result has been interpreted to a limit of 35 MeV $< L <$ 262 MeV [2].

1.2 Parity Violating Electron Scattering

In the Standard Model, the VA theory defines the interaction between fermions and the Z_0 boson with the Feynman diagram and the Lagrangian shown below

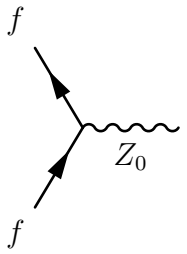

$$-i\frac{g}{2\cos\theta_W}\gamma^\mu(g_V^f - g_A^f\gamma^5).$$

In the 4-Fermi effective Lagrangian, the parity-violating part of the neutral-current (NC) interaction of the quark with the electron is

$$\mathcal{L}_{\rm NC}^{eq} = \frac{G_F}{\sqrt{2}}\sum_{q=u,d}\Big[C_{1q}(\bar{e}\gamma_\mu\gamma^5 e)(\bar{q}\gamma^\mu q) + C_{2q}(\bar{e}\gamma_\mu e)(\bar{q}\gamma^\mu\gamma^5 q)\Big], \tag{1.12}$$

where the tree-level electroweak coefficients are

$$C_{1u} = 2g_A^e g_V^u = -\frac{1}{2} + \frac{4}{3}\sin^2\theta_W, \qquad C_{2u} = 2g_V^e g_A^u = -\frac{1}{2} + 2\sin^2\theta_W, \tag{1.13}$$

$$C_{1d} = 2g_A^e g_V^d = \frac{1}{2} - \frac{2}{3}\sin^2\theta_W, \qquad C_{2d} = 2g_V^e g_A^d = \frac{1}{2} - 2\sin^2\theta_W, \tag{1.14}$$

and the vector and axial coupling constants g_v and g_A for fermions are defined in Table 1.1.

	g_V	g_A
e	$-\frac{1}{2} + 2\sin^2\theta_W$	$\frac{1}{2}$
u	$\frac{1}{2} - \frac{4}{3}\sin^2\theta_W$	$-\frac{1}{2}$
d	$-\frac{1}{2} + \frac{2}{3}\sin^2\theta_W$	$\frac{1}{2}$

Table 1.1: Vector and axial coupling constants for the electron (e), the up quark (u) and the down quark (d).

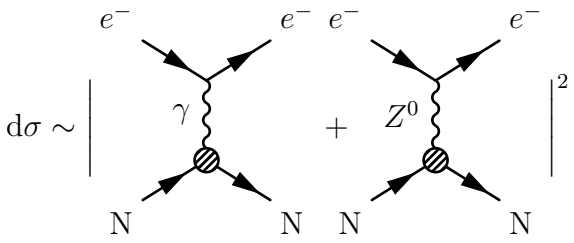

Figure 1.3: Cross-section of the electron scattered off a spin-0 nuclear target.

The cross-section of the electron elastically scattered off a spin-0 nuclear target is the squared scattering amplitudes including both electromagnetic (EM) and weak neutral current (WNC) interactions:

$$\mathrm{d}\sigma \propto |M_\gamma + M_Z|^2 = |M_\gamma|^2 + 2|M_\gamma M_Z| + |M_Z|^2, \tag{1.15}$$

of which the Feynman diagram at tree-level is shown in Figure 1.3 and both the EM and WNC scattering amplitudes can be expressed in terms of interaction currents J_γ and J_Z:

$$M_\gamma = \frac{e^2}{Q^2} J_\gamma^e J_\gamma^N, \quad M_Z = \frac{G_F}{\sqrt{2}} J_Z^e J_Z^N, \tag{1.16}$$

where J_z contains the vector and the axial currents

$$J_Z^e = g_V^e(\bar{e}\gamma_\mu e) - g_A^e(\bar{e}\gamma_\mu\gamma^5 e), \tag{1.17}$$

$$J_Z^q = g_V^q(\bar{q}\gamma_\mu q) - g_A^q(\bar{q}\gamma_\mu\gamma^5 q), \quad q = u, d. \tag{1.18}$$

Since $\sin^2\theta_W \approx 0.23$, the vector coupling constant of the electron g_V^e is negligible

$$g_V^e = -\frac{1}{2} + 2\sin^2\theta_W \approx 0, \tag{1.19}$$

therefore the axial coupling constant g_A^e is dominant in the Z-exchange scattering amplitude

$$M_Z \propto g_A^e(\bar{e}\gamma_\mu e) J_Z^N. \tag{1.20}$$

At tree-level, the effective axial and vector currents for a neutron (n) and a proton (p) are given below

$$g_V^p = 2g_V^u + g_V^d = \frac{1}{2} - 2\sin^2\theta_W \approx 0, \tag{1.21}$$

$$g_A^p = 2g_A^u + g_A^d = \frac{1}{2}, \tag{1.22}$$

$$g_V^n = 2g_V^d + g_V^u = -\frac{1}{2}, \tag{1.23}$$

$$g_A^n = 2g_A^d + g_A^u = \frac{1}{2}, \tag{1.24}$$

where the vector current contribution from the proton g_V^p is also negligible. For elastic scattering at $Q^2 \ll 1$ GeV , the contribution from the pure Z-exchange $|M_z|^2$ is suppressed by the Fermi constant G_F

$$(\sqrt{2}G_F)^2 = \frac{1}{(247\ \text{GeV})^4}, \tag{1.25}$$

Therefore the leading contributions to the cross-section are the pure photon-exchange and γ-Z interference terms

$$\mathrm{d}\sigma \propto |M_\gamma|^2 + 2|M_\gamma M_Z|. \tag{1.26}$$

Under the parity transformation ($\mathcal{P}$), the space-like components of an axial vector remain unchanged and its time-like component flips sign,

$$(j_A^0, j_A^1, j_A^2, j_A^3) \xrightarrow{\mathcal{P}} (-j_A^0, j_A^1, j_A^2, j_A^3), \tag{1.27}$$

thus the product of a vector current and an axial current is parity violating

$$j_A^\mu j_{V\mu} = (j_A^0, j_A^1, j_A^2, j_A^3) \cdot (j_V^0, j_V^1, j_V^2, j_V^3) = j_A^0 j_V^0 - \sum_{k=1}^{3} j_A^k j_V^k, \tag{1.28}$$

$$(-j_A^0, j_A^1, j_A^2, j_A^3) \cdot (j_V^0, -j_V^1, -j_V^2, -j_V^3) = -j_A^0 j_V^0 + \sum_{k=1}^{3} j_A^k j_V^k = -j_A^\mu j_{V\mu}, \tag{1.29}$$

so that in the weak neutral interaction, the cross-term of the electron axial current and the nuclear vector current is also parity violating

$$j_A^e j_V^N \xrightarrow{\mathcal{P}} -j_A^e j_V^N. \tag{1.30}$$

Because the left-handed and right-handed components in the electron axial current have opposite signs

$$\overline{e}\gamma^\mu\gamma^5 e = \overline{e}_R\gamma^\mu e_R - \overline{e}_L\gamma^\mu e_L, \tag{1.31}$$

the difference in the cross-section of the left-handed and the right-handed chiral electrons is proportional to the interference term

$$\mathrm{d}\sigma^R - \mathrm{d}\sigma^L \propto |M_\gamma M_Z| \propto j_\gamma^e j_\gamma^N \cdot j_A^e j_V^N. \tag{1.32}$$

In the ultra-relativistic limit $E \gg m$, the right-handed helicity state is identical to the right-handed chiral state

$$e_\uparrow = P_R e_\uparrow + P_L e_\uparrow = \frac{1}{2}(1 + \frac{|p|}{E+m})e_R + \frac{1}{2}(1 - \frac{|p|}{E+m})e_L \approx e_R, \tag{1.33}$$

and likewise for the left-handed chiral state and the left-handed helicity state. Relativistic electrons highly polarized along its momentum therefore can be used as a probe for the vector current in a nuclear target.

The parity-violating asymmetry is defined as the differential cross-section of the scattering of the left-handed and the right-handed polarized electrons and is sensitive to the neutral weak form factor $F_W(Q^2)$ of the nuclear target

$$A_{\mathrm{PV}} = \frac{\sigma^{\uparrow} - \sigma^{\downarrow}}{\sigma^{\uparrow} + \sigma^{\downarrow}} = \frac{2|M_\gamma M_Z|}{|M_\gamma|^2} \approx \frac{G_F Q^2 |Q_W|}{4\sqrt{2}\pi\alpha Z} \frac{F_W(Q^2)}{F_{\mathrm{ch}}(Q^2)}. \tag{1.34}$$

1.3 Weak Form Factor and Neutron Radius

To reveal the exact relation between the weak form factor F_W and the point neutron radius R_n for a nucleus, the $F_W(Q^2)$ is transformed to the neutral weak charge density ρ_W in the space coordinate

$$F_W(q) = \frac{1}{Q_W} \int \mathrm{d}^3 r \frac{\sin qr}{qr} \rho_W(r). \tag{1.35}$$

The neutral weak charge density ρ_W can also be decomposed as

$$\rho_W(r) = 4 \int \mathrm{d}^3 r' \Big[G_n^Z(|\vec{r} - \vec{r}\,'|)\rho_n(r') + G_p^Z(|\vec{r} - \vec{r}\,'|)\rho_p(r') \Big], \tag{1.36}$$

where the single proton and the single neutron weak charge densities $G_p^Z(r)$ and $G_n^Z(r)$ are the Fourier transforms of the nucleon Sachs form factors $G_p^Z(Q^2)$ and $G_n^Z(Q^2)$. And $\rho_p(r')$ and $\rho_n(r')$ are the spatial density distributions of the point protons and the point neutrons in the nucleus.

In the meantime, the electric Sachs form factors of a single proton and a single neutron contain contributions from the u, d and s quarks known as

$$G_E^p = \frac{2}{3}u_p - \frac{1}{3}d_p - \frac{1}{3}s_p, \tag{1.37}$$

$$G_E^n = \frac{2}{3}u_n - \frac{1}{3}d_n - \frac{1}{3}s_n. \tag{1.38}$$

And with the isospin symmetry:

$$G_E^u := u_p = d_n, \tag{1.39}$$

$$G_E^d := d_p = u_n, \tag{1.40}$$

$$G_E^s := s_p = s_n, \tag{1.41}$$

the quark flavor form factors can be formulated in terms of Sachs form factors

$$G_E^u = 2G_E^p + G_E^n + G_E^s, \tag{1.42}$$

$$G_E^d = 2G_E^n + G_E^p + G_E^s. \tag{1.43}$$

Assume the single nucleon density is a linear combination of the u, d and s quarks with neutral weak A-V coupling constants, the neutron weak charge Sachs form factor can be expressed in terms of nucleon electric Sachs form factors

$$\begin{aligned} G_n^Z &= g_{AV}^{ed} G_E^u + g_{AV}^{eu} G_E^d + g_{AV}^{ed} G_E^s \\ &= g_{AV}^{ed}(2G_E^p + G_E^n + G_E^s) + g_{AV}^{eu}(2G_E^n + G_E^p + G_E^s) + g_{AV}^{ed} G_E^s \\ &= (2g_{AV}^{ed} + g_{AV}^{eu})G_E^p + (2g_{AV}^{eu} + g_{AV}^{ed})G_E^n + (2g_{AV}^{ed} + g_{AV}^{eu})G_E^s, \end{aligned} \tag{1.44}$$

and similarly for the proton weak charge form factor

$$G_p^Z = (2g_{AV}^{eu} + g_{AV}^{ed})G_E^p + (2g_{AV}^{ed} + g_{AV}^{eu})G_E^n + (2g_{AV}^{ed} + g_{AV}^{eu})G_E^s. \tag{1.45}$$

where

$$\begin{aligned} 2g_{AV}^{eu} + g_{AV}^{ed} &= \frac{1}{4} - \sin^2\theta_W = \frac{1}{4}q_W^p, \\ 2g_{AV}^{ed} + g_{AV}^{eu} &= -\frac{1}{4} = -\frac{1}{4}q_W^n. \end{aligned} \tag{1.46}$$

For simplicity and convenience, the Sachs form factor relations between the neutral weak charge and the electric charge are shown as

$$\begin{aligned} 4G_p^Z &= q_W^p G_E^p + q_W^n G_E^n - G_E^s, \\ 4G_n^Z &= q_W^n G_E^p + q_W^p G_E^n - G_E^s. \end{aligned} \tag{1.47}$$

With the nucleus electric charge density defined as convolutions of the point nucleon density distributions with the single nucleon form factors,

$$\rho_{\rm ch}(r) = \int \mathrm{d}^3 r' \Big[G_E^n(|\vec{r} - \vec{r}\,'|)\rho_n(r') + G_E^p(|\vec{r} - \vec{r}\,'|)\rho_p(r') \Big], \tag{1.48}$$

the nuclear weak charge density can be further formulated as

$$\begin{aligned} \rho_W(r) &= \int \mathrm{d}^3 r' \Big[(q_W^n G_E^p + q_W^p G_E^n - G_E^s)\rho_n(r') + (q_W^p G_E^p + q_W^n G_E^n - G_E^s)\rho_p(r') \Big] \\ &= \int \mathrm{d}^3 r' \Big\{ q_W^n \Big[G_E^p \rho_n(r') + G_E^n \rho_p(r') \Big] + q_W^p \Big[G_E^n \rho_n(r') + G_E^p \rho_p(r') \Big] - \rho_b(r') G_E^s \Big\} \\ &= q_W^p \rho_{\rm ch}(r) + \int \mathrm{d}^3 r' \Big\{ q_W^n \Big[G_E^p \rho_n(r') + G_E^n \rho_p(r') \Big] - \rho_b(r') G_E^s \Big\}, \end{aligned} \tag{1.49}$$

where the baryon density $\rho_b(r) = \rho_n(r) + \rho_p(r)$.

The root-mean-square (RMS) radius of point neutrons R_n is the square root of the expectation value of r^2 with a given point neutron distribution $\rho_n(r)$:

$$R_n^2 = \frac{1}{N} \int \mathrm{d}^3 r r^2 \rho_n(r), \tag{1.50}$$

where $N = \int \mathrm{d}^3 r \rho_n(r)$. Likewise, similar integrals for the neutral weak and the electric charge density produce the neutral weak radius R_W and the electric charge radius R_{ch}

$$\int \mathrm{d}^3 r r^2 \rho_W(r) = Q_W R_W^2, \tag{1.51}$$

$$\int \mathrm{d}^3 r r^2 \rho_{\mathrm{ch}}(r) = Z R_{\mathrm{ch}}^2, \tag{1.52}$$

of which the normalization factors Q_W and Z are the total neutral weak charge and the total electric charge of the nucleus respectively

$$Q_W = \int \mathrm{d}^3 r \rho_W(r) = N q_W^n + Z q_W^p, \tag{1.53}$$

$$Z = \int \mathrm{d}^3 r \rho_{\mathrm{ch}}(r). \tag{1.54}$$

Integrals weighted by r^2 over the full space, i.e. $\int \mathrm{d}^3 r r^2$, on the both sides of Equation (1.49) resulted in an equation connecting the nucleus weak charge radius R_W, the nucleus electric charge radius R_{ch}, the point proton radius R_p, the single proton and the single neutron radius $\langle r_p^2 \rangle$ and $\langle r_n^2 \rangle$ and the nucleon strangeness radius $\langle r_s^2 \rangle$ together

$$Q_W R_W^2 = q_W^p Z R_{\mathrm{ch}}^2 + q_W^n \Big[N \langle r_p^2 \rangle + N R_n^2 + Z \langle r_n^2 \rangle \Big] - (N+Z) \langle r_s^2 \rangle, \tag{1.55}$$

with the following equalities for the single proton and the single neutron electric Sachs form factors and their electric charge RMS radii:

$$\int \mathrm{d}^3 r G_E^p(r) = 1, \tag{1.56}$$

$$\int \mathrm{d}^3 r G_E^n(r) = 0, \tag{1.57}$$

$$\int \mathrm{d}^3 r r^2 G_E^p(r) = \langle r_p^2 \rangle, \tag{1.58}$$

$$\int \mathrm{d}^3 r r^2 G_E^n(r) = \langle r_n^2 \rangle, \tag{1.59}$$

$$\int \mathrm{d}^3 r r^2 \int \mathrm{d}^3 r' G_f(|\vec{r} - \vec{r}\,'|) \rho_k(r') = Q_k \langle r_f^2 \rangle + Q_k \langle R_k^2 \rangle \int \mathrm{d}^3 r G_f(|\vec{r}|). \tag{1.60}$$

Therefore it is now straightforward to calculate the point neutron radius R_n with the experimental measurement of R_W

$$R_n^2 = \frac{Q_W}{q_W^n N} R_W^2 - \frac{q_W^p Z}{q_W^n N} R_{\mathrm{ch}}^2 - \langle r_p^2 \rangle - \frac{Z}{N} \langle r_n^2 \rangle + \frac{Z+N}{q_W^n N} \langle r_s^2 \rangle, \tag{1.61}$$

and recall that q_W^n and q_W^p are the single neutron weak charge and the single proton weak charge as defined in Equation (1.46). Given the measurement of $F_W(q)$ carried out at a

single value of the momentum transfer, assumptions on the surface thickness have to be made in order to extract R_W. To access R_W, the Helm model was used to model the weak form factor [47]

$$F_W(q) = \frac{3}{qR_0} j_1(qR_0) \mathrm{e}^{-\sigma^2 q^2/2}, \tag{1.62}$$

where R_0 is the diffraction radius characterizing the location of the zero point of $F_W(q_0) = 0$ and the width σ includes the effect from the surface thickness of point nucleon densities and the single-nucleon form factor. $j_1 = \sin x/x^2 - \cos x/x$ is the spherical Bessel function.

The Fourier transform of Equation (1.62) to the coordinate space is

$$\rho_W(r) = \frac{3Q_W}{8\pi R_0^3}\Big\{\mathrm{erf}\Big(\frac{R_0+r}{\sqrt{2}\sigma}\Big) - \mathrm{erf}\Big(\frac{r-R_0}{\sqrt{2}\sigma}\Big) + \sqrt{\frac{2}{\pi}}\frac{\sigma}{r}\Big[\mathrm{e}^{-\frac{1}{2}(\frac{r+R_0}{\sigma})^2} - \mathrm{e}^{-\frac{1}{2}(\frac{r-R_0}{\sigma})^2}\Big]\Big\}, \tag{1.63}$$

therefore the RMS radius of the weak charge is

$$R_W^2 = \frac{1}{Q_W}\int \mathrm{d}^3 r r^2 \rho_W(r) = \frac{3}{5}(R_0^2 + 5\sigma^2). \tag{1.64}$$

Based on Equation (1.62), for a given $F_W(q)$ at a single value of momentum transfer, once R_0 is fixed, it uniquely determines σ and vice versa. An exploration on seven mean-field models [47] shows a variation in σ less than 0.09 fm which results in a negligible uncertainty in R_W from model assumptions. Based on the parity-violating asymmetry measured by PREX-1 [11]

$$A_{\mathrm{PV}} = 656 \pm 60\ (\mathrm{stat}) \pm 14\ (\mathrm{syst})\ \mathrm{ppb} \tag{1.65}$$

at $\langle Q^2 \rangle = 0.00880 \pm 0.00011\ \mathrm{GeV}^2$, the weak radius R_W was obtained [11, 47]

$$R_W = 5.826 \pm 0.181\ (\mathrm{exp.}) \pm 0.027\ (\mathrm{mod.})\ \mathrm{fm}. \tag{1.66}$$

Figure 1.4 illustrates the correlation of A_{PV} and R_n [11]. Circles are distorted-wave calculations for seven nonrelativistic and relativistic mean-field models which reproduce charge densities and binding energies in good agreement with experiment and span a wide range in R_n. The red square is the PREX-1 result. The effect of Coulomb distortions can be seen by comparing the distorted-wave calculations with the plane-wave calculations which are shown in blue squares.

Based on Equation (1.61), a relation between R_W and R_n was given in [47]

$$R_n^2 = 0.9525 R_W^2 - 1.671\langle r_s^2 \rangle + 0.7450\ \mathrm{fm}^2, \tag{1.67}$$

where $\langle r_s^2 \rangle = 0.02 \pm 0.04\ \mathrm{fm}^2$ for $Q^2 < 0.11\ \mathrm{GeV}^2$[48, 49, 50, 51, 52, 53, 54, 55, 56, 57, 58, 59, 60, 61]. From Equation (1.66) and Equation (1.67), the neutron radius R_n was given by the PREX-1 result [47]

$$R_n = 5.751 \pm 0.175\ (\mathrm{exp.}) \pm 0.026\ (\mathrm{mod.}) \pm 0.005\ (\mathrm{str})\ \mathrm{fm}. \tag{1.68}$$

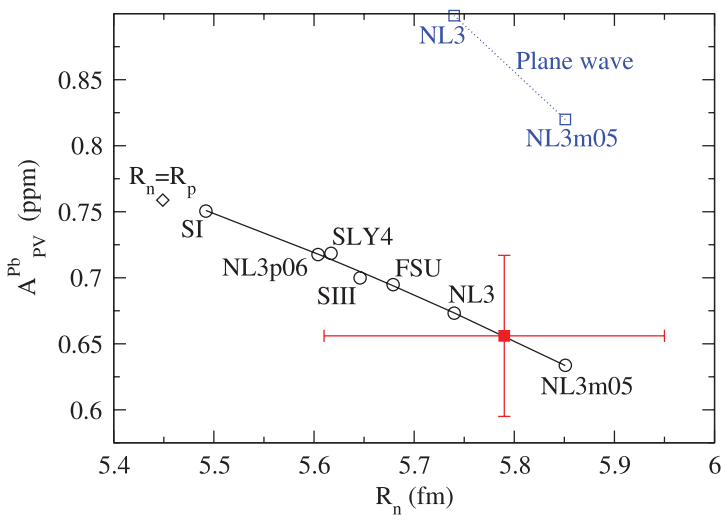

Figure 1.4: Results of PREX-1 data (red square) vs extracted point neutron RMS radius R_n shown in [11]. Circles are distorted-wave calculations for seven mean-field neutron densities. The diamond marks the point proton RMS radius $R_p = 5.449$ fm as a reference. The blue squares show plane wave impulse approximation results.

Therefore, with known of F_W at a single momentum transfer, the neutron skin thickness can be determined

$$\Delta R_{np} = R_n - R_p, \tag{1.69}$$

where the point proton RMS radius R_p for lead can be calculated from the electric charge RMS radius $R_{\rm ch}$ and Equation (1.48)

$$\begin{aligned} R_{\rm ch}^2 &= \frac{1}{Z}\int {\rm d}r^3 r^2 \rho_{\rm ch}(r) \\ &= R_p^2 + \langle r_p^2\rangle + \frac{N}{Z}\langle r_n^2\rangle + \frac{3}{4M^2} + \langle r^2\rangle_{\rm so} \\ &= R_p^2 + 0.5956 \text{ fm}^2, \end{aligned} \tag{1.70}$$

where the charge radius of a single proton is $\langle r_p^2\rangle = 0.769$ fm^2 and that of a neutron is $\langle r_n^2\rangle = -0.116$ fm^2 [62]. The contribution of spin-orbit currents $\langle r^2\rangle_{\rm so} = -0.028$ fm^2 and the Darwin contribution $3/4M^2$ is small with the nucleon mass M [47]. The charge radius of ^{208}Pb $R_{\rm ch} = (5.503 \pm 0.002)$ fm is given by [25]. Therefore, the point proton RMS radius is

$$R_p = (5.449 \pm 0.002) \text{ fm}, \tag{1.71}$$

where the ± 0.002 fm uncertainty of R_p is negligible compared with the uncertainty of R_n. The neutron skin thickness of ^{208}Pb measured by the PREX-1 data is

$$R_n - R_p = 0.302 \pm 0.175 \text{ (exp)} \pm 0.026 \text{ (mod)} \pm 0.005 \text{ (str) fm}. \tag{1.72}$$

1.4 Figure of Merit

A common concern of experimental measurements is the relative uncertainty, e.g. the relative uncertainty of a parity-violating asymmetry measurement is

$$\frac{\delta A}{A}, \tag{1.73}$$

where δA is the experimental uncertainty, typically dominated by the statistical uncertainty, and $\langle A \rangle$ is the averaged central value of the asymmetry measurement.

The statistical fluctuation of an asymmetry measurement depends on the detected scattered event counts N, which is proportional to the cross section σ with given experiment kinematics and the available beam time

$$(\delta A)^2 = \frac{1}{N} \propto \frac{1}{\sigma}, \tag{1.74}$$

Therefore the relative uncertainty of the asymmetry measurement is related with the asymmetry central value and the cross-section

$$\frac{\delta A}{A} \propto \frac{1}{\sqrt{\sigma} \times A}. \tag{1.75}$$

The figure of merit (FOM) for parity experiments is a conventional metric which is the product of the cross-section and the asymmetry central value

$$\text{FOM} = \sigma \times A^2. \tag{1.76}$$

therefore the maximized FOM is equivalent to the optimized relative uncertainty with the available experiment run time.

PREX-2 was proposed to measure the point neutron radius in ^{208}Pb R_n with 1 % accuracy, therefore the sensitivity of the parity-violating asymmetry A_{PV} to R_n should be taken into account for choosing the optimal kinematics. The optimal FOM minimizes the experiment run time required by the 1 % accuracy in R_n.

The sensitivity to the neutron radius ϵ quantifies the fractional change in the asymmetry with the neutron radius increased by 1 % at given experiment kinematics

$$\epsilon = \frac{A_1 - A}{A}, \tag{1.77}$$

where A_1 is the asymmetry with the neutron radius increased by 1%. The overall FOM for PREX-2 is

$$\text{FOM} = \sigma \times A^2 \times \epsilon^2. \tag{1.78}$$

The sensitivity to R_n was explored in a mean field theory (MFT) calculation [12]. The sensitivity to R_n, the cross section, the parity violating asymmetry as functions of the momentum transfer q are shown in Figure 1.5. And the beam energy E and scattering angle Θ dependence of the overall FOM ($\sigma \times A^2 \times \epsilon^2$) is illustrated in the bottom right plot of Figure 1.5 and suggests an optimal point at 0.85 GeV beam with 6° scattering angle, corresponding to q=0.45 fm^{-1}.

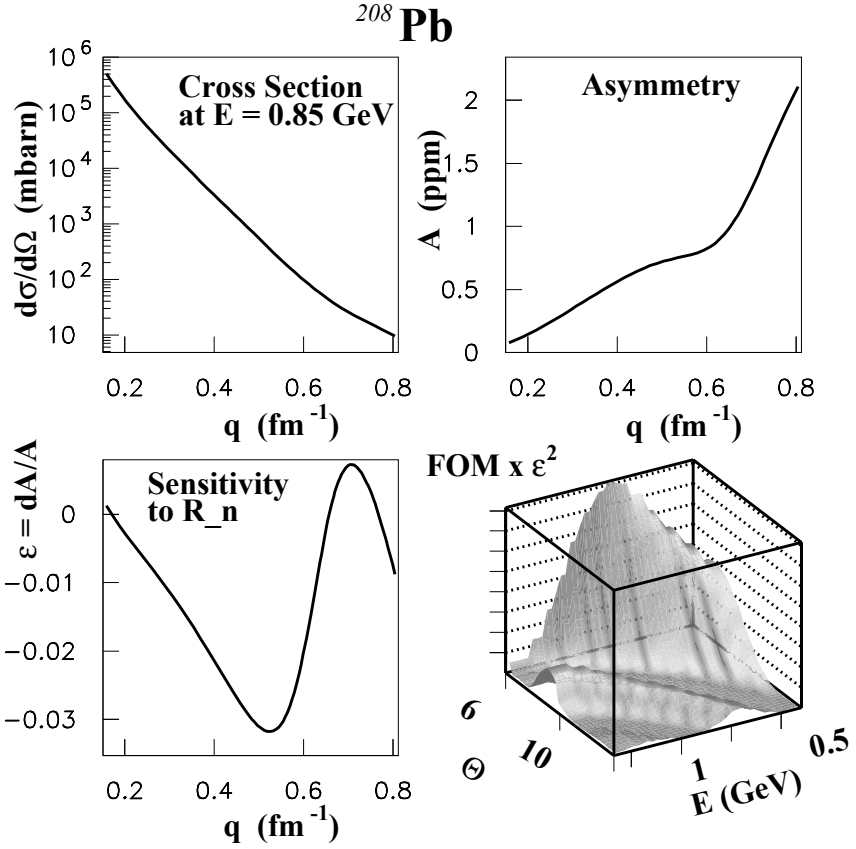

Figure 1.5: Cross section, parity violating asymmetry and sensitivity to R_n for ^{208} Pb elastic scattering as a function of momentum transfer q. The bottom right plot shows the FOM ($\sigma \times A^2 \times \epsilon^2$) with beam energy and scattering angle. One optimal choice at 0.85 GeV beam with 6° scattering angle, corresponding to q=0.45 fm^{-1}. [12]

A more recent MFT calculation for the sensitivity to R_n was carried out [13] and the sensitivities at two fixed beam energies with varying scattering angles is shown in Figure 1.6 and the results are summarized in Table 1.2.

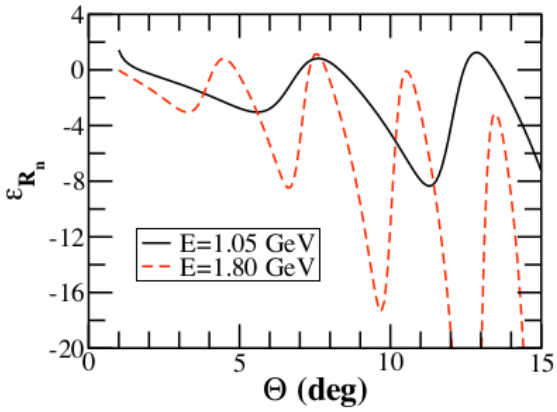

Figure 1.6: Sensitivity of the parity violating asymmetry to the changes of R_n in ^{208}Pb versus scattering angle at beam energies of 1.05 GeV and 1.8 GeV. The SLY4 neutron density was used.[13]

E [GeV]	1.05
θ [°]	5.0
$A_{\rm PV}$ [ppm]	0.719
$\frac{d\sigma}{d\Omega}$ [mb/str]	1339
ϵ	-2.76

Table 1.2: Calculation results from [13] for expected rate and the sensitivity to R_n at 1.05 GeV beam and 5° scattering angle. The neutron and proton densities are calculated in the Skyrme HF theory with the SLY4 interaction.

Based on the sensitivity ϵ, the uncertainty of R_n can be translated from the experimental uncertainty of the measured asymmetry

$$\frac{dR_n}{R_n} = \frac{1}{\epsilon}\frac{dA_{\rm PV}}{A_{\rm PV}}, \tag{1.79}$$

$$\frac{dA_{\rm PV}}{A_{\rm PV}} = \frac{1}{\sqrt{N_{\rm tot}}}/(P \cdot A_{\rm PV}), \tag{1.80}$$

where $N_{\rm tot}$ is the total number of asymmetry patterns collected and the measured asymmetry $P \cdot A_{\rm PV}$ is the product of the longitudinal polarization for the electron beam $P \approx 90$ % and the parity violating asymmetry $A_{\rm PV}$.

The total number of scattered events detected can be estimated from the following

$$N_{\rm tot} = I \cdot T \cdot \rho_{\rm tar} \cdot \frac{d\sigma}{d\Omega} \cdot \zeta \cdot \Delta\Omega \cdot N_{\rm arm}, \tag{1.81}$$

where the beam current I is 70 μA, T is the experiment run time to be optimized, $\rho_{\text{tar}} = 1.6 \times 10^{21}$ cm^{-2} is the number of atoms per target area, $\zeta = 0.34$ is the radiation loss factor, $\Delta\Omega = 0.0037$ sr is the acceptance solid angle of each individual spectrometer arm and $N = 2$ for the two HRS arms configuration in the experimental hall.

To achieve the 1 % accuracy in R_n , a 2.76 % experimental uncertainty in A_{PV} is required and needs approximately 15.4 days beam time

$$T = \Big(\frac{1}{P \cdot A_{\text{PV}} \cdot \frac{\mathrm{d}A_{\text{PV}}}{A_{\text{PV}}}}\Big)^2 \frac{1}{I \cdot \rho_{\text{tar}} \cdot \frac{\mathrm{d}\sigma}{\mathrm{d}\Omega} \cdot \zeta \cdot \Delta\Omega \cdot N_{\text{arm}}} \approx 15.39 \text{ days.} \tag{1.82}$$

Chapter 2

The PREX-2 Experiment

This chapter discusses instrumentation for the PREX-2 experiment. The topics are organized as the voyage of an electron beam in chronological order, starting from the generation of a polarized electron beam to the detection and digitization of scattered electron events. A brief overview of the accelerator facility in Jefferson Lab is given in Section 2.1. The production of a longitudinally polarized electron beam is discussed in Section 2.2 and three techniques for measuring the electron polarization are described in Section 2.3. The hardware and principles of the beam monitors in Hall A are discussed in Section 2.4. The accelerated electrons are transported through the Hall A beamline and interact with the ^{208}Pb foil supported by a target system of which the design is discussed in Section 2.5. Electrons scattered off the target at $4^\circ \lesssim \theta \lesssim 7^\circ$ are guided by a pair of septum magnets and enter the Hall A high resolution spectrometers (HRSs). The magnet arrangement and the tracking system of the HRS are introduced in Section 2.6. The elastically scattered events with the desired kinematics are eventually delivered to the integrating detectors made of fused silica. The signal production of the integrating detector is discussed in Section 2.7. Electron properties measured by the beam monitors and the detectors are digitized and recorded by the data acquisition system of which the framework is outlined in Section 2.8.

2.1 Continuous Electron Beam Accelerator Facility

The PREX-2 experiment was performed in Jefferson Laboratory (JLab) utilizing the Continous Electron Beam Accelerator Facility (CEBAF) in 2019. The maximum design current of CEBAF is 200 μA and the accelerator facility is capable of a simultaneous beam delivery to the four experimental halls shown in Figure 2.1. The CEBAF injector is located in the green box in Figure 2.1.

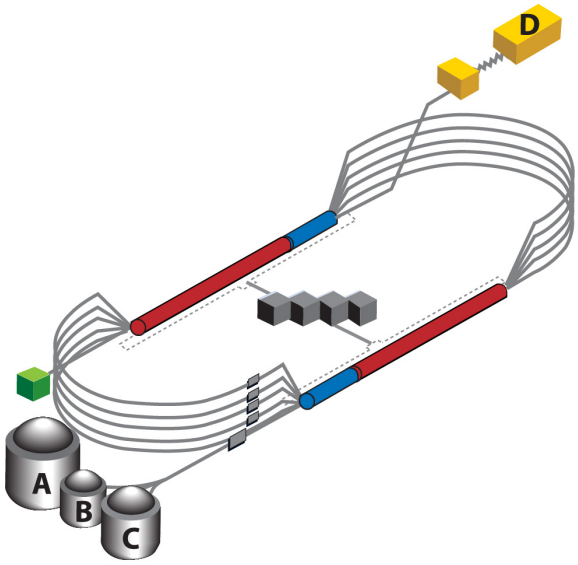

Figure 2.1: CEBAF layout. The four experimental halls A, B, C and D are indicated. The injector of the accelerator is shown as the green box.

The electron source in the injector is a strained Gallium Arsenide (GaAs) photocathode. The photocathode is illuminated by a 1497 MHz 780 nm diode laser. The electron bunches can be split into three 499 MHz bunch trains and enter the desired experimental halls using radio-frequency (RF) separators.

The accelerator has two linear accelerators (linacs), a north linac and a south linac. Each linac contains 200 RF cavities assembled into 25 cryomodules cooled by 2 K liquid Helium-4. The two linacs are joined by 180° circular arcs with magnetic fields. An electron beam gains energy up to 2 GeV with one full pass of the accelerator. During the PREX-2 run, the accelerated beam energy is set to 1 GeV for optimizing the statistical efficiency for the parity violating asymmetry measurement of ^{208}Pb.

2.2 Polarized Electron Beam

A Pockels cell is a voltage-controlled wave-plate to convert linearly polarized light to circularly polarized light. The voltage applied to a Pockels cell affects the birefringent retardation in the Pockels cell crystal therefore changes the degree of polarization of the outgoing photons. The voltage applied to the Pockels cell is controlled by a helicity generator which flips the voltage polarity at a desired rate, e.g. 120 Hz or 240 Hz. In addition, an insertable

$\lambda/2$-plate (IHWP) reverses the sign of the laser polarization.

The strained GaAs photocathode is optically pumped by circularly polarized light to produce polarized electrons, with the ability to rapidly and randomly flip the sign of the electron beam helicity. The strained substrate layer of GaAsP underneath the surface of GaAs breaks the degeneracy of the valence band into two states $P_{1/2}$ and $P_{3/2}$. The polarized photons excite the electrons from $P_{3/2}$ in the valence band to $S_{1/2}$ in the conduction band. This procedure is shown in Figure 2.2. The relatively larger gap between $P_{1/2}$ and $S_{1/2}$ suppresses the probability of $P_{1/2} \rightarrow S_{1/2}$ transition ensuring that only one state in the conduction band is populated.

The longitudinal polarization of an electron beam, P_b, is defined as the difference between the number of electrons that have spin parallel to their momentum, n^+, and the number of those that have spin anti-parallel to their momentum, n^-, normalized by the total number of electron

$$P_b = \frac{n^+ - n^-}{n^+ + n^-}. \tag{2.1}$$

In practice, the longitudinal polarization of the electron beam for the PREX-2 is measured to 90 %.

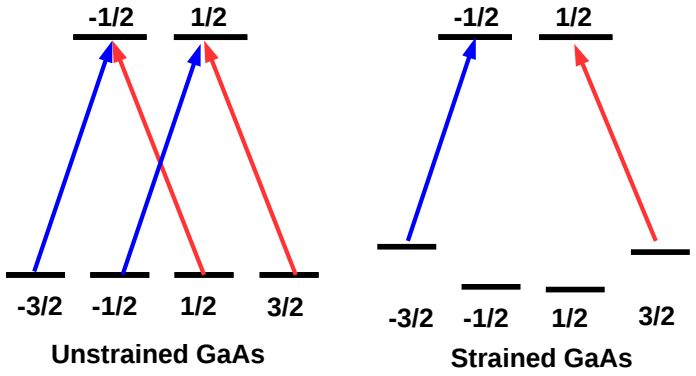

Figure 2.2: The photo-emission process. Blue and red arrows indicate the helicity of photon to cause the transition.

2.3 Beam Polarimetry

The longitudinal polarization of the electron beam for the PREX-2 is measured by three independent experimental setups, a Mott polarimeter near the injector, a Møller polarimeter and a Compton polarimeter in Hall A.

2.3.1 Mott Polarimeter

The Mott polarimeter is located near the injector where the electrons have reached 5 MeV in energy. The Mott polarimeter is based on the scattering of polarized electrons from unpolarized high-Z nuclei. The spin-orbit interaction arises from the electron's spin with the magnetic field due to its motion relative to the target nucleus. Therefore its cross-section depends on the electron spin

$$\sigma_{\text{Mott}}(\theta) = \sigma(\theta)(1 + S(\theta)\vec{P}_e \cdot \hat{n}), \tag{2.2}$$

where $\sigma(\theta)$ is the spin-averaged cross-section, $S(\theta)$ is the Sherman function characterizing the analyzing power of the polarimeter, and $\vec{P}_e \cdot \hat{n}$ is the projection of the electron polarization vector normal to the scattering plane.

Therefore the measurement for the asymmetry of the number of electrons scattered to the left and the right is sensitive to the magnitude of the electron polarization, P_e, with known of the Sherman function $S(\theta)$

$$A(\theta) = \frac{N_L - N_R}{N_L + N_R} = P_e S(\theta). \tag{2.3}$$

The nuclear target of the Mott polarimeter is a 0.1 μm thick gold foil and the scattered electrons reaching the maximum analyzing power at $\theta = 172^\circ$ are detected by four identical plastic scintillators symmetrically around the beamline longitudinal axis. A Wien filter upstream of the polarimeter rotates the electron's spin from longitudinal to transverse polarization for the Mott measurement. The Mott measurement is invasive and requires interruption of beam delivery to all experimental halls.

2.3.2 Møller Polarimeter

The Møller polarimeter in Hall A measures the asymmetry in the electron beam scattering off electrons in the nuclear target. The measured asymmetry A_{meas} depends on the beam longitudinal polarization P_e, the target polarization $\hat{Z}$-component P_{target} and the analyzing power A_{ZZ} of Møller scattering

$$A_{\text{meas}} = P_e \cdot P_{\text{target}} \cdot A_{ZZ}, \tag{2.4}$$

where Z is the direction parallel to the beam. The analyzing power A_{ZZ} is characterized by the scattering process where both beam and target are polarized longitudinally. In the center-of-mass (CM) frame, A_{ZZ} can be calculated from quantum electrodynamics (QED) theory

$$A_{ZZ} = -\frac{\sin^2\theta_{\text{CM}}(7 + \cos^2\theta_{\text{CM}})}{(3 + \cos^2\theta_{\text{CM}})^2}. \tag{2.5}$$

The maximum longitudinal analyzing power -7/9 is reached at $\theta_{\mathrm{CM}} = 90°$. The target of the Møller polarimeter is a magnetized ferromagnetic 99.99 % pure iron foil placed in a 4 T holding field generated by a set of cryogenically cooled Helmholtz coils. The target foil is guaranteed to saturate magnetically in the 4 T field [63, 64]. The Møller spectrometer, shown in Figure 2.3, consists of a series of quadrupole magnets and a dipole magnet. The spectrometer selects electrons in a bite of $78° < \theta_{\mathrm{CM}} < 102°$. Electrons in coincidence are detected by the lead-glass calorimeter modules in two arms.

During the PREX-2 run, the target foil polarization is theoretically constrained to 8.005% and its uncertainty 0.6% is the largest systematic uncertainty in the beam polarization result. The beam polarization is periodically measured using the Møller polarimeter in dedicated low current runs.

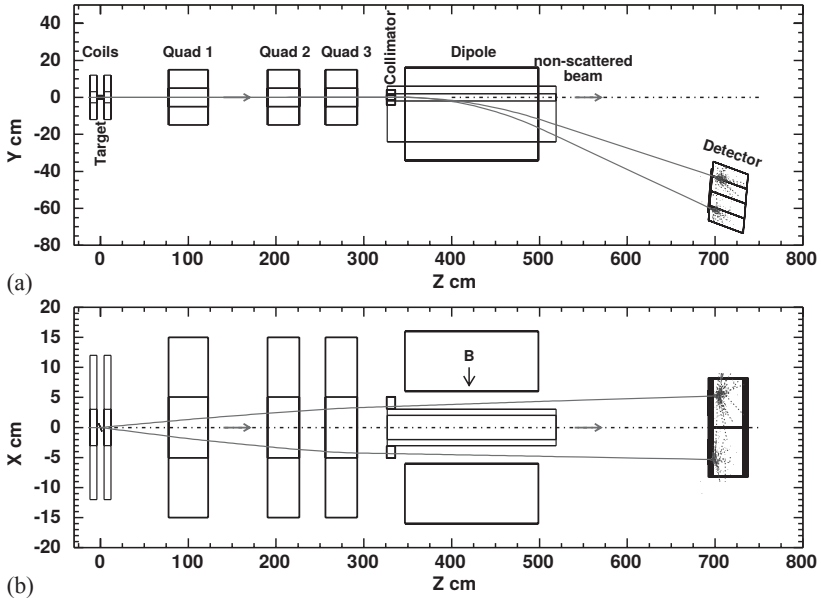

Figure 2.3: Layout of the Hall A Møller Polarimeter

2.3.3 Compton Polarimeter

The Compton polarimeter measures the asymmetry from $e - \gamma$ scattering. The electron beam is transported into the Compton chicane in the Hall A beamline, see in Figure 2.4 and interacts with circularly polarized photons. The beam polarization P_e is extracted from the measured beam-helicity-correlated counting rate asymmetry A_c^{exp} which is the product of the electron beam polarization P_e, the photon polarization P_γ and the theoretical analyzing

power of the Compton polarimeter A_c^{th}:

$$A_c^{\text{exp}} = \frac{N^+ - N^-}{N^+ - N^-} = A_c^{\text{th}} P_\gamma P_e. \tag{2.6}$$

The photon density is amplified by a Fabry-Perot cavity to increase the statistics to measure the Compton cross-section asymmetry of a few percent level given the typical JLab beam energies at a few GeV.

Since less than 10^{-9} of the beam undergoes Compton scattering and the field integral of the magnetic chicane sums up to zero, the Compton polarimeter is a non-invasive measurement and is simultaneously commissioned with physics data production runs.

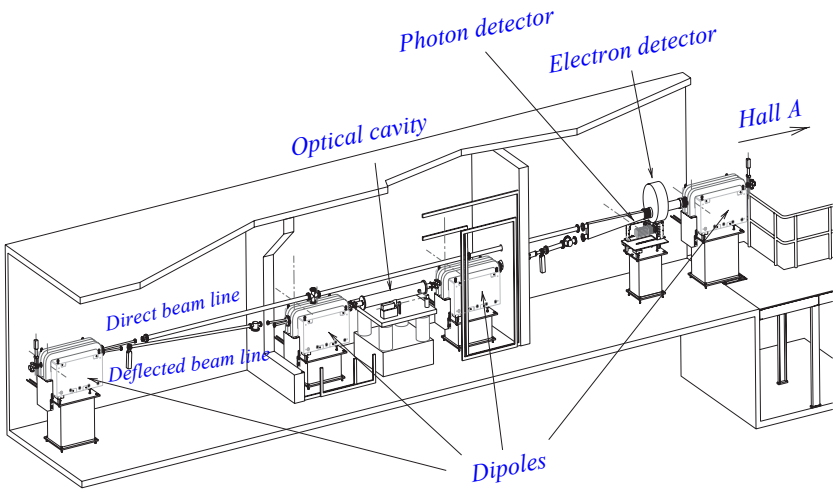

Figure 2.4: Layout of the Hall A Compton Polarimeter

2.4 Beam Monitors

2.4.1 Beam Current Monitors

The Hall A beam current measurement system [65] consists of an Unser monitor, two radio-frequency (RF) cavities, the associated electronics and a data acquisition system. The system layout is shown in Figure 2.5. The two cavities and the Unser monitor are enclosed by one thermally regulated Aluminum shield and three layers of magnetic shields, two of iron and the innermost one of μ-metal.

The Unser monitor is a parametric current transformer, which is a non-invasive absolute current reference. The excessive baseline drift in the Unser monitor limits its capability for

continuous monitoring, therefore the Unser monitor is dedicated as a calibration reference for the upstream and the downstream RF cavities.

The two RF cavities are pill box type stainless steel waveguides, tuned on the 1497 MHz component of the beam current spectrum corresponding to the TE010 mode, which is sensitive to the beam intensity but independent of the beam position. The output signal of a RF cavity is split into two paths. Signal in one of the two paths is down-converted to 10 kHz, reshaped in an RMS-to-DC converter with 50 kHz bandwidth to filter noise, and then further split and transformed independently by voltage-to-frequency (V2F) converters. The frequency of the output from a V2F is proportional to the integrated input voltage level and can be measured as a scaler count.

The other signal split is down-converted to 1 MHz with a 100 kHz bandwidth filter and follows a similar signal processing with the 10 kHz path. The 1 MHz down-converted signal is received by the parity data acquisition system for beam current stability monitoring, detector signal normalization and the feedback control for the beam intensity asymmetry.

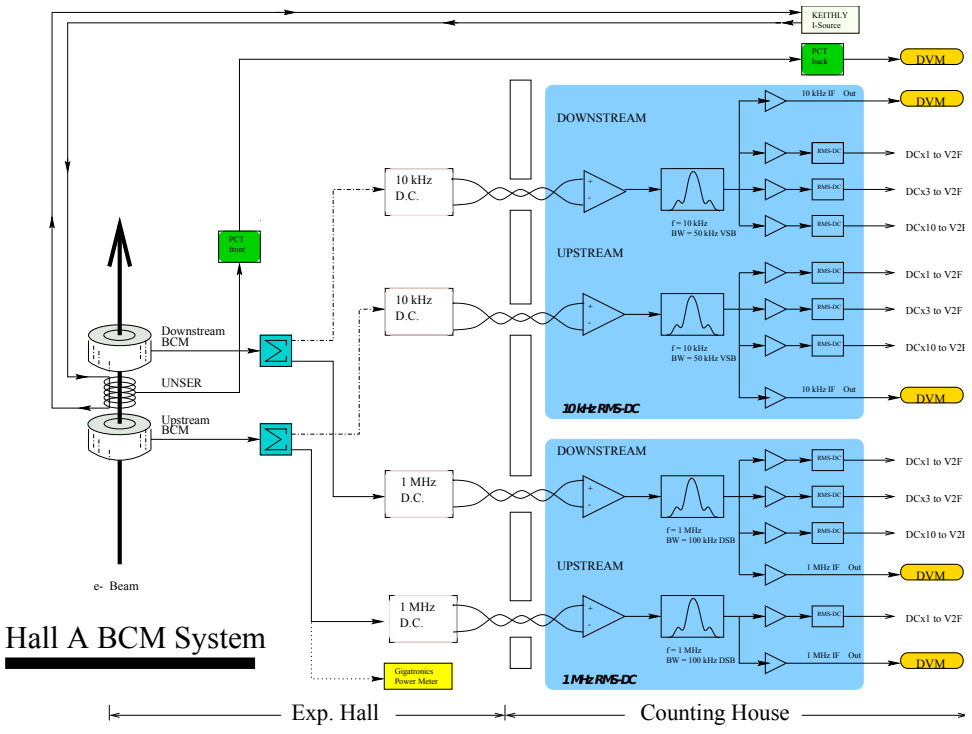

Figure 2.5: Hall A beam current measurement system [14]

2.4.2 Beam Position Monitors

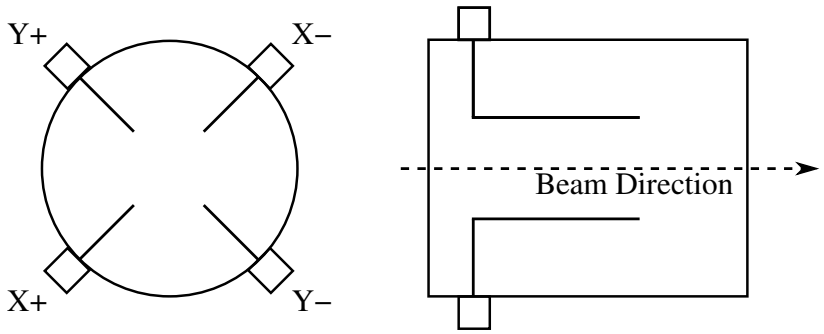

Figure 2.6: Stripline BPM layout [15]

The transverse beam position at a location in the beamline is measured from the signals of four open-ended antennas in the stripline type Beam Position Monitor(BPM). The four antennas are placed inside the BPM chamber with 90° intervals to each other and are schematically illustrated in Figure 2.6. The BPM coordinate is rotated by 45° around the beam pipe longitudinal axis with respect to the Hall coordinate to reduce the exposure to synchrotron radiation.

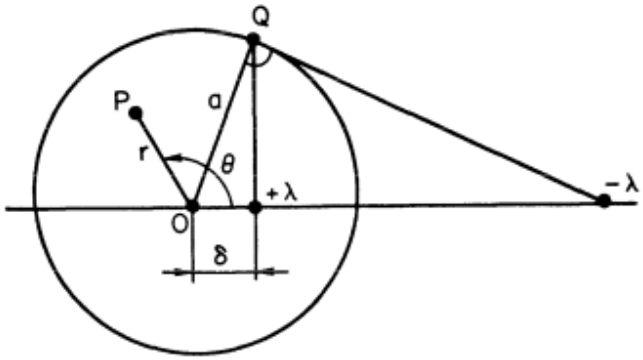

Figure 2.7: Coordinate system for the field calculation [16].

The signal received in each antenna is a function of chamber radius a, beam intensity I and beam position (δ, θ) and can be calculated from the image charge method [16] using the coordinate system shown in Figure 2.7

$$\phi_i \propto I \frac{a^2 - \delta^2}{a^2 + \delta^2 - 2a\delta\cos\theta}, \tag{2.7}$$

where δ is the distance from the electron to the center of the BPM chamber and θ is the angle of the electron relative to the antenna. The Δ/Σ ratio of each pair of diagonal antennas is sensitive to the beam position projected to the diagonal line denoted as (u, v), and with $\delta \ll a$ approximation

$$\frac{\phi_{u+} - \phi_{u-}}{\phi_{u+} - \phi_{u-}} = \frac{2}{a}\frac{a\cos\theta}{1+\delta^2/a^2} = \frac{2}{a}\frac{u}{1+\delta^2/a^2} \Rightarrow \; u \approx \frac{a}{2}\frac{\phi_{u+} - \phi_{u-}}{\phi_{u+} - \phi_{u-}}, \tag{2.8}$$

To calculate the actual beam position in the Hall $x - y$ coordinates, beam position in the BPM $u - v$ coordinate is rotated by 45°

$$\begin{pmatrix} x \\ y \end{pmatrix} = \begin{pmatrix} \cos 45^\circ & -\sin 45^\circ \\ \sin 45^\circ & \cos 45^\circ \end{pmatrix} \begin{pmatrix} u \\ v \end{pmatrix}. \tag{2.9}$$

The beam position measurement using BPMs is a critical input for the beam modulation control and the correction for the beam-induced fluctuations in the detected asymmetry.

2.5 Target System

The PREX-2 target system shown in Fig. 2.8 has a 45 ° arm, which holds targets for optics calibration and is cooled by water at room temperature, and an arm installed horizontally holding targets for the parity production mode. The horizontal arm is cooled by 15 K Helium flow at 10 g/sec rate, which is sufficient to provide 120 W cooling power [24].

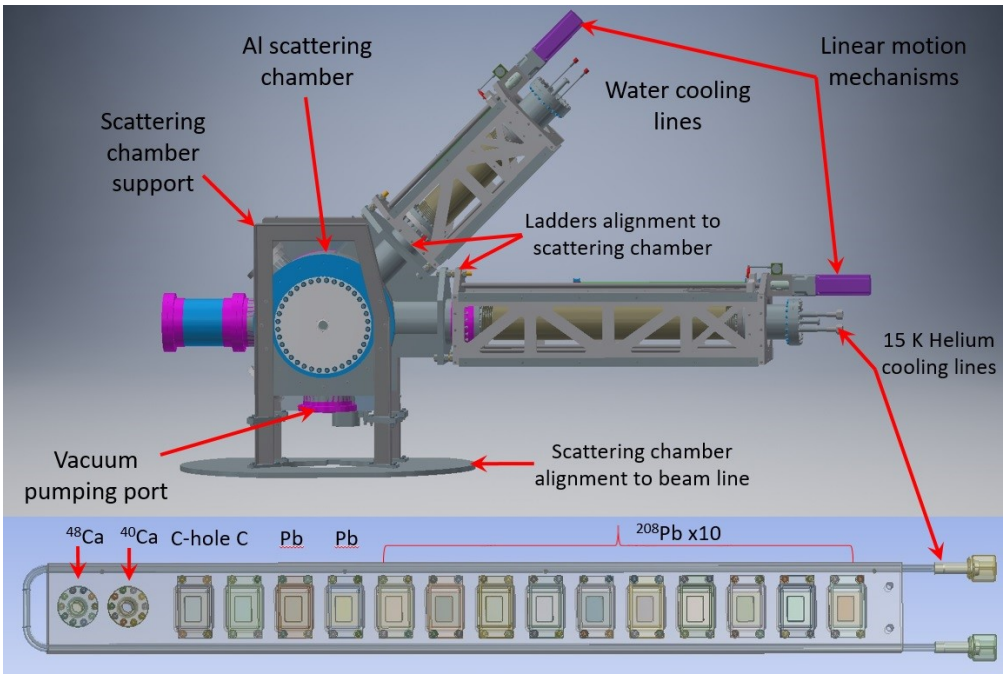

Figure 2.8: The PREX-2 Target CAD drawing.

Ten ^{208}Pb foils sandwiched by diamond or carbon foils were prepared by the JLab target group and are listed in Table 2.1. As shown in Table 2.2, diamond has a thermal conductivity better than 1000 W/(m·K) which improves heat transfer and establishes a gentle temperature gradient acrossing the surface of the target. Meanwhile it only produces a relative small amount of heat 13.5 W, compared with 70 W for the main target, see in the last column in Table 2.1.

Target	CAD position(mm)
C-208Pb1-C	667.3
DA-208Pb2-DB	591.1
DC-208Pb3-DD	553
DE-208Pb4-DF	514.9
DG-208Pb5-D20	476.8
D1-208Pb6-D2	438.7
D3-208Pb7-D4	400.6
D5-208Pb8-D6	362.5
D7-208Pb9-D8	324.4
D9-208Pb10-D10	286.3

Table 2.1: List of PREX-II ^{208}Pb target. "C" stands for carbon foil while "D" stands for diamond foil.

	T_{melt}	ρ	c_p	k	L	$\mathrm{d}E/\mathrm{d}x$	I	P_{beam}
unit	K	g/cm^3	J/(kg·K)	W/(m·K)	mm	Mev/(g·cm^2)	μA	W
Pb	600	11.34	130	35	0.55	1.6	70	70
Diamond	5000	3.51	435	>1000	0.25	2.2	70	13.5
Carbon	3923	1.83	700	150	0.25	2.2	70	7

Table 2.2: The installed target material properties reproduced from Ref. [24]

The heating power from an electron beam interacting with the target material can be calculated based on [66]

$$P_{\text{beam}} = \rho \cdot \frac{\mathrm{d}E}{\mathrm{d}x} \cdot L \cdot I, \tag{2.10}$$

where ρ, L are the mass density and the thickness of the target, $\mathrm{d}E/\mathrm{d}x$ is the electron energy loss along its path in the target and I is the beam current. And the temperature rise on the

target by beam heating is

$$\Delta T = \frac{P_{\text{beam}} - P_{\text{cool}}}{M \cdot c_p} \cdot t, \tag{2.11}$$

where M is the mass of the target intercepted with the electron beam so it depends on the beam raster size $d_x \times d_y$

$$M = d_x \cdot d_y \cdot L \cdot \rho. \tag{2.12}$$

Although Eq. (2.11) suggests so long as the cooling power meets the balance, the temperature rise in the target will be zero when the heat transfer reaches thermal equilibrium, an instantaneous change in the beam spot size or beam position would produce local heating which takes a considerable amount of time to diffuse before a new thermal equilibrium is established. For this case, the beam raster system plays a key role in reducing instant local heating. The technical details of the beam raster system will be discussed in Section 3.5.

2.6 High Resolution Spectrometer

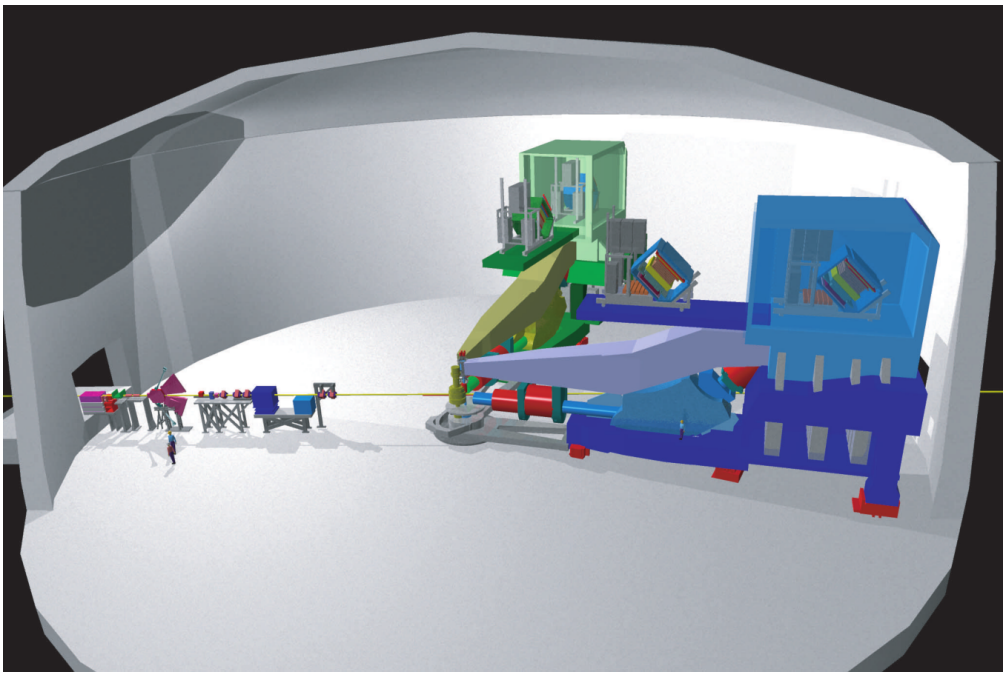

Figure 2.9: Hall A Layout [14]

The pair of High Resolution Spectrometer (HRS) arms in Hall A, shown in Figure 2.9 is designed to study electromagnetic interactions and hadronic structures with high precision. Both HRSs on the left and the right can be rotated independently around the Hall A pivot

from 12.5° upto 150°. During the PREX-2 run, the two HRSs are both parked at 12.5° to accept the scattering flux at 5° transported from a pair of septum magnets.

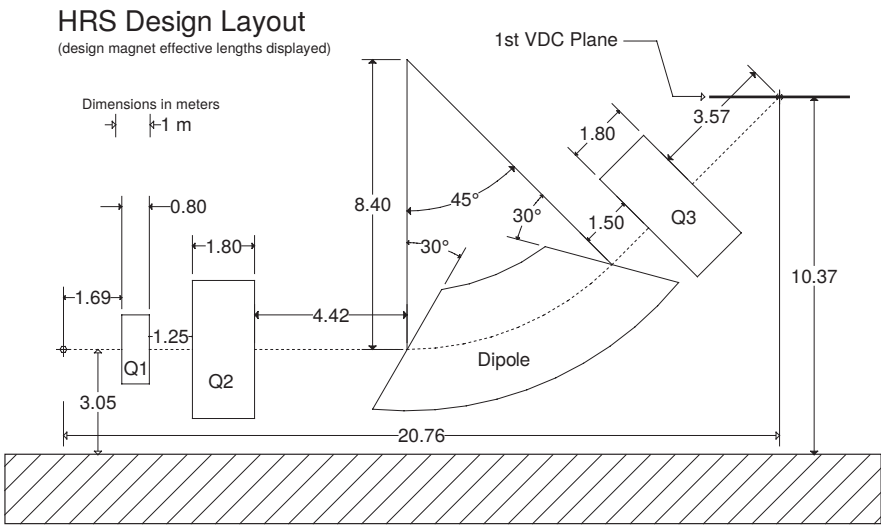

Figure 2.10: HRS layout [17]

The HRS layout is shown in Figure 2.10, each HRS has four superconducting magnets: three quadrupoles (Q) and one dipole (D). The QQDQ magnet layout achieves a high momentum resolution at the 10^{-4} level over the 0.8 GeV/c to 4.0 GeV/c momentum range and a good position and angular resolution in the scattering plane. The first quadrupole (Q1) is used to focus the scattered electrons in the dispersive direction and the last two quadrupoles (Q2 and Q3) focus in the non-dispersive direction. The dipole is mainly used to bend the electron trajectory by 45° for a good momentum resolution.

The position and angle of charge particles at the focal plane are recorded by the vertical drifting chambers (VDCs). Two VDCs locate approximately 3.5 m downstream of the Q3 exit and separate by a vertical distance of 0.335 m to each other, see in Figure 2.11. Each VDC chamber consists of two wire planes in the standard UV configuration. The particle's central trajectory crosses the wire planes at an angle of 45° vertically.

The electric field of the VDCs is shaped by gold-plated Mylar planes at - 4.0 kV while the sensing wires are grounded. The chamber is circulated with the gas mixture of argon and ethane. Ionized electrons are accelerated by the electric field and collected at the sensing wires producing the timing and coordinate information of the charged particles passing through.

During the PREX-2 run, a momentum resolution of 0.6 MeV [37] was achieved and

ensured that the closest inelastic state of 208Pb at 2.6 MeV was not intercepted by main detectors, see in Figure 2.12.

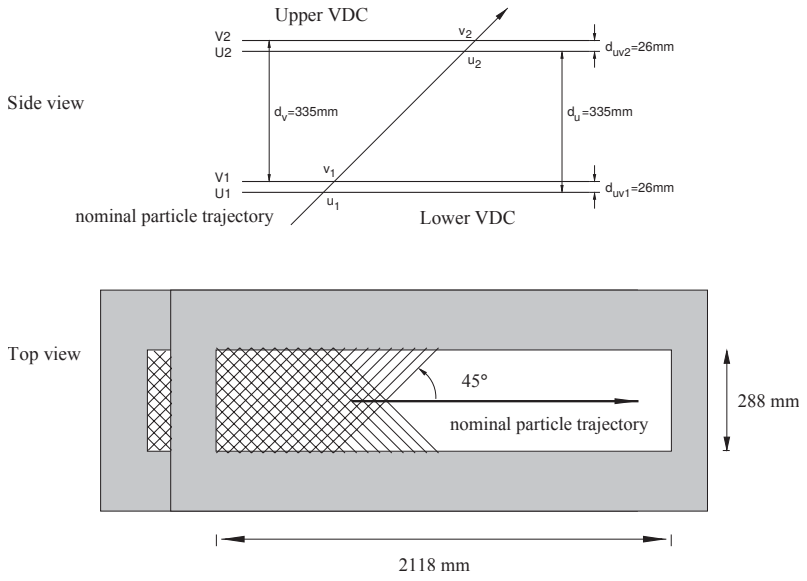

Figure 2.11: HRS VDC schematic drawing. [18]

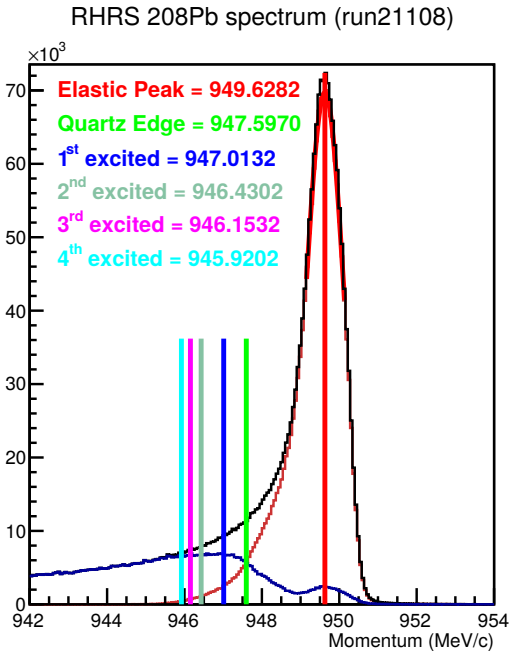

Figure 2.12: An example of Right HRS momentum spectrum for ^{208}Pb [19].

2.7 Integrating Detectors

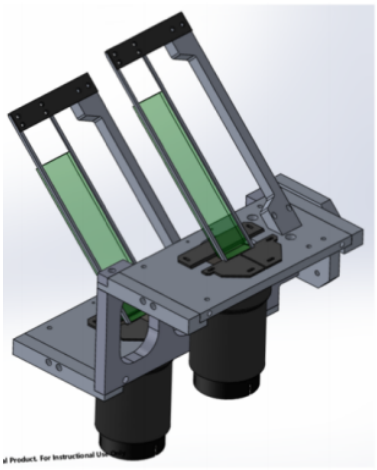

Figure 2.13: the PREX-2 main detector CAD drawing

The scattered electrons are detected by two identical fused-silica tiles ($16 \times 3 \times 0.5$ cm^3) in the integrating mode in each HRS, shown in Figure 2.13. The upstream tile provides the main measurement while the downstream one is for redundancy. The long side of the tile is orientated along the dispersive direction and approximately 7 cm of its full length is used to sample the elastically scattered electrons, see in Figure 2.14. Events in excited states falling outside of the quartz edge are not accepted by main detectors.

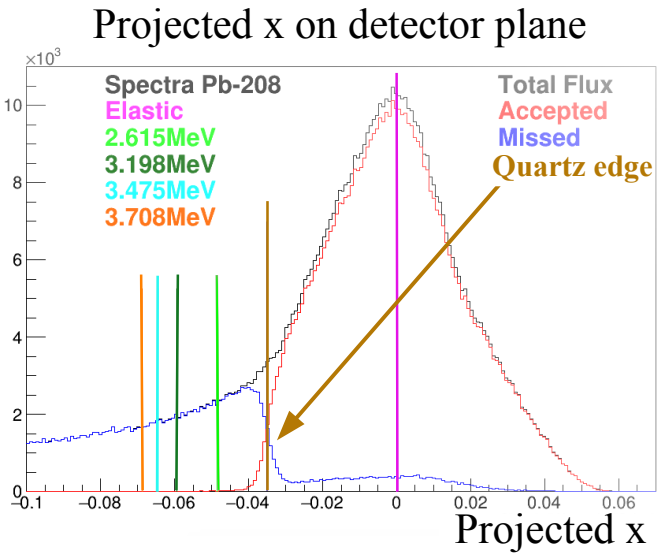

Figure 2.14: Data sampled in counting mode are projected in the dispersive direction (x) in meters to the detector plane. This figure is adapted from [20].

The Cherenkov light is produced in the tile when scattered electrons passing through and is collected by a Hamamatsu® R7723 2.5" photomultiplier tube (PMT) attached to each tile on the far end from the beam spot.

The expected signal yield of the PMT $\langle s \rangle$ is the product of the number of electrons N detected by the fused-silica tile within a given time, the electron deposited energy in the fused-silica E, the Cherenkov light collection efficiency η, the photocathode quantum efficiency Q_E and the PMT dynode stages multiplicative gain g

$$\langle s \rangle = N \cdot E \cdot \eta \cdot Q_E \cdot g = N \cdot E \cdot k, \tag{2.13}$$

where $k = \eta \cdot Q_E \cdot g$ quantifies the PMT signal production per unit amount of energy deposited in the detector.

Assuming the Cherenkov light yield and collection is an identical process for each single electron, the total PMT signal yield is then the sum of light production of N electrons

$$s = k \sum_{i=1}^{N} E(i). \tag{2.14}$$

The random fluctuation width in the PMT signal σ_s is characterized by a Poisson distribution convoluted with a Landau distribution originated from the electron energy loss in the material,

$$\sigma_s^2 = \sigma_L^2 + \sigma_{\text{count}}^2, \tag{2.15}$$

where σ_L and σ_{count} represent the 1-σ standard deviation induced by the random energy loss and the counting statistics respectively.

The total fluctuation from the random energy loss can be expressed as contributions from each individual electron

$$\sigma_L^2 = k^2 \sum_{i}^{N} \sigma_E^2 = k^2 N \sigma_E^2, \tag{2.16}$$

where σ_E is the actual fluctuation in energy dimension which contributes the observed fluctuation σ_L in the detector signal scaled by the PMT signal production coefficient k and the amount of the detected electrons N. The ratio $\sigma_E / \langle E \rangle$ is also known as the detector energy resolution.

The Poissonian counting fluctuation is

$$\sigma_{\text{count}}^2 = k^2 \langle E \rangle^2 \sigma_N^2 = k^2 \langle E \rangle^2 N, \tag{2.17}$$

where the variance of a Posson distribution σ_N^2 is known to be its mean N.

For an asymmetry measurement using detector signal s

$$A = \frac{s^+ - s^-}{2\langle s \rangle}, \tag{2.18}$$

with $s^+ - s^- \ll s$, the random fluctuation in A can be calculated from error propagation

$$\begin{aligned}
\sigma_A^2 &= \frac{1}{2\langle s\rangle^2}\sigma_s^2 \\
&= \frac{1}{2\langle s\rangle^2}\Big(\sigma_L^2 + \sigma_{\text{count}}^2\Big) \\
&= \frac{1}{2N\langle E\rangle^2}\Big(\sigma_E^2 + \langle E\rangle^2\Big) \\
&= \frac{1}{2N}\Big[1 + \Big(\frac{\sigma_E}{\langle E\rangle}\Big)^2\Big], \qquad (2.19)
\end{aligned}$$

which indicates the dilution effect from the finite detector energy resolution to the statistical power of the asymmetry measurement. The energy resolution of the fused-silica used in PREX-2 is measured to 20% and the dilution factor is

$$\sqrt{1 + \Big(\frac{\sigma_E}{\langle E\rangle}\Big)^2} = 1.019, \qquad (2.20)$$

which is less than 2%.

2.8 Parity Data Acquisition System

CEBAF Online Data Acquisition (CODA) is the framework commonly used for acquiring experiment data in Jefferson Lab. The system is scalable for different applications from a test stand with a few detector channels to a full scale detector with tens of thousands independent channels. The most common format of the front-end electronics digitizing data is based on the Versa Module Europa bus (VMEbus).

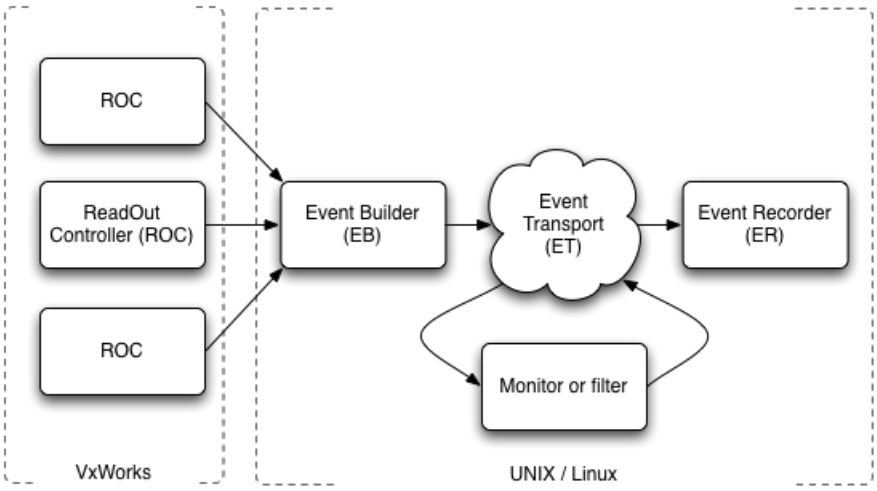

Figure 2.15: An example of CODA implementation [21]

Figure 2.15 shows the main components of the CODA back-end: the Read-Out Controller (ROC), the Event Builder (EB), the Event Transport (ET) and the Event Recorder (ER). Every front-end crate, e.g. a VME or CAMAC crate, contains a single board computer running a realtime operating system, such as VxWorks. The ROC runs on this single board computer and is programmed to process events and send data to the EB. The information of events from multiple ROCs are collected and re-formatted in the EB then is received by the ET which moves events efficiently from one Unix process to another on the same CPU or across the network. The ET station is also where online processing launches. The ER assembles events from the ET and writes them to a storage disk.

During the PREX-2 run, four ROCs located at the injector, the Hall A counting house, the left HRS and the right HRS are connected in the same network. Data stream from these four ROCs is synchronized and transferred to the same ER and written to the same data file stored in a hard disk.

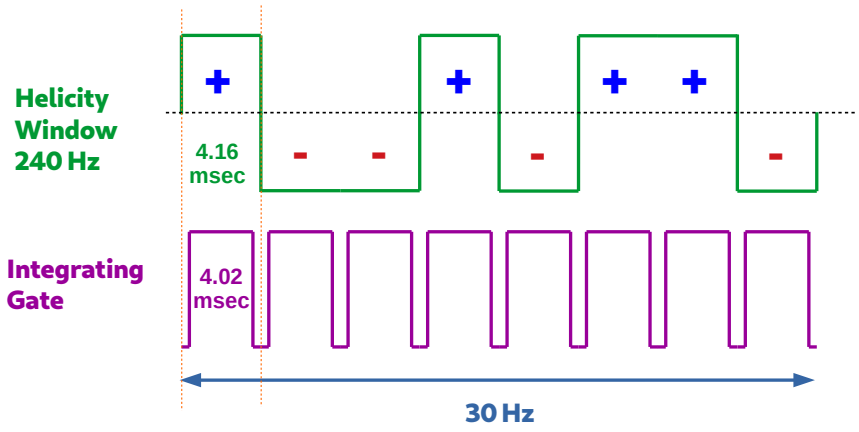

Figure 2.16: Integrating DAQ timing diagram for 240 Hz octets.

Regarding the timing for the parity data acquisition (DAQ), the parity DAQ receives a trigger constantly at 240 Hz or 120 Hz from the helicity control board. The top panel in Figure 2.16 shows an example of a complete 240 Hz octet pattern. The helicity control board switches the voltage polarity applied to the Pockels cell based on the generated pseudo-random binary sequence. To avoid the direct helicity pickup via hardware cross-talk, helicity pulses are first delayed by 8 helicity windows then sent to the parity DAQ and other timing control units. A macro-pulse (MPS) signal indicates the beginning of a helicity window. In addition, a timing signal named "PairSync" is used to distinguish between the first and the second windows of a helicity windows pair. The HAPPEX timing board receives the MPS and instructs ADC units and scalers in the parity DAQ with timing of the integrating gate. The timing of the integrating gate relative to helicity windows is shown in Figure 2.16.

The customized VQWK ADC unit integrates the signal within each integrating gate and is capable of over-sampling at four times of the trigger rate for diagnostic purposes.

Chapter 3

Experimental Technique

Topics in this chapter are selected to discuss the experimental technique closely related to the systematic control in the PREX-2 run. Section 3.1 discusses the effect of the helicity sequence arrangement for the power line 60 Hz noise cancellation as well as any other periodic perturbation. Section 3.2 focuses on the additional cancellation of possible systematic effects using the insertable half-wave plate and double Wien filters in the accelerator injector. Section 3.3 covers the hardware and the timing structure of the beam modulation control system, while the beam modulation analysis will be discussed and compared with other beam correction techniques in Section 5.3. The pedestal and linearity calibrations for the beam current monitors and the integrating detectors are reviewed in Section 3.4. The PREX-2 beam raster system is described in Section 3.5. Section 3.6 reviews the offline analysis software developed for PREX-2.

3.1 Pseudo-random Rapid Helicity Reversal

The key components of the pseudo-random rapid helicity reversal are

1. The helicity sign flips rapidly at a multiple mode of 60Hz, e.g. 120 Hz or 240 Hz.
2. Sequences of the helicity sign form a reversal within each 30 Hz DAQ window, e.g. an octet with sequence $+--+-++-$ or a quartet with sequence $+--+$.
3. The polarity of a whole octet or quartet pattern, e.g. $+--+$ or $-++-$ for a quartet pattern, is determined by a pseudo-random number generator at 30 Hz.
4. Communication between the helicity control board and the data acquisition electronics is delayed from the electronically isolated injector controls by multiple full 30 Hz patterns.

The 60 Hz power line noise can be picked up by electronic devices, e.g. ADC channels, and introduces fluctuations if the helicity sequence is not chosen carefully. Possible choices of the helicity sequence are the 120 Hz quartet and the 240 Hz octet. Though these two helicity sequence have the same cancellation effect on the 60 Hz noise, their suppression for the lower harmonic components, e.g. 30 Hz and 15 Hz, are different, see Table 3.1 calculated from the analytical integration approach ignoring the hardware deadtime:

	f =60 Hz	f =30 Hz	f =15 Hz
120 Hz quartet	0	$0.64B\sin\phi$	$-0.26B\cos\phi$
240 Hz octet	0	$-0.26B\cos\phi$	$-0.05B\sin\phi$

Table 3.1: Analytical calculation for noise cancellation for the two helicity sequences. All calculations assume the same sine wave electronic noise $s(t) = B\sin(2\pi ft + \phi)$ and vary with three frequencies. In all these examples, helicity sequences always start with a positive helicity.

An example of this calculation is shown below for the 15 Hz noise cancellation with 240 Hz octets. The i-th ADC integrated sample over ~ 4.16 msec at 240 Hz is

$$F(i) = \frac{1}{T}\int_{(i-1)/240}^{i/240} B\sin(2\pi\cdot 15\cdot t+\phi)\mathrm{d}t, \tag{3.1}$$

and the helicity-correlated octet difference in the first half of 15 Hz cycle

$$\begin{aligned}\Delta F &= \frac{1}{8}[F(1)-F(2)-F(3)+F(4)-F(5)+F(6)+F(7)-F(8)]\\ &= -\frac{2(1-2\cos\frac{\pi}{8}+2\sin\frac{\pi}{8})}{\pi}B\sin\phi\approx -0.05\cdot B\sin\phi.\end{aligned}$$

In general, a higher helicity flip rate leads to a better suppression for the time dependent noise, e.g. the harmonic noise and the slow baseline drift. The effect of sampling sequence on the slow baseline drift has been discussed in the Ref [67] where the drifting baseline is characterized by high-order series in the Taylor expansion of the signal in the time domain. Limitations for higher helicity flip rate are the ADC maximum sampling rate, the network capacity for data transfer, the disk read/write speed and the Pockels cell settle time for each HV polarity transition.

Although ground loop isolation is implemented through the entire network of the helicity control and the parity DAQ system, a direct communication between the helicity control board and the ADC electronics potentially could introduce a non-zero false asymmetry in the measured parity-violating asymmetry.

Techniques to eliminate the helicity-correlated false asymmetry are alternating helicity pattern polarity pseudo-randomly and delaying helicity signal by multiple full patterns before being acquired by the DAQ hardware. The following example (Table 3.2) describes this effect and assumes the helicity sign dependent noise has a constant strength δ, which is the electronic pick-up from the helicity control signal seen by the ADC electronics.

Event Number	1	2	3	4
Real-time Helicity	+	-	-	+
Delayed Helicity 1	+	-	-	+
Helicity Pick-up 1	δ	-δ	-δ	δ
Delayed Helicity 2	-	+	+	-
Helicity Pick-up 2	-δ	δ	δ	-δ

Table 3.2: An example of helicity pickup with delayed helicity quartets.

In Table 3.2, the real-time helicity is the actual helicity of an event, from which the parity-violating asymmetry is calculated. The delayed helicity is the signal seen by the ADC channel at the same time. Since the pattern polarity is pseudo-randomly chosen, the delayed helicity can either coincide with or differ from the real-time helicity. Both cases are enumerated in the table as "Delayed Helicity 1" and "Delayed Helicity 2". The sign of the pick-up noise follows the signal seen at present, which is the delayed helicity signal sent to the ADC.

For Case 1 where the delayed helicity sequence happens to be the same with the actual one, the noise in the helicity-correlated difference form is

$$\Delta_1 = \frac{1}{4}[\delta - (-\delta) - (-\delta) + \delta] = \delta. \tag{3.2}$$

This is also the situation when the helicity signal is not delayed. Likewise for Case 2, the noise can be calculated in the same manner

$$\Delta_2 = \frac{1}{4}[(-\delta) - \delta - \delta + (-\delta)] = -\delta. \tag{3.3}$$

Case 2 could also be the case when the helicity sequence is delayed, but not pseudo-random.

With pseudo-random and delayed helicity patterns, for all events, 50% of them meet the delayed helicity signal with the same polarity while the other 50% meet the complementary delayed signal, thus the expectation value of the helicity pickup sums up to zero

$$\langle\Delta\rangle = 0.5 \cdot \Delta_1 + 0.5 \cdot \Delta_2 = 0. \tag{3.4}$$

Though in this example, the real-time helicity sequence is specifically $+--+$, the conclusion is also true for real-time helicity sequence $-++-$. Also, the same conclusion applies for 240 Hz octets.

3.2 Slow Reversal

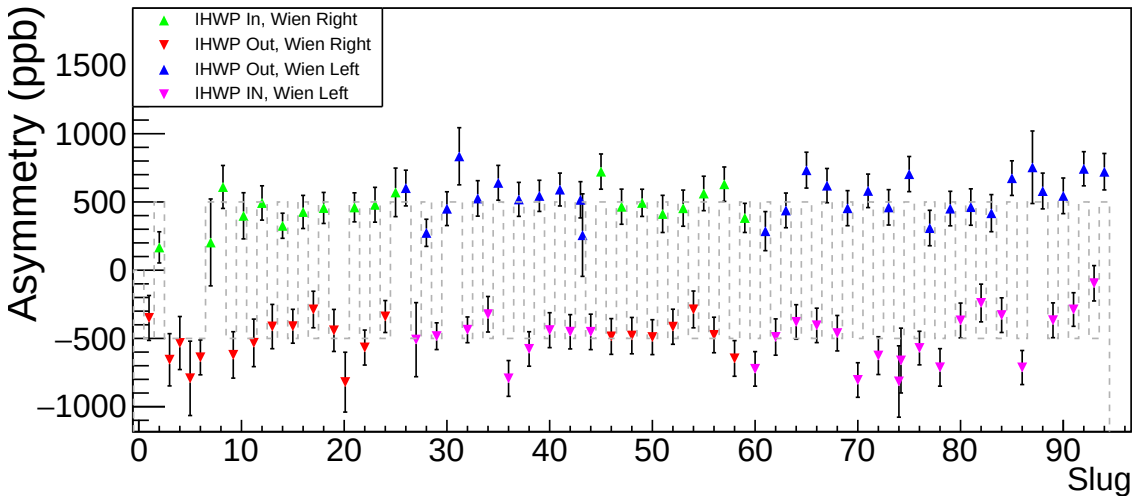

Figure 3.1: Slug averages of the beam corrected asymmetry using Lagrange multiplier regression without sign correction.

In contrast to the rapid helicity reversal, the slow reversal happens about every 8 hours to change the sign of the measured asymmetry. During the PREX-2 run, the slow reversal is done by changing the laser polarization or manipulating the electron spin directly in the injector. An insertable half-wave plate (IHWP) is toggled to be IN or OUT approximately every 8 hours to flip the sign of the laser polarization with respect to the polarity of the HV on the Pockels cell. Data taken between each IHWP state reversal are combined into "slugs". In addition, the double-Wien filter in the injector add 180° spin precession to the electrons. The Wien setting was changed twice during the PREX-2 run. Amounts of data for each IHWP/Wien combination are approximately equal and provide critical cancellation of the systematic beam asymmetry and potential sources of spurious asymmetry in the grand average. The slug-wise history of the slow reversal for PREX-2 is shown in Figure 3.1 where the data points are the beam corrected asymmetries without sign correction for the state of the half-wave plate and the setting of the double-Wien filter.

The effect of the slow reversal on the measured asymmetry is demonstrated in Table 3.3. A potential source of false asymmetry δ_0 does not change its sign with IHWP or Wien setting.

The other false asymmetry term δ_1 changes its sign with the IHWP status, therefore the IHWP reversal alone is not sufficient to cancel this effect. With IHWP and Wien reversals, both δ_0 and δ_1 are cancelled out in the average of the sign corrected asymmetries and the parity violating asymmetry $A_{\rm PV}$ is recovered.

	IHWP	Wien	Measured Asymmetry	Sign Corrected Asymmetry
1	IN	RIGHT	$+A_{\rm PV} + \delta_0 + \delta_1$	$A_{\rm PV} + \delta_0 + \delta_1$
2	OUT	RIGHT	$-A_{\rm PV} + \delta_0 - \delta_1$	$A_{\rm PV} - \delta_0 + \delta_1$
3	IN	LEFT	$-A_{\rm PV} + \delta_0 + \delta_1$	$A_{\rm PV} - \delta_0 - \delta_1$
4	OUT	LEFT	$+A_{\rm PV} + \delta_0 - \delta_1$	$A_{\rm PV} + \delta_0 - \delta_1$
	Grand Average		δ_0	$A_{\rm PV}$

Table 3.3: Example of noise cancellation by slow reversals.

3.3 Beam Modulation System

The sensitivity of the detector response to the beam is calibrated by beam parameter modulation and is used as an input for the systematic correction to the measured asymmetry for beam fluctuations. The beam modulation system intentionally varies beam parameters concurrently with production data taking. Relevant parameters are the beam positions in x and y projected to the target, the beam angles respect to the x and y directions and the beam energy. Beam positions are measured at two points in the field free region, 1.7 m (BPM 4e) and 5.7 m (BPM 4a) upstream of the target and at a point of high dispersion in the magnetic arc leading into Hall A, as well as several other locations along the Hall A beamline for redundancy.

The energy of the beam is varied by the control voltage for the vernier input [68] on SL20, a RF cavity in the accelerator's South Linac. To vary beam positions and angles, six air-core corrector coils in the Hall A beamline upstream of the dispersive arc are chosen according to the beam transport optics to fully span the beam parameters phase space using only four of the six coils. The additional two coils are for redundancy so that the orthogonality and completeness of a four-coil measurement can be cross validated. The coils are driven by power supply trim cards with separate control voltage inputs to regulate the amplitude and time steps of their field strength independently. The relative location of BPMs and coils for the beam modulation system are shown in Figure 3.2.

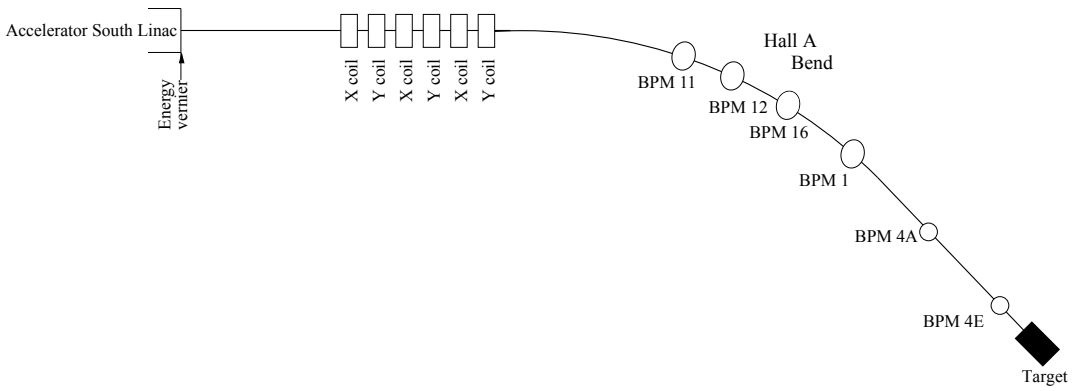

Figure 3.2: Schematic diagram of the Hall A beamline with BPMs and coils for the beam modulation system. The relative positions are not to scale in this plot. This diagram is modified from [22].

The three coils controlling the horizontal perturbation are labeled with numbers 1, 3 and 5, while numbers 2, 4 and 6 are associated with the coils for the vertical perturbation. Number 7 is assigned to the unique vernier input for the beam energy modulation. The typical peak-to-peak beam deflection at BPMs is $\approx \pm$ 200 μm and is apparent over the BPM resolution ($\approx$ 0.5 μm) and intrinsic beam fluctuations ($\approx$ 100 μm). For example, Figure 3.3 shows the BPM 4eX responses in one full supercycle and data points from different coil modulations are distinguished by color. For reference, the intrinsic beam fluctuations in BPM 4eX sampled when beam modulation is paused are shown in gray. When vertical modulations (Coil 2,4,6) and vernier modulation (Coil 7) are activated, the peak-to-peak amplitude in BPM 4eX stays at a similar level as the intrinsic fluctuations, as expected. When horizontal modulations are operating, the peak-to-peak amplitude in BPM 4eX increases upto $\pm$ 300 μm (relative to the central position).

The 6 coils and the vernier input are modulated in sequence. One period of a coil cycle consists of 16 (8) steps at the 240 Hz (120 Hz) sampling rate and forms a sine wave, see in Figure 3.4. A complete cycle for one coil repeats the sine wave for 50 periods, equivalently 3.33 seconds in duration. A supercycle is a group of modulation cycles throughout the six air-core coils and the vernier input with pauses for 16.4 sec between cycles. Each supercycle lasts for 2 minutes with a duty factor of 16.6 % and then idles in the next 10 minutes for production data taking. The duty cycle of each coil in a full supercycle is illustrated in Figure 3.5.

Details on the beam modulation sensitivity extraction and its analysis will be discussed

in Section 5.3.

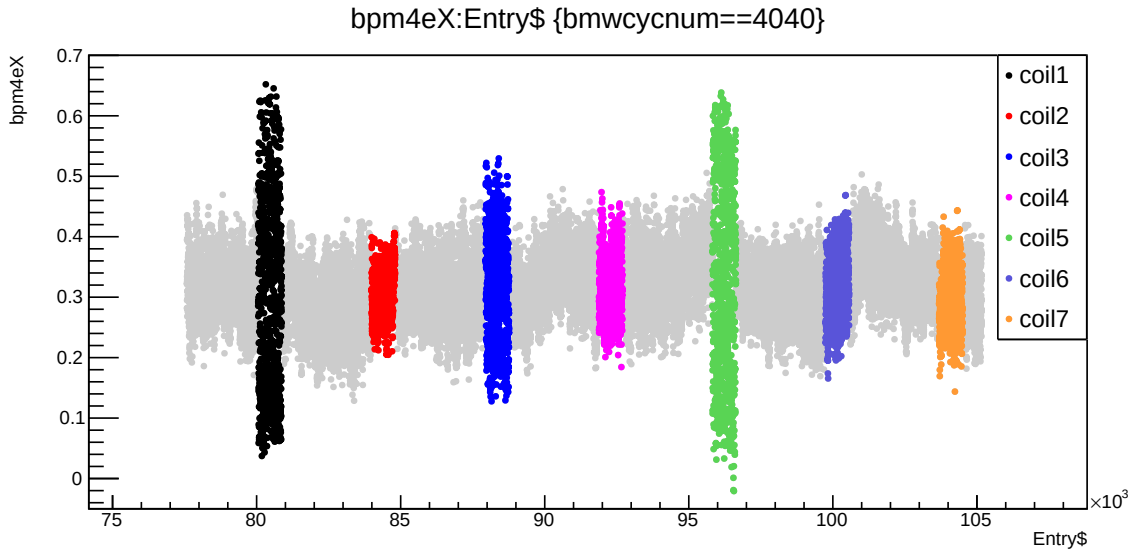

Figure 3.3: Transverse beam position in x at BPM 4e. The unit of y-axis is mm. The length of the time window in this plot is 2 minutes. Data points in gray are taken when beam modulation is paused.

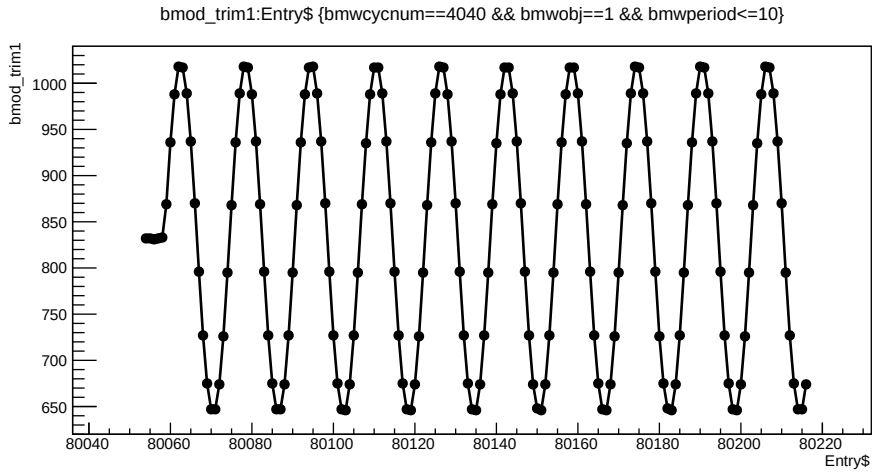

Figure 3.4: Modulation control signal in the first ten periods of the coil-1 cycle. Round dots are sampled at 240 Hz.

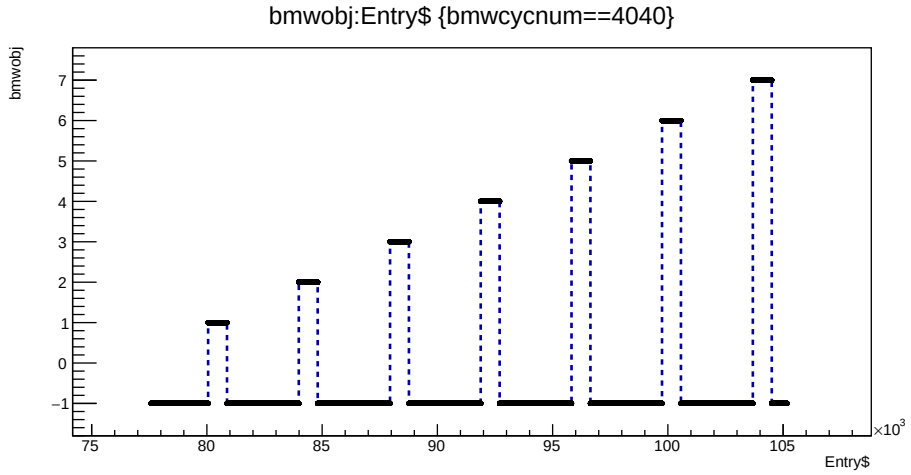

Figure 3.5: An example of one supercycle. The y-axis shows the value of "bmwobj" which is the software key word to identify the coil in activation, starting from 1 to 7. While beam modulation is paused, "bmwobj" is assigned to -1. The time scale in this plot is 2 minutes.

3.4 Pedestal and Linearity Calibration

In practice, the strength of a signal from a beam monitor or detector not only can deviate from linearity over the dynamic range but also extrapolate to a non-zero pedestal. In general, an observed signal S_{meas} is a function of its true strength S and if one assumes a quadratic dependence:

$$S_{\text{meas}} = a_0 + a_1 S + a_2 S^2. \tag{3.5}$$

With $|a_0| \ll |a_1 S|$ and $|a_2 S^2| \ll |a_1 S|$ approximation, the measured asymmetry is

$$A_{\text{true}} = \frac{S^+ - S^-}{S^+ + S^-}, \tag{3.6}$$

$$A_{\text{meas}} \approx A_{\text{true}}\Big(1 + \frac{a_2 S^2}{a_1 S} - \frac{a_0}{a_1 S}\Big), \tag{3.7}$$

that is the measured asymmetry A_{meas} is the true asymmetry A_{true} increased by the size of the quadratic term relative to the linear term, and decreased by the size of the pedestal relative to the linear term.

3.4.1 Pedestal

To extrapolate the pedestal of a beam current monitor (BCM), the BCM response is compared to the Unser monitor, a parametric current transformer which can be used as an

absolute reference of current. The Unser monitor shows its advantage of an excellent linearity in a wide dynamic range therefore is used as the reference to calibrate the BCM pedestal by linear fit. The Unser monitor signal drifts significantly and randomly at a time scale of several minutes, which limits its precision for continuous beam intensity monitoring. Therefore, once the BCM pedestal is calibrated using the Unser monitor, the detector pedestals are calibrated against the calibrated BCM.

The BCM pedestal is the extrapolated intercept at zero beam current from the linear fit of the BCM output to the Unser output. Such an extrapolation requires knowledge of the average Unser pedestal which is obtained from the beam-off data in the calibration run, shown as the blue points selected during the beam off periods in Figure 3.6. The integrating detector pedestal is calculated in a similar way by fitting the detector response to the calibrated BCM output from a dedicated beam current ramping scan.

An example of the BCM pedestal calibration is shown in Figure 3.6 and Figure 3.7. In Figure 3.6, data points in blue are selected from steady stages during the current scan. Typically, a calibration run takes 7 steps from 10 μA to 70 μA. The central mean value and the root-mean-square value of each step are used as the data points and error bars for the linear fit shown in Figure 3.7. In this example, the pedestal is obtained from the intercept of the linear function and reads -606.9 in the ADC unit referring to the text box of Figure 3.7. Data points in blue when the beam current is zero are only used to correct the time dependent offset for the Unser signal. The residual plot on the right panel of Figure 3.7 shows the differences between the calibrated BCM output and the beam current predicted from the linear fit. At high current (50 μA to 70 μA), the residuals are consistent within zero.

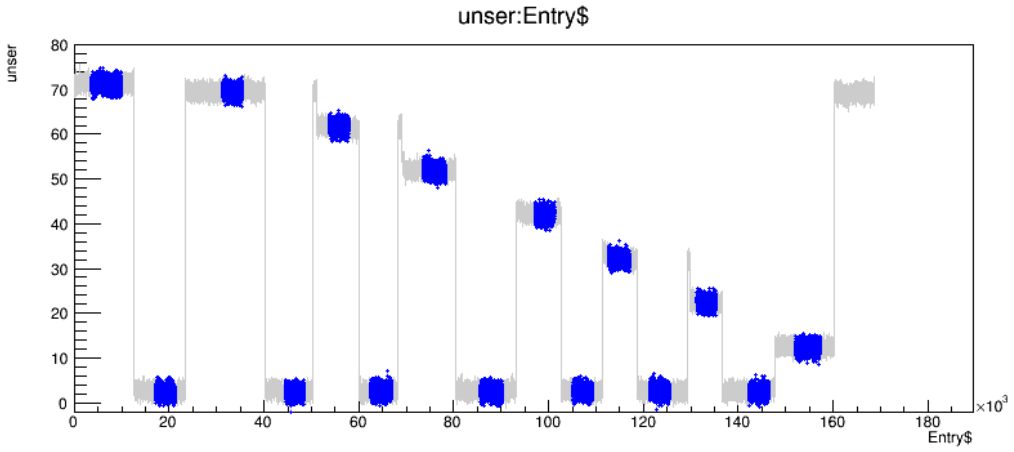

Figure 3.6: An example of a calibration run with beam current scan.

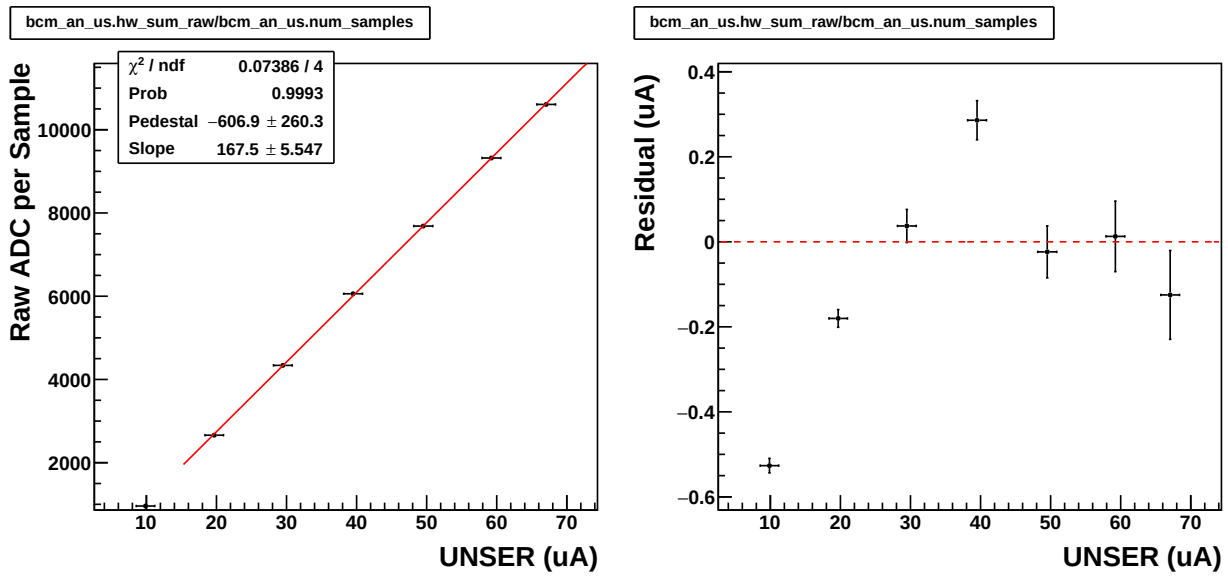

Figure 3.7: An example of the BCM calibration using BCM current scan.

3.4.2 Linearity

The linear response of the integrating detector signal is demonstrated to be better than 0.5%, see Table 3.4 from a bench test using a calibration system with multiple light sources shown in Figure 3.8. The linearity of the detector response is also monitored throughout the data taking period by comparison with BCM measurements of beam current fluctuations.

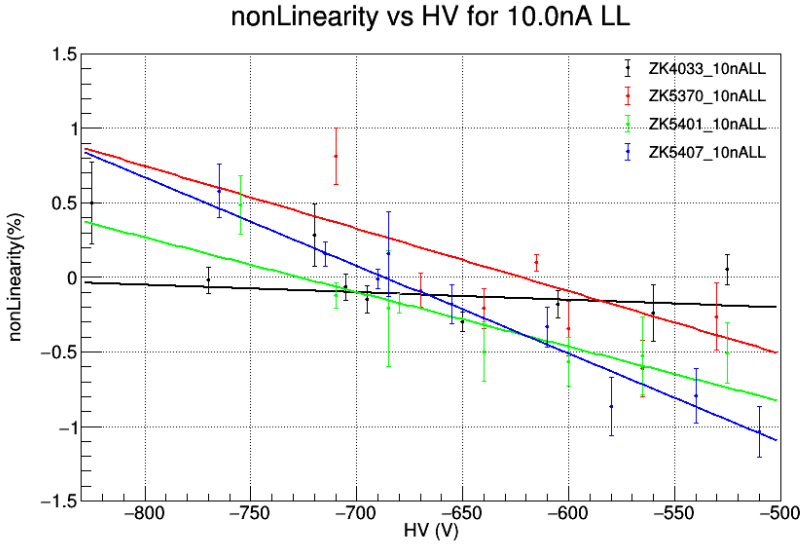

Figure 3.8: PMT non-linearity HV-scan.

PMT	HV (V)	Non-Linearity (%)	location
ZK4033	-705	-0.063	downstream right
ZK5407	-685	0.157	downstream left
ZK5401	-685	-0.208	upstream right
ZK5307	-615	0.100	upstream left

Table 3.4: PREX-2 PMT non-linearity at nominal HV setting.

3.5 Beam Raster System

For a precise asymmetry measurement at a event rate of a few GHz like PREX-2, the condition of the target material is extremely critical. A degraded target not only adds random noise in the measured asymmetry, but also potentially introduces helicity-correlated false asymmetries. The noise induced from a degraded target behaves as a residual correlation among detectors even after beam correction applied. A target foil exposed in a continuous high beam current degrades quickly if it is not properly protected. A melting target causes a time-dependent density variation and the unevenness on the target surface, i.e. position-dependent density variation. Target density variation in time or coordinate changes the scattered event rate from time to time and from spot to spot, thus leads to fluctuations in the measurement.

To maintain the target condition during the beam time without sacrificing the beam luminosity, each of the lead targets is sandwiched by diamond or carbon foils to improve heat transfer from the target bulk to a Helium cooling flow. In the meantime, to reduce the beam local heating, a high frequency beam raster system, a pair of two air-core magnetic coils, spreads the original beam spot size from $\approx 100\times100$ μm^2 to 4×4 mm^2 . Furthermore, the frequency of the raster scan current is synchronized with the helicity signal to reduce noise in the asymmetry width.

The beam raster used in the PREX-2 run is a pair of two air-core magnets which deflects electrons in both X and Y directions in its dipole fields. The design of the raster is shown in Figure 3.9. The magnetic rigidity of a dipole field is the magnetic bending strength for given radius and energy and is approximately

$$B\rho = 33.356 \cdot p, \tag{3.8}$$

where B is the magnetic strength in kG and ρ is the deflection radius in meter and p is the charged particle momentum in GeV/c. And the deflecting angle in the unit of radian can

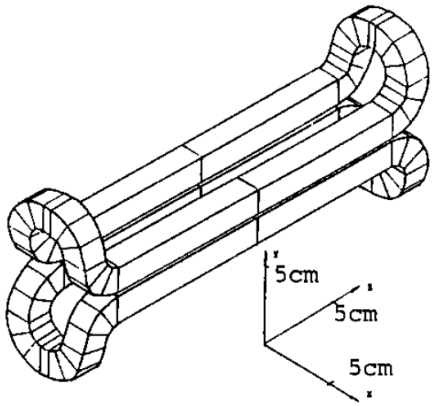

Figure 3.9: Raster magnet layout from Ref. [23]

be expressed as

$$\phi = \frac{\int B\mathrm{d}l}{33.356 \cdot p}, \tag{3.9}$$

so that the projection of the electron beam with momentum p on the target is

$$d \approx L \cdot \phi, \tag{3.10}$$

where L is the distance from the exit of the raster magnetic field to the target. Therefore the amplitude of the raster deflection depends on the amplitude of current flowing through the coil wires. Although a larger raster amplitude reduces local heating more efficiently, it also affects the resolution of the spectrometer and introduces a larger beam incident angle near the edge. In addition, a larger raster pattern increases the risk of intercepting with the copper frame holding the lead targets. With concerns mentioned above, the PREX-2 raster size is chosen to be 4×4 mm^2.

Raster currents with different waveforms produce different beam density distributions in the X-Y plane of the target, see the simulated examples in Fig. 3.11. The top part of the figure is generated from a sine waveform raster current and hot spots are localized at the four vertices due to the fact that the sine wave has a zero derivative at its peaks and valleys. In contrast, when the raster current is scanned in a triangular waveform, the beam density profile is more uniformly distributed on the target. Therefore, the raster scan current in a triangular waveform is often used in Hall A experiments, including PREX-2.

The scan frequency of the raster current in X and Y is centered around 25 kHz and differs by 960 Hz so that the beam trajectory projected to the target completes a closed Lissajous

orbit in every 8 events at 120 Hz or every 16 events at 240 Hz.

$$f_x = 25.55994888 \text{ kHz} \approx 213 \times 120 \text{ Hz}, \tag{3.11}$$

$$f_y = 24.59995080 \text{ kHz} \approx 205 \times 120 \text{ Hz}, \tag{3.12}$$

$$\Delta f = f_x - f_y = 960 \text{ Hz}. \tag{3.13}$$

For a given time period, a larger frequency difference between X and Y current yields a more uniform rastered beam density, see the examples in Figure 3.10. The X-Y frequency difference of 960 Hz is used in PREX-2 because its coverage is more uniformly spread compared with those of the other two options.

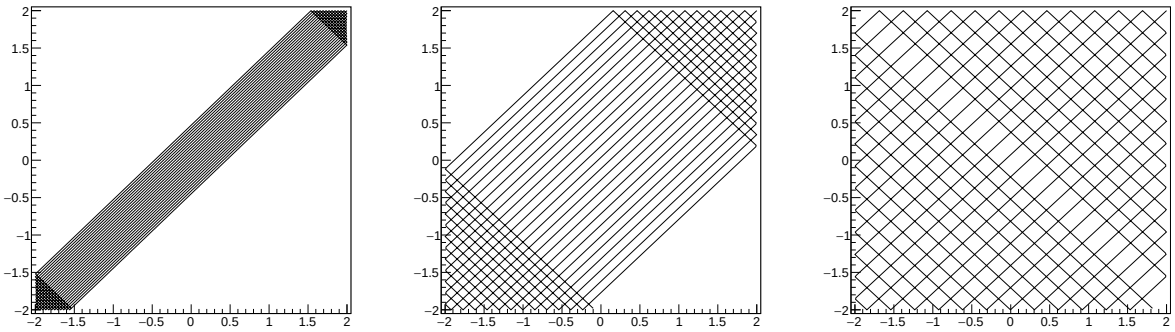

Figure 3.10: Left: $|f_y - f_x| = 120$ Hz; Middle: $|f_y - f_x| = 480$ Hz; Right: $|f_y - f_x| = 960$ Hz. By increasing the frequency difference, the raster pattern is more spread and uniform in the same time period. Reproduced from Ref. [24].

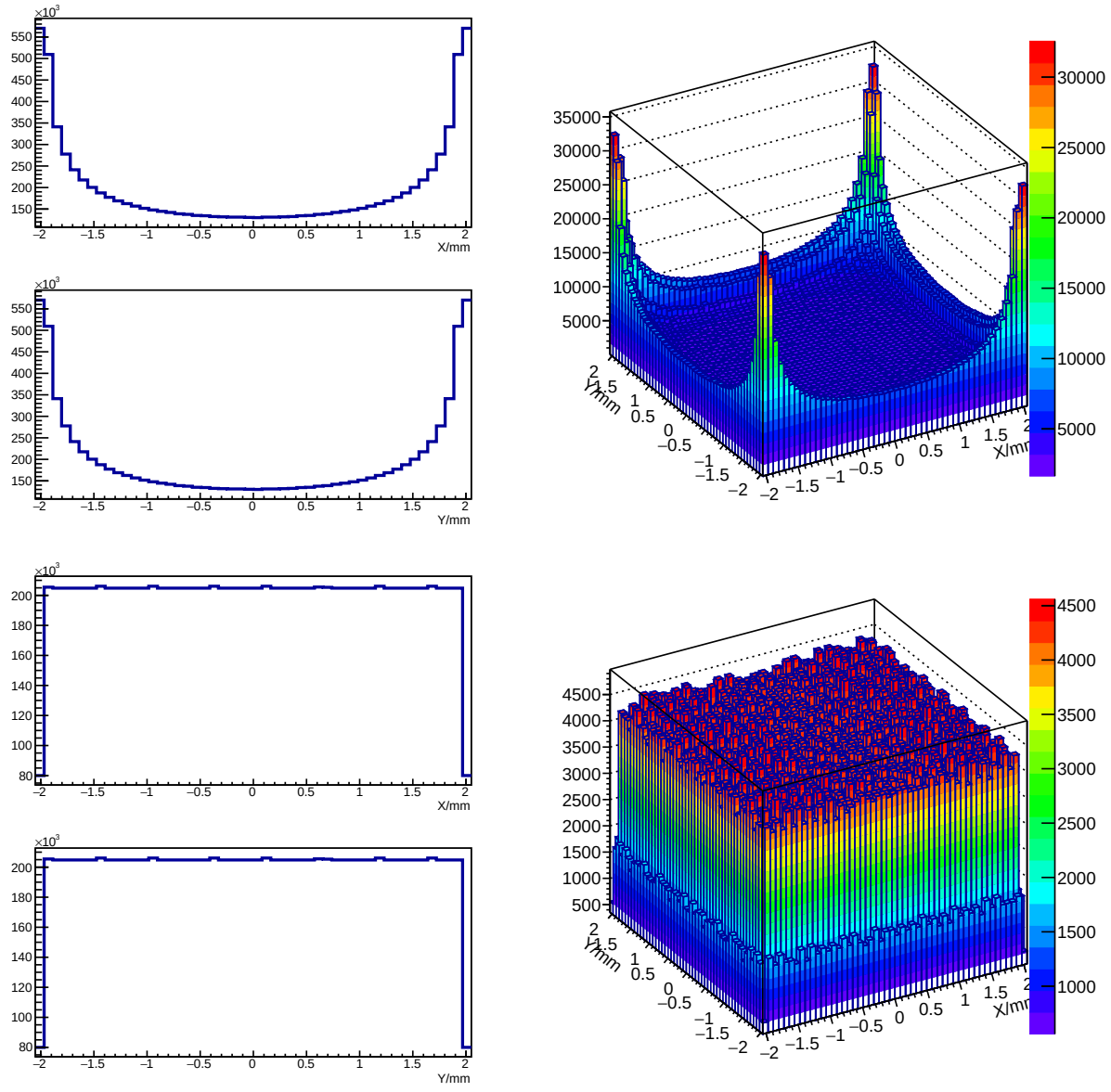

Figure 3.11: Raster spatial density from simulations. Top: Raster density generated from a sine wave function ; Bottom: Raster density generated from a triangular wave function. Reproduced from Ref. [23].

3.6 Off-line Analysis Software

The offline data analysis framework for PREX-2 has following components:

1. Just Another Parity Analyzer(JAPAN)[69]: processing and packing parity data into ROOT files, computing correlational variables for LRB correctors.

2. prex-prompt[70]: generating run summary plots and texts, uploading results automatically to the JLab web server.

3. Beam modulation analysis: calculating beam modulation sensitivities and slopes.

4. Parallel post-processing:

   - postpan: performing multivariate linear regression
   - JAPAN LRB-Corrector: performing multivariate linear regression
   - JAPAN Combiner: applying correction slopes deduced from beam modulation
   - Lagrange multiplier analysis [71]: computing eigenvectors for BPMs and applying corrections using Lagrange multiplier regression.

5. prex-stat[72]: extracting and aggregating statistics at minirun, Slug, Pitt, Wien and grand levels, handling weighting and sign correction schemes.

The first version of the off-line analysis chain was developed into a working stage in the first few weeks of the PREX-2 run and successfully completed beam corrections for 80% of the production data at the end of PREX-2 run. This analysis chain also provides the first-hand outputs for the daily data quality review during the PREX-2 run. In the next year after the PREX run completed, the offline analysis chain was armed with the statistics analysis tool and the Lagrange multiplier regression module, and continued its commission throughout all the PREX-2 parity analysis rounds.

Learning from the software development experience in previous parity experiments, a newly-built parity analyzer, named Just Another Parity Analyzer (JAPAN) becomes the pivot of the PREX-2 parity analysis, for both the online part and the offline part. All the post-processing and calibration analyses are built upon the output from JAPAN.

JAPAN was built and developed from "QwAnalysis" for the Qweak experiment and "pan" for the previous Hall A parity experiments.

The JAPAN engine handles decoding, calibration and asymmetry calculation. The JAPAN output for a run is a ROOT file containing a helicity Tree which holds helicity-correlated pattern differences, parity asymmetries and pattern averages for detectors and monitors. Helicity pattern differences and averages in JAPAN are both normalized by the size of pattern, for example with a 120 Hz quartet pattern,

$$\langle Y \rangle = \frac{1}{4}(Y_1 + Y_2 + Y_3 + Y_4), \tag{3.14}$$

$$\Delta Y = \frac{1}{4}(Y_1 - Y_2 - Y_3 + Y_4). \tag{3.15}$$

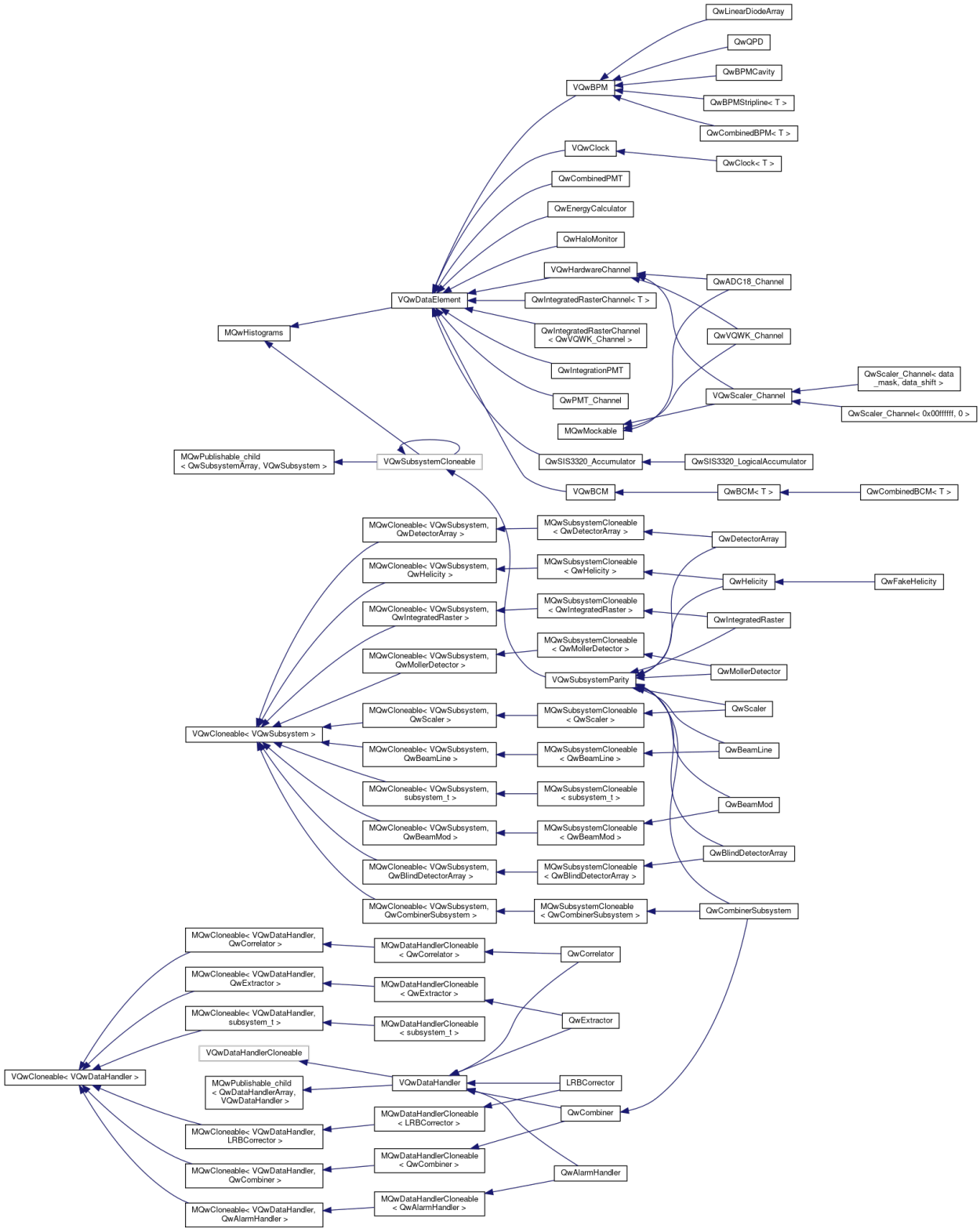

Figure 3.12: Class inheritance diagram stemmed from VQwDataHandler, VQwSubsystem, MQwHistograms. An arrow is pointing from the daughter class to its parent.

The advantage of this normalization scheme is that the ratio of a pattern difference over its pattern average turns into the corresponding pattern asymmetry without extra scaling factors

$$A = \frac{\Delta Y}{\langle Y \rangle} = \frac{Y^L - Y^R}{Y^L + Y^R}. \tag{3.16}$$

Note that this definition is different from that in the previous parity analyzer "pan" which does not apply normalization in differences. Different conventions on the helicity correlated difference would require different normalization factors for beam modulation slope calculation, see the related discussion in Section 5.3 for details.

The core classes of JAPAN and their dependencies on each other are shown in Fig. 3.12. The key data structures of JAPAN are `DataElement`, `Subsystem` and `SubsystemArray`. `DataElement` can be a single hardware channel, e.g. `QwVQWK_Channel` or composite channels e.g. `QwBPMStripline` for a rotated coordinate in a BPM. The `Subsystem` is a container of `DataElements`. Usually the data comes from identical modules connected to similar physics devices, e.g. `QwBeamLine`, `QwDetectorArray` and `QwHelicity`. The `SubsystemArray` contains all the `Subsystems` which hold `DataElements` for a particular time interval.

Classes interfacing post-processing analysis such as regression and beam modulation event extraction are all inherited from `DataHandler`. The `QwCorrelator` computes the correlation among specified channels from the helicity tree and evaluates the linear regression slopes. The `LRBCorrector` applies the linear regression slopes to detected asymmetries for data in each 5 minutes. The `QwCombiner` allows users to mix channels from the helicity Tree in linear combination therefore provides an option to apply asymmetry correction at run level, such as beam modulation correction. Additionally, the `QwExtractor` outputs an independent event Tree which contains beam modulation events only.

The blinding mechanism for PREX-2 is additive. A constant offset is added in the blindable asymmetry, such the main detector asymmetry

$$A_{\text{blinded}} = \frac{Y^L - Y^R}{Y^L + Y^R} + (\text{sign of helicity}) \cdot A_{\text{const}}. \tag{3.17}$$

The blinding factor A_{const} can be any value in the blinding box of which the size is 150 ppb, approximately 10 times of estimated final experimental uncertainties. The value of A_{const} is calculated based on the hash value of a given text sentence and it is not easily tractable.

The software blinder is also aware of the sign of the electron helicity, because the slow reversal, e.g. the IHWP change or the double-Wien flip, changes the sign of the measured asymmetry. When a target other than ^{208}Pb targets is presented, the blinder disables its blinding mechanism since a zero asymmetry measurement from other nuclear target may expose the blinding factor to a certain degree. Also when the main detector hardware

channel is known with an device error, the blinder forces the measured asymmetry to be zero without taking any risk of the blinding factor leakage.

The JAPAN online mode decodes events from CODA data stream directly. The online mode not only serves as the helicity-correlated feedback engine but also creates memory-mapped ROOT files for real-time event monitoring.

JAPAN also handles the evaluation for event cuts at event level. The event cut deployment will be discussed in the next chapter.

Chapter 4

Statistical Properties of the Data

This chapter discusses the statistical properties of the full data set and the event cuts and selection strategy. Section 4.1 summarizes the grand average statistics for the sign corrected asymmetry and the null asymmetries. Section 4.2 describes the event cuts and selection strategy for the data quality control.

4.1 Statistic Summary

4.1.1 Overview

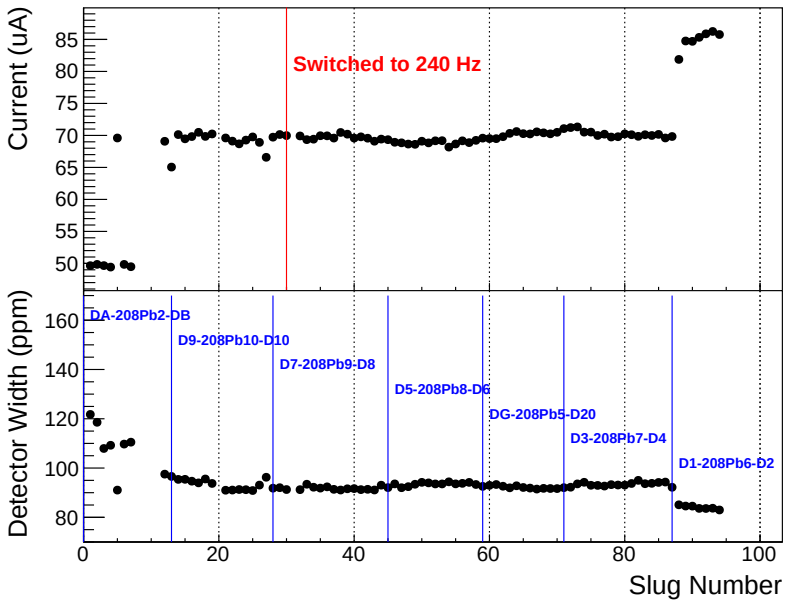

Figure 4.1: Slugs plot of PREX-II beam current and target change-out.

During the PREX-2 run, approximately 80 % of the beam time, the beam current is stable at 70 μA, see in the top panel of Figure 4.1, and produced an event rate of approximately 4 GHz in the detectors. The typical root-mean-square (RMS) width of the corrected average asymmetry at this beam condition is around 92 parts-per-million (ppm) for quartets and octets and stays at the same level through all ^{208}Pb targets. With the event cut and selection, no sign of target degradation effect on the measured asymmetry can be seen. The first $\approx$ 30% of the data are taken at a 120 Hz helicity flip rate and the rest are taken at a 240 Hz helicity flip rate. Since a 120 Hz quartet and a 240 Hz octet cover the same integrating length of 33.33 msec, the observed statistical fluctuations in the asymmetry measurement is also the same at both helicity flip rates. The last seven slugs of data are produced with a beam current of 85 μA and this higher luminosity gives a narrower RMS width of 82 ppm which remains steady till the end of the PREX-2 run.

4.1.2 Sign Corrected Grand Averages

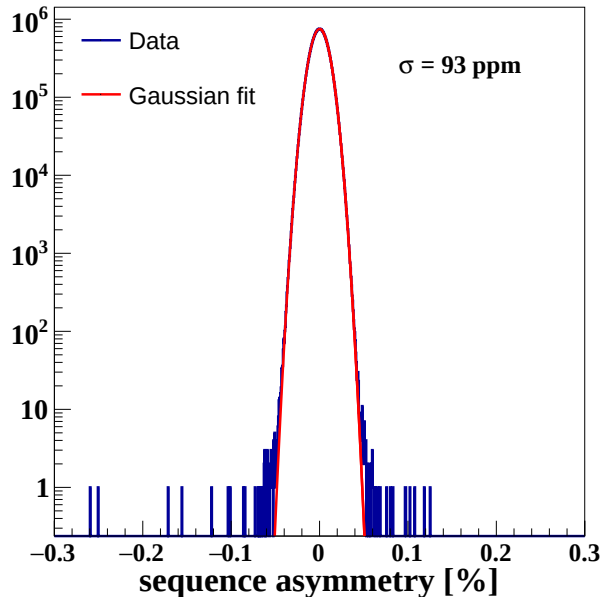

Figure 4.2: Distribution of 30 million asymmetries measured over 1/30 s sequences formed with 240 Hz helicity flips. Only data taken with a beam current near to 70 μ A is included.

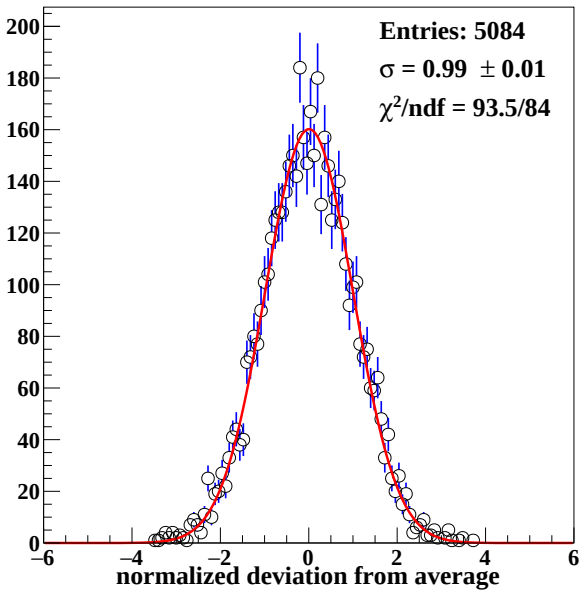

Figure 4.3: Distribution of normalized deviations from the average(blue) for 5-minute asymmetry data sets after beam corrections, compared to a Gaussian fit (red).

Figure 4.2 shows the distribution after beam correction of the sequence asymmetry for data collected with 240 Hz flip rate and 70 μA beam current. Approximately 62% of the total

statistics are included in this histogram. The remarkably high level of agreement between the data and the normal distribution fit over five orders of magnitude is achieved without the application of a single helicity-correlated data quality cut on any measured parameter.

The beam-corrected asymmetry data are dominated by statistical fluctuations around a single mean, as demonstrated in Figure 4.3. This plot shows the deviations from the grand average central value for all 5084 5-minute data segments, with each entry normalized to its own statistical uncertainty of ≈ 1 ppm. The data describe a normal distribution with unit variance and zero mean, as expected.

With beam correction using Lagrange multiplier regression, to be discussed in Chapter 5, the grand averaged sign corrected asymmetry is

$$A_{\text{corr}} = 492.02 \pm 13.52 \text{ (stat.)} \pm 2.5 \text{ (syst.) ppb.} \tag{4.1}$$

The 5-minute data segments, named "mini-run", are first aggregated to the slug level for each slow reversal window. The slug average $\langle A_s \rangle$ and its standard error are calculated with weights

$$\langle A_S \rangle = \sum_i w_i A^{(i)} / \sum_i w_i, \tag{4.2}$$

$$\sigma(A_S) = 1/\sqrt{\sum_i w_i}, \tag{4.3}$$

where weighting factor w_i is determined by the statistical uncertainty σ_i of the corrected asymmetry in the i-th mini-run

$$w_i = 1/\sigma_i^2. \tag{4.4}$$

Total 96 Slugs data are collected during the PREX-2 run and they are further partitioned into 23 Pitts, each has 4 or 5 Slugs with approximately equal statistical uncertainties between IHWP IN and OUT states at the same Wien setting. The partitions of Pitts can be found in Table A.1 in Appendix A. The slow noise cancellation between Slugs improves the χ^2/ndf at Pitt level, shown in the second last column in Table 4.1. The Pitt average is the Slugs weighted average in this Pitt according to the statistical uncertainties σ_S of the Slugs, that is

$$\langle A_P \rangle = \sum_S w_S A^{(S)} / \sum_S w_S, \quad \sigma(A_P) = 1/\sqrt{\sum_S w_S}, \quad w_S = 1/\sigma_S^2. \tag{4.5}$$

Following the same averaging approach, the Slug averages are also aggregated into four averages for Wien states: LEFT-1, RIGHT-1, LEFT-2 and RIGHT-2,

$$\langle A_W \rangle = \sum_S w_S A^{(S)} / \sum_S w_S, \quad \sigma(A_W) = 1/\sqrt{\sum_S w_S}. \tag{4.6}$$

Figure 4.5, Figure 4.6 and Figure 4.7 show the central value fits and pull plots of four beam techniques at Slug, Pitt and Wien levels. The grand averaged statistics are summarized in Table 4.1 of which the last three columns show the values of χ^2/ndf at Slug, Pitt and Wien levels respectively.

	Mean (ppb)	Stat. Err. (ppb)	RMS (ppm)	χ^2/ndf	χ^2/ndf	χ^2/ndf
Reg(5bpm)	497.72	13.73	101.54	119.1/95	20.3/22	2.9/3
Dithering	494.14	14.05	105.48	115.9/95	22.1/22	3.0/3
Reg(all)	492.95	13.43	98.68	118.5/95	22.3/22	3.9/3
Lagrange(all)	492.02	13.52	99.61	117.5/95	23.8/22	3.7/3

Table 4.1: Corrected Asymmetry by Slugs, Pitts and Wiens

Also Slug averages can be grouped by combination of IHWP state (IN/OUT) and Wien flip (Left/Right). Figure 4.4 displays the averages of the four combinations together with the grand averaged central value and its statistical uncertainty.

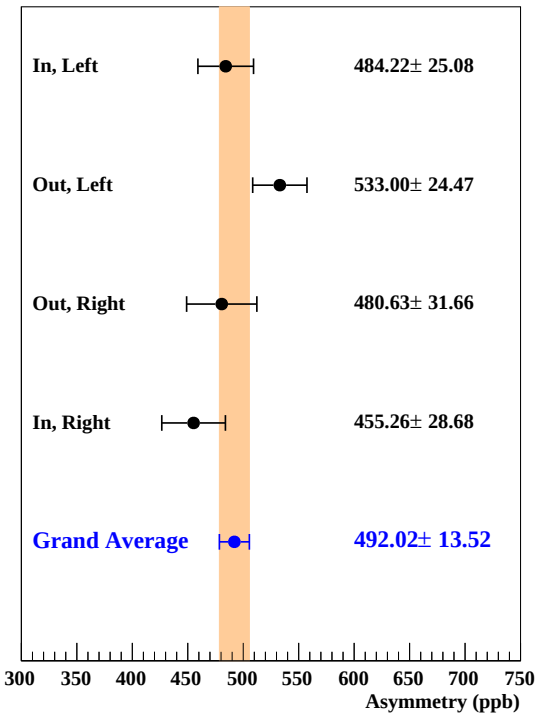

Figure 4.4: Beam corrected grand averages using Lagrange Multipliers.

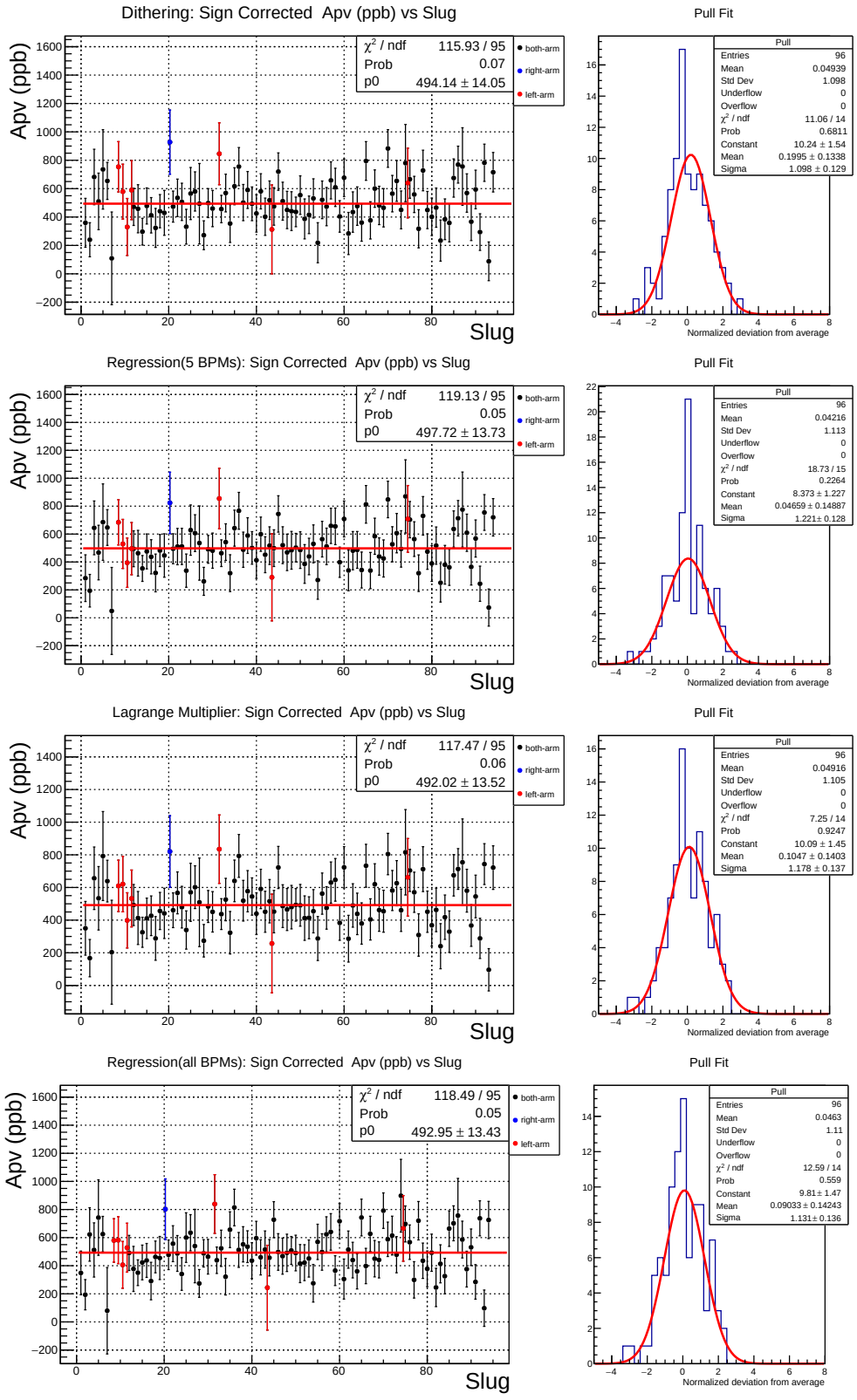

Figure 4.5: Slug Averages from different beam corrected results. From top to bottom: 1) Dithering; 2) Regression (5 BPM); 3) Lagrange Multiplier; 4) Regression (all BPMs). Right-arm-only and Left-arm-only slugs are marked with blue dots and red dots respectively.

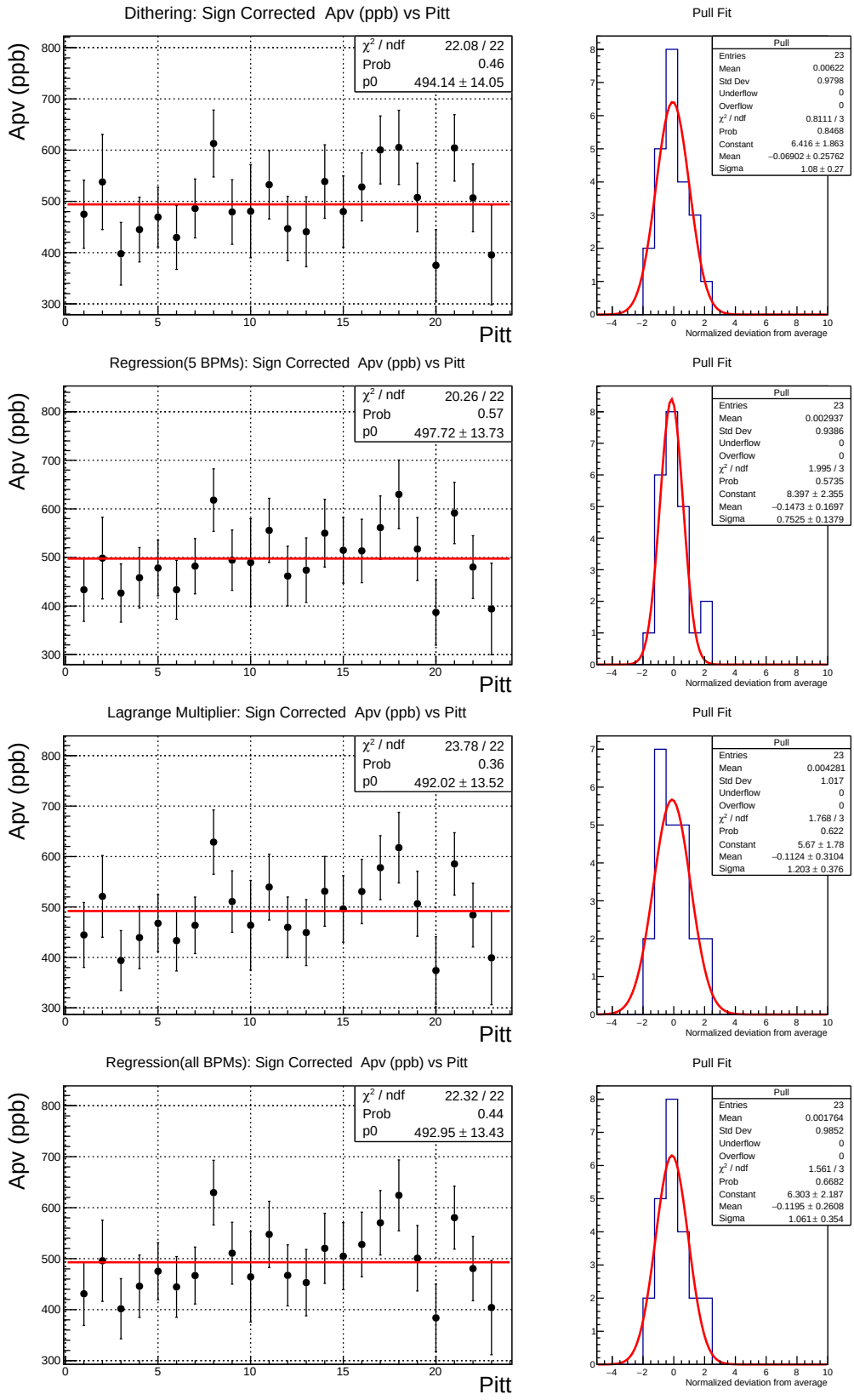

Figure 4.6: Pitt Averages from different beam corrected results. From the top to the bottom: 1) Dithering; 2) Regression (5 BPM); 3) Lagrange Multiplier; 4) Regression (all BPMs).

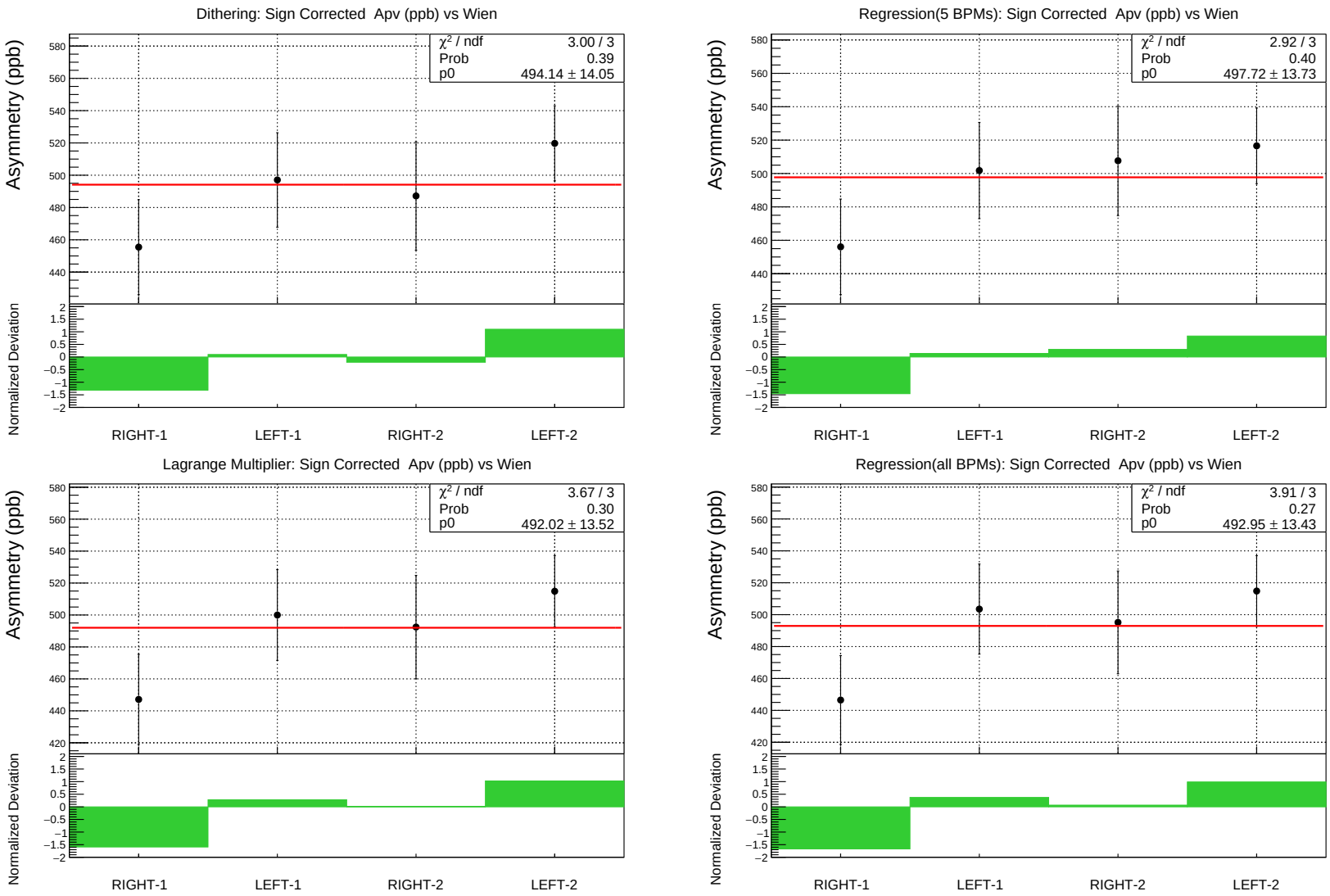

Figure 4.7: Wien Averages from different beam corrected results. From left to right, then top to bottom: 1) Dithering; 2) Regression (5 BPM); 3) Lagrange Multiplier; 4) Regression (all BPMs).

4.1.3 Null Asymmetry

Null asymmetries are sensitive to potential cancellation by the slow reversals, i.e. the IHWP flips and the Wien flips. A null asymmetry consistent with zero is a good indication of no significant sources of systematic false asymmetry being canceled by the slow reversals. Also, it is not necessary that null asymmetries have to be consistent with zero.

Depending on the type of source of interest, the way to define a null asymmetry can be different. The null asymmetries to discuss here are the "IHWP+Spin" reversal null asymmetry and the "IHWP" reversal null asymmetry

The "IHWP+Spin" reversal null, A_{null}, is the average of the asymmetries in both insertable half-wave plate (IHWP) states with no sign correction applied. For a given time period, the "IHWP+Spin" null asymmetry is sensitive to the false asymmetry being canceled from the slow reversals:

$$A_{\text{null}} = \frac{1}{2}(A_{\text{IN}} + A_{\text{OUT}}), \tag{4.7}$$

$$\sigma_{\text{null}} = \frac{1}{2}\sqrt{\sigma_{\text{IN}}^2 + \sigma_{\text{OUT}}^2}, \tag{4.8}$$

where A_{IN} and A_{OUT} are the measured asymmetries from the IHWP-IN and the IHWP-OUT states respectively without sign correction and σ_{IN} and σ_{OUT} are their statistical uncertainties.

The "IHWP" reversal null, denoted as A^*_{null}, is the difference between the sign corrected asymmetry of the IHWP-IN state and the sign corrected asymmetry of the IHWP-OUT state

$$A^*_{\text{null}} = \frac{1}{2}(A^*_{\text{IN}} - A^*_{\text{OUT}}), \tag{4.9}$$

$$\sigma_{\text{null}} = \frac{1}{2}\sqrt{\sigma_{\text{IN}}^2 + \sigma_{\text{OUT}}^2}, \tag{4.10}$$

In the "IHWP" reversal null asymmetry, the effect of the IHWP reversal is isolated so that the "IHWP" null indicates the false asymmetry canceled with the IHWP reversal but survived the spin reversal using the double-Wien filters. The following calculation in Table 4.2 provides an example to demonstrate the difference of these two null asymmetries.

	IHWP	Wien	Measured Asymmetry	Sign Corrected Asymmetry
1	IN	RIGHT	$A_{\text{PV}} + \delta_0 + \delta_1$	$A_{\text{PV}} + \delta_0 + \delta_1$
2	OUT	RIGHT	$-A_{\text{PV}} + \delta_0 + \delta_1$	$A_{\text{PV}} - \delta_0 - \delta_1$
3	IN	LEFT	$-A_{\text{PV}} + \delta_0 - \delta_1$	$A_{\text{PV}} - \delta_0 + \delta_1$
4	OUT	LEFT	$A_{\text{PV}} + \delta_0 - \delta_1$	$A_{\text{PV}} + \delta_0 - \delta_1$

Table 4.2: Example of null asymmetries sensitivity to canceled noise by slow reversal.

δ_0 represents the type of false asymmetry which cancels with all slow reversals, that is, δ_0 is always the same change to measured asymmetries. One example for δ_0 would be electronics pick-up from the Pockels cell. δ_0 can be obtained from the "IHWP+Spin" reversal null asymmetry:

$$A_{\text{null}} = \frac{1}{4}(A_1 + A_2 + A_3 + A_4) = \delta_0. \tag{4.11}$$

While δ_1 is the type of false asymmetry which cancels between IN and OUT states and it only changes sign with spin rotation, e.g. in A_1 and A_3. One possible source of δ_1 is a polarization-dependent beam asymmetry. Therefore δ_1 survives the Wien flip and can only be obtained from the "IHWP" reversal null asymmetry:

$$A^*_{\text{null}} = \frac{1}{4}(A^*_1 + A^*_3 - A^*_2 - A^*_4) = \delta_1. \tag{4.12}$$

Table 4.3 shows the grand averaged null asymmetry from the four beam correction methods. The Pitt history of the null asymmetry is also shown in Figure 4.8 (IHWP+Spin Null) and Figure 4.9 (IHWP Null). Table 4.4 lists the beam corrected asymmetry measured at IN and OUT states and their null asymmetries in each Pitt. Note that IN, OUT and Wien averages in this table can be slightly different from the sign corrected results. This is because a few slugs are excluded in null asymmetry calculation for balancing statistical power between IN and OUT states. Also note that IHWP+Spin reversal null and IHWP reversal null have the exact same magnitude and differ only by sign in the Wien-Left state. And this is expected by definition in the absence of additional systematics.

The sign flip between grand averages of "IHWP+Spin" null and "IHWP" null can be understood from the "Wien Average" rows in Table 4.4. In the first two Wien flips, i.e. Right-1 and Left-1, the "IHWP+Spin" null flips sign while the "IHWP" null stays at the same sign. This indicates the δ_1 type noise cancellation is more significant in the first two Wiens and has a negative value. In contrast, the last two Wien flips, i.e. Right-2 and Left-2, the "IHWP" null reverses its sign while the "IHWP+Spin" null keeps the sign unchanged so that δ_0 type noise cancellation is dominant in the last two Wiens and has a positive sign.

	IHWP+Spin Null Asym.			IHWP Null Asym.		
	Mean (ppb)	Std. Err. (ppb)	χ^2/ndf	Mean (ppb)	Std. Err. (ppb)	χ^2/ndf
dit	13.23	14.52	42.11/22	-14.25	14.52	41.98/22
reg_5bpm	18.30	14.09	43.78/22	-14.57	14.09	44.39/22
lagr_all	14.50	13.91	42.48/22	-15.61	13.91	42.31/22
reg_all	15.69	13.75	42.48/22	-15.20	13.75	42.40/22

Table 4.3: Summary of null asymmetries

As a summary, although the null asymmetries fluctuate from Pitt to Pitt, the grand averages of both types of null asymmetry converge to a small value comparable to the grand statistical uncertainty (13.5 ppb). The small null asymmetries in both cases indicate a nearly perfect cancellation by the IHWP and Wien reversals and a reliable systematic control over the beam quality for parity experiments.

Wien	Pitt	IN Measured	OUT Measured	IHWP+Spin Null	IHWP Null
Right-1	1	167.25 ± 114.24	-495.82 ± 104.98	-164.29 ± 77.58	-164.29 ± 77.58
	2	476.05 ± 108.34	-577.74 ± 121.64	-50.84 ± 81.45	-50.84 ± 81.45
	3	383.84 ± 74.26	-411.65 ± 98.58	-13.91 ± 61.71	-13.91 ± 61.71
	4	442.37 ± 82.97	-435.76 ± 91.76	3.30 ± 61.85	3.30 ± 61.85
	5	468.28 ± 81.69	-442.96 ± 86.47	12.66 ± 59.48	12.66 ± 59.48
Wien Average		403.29 ± 39.58	-462.09 ± 44.12	-29.40 ± 29.64	-29.40 ± 29.64
Left-1	6	-486.58 ± 92.14	393.94 ± 79.18	-46.32 ± 60.74	46.32 ± 60.74
	7	-397.66 ± 76.40	540.49 ± 82.39	71.42 ± 56.18	-71.42 ± 56.18
	8	-681.16 ± 91.00	578.16 ± 89.14	-51.50 ± 63.69	51.50 ± 63.69
	9	-445.52 ± 89.65	566.61 ± 82.86	60.55 ± 61.04	-60.55 ± 61.04
	10	-452.09 ± 129.82	515.86 ± 132.78	31.88 ± 92.85	-31.88 ± 92.85
Wien Average		-488.45 ± 41.04	514.94 ± 39.68	13.25 ± 28.54	-13.25 ± 28.54
Right-2	11	593.51 ± 91.13	-482.65 ± 93.38	55.43 ± 65.24	55.43 ± 65.24
	12	493.52 ± 99.64	-452.77 ± 90.62	20.38 ± 67.35	20.38 ± 67.35
	13	511.05 ± 91.39	-384.49 ± 93.64	63.28 ± 65.42	63.28 ± 65.42
	14	630.13 ± 126.11	-646.66 ± 130.62	-8.26 ± 90.78	-8.26 ± 90.78
Wien Average		549.81 ± 49.77	-469.89 ± 49.44	39.96 ± 35.08	39.96 ± 35.08
Left-2	15	-612.29 ± 91.68	371.26 ± 95.03	-120.52 ± 66.02	120.52 ± 66.02
	16	-391.98 ± 89.34	673.82 ± 90.74	140.92 ± 63.67	-140.92 ± 63.67
	17	-637.58 ± 90.67	520.84 ± 88.74	-58.37 ± 63.44	58.37 ± 63.44
	18	-666.40 ± 108.75	583.22 ± 91.34	-41.59 ± 71.01	41.59 ± 71.01
	19	-633.75 ± 91.69	382.17 ± 90.58	-125.79 ± 64.44	125.79 ± 64.44
	20	-309.58 ± 93.73	440.73 ± 95.22	65.58 ± 66.81	-65.58 ± 66.81
	21	-524.72 ± 89.00	642.21 ± 86.23	58.75 ± 61.96	-58.75 ± 61.96
	22	-326.22 ± 88.59	648.22 ± 90.34	161.00 ± 63.26	-161.00 ± 63.26
	23	-95.89 ± 129.54	721.70 ± 133.55	312.90 ± 93.03	-312.90 ± 93.03
Wien Average		-481.70 ± 31.68	547.15 ± 31.25	32.73 ± 22.25	-32.73 ± 22.25

Table 4.4: Summary of null asymmetries at Pitt level with beam correction by Lagrange multiplier.

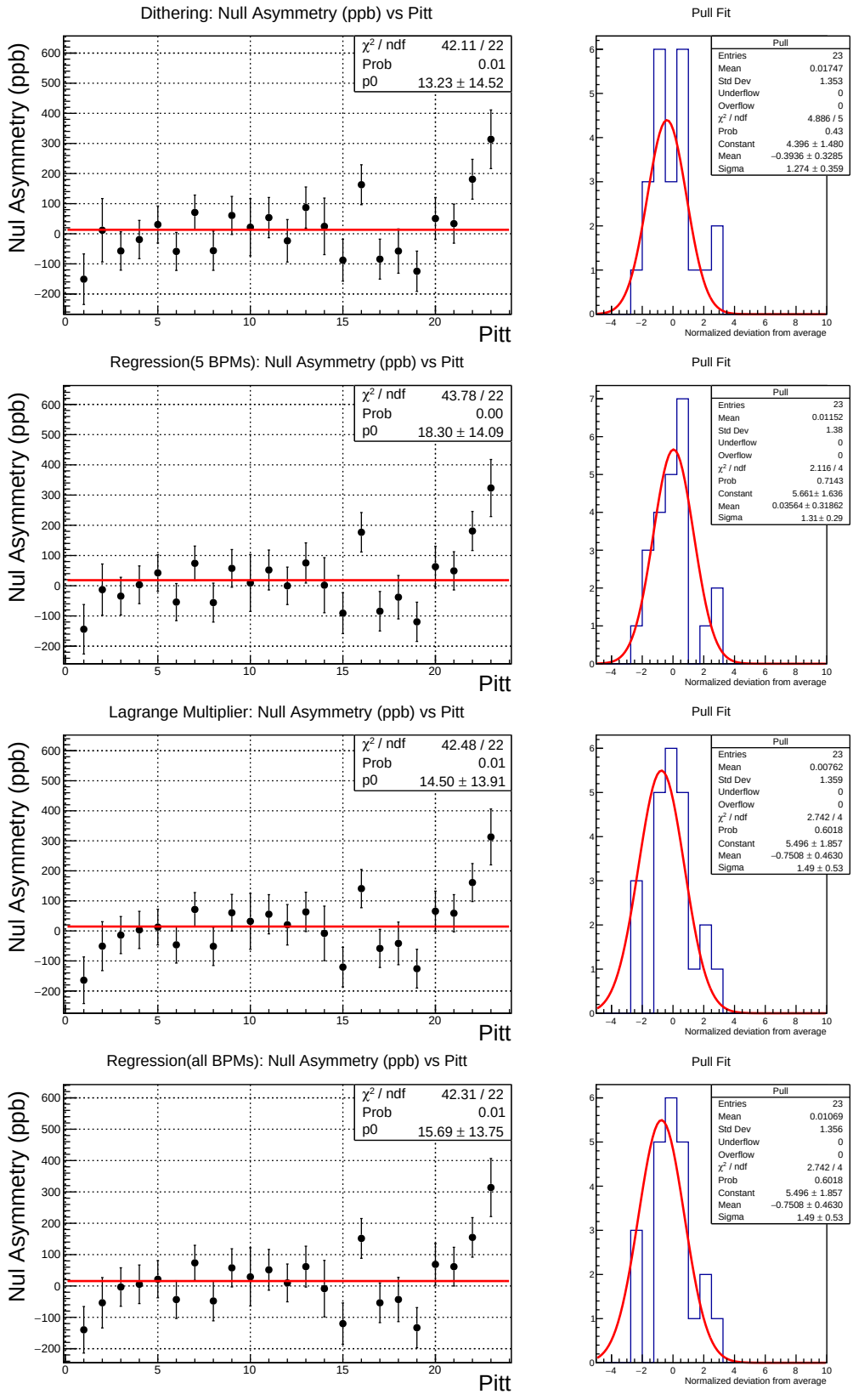

Figure 4.8: Pitts summary of "IHWP+Spin" Reversal Null

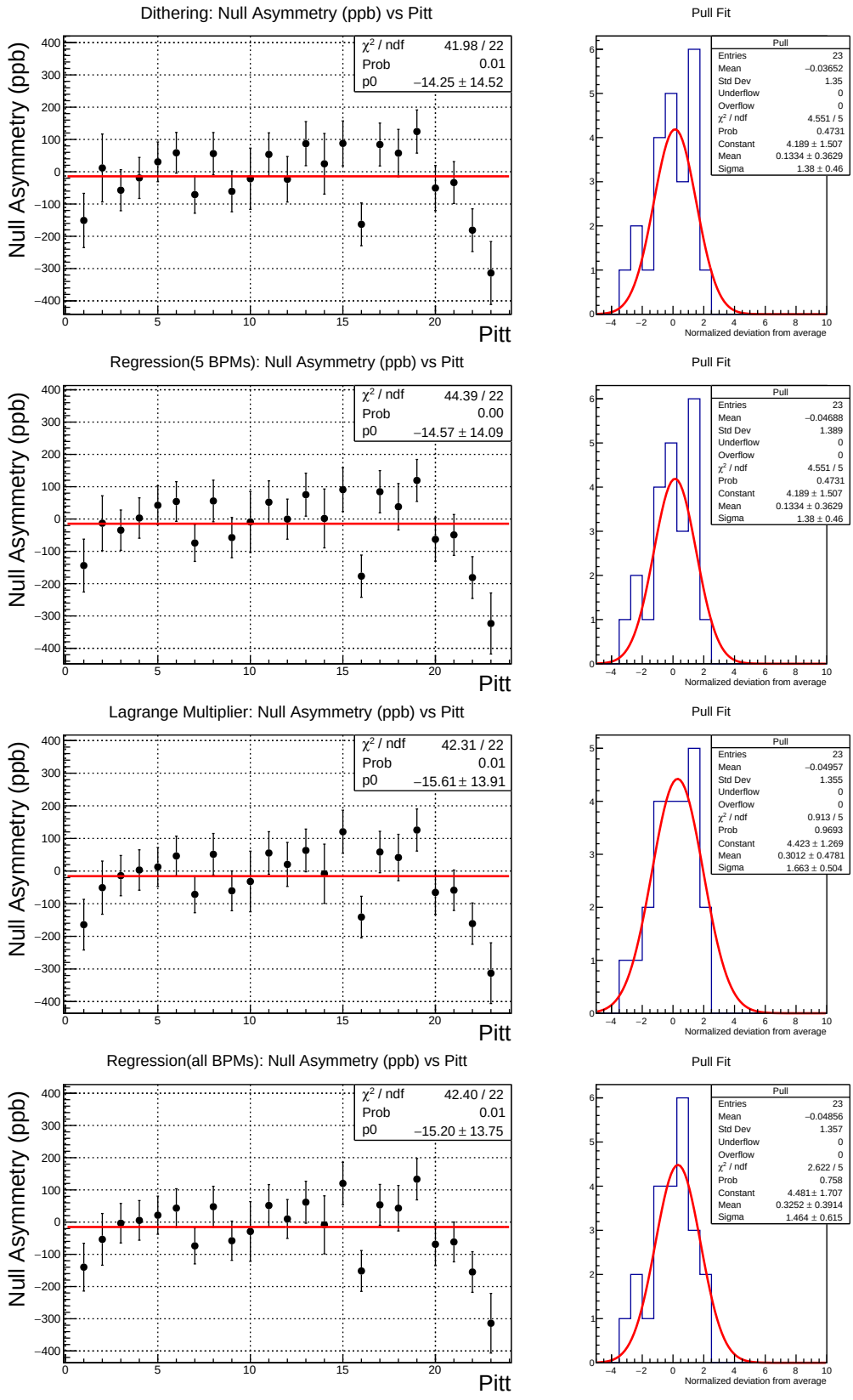

Figure 4.9: Pitts summary of "IHWP" Reversal Null

4.2 Event Cut and Selection

The primary goal of event cuts is accepting events with quality and efficiency while avoiding systematic bias. To avoid introducing bias to the asymmetry measurement directly, event cuts are only applied to data at event level, i.e. the 120 Hz or 240 Hz samples. Also, the evaluation of events stability is based on the mean and the root-mean-square (RMS) of the data in a moving time window and does not require knowing helicity information. In the meantime, the length of the moving time window is typically ≈ 6 seconds which is much longer than that of a helicity pattern (≈ 0.033 seconds). Therefore, data at helicity pattern level are free from potential effects implicitly imposed by cuts at event level. As a result, the effects of event cuts on helicity-correlated differences and asymmetries are extremely loose.

The software event cuts in JAPAN, the parity analyzer discussed in Section 3.6 , evaluate data quality from the following aspects simultaneously:

- Detecting ADC hardware failures, e.g. saturation, null or frozen readback.
- Validating the event timing sequence and the reported helicity information.
- Protecting the experiment blinding factor from target changes and ADC hardware failures.
- Rejecting signals outside the customized lower and the upper limits.
- Qualifying events with stable beam parameters, e.g. beam current and position, within a sliding time window.
- Tagging events taken from the beam modulation period.

In practice, these aspects are further categorized into 23 types to indicate single event errors, see in Table 4.5. Each single event error type is registered by a binary bit. For every single event, information of all the 23 error types is amalgamated by bitwise OR manipulations into one unsigned 32-bit integer, named `ErrorFlag`, which is the criterion for event selection. By convention, a boolean true confirms a single event error, therefore a single event which passes all the 23 types of event error check will receive a nulled `ErrorFlag`.

Not all hardware channels are relevant to the asymmetry analysis. To select qualified events for the asymmetry analysis, a "global" `ErrorFlag` only evaluates the relevant hardware channels, e.g. a BCM for normalization and BPMs for beam correction, and labels whether an event is qualified for the asymmetry analysis or not. In contrast, each device error code is "locally" associated with only one hardware channel. A device error code is primarily used for subsystem diagnosis.

Hexadecimal	Decimal	Description
0x1	1	a VQWK is saturating
0x2	2	for sample size check
0x4	2^2	check hardware sum equals to software sums
0x8	2^3	sequence number check
0x10	2^4	check to see ADC returning same HW value
0x20	2^5	check to see ADC returning zero
0x40	2^6	check to see ADC failed lower limit of the event cut
0x80	2^7	check to see ADC failed upper limit of the event cut
0x100	2^8	identify the single event cut is failed for a BCM
0x200	2^9	to identify the blinder flag
0x400	2^{10}	the single event cut is failed for a BPM
0x800	2^{11}	the single event cut is failed for a PMT
0x1000	2^{12}	the FFB OFF periods for Energy modulation
0x8000	2^{15}	the single event cut is failed for a BMod channel
0x10000	2^{16}	the mode 3 where we only flag event cut failed events
0x20000	2^{17}	any type of helicity decoding problem
0x1000000	2^{24}	identify the stability cut
0x2000000	2^{25}	the single event cut is a local cut
0x4000000	2^{26}	the single event cut is a global cut
0x8000000	2^{27}	an event within a beam trip range set by ring parameters
0x10000000	2^{28}	identify the stability cut for beam current
0x20000000	2^{29}	identify the burp cut
0x80000000	2^{31}	an event range being masked

Table 4.5: Table of event cut bits and descriptions.

Besides the single event error flag from JAPAN, a secondary event cut strategy is applied regarding the lead target condition. Since the diamond foils on the target play a key role in dissipating local beam heating, the cracking of the diamond foil due to the tension from thermal expansion reduces the contact area between the lead and the diamond foil and consequently results in a melting lead target, see the leftmost target in Figure 4.10.

Target degradation not only introduces helicity-correlated noise in the detected asymmetry, but also adds a noticeable amount of systematic fluctuations. The strategy of event cut based on the target condition is to filter out events during an instant increase of the regressed asymmetry width, masked with the gray region in Fig 4.11. As a validation, the

main detector signals in both HRSs show a significant loss in yields. All these events within the gray region are excluded in the grand average of the PREX-2 result.

With both JAPAN ErrorFlag and the target condition filter applied, about 50 millions of helicity patterns, equivalent to 113.6 C charge on target, are included in the final PREX-2 results, see in Table 4.6.

	Number Patterns	Charge on Target(Coulomb)
Event Flag	51666674	117.0
Filtered for Target	50102805	113.6

Table 4.6: Summary of pattern counts with event error cuts and end-of-target-life filters

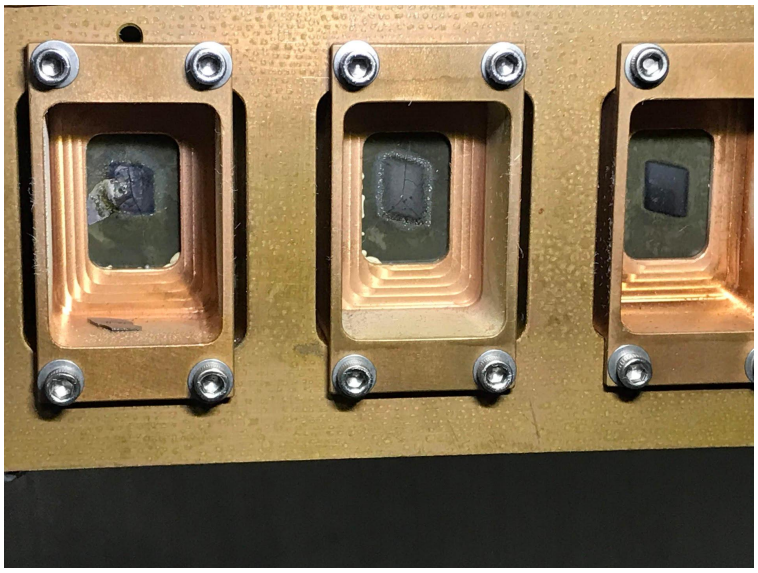

Figure 4.10: A picture of PREX-2 ^{208}Pb target after the production run ended. The target number from the left to the right: 8, 7 and 6. Target ^{208}Pb-6 remained at good condition to the end of the run. The beam raster trace is visible as the darkened region on the diamond surface.

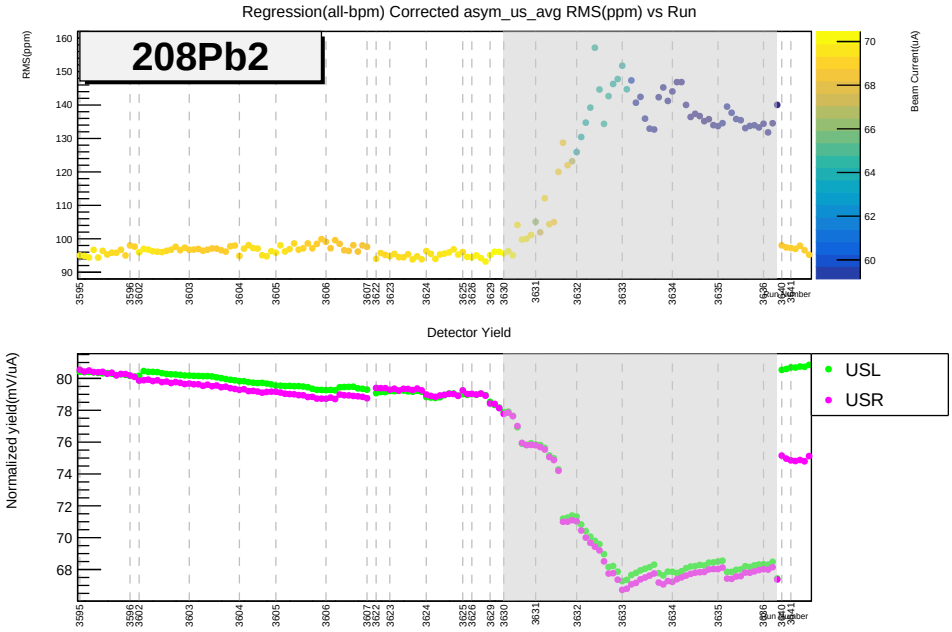

Figure 4.11: Minirun summary plots of at the end run of Target ^{208}Pb-2. The signatures of damaged targets are increasing regression width and sudden change in detector yield. The gray region in the plot indicates the run being filtered out from grand averaging.

Chapter 5

Systematic Control of Beam Fluctuations

In this chapter, the correction to the detected asymmetry for both random fluctuations and helicity-correlated fluctuations in the beam motion is discussed. Section 5.1 introduces the linear model to correct the beam induced asymmetry. From Section 5.2 to Section 5.4, the precision and systematic uncertainties of three different beam correction techniques will be reviewed. Section 5.4 elaborates on the discussion for Lagrange multiplier and explores its advantages over techniques based on linear regression or beam modulation alone. Eigenvector decomposition provides convenience to compare Lagrange multiplier and regression results on an orthogonal basis and its mathematical foundation is provided in Section 5.5. Results based on different techniques are compared to each other in Section 5.6 as a validation of the overall systematic uncertainty from the beam correction.

5.1 Beam-induced Fluctuation in the Detected Asymmetry

The beam correction to the raw detected asymmetry can be expressed in linear form:

$$A_{\text{corr}} = A_{\text{raw}} - \sum_{i=1}^{5} \alpha_i \Delta B_i, \tag{5.1}$$

where $\vec{B} = (X, Y, \theta_X, \theta_Y, E_{\text{beam}})$ are beam positions X/Y, angles θ_X $/\theta_Y$ and beam energy E_{beam} on the ^{208}Pb target. ΔB_i is the helicity-correlated beam parameter difference:

$$\Delta B_i = \frac{B_i^+ - B_i^-}{2}. \tag{5.2}$$

And α_i is the sensitivity of the measured asymmetry to the fluctuation in beam parameter ΔB_i

$$\alpha_i = \frac{\partial A_{\text{raw}}}{\partial \Delta B_i}. \tag{5.3}$$

Beam parameters on target, such as beam position and angle on a target, can be extrapolated from the beam transverse position measured by beam position monitors (BPMs) at different locations along the beam line. Meanwhile, dispersion in the magnetic dipole field at the arc region is sensitive to beam energy fluctuations. Therefore, the phase space of five beam parameters can be spanned by the transverse beam positions along the beamline with linear transformation:

$$\Delta\vec{B} = \mathcal{R}\ \Delta\vec{M}. \tag{5.4}$$

This allows us to perform beam corrections on the basis of BPM measurements in practice:

$$A_{\text{corr}} = A_{\text{raw}} - \sum_i \beta_i \Delta M_i, \tag{5.5}$$

where the helicity-correlated difference of a BPM ΔM_i takes the place of ΔB_i in the previous formula. And sensitivities β_i are now partial derivatives against BPM measurements. The main task of obtaining beam corrections is to choose a set of BPMs to explore the full phase space and calibrate sensitivities to beam fluctuations with accuracy and precision.

PREX was proposed to measure the $\sim$ 0.6 ppm asymmetry with an overall uncertainty of better than 20 ppb (3%). The total scattering event rate at the detectors is $\sim$4 GHz and is characterized by event-by-event statistical fluctuation in the raw asymmetry of $\sim$90 ppm standard deviation over the 33 ms integrating time. In such a high rate measurement, detected asymmetries can be overwhelmed by fluctuations induced by random as well as helicity-correlated beam motion. An example of such a case is shown in Figure 5.1. The distribution of the raw detected asymmetry has a width of 269 ppm dominated by the random fluctuations in beam energy. After beam correction is applied, the RMS width of the detected asymmetry is reduced to 92 ppm, as expected with 70 μA beam current on target integrated in the 33 ms window.

Calibrating sensitivity to beam motion provides linear coefficients to remove its effect on the detected asymmetry to first order. In addition, the grand averaged correction for beam motion can potentially make a sizable contribution to the central value of the observed raw detector asymmetry. Therefore precise and accurate sensitivity calibration techniques are crucial to achieve a small systematic uncertainty.

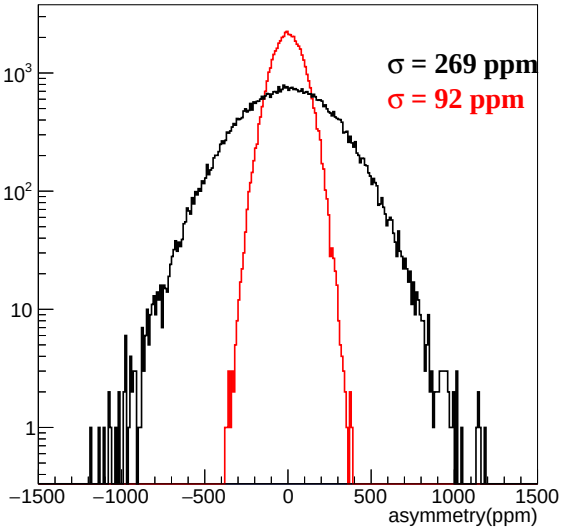

Figure 5.1: Distribution of beam corrected asymmetries sampled from the PREX-2 data compared with the raw detected asymmetries from the exact same data set.

5.2 Multivariate Linear Regression

5.2.1 Overview

Multivariate linear regression is based on the assumption that the false asymmetry induced by fluctuations in beam motion has a linear dependence on the helicity-correlated differences of the BPM measured X and Y coordinates, denoted as x_μ here for convenience

$$f(\mathbf{x}) = \sum_{\mu=1}^{M} \beta_\mu x_\mu + \beta_0, \tag{5.6}$$

$$\mathbf{x} = (x_1, \ldots, x_\mu, \ldots x_M), \tag{5.7}$$

where $f(\mathbf{x})$ is the model predicted false asymmetry induced by fluctuations in beam motion, $M \geq 5$ is the total number of BPM readout channels and βs are parameters. Concretely, β_0 is the intercept and β_μ with μ from 1 to M represents the linear slope of each BPM coordinate. With the raw measured asymmetry denoted as y, the beam corrected asymmetry can be expressed as

$$y - f(\mathbf{x}). \tag{5.8}$$

The second assumption of regression is the corrected asymmetry, that is the difference between measured asymmetry, is dominated by the statistical fluctuation in the asymmetry measurement and the instrumental noise in $\mathbf{x}$ is negligible. Also the noise is assumed to be

independent from event to event. The counting statistic of the i-th event y_i is determined by the normal distribution $\mathcal{N}(\mu = 0, \sigma_i)$ and so that the likelihood function of all samples is

$$P = \prod_i^n p(y_i - f(\mathbf{x}_i)) \propto \exp\Big\{ - \sum_i^n \frac{[y_i - f(\mathbf{x}_i)]^2}{\sigma_i^2} \Big\}. \tag{5.9}$$

Therefore a linear regression minimizing the χ^2, i.e.

$$\chi^2 = \frac{1}{n} \sum_i^n \frac{[y_i - f(\mathbf{x}_i)]^2}{\sigma_i^2}, \tag{5.10}$$

leads to the maximum likelihood.

From the experimental point of view, for a given beam current and detector acceptance, the statistical noise in y from event to event independently follows the same normal distribution $\mathcal{N}(\mu = 0, \sigma)$. In other words, the event-by-event statistical fluctuations in asymmetry measurement is sampled from the same parent distribution. Therefore one can factorize the χ^2 with an universal statistical uncertainty σ

$$\chi^2 = \frac{1}{n\sigma^2} \sum_i^n [y_i - f(\mathbf{x}_i)]^2, \tag{5.11}$$

The statistical uncertainty σ now becomes an overall normalization in χ^2.

In fact, the χ^2 at the minimum corresponds to the root-mean-square (RMS) value of the regressed asymmetry. Therefore regression yields the RMS lower limit of the corrected asymmetry among all techniques given the same BPM data sets under the assumption that the dependence on the helicity-correlated beam position difference is linear.

5.2.2 χ^2 Minimization

The task of χ^2 minimization is to estimate the parameters β_μs based on the observed samples y_i and $\mathbf{x}_i$. The positive quadratic form of χ^2 guarantees that it is a convex parabola surface in the parameter space therefore the global minimum exists and must be unique. And at the global minimum, gradients $\partial\chi^2/\partial\beta_\mu$ in all directions vanish and provide the criterion to search for the minimum

$$\frac{\partial \chi^2}{\partial \beta_\mu} = 0, \ \mu = 0, ..., M. \tag{5.12}$$

For example, one can solve for the intercept term β_0 from the following equation

$$\frac{\partial \chi^2}{\partial \beta_0} = 2 \cdot \frac{1}{n\sigma^2} \sum_i^n [y_i - \sum_{\mu=1}^M \beta_\mu x_{\mu;i} - \beta_0] = 0, \tag{5.13}$$

which requires the sample means of y and $\vec{x}$ have to be in the plane of the optimized $f(\mathbf{x})$, that is,

$$\beta_0 = \overline{y} - \sum_{\mu=1}^{M} \beta_\mu \overline{x}_\mu, \tag{5.14}$$

where $\overline{y}$ and $\overline{x}_\mu$ are sample means calculated as

$$\overline{y} = \frac{1}{n}\sum_{i=1}^{n} y_i, \tag{5.15}$$

$$\overline{x}_\mu = \frac{1}{n}\sum_{i=1}^{n} x_{\mu,i}. \tag{5.16}$$

With the property given by Equation (5.14), the centralized form of χ^2 is practically convenient and more commonly used

$$\chi^2 = \frac{1}{n\sigma^2}\sum_{i}^{n}[(y_i - \overline{y}) - \sum_{\mu=1}^{M}\beta_\mu(x_{\mu;i} - \overline{x}_\mu)]^2 \tag{5.17}$$

$$= \frac{1}{n\sigma^2}\sum_{i}^{n}[y'_i - f(\mathbf{x}'_i)]^2, \tag{5.18}$$

where centralized y'_i and $\mathbf{x}'_i$ are subtracted their sample means.

To solve the slope terms, i.e. β_μ for $\mu \neq 0$, the vanishing gradients must be satisfied

$$\frac{\partial\chi^2}{\partial\beta_\mu} = 2\cdot\frac{1}{n\sigma^2}\sum_{i=1}^{n}(y'_i - \sum_{\nu=1}^{M}\beta_\nu x'_{\nu;i})\cdot x'_{\mu;i} \tag{5.19}$$

$$= 2\cdot\frac{1}{n\sigma^2}\Big[\sum_{i=1}^{n} y'_i x'_{\mu;i} - \sum_{\nu=1}^{M}\beta_\nu\sum_{i=1}^{n} x'_{\nu;i}x'_{\mu;i}\Big] = 0,\ \ \mu = 1, ..., M \tag{5.20}$$

where $\sum_i y'_i x'_{\mu;i}$ and $\sum_i x'_{\nu;i}x'_{\mu;i}$ can be recognized as the covariance between y and x_μs:

$$\mathrm{cov}(y, x_\mu) = \frac{1}{n}\sum_{i=1}^{n}\Big[(y_i - \overline{y})(x_{\mu;i} - \overline{x}_\mu)\Big] = \frac{1}{n}\sum_{i} y'_i x'_{\mu;i}, \tag{5.21}$$

$$\mathrm{cov}(x_\nu, x_\mu) = \frac{1}{n}\sum_{i=1}^{n}\Big[(x_{\nu;i} - \overline{x}_\nu)(x_{\mu;i} - \overline{x}_\mu)\Big] = \frac{1}{n}\sum_{i} x'_{\mu;i}x'_{\nu;i}, \tag{5.22}$$

The gradient Equation (5.20) are now reduced to

$$\mathrm{cov}(y, x_\mu) - \sum_{\nu=1}^{M}\beta_\nu \mathrm{cov}(x_\nu, x_\mu) = 0,\ \ \mu = 1, ..., M \tag{5.23}$$

To solve Equation (5.23) for β_μs for all μ simultaneously, the matrix representing this linear regression system is constructed as

$$\begin{pmatrix} \vdots \\ \mathrm{cov}(y, x_\mu) \\ \vdots \end{pmatrix}_{M\times 1} = \begin{pmatrix} \ddots & & \\ & \mathrm{cov}(x_\mu, x_\nu) & \\ & & \ddots \end{pmatrix}_{M\times M} \begin{pmatrix} \vdots \\ \beta_\nu \\ \vdots \end{pmatrix}_{M\times 1}. \tag{5.24}$$

The column vector $\mathbf{B} = \vec{\beta}$ on the right-hand side can be solved by matrix inversion

$$\mathbf{Y} = \mathbf{XB} \rightarrow \mathbf{B} = \mathbf{X}^{-1}\mathbf{Y}, \tag{5.25}$$

where $\mathbf{X}^{-1}$ is the inverse matrix of $\mathbf{X}$ of which the elements are the covariance between x_μ and x_ν, that is $\mathbf{X}_{\mu\nu} = \mathrm{cov}(x_\mu, x_\nu)$.

5.2.3 Slope Dilution

Consider a one-dimensional linear regression model , $f(x)$ and the χ^2 minimization

$$f(x) = \beta_1 \cdot x, \tag{5.26}$$

$$\frac{\partial \chi^2}{\partial \beta_1} = 0 \ \rightarrow \beta_1 = \frac{\mathrm{cov}(y, x)}{\mathrm{var}(x)}. \tag{5.27}$$

Suppose x can be decomposed into two independent sources: fluctuations in real signal s and instrumental Gaussian noise $\varepsilon \sim \mathcal{N}(0, \sigma_\varepsilon)$

$$x = s + \varepsilon. \tag{5.28}$$

The contribution from instrumental noise ε in the numerator of Equation 5.27 is expected to be zero, since it is an independent random variable centered at zero:

$$\mathrm{cov}(y, x) = \mathrm{cov}(y, s) + \mathrm{cov}(y, \varepsilon) = \mathrm{cov}(y, s) + 0, \tag{5.29}$$

while in the denominator, the variance of x is

$$\mathrm{var}(x) = \sigma_s^2 + \sigma_\varepsilon^2. \tag{5.30}$$

And the dilution of regression slope β_1 can be viewed in the following

$$\beta_1 = \frac{\mathrm{cov}(y, x)}{\sigma_s^2 + \sigma_\varepsilon^2} = \frac{\mathrm{cov}(y, x)}{\sigma_s^2(1 + \sigma_\varepsilon^2/\sigma_s^2)} \approx \frac{\mathrm{cov}(y, x)}{\sigma_s^2}(1 - \sigma_\varepsilon^2/\sigma_s^2). \tag{5.31}$$

The relative ratio between finite instrumental resolution and signal fluctuation flattens the regression slope from the "true" value as a consequence of the direction that regression chose

(y-direction in this case) to minimize. This effect is also known as the "dilution" effect, as the size of the regression slope is always smaller than that of the "true" value.

The typical BPM resolution is known to be 0.3 μm - 0.5 μm and the transverse beam position fluctuation at different locations along the beam line depends on beam optics and ranges from 1 μm - 10 μm. Therefore the dilution effect can be larger than 10% for highly correlated monitors or less than 1% in other cases. Whether the dilution effect matters nor not will be discussed in Section 5.6 during the systematic uncertainty evaluation.

5.2.4 Multi-dimensional Parameters Correlation

The general way to define the standard-deviation error on a regression slope is in terms of the error matrix, the inverse of the second derivative matrix of χ^2 with respect to the parameters. The difficulty of interpreting the errors arises when the independent variables are correlated with each other.

The second derivative matrix is also known as the χ^2 curvature matrix, of which the elements are the second derivatives of χ^2 with respect to parameter β_μ

$$\mathbf{C}_{\mu\nu} = \frac{1}{2}\frac{\partial^2\chi^2}{\partial\beta_\mu\partial\beta_\nu} = \frac{1}{\sigma^2}\mathrm{cov}(x_\mu, x_\nu) = \frac{1}{\sigma^2}\mathbf{X}_{\mu\nu}, \tag{5.32}$$

and turns out to be the covariance matrix $\mathbf{X}$.

From Equation 5.25, the sensitivity of fitting parameters to statistical fluctuation in y can be expressed as

$$\frac{\partial\beta_\mu}{\partial y_i} = \sum_\nu (\mathbf{X}^{-1})_{\mu\nu}\frac{1}{n}(x_{\nu;i} - \overline{x}_\nu). \tag{5.33}$$

Since the statistical noise for each y_i is sampling the same parent Gaussian distribution, the squared uncertainty of β_μ is in terms of the diagonal element in the inverse of $\mathbf{X}$

$$\sigma^2_{\beta_\mu} = \sigma^2_y \sum_i^n (\frac{\partial\beta_\mu}{\partial y_i})^2 = \frac{1}{n}\sigma^2_y(\mathbf{X}^{-1})_{\mu\mu}, \tag{5.34}$$

which also includes the effects of correlation from other free parameters. The correlations are picked up when the curvature matrix is inverted. Although a parameter can be either positively or negatively correlated with others, the effect of correlation always has the errors overestimated. One way to study regression's precision without correlation effects is to diagonalize the covariance matrix $\mathbf{X}$ in the first place and solve slopes in the eigenvector orthogonal basis. This eigenvector analysis is covered in Section 5.5.

The correlation of regression's free parameter can be the beam position correlation at different BPMs, e.g. the beam angle fluctuations observed in two BPMs depend on their

geometrical relation in the beamline. Meanwhile, the instrumental noise among BPM channels can be correlated or anti-correlated due to electronic cross-talk, and distorts the beam parameter correlation. Along with the dilution effect, the instrumental noise not only introduces error in the regressed central value but also increases residual beam noise in the regressed asymmetries.

Since the instrumental noise among BPM channels is not uniform in both magnitude and sign, it is hard to quantify its impact on matrix inversion analytically. The following results in Table 5.1 from a generated data based on Monte Carlo sampling shows the increasing electronic pickup between BPM devices not only increases the regression RMS width but also shifts the central value from the expected true value. The simulation test in Table 5.1 uses 5 BPMs to regress 5-dimensional independent physical beam fluctuations. All of the following regression tests were based on the same random seed and the only difference is the amplitude of instrumental correlated noise.

	Mean (ppb)	Std. Err. (ppb)	RMS (ppm)	χ^2 / NDF
True Value	-41	204	87	14.0 /19
Uncorrected	2290	643	273	13.7 /19
Reg_5BPM (1x Noise)	188	211	90	12.5 /19
Reg_5BPM (2x Noise)	581	219	93	12.2 /19
Reg_AllBPM (1x Noise)	-25	206	87	13.3 /19
Reg_AllBPM (2x Noise)	-25	206	87	13.3 /19

Table 5.1: Run averages over 20 Monte Carlo runs. The second column "Std. Err." is the estimated statistical uncertainty.

The impacts from the instrumental correlated noise can be largely mitigated by increasing the number of redundant BPM channels. This effect is demonstrated in the last two rows named "Reg_AllBPM" in Table 5.1, where 12 BPM channels are used in the same simulated dataset. Results from real data shown in Table 5.7 in Section 5.6 compares the dithering analysis (5-BPMs) with regression (all-BPMs) and indicates that the simulated situation in Table 5.1 where the instrumental noise is significant is not a problem for the PREX-2 data.

Another type of harmful parameter correlation comes from the electronic pickup between the hardware channels of detectors and BPMs, since regression relies on the observed covariance between detected asymmetry y and monitored x_μs in Equation (5.25). If the electronic noise ϵ_1 and ϵ_2 in the detector y and BPM channels x_μs are correlated ,

$$\mathrm{cov}(y+\epsilon_1, x_\mu+\epsilon_2) = \mathrm{cov}(y, x_\mu) + \mathrm{cov}(\epsilon_1, \epsilon_2), \tag{5.35}$$

the non-zero $\mathrm{cov}(\epsilon_1, \epsilon_2)$ directly deviates the regression slope from true value to any direction at any magnitude.

5.3 Beam Modulation Analysis

5.3.1 Overview

In Section 3.3, the hardware and the timing structure of the beam modulation system were discussed. This section focuses on the analysis of the beam modulation data. "beam modulation" and "dithering" are interchangeable terms within the context of this work. Beam modulation analysis is often referred to as "dithering analysis".

The beam modulation analysis calibrates the correction slopes using the derivative chain rule between the detector sensitivities and BPM sensitivities :

$$\frac{\partial \hat{D}}{\partial C_\mu} = \sum_\nu \frac{\partial \hat{D}}{\partial M_\nu} \frac{\partial M_\nu}{\partial C_\mu} \tag{5.36}$$

where detector yield D, normalized by the beam current, is further normalized by the mean $\langle D \rangle$ of all data selected during the dithering step so that $\hat{D}$ becomes the fractional yield:

$$\hat{D} = \frac{D}{\langle D \rangle}. \tag{5.37}$$

M_k is the beam position monitored by k-th BPM channel and C_j is the trimcard counts for j-th coil.

Note that the normalization factor of $\hat{D}$ in Equation (5.37) should also depend on the software normalization of helicity-correlated differences in the parity analyzer. For example, in JAPAN, the helicity-correlated difference of BPM computed from a full pattern of 240 Hz octets is normalized by a factor of 2

$$\Delta M = \frac{1}{8}(M_1 - M_2 - M_3 + M_4 - M_5 + M_6 + M_7 - M_8) = \frac{1}{2}(\langle M^L \rangle - \langle M^R \rangle), \tag{5.38}$$

and the same rule applies for detector differences so that the ratio of ΔD over $\langle D \rangle$ naturally becomes the detected asymmetry

$$A = \frac{\Delta D}{\langle D \rangle} = \frac{\langle D^L \rangle - \langle D^R \rangle}{2\langle D \rangle}. \tag{5.39}$$

Using this convention, the scale of dithering slope $\partial \hat{D}/\partial M_\mu$ is consistent with that of the correction slope of detected asymmetry with respect to helicity-correlated BPM differences

$$\frac{\partial \hat{D}}{\partial M_\mu} \sim \left[\frac{D^L - D^R}{\langle D \rangle (M_\mu^L - M_\mu^R)}\right] \sim \frac{\partial A}{\partial \Delta M_\mu}. \tag{5.40}$$

In the previous version of parity analyzer, e.g. PAN, helicity correlated difference is defined without the factor of 2 in Equation (5.38). In order to match the scale and dimension of dithering slopes and correction slopes, Equation (5.37) has to be scaled as

$$\hat{D} = \frac{D}{2\langle D \rangle}, \tag{5.41}$$

which appears in multiple publications and reports of previous parity experiments using this different convention of helicity-correlated differences.

5.3.2 Sensitivities Calculation

Sensitivities are calculated from the least square linear fit based on the following linear model:

$$\hat{D}(C) = \frac{\partial \hat{D}}{\partial C}(C - C_0) + \hat{D}_0, \tag{5.42}$$

$$M(C) = \frac{\partial M}{\partial C}(C - C_0) + M_0. \tag{5.43}$$

where $\hat{D}_0$ and M_0 are the response of a detector and a BPM when modulation is not activated. And C is the generated function with the magnitude B proportional to the driving current strength in the beam modulation coils

$$C(t) = B\sin(2\pi f t + \phi) + C_0, \tag{5.44}$$

where frequency f is set to 15 Hz and ϕ is the initial phase relative to DAQ trigger time. C_0 is the constant electronic baseline. The linear slope is calculated from the covariance between the monitor response and the coil driving signal:

$$\frac{\partial \hat{D}}{\partial C} = \frac{1}{\langle D \rangle} \frac{\sum_i (D_i - D_0)(C_i - C_0)}{\sum_i (C_i - C_0)^2}, \tag{5.45}$$

$$\frac{\partial M}{\partial C} = \frac{\sum_i (M_i - M_0)(C_i - C_0)}{\sum_i (C_i - C_0)^2}, \tag{5.46}$$

where i is the index of events and increments with time.

Figure 5.2 displays an example of sensitivities extraction. Data points (gray) grouped by the modulation phase follow the 15 Hz sine waveform (blue dash) as expected. And the linear correlation between the monitor response and the magnitude of the driving signal is shown in the right panel. The linear fit to the data is shown as the red line.

The intrinsic random fluctuations of the detector response and the beam position have no correlation with the modulation signal, therefore their contribution to the sensitivity extraction is expected to be zero when being integrated over complete modulation cycles.

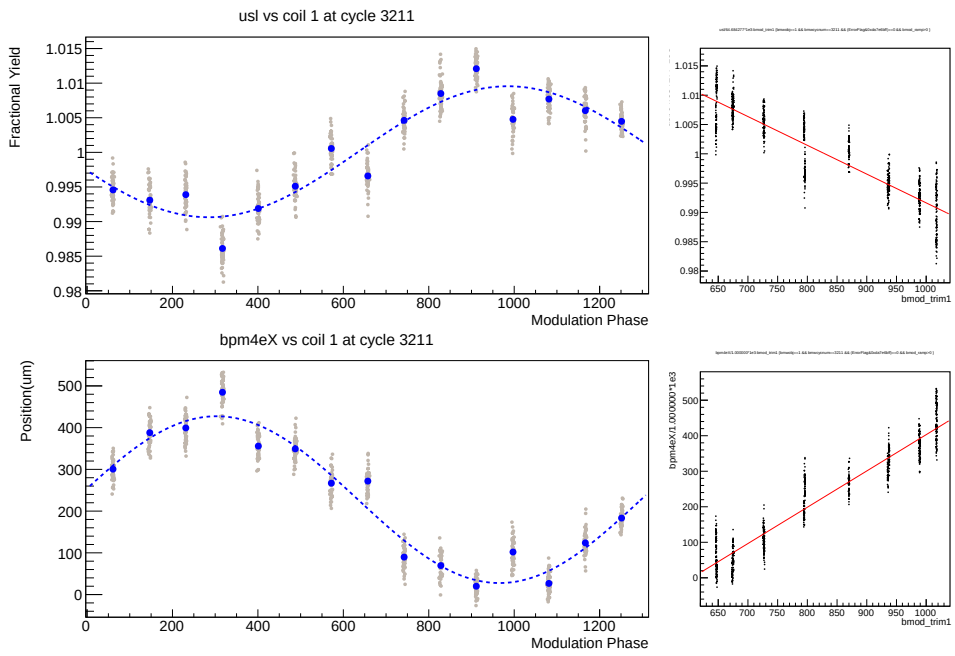

Figure 5.2: Example of beam modulation cycle and the linear fit for dithering sensitivity. Top: Fractional left-arm detector response ($\hat{D}$); Bottom: beam position at BPM 4eX in mm.

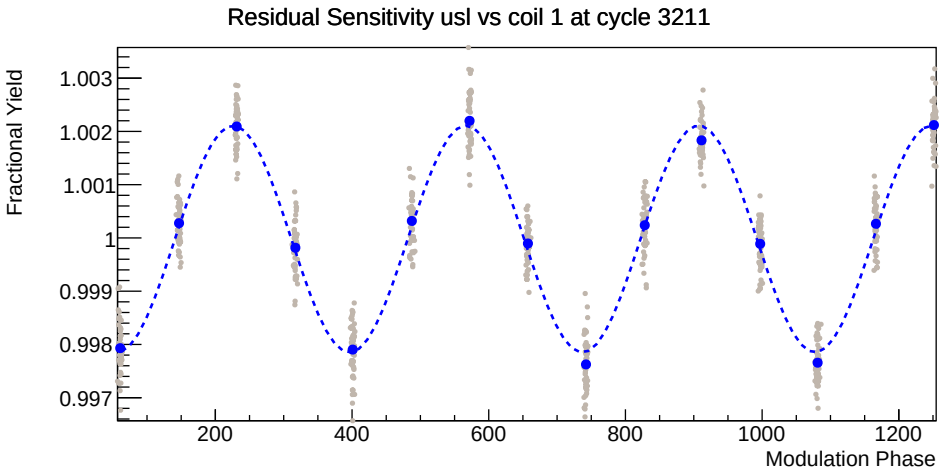

Figure 5.3: The left-arm detector residual response as a function of the modulation phase. The frequency of the residual response is 60 Hz.

Fluctuations in the response coherent to the 15 Hz modulation signal, e.g. subharmonic modes of 15 Hz, potentially distort the extracted sensitivities from their true values. The dominant coherent subharmonic mode is the 60 Hz noise introduced from the power line. The 60 Hz oscillation is apparent and visualized in Figure 5.3 when the 15 Hz component is

corrected by subtraction. Also notice that

$$B_{15\text{Hz}} = 0.01, \tag{5.47}$$

$$B_{60\text{Hz}} = 0.002. \tag{5.48}$$

To evaluate the effect from the 60 Hz on (5.45) and (5.46) for the sensitivity extraction, a response, either in detectors or BPMs, can be decomposed into different frequency components (f_i)

$$S(t) = \sum_i S_i(t) = \sum_i B_i \sin(2\pi f_i t + \phi_i). \tag{5.49}$$

When one performs calculation for the numerator part of (5.45) and (5.46), the summation can be approximately processed as an integral over time in the continuous limit. For a given frequency component f_i, that is

$$\sum_i S_i(t) \times C(t) \to \int \mathrm{d}t S_i(t) \times C(t). \tag{5.50}$$

With the trigonometry product-to-sum formula applied, one can obtain the integral over multiple full 15 Hz cycles ($T = N/f,\ f = 15$ Hz)

$$\begin{aligned}
&\int_0^T \mathrm{d}t S_i(t) \times C(t) = \int_0^T \mathrm{d}t B_i \sin(2\pi f_i t + \phi_i) \times \sin(2\pi f t + \phi) \\
= &\int_0^T \mathrm{d}t \frac{1}{2}\Big\{ B_i \cos[2\pi(f_i - f)t + \phi_i - \phi] - B_i \cos[2\pi(f_i + f)t + \phi_i + \phi]\Big\} \\
= &\frac{1}{2}\Big\{ \frac{B_i}{2\pi(f_i - f)} \sin[2\pi(f_i - f)T + \phi_i - \phi] - \frac{B_i}{2\pi(f_i - f)} \sin[\phi_i - \phi] \\
&- \frac{B_i}{2\pi(f_i + f)} \sin[2\pi(f_i + f)T + \phi_i + \phi] + \frac{B_i}{2\pi(f_i + f)} \sin[\phi_i + \phi]\Big\}.
\end{aligned} \tag{5.51}$$

The 'resonance' contribution , i.e. $f_i = f = 15$ Hz, which is the signal of interest

$$\int_0^T \mathrm{d}t S_{15\text{Hz}}(t) \times C(t) = \frac{T}{2} B_{15\text{Hz}}. \tag{5.52}$$

The 60 Hz contribution is bounded by the amplitude terms $\frac{B_{60\text{Hz}}}{2\pi(60+15)}$ and $\frac{B_{60\text{Hz}}}{2\pi(60-15)}$ respectively, and it is tiny compared with the 'resonance' contribution

$$\begin{aligned}
&\frac{B_{60\text{Hz}}}{2\pi(60 \pm 15)} / (\frac{T}{2} B_{15\text{Hz}}) \\
= &\frac{1}{\pi} \cdot \frac{B_{60\text{Hz}}}{B_{15\text{Hz}}} \cdot \frac{1}{N} \cdot \frac{15}{60 \pm 15} < 4 \times 10^{-4},
\end{aligned} \tag{5.53}$$

where the repeats of 15 Hz cycles $N = 50$ for one single beam modulation supercycle. The suppression shown here on the 60 Hz is essentially an example of the lock-in amplification technique.

5.3.3 Solving Slopes

In the general case, for which number of BPMs and number of coils in use may not be equal, to solve dithering slope from Equation (5.36), the least square approach can be applied as follow

$$\chi^2 = \sum_{\mu} \frac{1}{\sigma_\mu^2} \Big(\frac{\partial \hat{D}}{\partial C_\mu} - \sum_{\nu} \frac{\partial \hat{D}}{\partial M_\nu} \frac{\partial M_\nu}{\partial C_\mu} \Big)^2 \tag{5.54}$$

For convenience,

$$y_\mu := \frac{\partial \hat{D}}{\partial C_\mu}, \quad x_{\mu\nu} := \frac{\partial M_\nu}{\partial C_\mu}, \quad \beta_\nu := \frac{\partial \hat{D}}{\partial M_\nu}, \tag{5.55}$$

$$\chi^2 = \frac{1}{\sigma^2} \sum_{\mu} \Big(y_\mu - \sum_{\nu} x_{\mu\nu} \beta_\nu \Big)^2, \tag{5.56}$$

where the noise of each measurement, σ_μ is assumed to be the same so that all equations are equally weighted. And the matrix form of Equation (5.36) becomes

$$\begin{pmatrix} \vdots \\ y_\mu \\ \vdots \end{pmatrix}_{m\times 1} = \begin{pmatrix} \ddots & & \\ & x_{\mu\nu} & \\ & & \ddots \end{pmatrix}_{m\times n} \begin{pmatrix} \vdots \\ \beta_\nu \\ \vdots \end{pmatrix}_{n\times 1} \rightarrow \mathbf{Y} = \mathbf{XB}, \tag{5.57}$$

To solve $\mathbf{B}$, χ^2 is minimized

$$\frac{\partial \chi^2}{\partial \beta_\nu} = \frac{2}{\sigma^2} \sum_{\mu} \Big(y_\mu - \sum_{\gamma} x_{\mu\gamma} \beta_\gamma \Big) x_{\mu\nu} \tag{5.58}$$

$$= \frac{2}{\sigma^2} \Big(\sum_{\mu} y_\mu x_{\mu\nu} - \sum_{\mu} \sum_{\gamma} x_{\mu\gamma} \beta_\gamma x_{\mu\nu} \Big) = 0, \tag{5.59}$$

and terms within the braces can be assembled into a matrix form

$$\sum_{\mu} y_\mu x_{\mu\nu} - \sum_{\mu} \sum_{\gamma} x_{\mu\gamma} \beta_\gamma x_{\mu\nu} = 0 \rightarrow \mathbf{X^T Y} = \mathbf{X^T X B} \tag{5.60}$$

The dithering slope matrix $\mathbf{B}$ now can be solved from the inversion of the square matrix $\mathbf{X^T X}$

$$\mathbf{B} = (\mathbf{X^T X})^{-1} \mathbf{X^T Y}. \tag{5.61}$$

which is also known as Moore-Penrose inverse or pseudo-inverse.

When the number of dithering coils is more than that of BPMs in the equations, the dithering slopes solved in this configuration are called over-constrained slopes. The core of this approach is to minimize the residual sensitivities of all dithering measurements simultaneously.

When the number of BPMs and the number of coils are equal and $\mathbf{X}$ itself is squared, the solution of $\mathbf{B}$ from the inversion of $\mathbf{X}$ is more commonly used and is the special case of Moore-Penrose inverse

$$\mathbf{B} = (\mathbf{X^T X})^{-1}\mathbf{X^T Y} = \mathbf{X}^{-1}\mathbf{Y}. \tag{5.62}$$

In the PREX-2 dithering analysis, only five coils were included therefore the dithering slopes were calculated using Equation (5.62). The rest of coils data are for redundancy and are primarily used in checking residual sensitivities, which will be discussed in Section 5.4.4.

The BPM channels used for the PREX-2 dithering analysis are 4aX, 4aY , 4eX, 4eY and a combined channel of 11X and 12X (11X + 0.4×12X), which are also used for the regression in the 5 BPMs configuration. The combination of 11X and 12X was determined from data runs in the early stage for an improvement in the sensitivity to energy fluctuation and it was fixed for all the rest of the runs when the 11X channel was available. The linear combination of BPMs for the optimal sensitivity to the energy fluctuation is time dependent and changes with the accelerator beam optics, therefore the fixed ratio between 11X and 12X is not guaranteed to provide the optimal energy fluctuation observable all the time.

In the meantime, the number of BPM channels is constrained by the number of dithering coils included for the analysis, i.e. $N_{\text{BPM}} \leq N_{\text{coil}} = 5$. The lack of flexibility in the BPMs choice and composition limits the resolution for monitoring beam parameters and results in a relatively larger random fluctuation in the corrected asymmetry compared with all other beam correction techniques. For the detailed discussion and comparison, see Figure 5.5 and the context in Section 5.4.

5.4 Lagrange Multiplier Regression

The multivariate linear regression gives corrected RMS width at the lower limit while it is susceptible to instrumental noise for both random and common mode noise. The beam modulation is more reliable in terms of accuracy while its precision is limited by both the number of BPMs that can be included in the linear system framed by the number of coils and the flexibility of BPM composition, as discussed in Section 5.3.3. The idea of regression with the Lagrange multiplier is to combine the advantages of these two techniques while reducing the impacts from their drawbacks.

In the Lagrange multiplier analysis for PREX-2, the BPM configuration includes all the available BPMs in the Hall A beamline. From Slug 1 to Slug 2, due to the hardware malfunction in the BPM-14 sampling module, 10 BPM channels are included in total. From Slug 3 to Slug 94, BPM-8 and BPM-14 were replaced by BPM-11 and BPM-16 and totally

12 BPM channels are included in this run period. The constraints assigned for the Lagrange multiplier are the measured dithering sensitivities from 5 coils. The number of constraining coils are fixed for all runs while the choice of the 5 coils out of the total 7 coils are run-period dependent. Compared with the dithering analysis with 5 BPMs, the Lagrange multiplier analysis gains more flexibility and precision in monitoring beam fluctuations and a better control in the relative contribution from each BPM in each dimension of beam fluctuations, which is now naturally determined from the correlations in beam modulation sensitivities. Therefore the monitor sensitivity for beam fluctuations provided by the Lagrange multiplier is reliable and optimal over the time.

5.4.1 Example with Two BPMs and One Beam Modulation Coil

Assume a beam correction for one dimensional beam parameter phase space spanned by measurements from two BPMs:

$$A_{\rm corr} = A - \beta_1 \Delta M_1 - \beta_2 \Delta M_2. \tag{5.63}$$

And the goal is to solve two unknown variables β_1 and β_2

$$\beta_1 = \frac{\partial A}{\partial \Delta M_1},\ \beta_2 = \frac{\partial A}{\partial \Delta M_2}, \tag{5.64}$$

given one linear constraint from one single beam modulation measurement

$$\frac{\partial \hat{D}}{\partial C} = \beta_1 \frac{\partial M_1}{\partial C} + \beta_2 \frac{\partial M_2}{\partial C}. \tag{5.65}$$

$$\mathcal{L} = \chi^2 + \lambda(\frac{\partial \hat{D}}{\partial C} - \beta_1 \frac{\partial M_1}{\partial C} - \beta_2 \frac{\partial M_2}{\partial C}), \tag{5.66}$$

where

$$\chi^2 = \sum_i \left(A^{(i)} - \beta_1 \Delta M_1^{(i)} - \beta_2 \Delta M_2^{(i)} \right)^2, \tag{5.67}$$

Also, without loss of generality, the covariance between ΔM_1 and ΔM_2 is assumed to be zero

$$\mathrm{cov}(\Delta M_1, \Delta M_2) = 0 \tag{5.68}$$

The Lagrange multiplier method is to solve the following equations simultaneously

$$\frac{\partial \mathcal{L}}{\partial \beta_1} = -2\mathrm{cov}(A, \Delta M_1) + 2\beta_1 \sigma^2_{\Delta M_1} - \lambda \frac{\partial M_1}{\partial C} = 0 \tag{5.69}$$

$$\frac{\partial \mathcal{L}}{\partial \beta_2} = -2\mathrm{cov}(A, \Delta M_2) + 2\beta_2 \sigma^2_{\Delta M_2} - \lambda \frac{\partial M_2}{\partial C} = 0 \tag{5.70}$$

$$\frac{\partial \mathcal{L}}{\partial \lambda} = \frac{\partial \hat{D}}{\partial C} - \beta_1 \frac{\partial M_1}{\partial C} - \beta_2 \frac{\partial M_2}{\partial C} = 0 \tag{5.71}$$

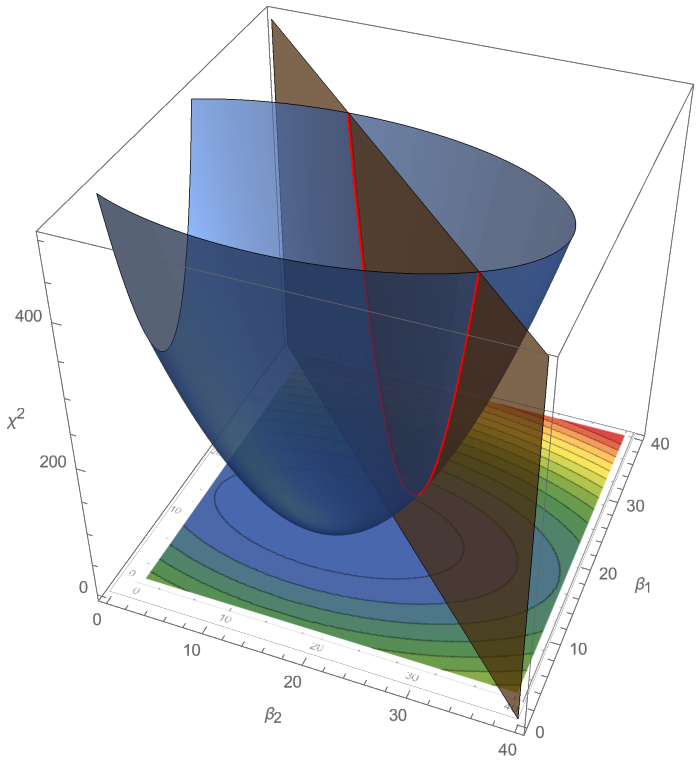

Figure 5.4: χ^2 vs (β_1, β_2)- Visualization of 2-dim Lagrange Multiplier in an arbitrary unit. Blue: surface of χ^2 in parameter space. Orange: constraint $\beta_1 + \beta_2 = 40$. Red: Intersection between χ^2 surface and the constraint.

From Equation 5.69 and Equation 5.70

$$\beta_1 = \frac{\lambda}{2\sigma^2_{\Delta M1}} \frac{\partial M_1}{\partial C} + \beta'_1, \tag{5.72}$$

$$\beta_2 = \frac{\lambda}{2\sigma^2_{\Delta M2}} \frac{\partial M_2}{\partial C} + \beta'_2. \tag{5.73}$$

where β'_1 and β'_2 are regression slopes without constraints:

$$\beta'_1 = \frac{\mathrm{cov}(A, \Delta M_1)}{\sigma^2_{\Delta M_1}}, \tag{5.74}$$

$$\beta'_2 = \frac{\mathrm{cov}(A, \Delta M_2)}{\sigma^2_{\Delta M_2}}. \tag{5.75}$$

And the Lagrange multiplier factor

$$\frac{\lambda}{2} = \Big(\frac{\partial \hat{D}}{\partial C} - \beta'_1 \frac{\partial M_1}{\partial C} - \beta'_2 \frac{\partial M_2}{\partial C}\Big) / \Big(\frac{1}{\sigma^2_{\Delta M_1}} \frac{\partial M_1}{\partial C} + \frac{1}{\sigma^2_{\Delta M_2}} \frac{\partial M_2}{\partial C}\Big), \tag{5.76}$$

of which the numerator is so-called dithering residual sensitivities corrected by regression slopes. The Lagrange multiplier factor also determines the slope differences from regression

$$\frac{\lambda}{2\sigma^2_{\Delta M1}}\frac{\partial M_1}{\partial C} = \beta_1 - \beta'_1, \tag{5.77}$$

$$\frac{\lambda}{2\sigma^2_{\Delta M2}}\frac{\partial M_2}{\partial C} = \beta_2 - \beta'_2. \tag{5.78}$$

The difference between regression and the Lagrange multiplier regression can be visualized in Figure 5.4 showing the χ^2 dependence on the slopes β_1 and β_2 along with the linear constraint constructed by one beam modulation. The lowest bottom of the blue surface is the solution from linear regression. Due to the slope dilution caused by the limited BPM resolution, its location is shifted out of the plane defined by the beam modulation data and usually results in systematic bias. Meanwhile, with the constraint from the beam modulation alone, the χ^2 is not guaranteed to be optimal.

5.4.2 Generalized Lagrange Multiplier Regression

So long as the number of BPMs is greater than the number of dithering coils as constraints, the problem can be solved with Lagrange multiplier method to minimize

$$\chi^2 = \sum_i \left(A^{(i)} - \sum_\mu \beta_\mu \Delta M^{(i)}_\mu\right)^2, \tag{5.79}$$

which is similar to Equation (5.67), with constraints from dithering measurement as in Equation (5.65)

$$\frac{\partial \hat{D}}{\partial C_\mu} = \sum_\nu \frac{\partial \hat{D}}{\partial M_\nu}\frac{\partial M_\nu}{\partial C_\mu}. \tag{5.80}$$

For the PREX-2 parity-violating asymmetry analysis, 12 BPM channels were available in the Hall A beamline and are all used for the beam correction. And 5 beam modulation coils were selected out of total 7 coils to optimize the phase space orthogonality. Therefore the indices of BPMs and coils run from 1 to 12 and from 1 to 5 respectively

$$\Delta M_\mu : \ \mu = 1, 2, \ldots, 12, \tag{5.81}$$

$$C_\mu : \ \mu = 1, 2, \ldots, 5. \tag{5.82}$$

For simplification, the following notations are defined and drop partial derivative symbols

$$\frac{\partial \hat{D}}{\partial C_\mu} = d_\mu, \quad \frac{\partial M_\nu}{\partial C_\mu} = m_{\mu\nu}, \tag{5.83}$$

For a given detector, to minimize the width under constraints, the Lagrangian is constructed as

$$\mathcal{L} = \chi^2 + \sum_{\gamma} \lambda_\gamma \Big(\sum_{\nu} \beta_\nu m_{\gamma\nu} - d_\gamma \Big), \tag{5.84}$$

and reaches the minimum when

$$\begin{cases} \dfrac{\partial \mathcal{L}}{\partial \beta_\mu} = 2 \sum_{\nu} \mathrm{cov}(\Delta M_\mu, \Delta M_\nu)\beta_\nu - 2\mathrm{cov}(A, \Delta M_\mu) + \sum_{\gamma} m_{\mu\gamma}\lambda_\gamma = 0 \\ \dfrac{\partial \mathcal{L}}{\partial \lambda_\tau} = \sum_{\nu} m_{\tau\nu}\beta_\nu - d_\tau = 0, \end{cases} \tag{5.85}$$

or in matrix form

$$\begin{pmatrix} \ddots & & & \ddots & & \\ & \mathrm{cov}(\Delta M_\mu, \Delta M_\nu) & & & m_{\mu\gamma} & \\ & & \ddots & & & \ddots \\ \ddots & & & \ddots & & \\ & m_{\nu\tau}^T & & & 0 & \\ & & \ddots & & & \ddots \end{pmatrix} \begin{pmatrix} \vdots \\ \beta_\nu \\ \vdots \\ \vdots \\ \lambda_\gamma/2 \\ \vdots \end{pmatrix} = \begin{pmatrix} \vdots \\ \mathrm{cov}(A, \Delta M_\mu) \\ \vdots \\ \vdots \\ d_\tau \\ \vdots \end{pmatrix}. \tag{5.86}$$

For simplicity of discussion in the following, Equation (5.86) is expressed in term of block submatrices

$$\begin{pmatrix} \mathbf{A} & \mathbf{B} \\ \mathbf{B^T} & \mathbf{0} \end{pmatrix} \begin{pmatrix} \mathbf{X} \\ \mathbf{L} \end{pmatrix} = \begin{pmatrix} \mathbf{Y} \\ \mathbf{D} \end{pmatrix}. \tag{5.87}$$

The slopes, β_ν in $\mathbf{X}$ can be solved by matrix inversion

$$\begin{pmatrix} \mathbf{X} \\ \mathbf{L} \end{pmatrix} = \begin{pmatrix} \mathbf{A} & \mathbf{B} \\ \mathbf{B^T} & \mathbf{0} \end{pmatrix}^{-1} \begin{pmatrix} \mathbf{Y} \\ \mathbf{D} \end{pmatrix}. \tag{5.88}$$

5.4.3 Comparison with Regression

To quantify the differences between the results from regression and Lagrange multipliers, the matrix inversion part of Equation (5.88) is represented blockwise

$$\begin{pmatrix} \mathbf{A} & \mathbf{B} \\ \mathbf{B^T} & \mathbf{0} \end{pmatrix}^{-1} = \begin{pmatrix} \mathbf{A^{-1}} + \mathbf{A^{-1}BC^{-1}B^TA^{-1}} & -\mathbf{A^{-1}BC^{-1}} \\ -\mathbf{C^{-1}B^TA^{-1}} & \mathbf{C^{-1}} \end{pmatrix}, \tag{5.89}$$

where $\mathbf{C}$ is the **Schur complement** of block $\mathbf{A}$

$$\mathbf{C} := \mathbf{0} - \mathbf{B^T A^{-1} B} = -\mathbf{B^T A^{-1} B}. \tag{5.90}$$

With Equation (5.89), Equation (5.88) becomes

$$\begin{pmatrix}\mathbf{X}\\ \mathbf{L}\end{pmatrix} = \begin{pmatrix}\mathbf{A}^{-1}\mathbf{Y} + \mathbf{A}^{-1}\mathbf{B}\mathbf{C}^{-1}\mathbf{B}^{\mathbf{T}}\mathbf{A}^{-1}\mathbf{Y} - \mathbf{A}^{-1}\mathbf{B}\mathbf{C}^{-1}\mathbf{D}\\ -\mathbf{C}^{-1}\mathbf{B}^{\mathbf{T}}\mathbf{A}^{-1}\mathbf{Y} + \mathbf{C}^{-1}\mathbf{D}\end{pmatrix}, \tag{5.91}$$

and the difference between Lagrange multiplier and regression can be quickly recognized as

$$\mathbf{X} - \mathbf{A}^{-1}\mathbf{Y} = \mathbf{A}^{-1}\mathbf{B}\mathbf{C}^{-1}\mathbf{B}^{\mathbf{T}}\mathbf{A}^{-1}\mathbf{Y} - \mathbf{A}^{-1}\mathbf{B}\mathbf{C}^{-1}\mathbf{D} = -\mathbf{A}^{-1}\mathbf{B}\mathbf{L}, \tag{5.92}$$

which depends on the Lagrange multiplier factors λ_i of block $\mathbf{L}$. Recall that the solution of slopes from regression is

$$\mathbf{X}' = \mathbf{A}^{-1}\mathbf{Y}. \tag{5.93}$$

The meaning of these Lagrange multiplier factors can be understood by rearranging the following equation

$$\mathbf{L} = -\mathbf{C}^{-1}\mathbf{B}^{\mathbf{T}}\mathbf{A}^{-1}\mathbf{Y} + \mathbf{C}^{-1}\mathbf{D} = \mathbf{C}^{-1}(\mathbf{D} - \mathbf{B}^{\mathbf{T}}\mathbf{A}^{-1}\mathbf{Y}) = \mathbf{C}^{-1}(\mathbf{D} - \mathbf{B}^{\mathbf{T}}\mathbf{X}'), \tag{5.94}$$

where the part within the braces are also known as the dithering residual sensitivities with regression slopes used. Explicitly, the Lagrange multiplier factor can be expressed as

$$\frac{\lambda_\gamma}{2} = \sum_\nu (C^{-1})_{\gamma\nu}\Big(d_\nu - \sum_\mu m^T_{\nu\mu}\beta'_\mu\Big). \tag{5.95}$$

If $\mathbf{A}$ is diagonalized using eigenvalue decomposition (to be discussed in Section 5.5), its pivot elements are orthogonal monitor-μ's RMS σ^2_μ. On this orthogonal basis, difference in slope between Lagrange multiplier and regression for a given monitor-μ unfolded from Equation (5.92) is

$$\begin{aligned}\beta_\mu - \beta'_\mu &= \sum_\nu \frac{\lambda_\nu}{2}\cdot\frac{m_{\mu\nu}}{\sigma^2_\mu} &(5.96)\\ &= \sum_\nu\sum_\gamma (C^{-1})_{\nu\gamma}\Big(d_\gamma - \sum_\tau m^T_{\gamma\tau}\beta'_\tau\Big)\frac{m_{\mu\nu}}{\sigma^2_\mu}. &(5.97)\end{aligned}$$

Those terms summing over indices ν and γ, e.g. regression's residual sensitivities, are common for all monitors thus defining the overall common strength in modifying regression slopes. Terms associated with index μ, i.e. the monitor-μ 's sensitivity to coil-ν $m_{\mu\nu}$ and the eigenvalue of monitor σ^2_μ, represents the local effect in each individual monitor. Since the eigenvalue σ^2_μ is in the denominator, modification in the lower ranked eigenvector is generally enhanced because of the lower cost in χ^2 to satisfy the beam modulation constraints.

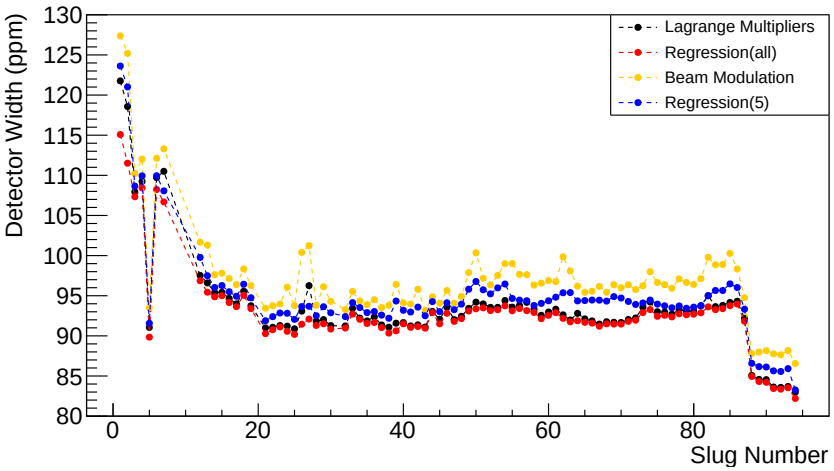

Figure 5.5: Slugs history of the RMS width of corrected asymmetries with different approaches. Only the two-arm runs are included.

The RMS values of the beam corrected asymmetries using different methods are compared in Figure 5.5. Both regression with 5 BPMs and beam modulation show a relatively larger RMS value, which is a clear sign of lacking precision. The accuracy of Lagrange multipliers and regression with all the available BPMs will be examined in the next section by evaluating the beam modulation residual sensitivity.

5.4.4 Verifying Lagrange Multiplier and Regression Using Dithering Residual Sensitivity

In this part, the dithering residual sensitivities from both linear regression and Lagrange Multipliers using all available BPM channels are compared to reveal the precision for both methods.

The residual sensitivity for a given detector with γ-th coil modulation r_γ is defined as:

$$r_\gamma = \frac{\partial \hat{D}}{\partial C_\gamma} - \sum_\mu \beta_\mu \cdot \frac{\partial M_\mu}{\partial C_\gamma}, \tag{5.98}$$

where β_μ is the slope solved from Equation (5.85) and $\frac{\partial \hat{D}}{\partial C_\gamma}$ and $\frac{\partial M_\mu}{\partial C_\gamma}$ are dithering sensitivities defined in Equation (5.45) and Equation (5.46). Only five coils are used for Lagrange multiplier analysis at once and the choice of coils is run dependent. Dithering sensitivities are averaged over supercycles within each stable run period, which are also known as the segment averaged dithering sensitivities. The supercycle-wise residual sensitivities r_γ for

both left-arm and right-arm detectors are calculated from the supercycle-wise dithering sensitivities corrected by the minirun-wise Lagrange multiplier slopes $\frac{\partial \hat{D}}{\partial M_\mu}$ constrained by the segment averaged dithering sensitivities.

The supercycle-wise history of the dithering and residual sensitivities for all seven coils can be found in Appendix B. As an example, the supercycle-wise history of the Coil 5 dithering and residual sensitivities spanning the full PREX-2 run is shown in Figure 5.7 for the left-arm detector and in Figure 5.8 for the right-arm detector. Red dots and black dots in the plots on the left represent dithering data treated as the redundant sensitivities and the constraining sensitivities respectively. The histograms in blue curve in the middle shows the distributions of the constraining dithering data on the left projected to their y-axis. The histograms in red curve on the right are for the redundant data showing their distributions with the same projecting direction.

The grand averaged measured sensitivities for each detector and coil are summarized in the first column in Table 5.2 and Table 5.3. For example, data for coil 5 in this column were extracted from the values named "Mean" in the text box of the top middle plot of Figure 5.7 and Figure 5.8. The same extraction was done for other coils and detectors from similar supercycle-wise history plots.

The grand averaged residual sensitivities mean and root-mean-square (RMS) of the dedicated coils for Lagrange multiplier constraints are listed in the second and third column in Table 5.2. Data for Coil 5 in these two columns can also be obtained from values named "Mean" and "Std. Dev." in the text box of the middle plot in the second row of Figure 5.7 and Figure 5.8. A similar procedure can be done for other coils to reproduce these columns in Table 5.2. The deviation of the central value from zero is consistent with the numerical tolerance and is a negligible contribution to the systematic error. The RMS fluctuation of residuals is determined by both the statistical precision and the stability of the accelerator beam tune. For the energy vernier which is the largest sensitivity in the averaged asymmetry (in the row "us avg vs coil 7" of Table 5.2), the nominal sensitivity is 43.89 ppm/count and the RMS of residual is 0.82 ppm/count. The ratio between the residual RMS over the nominal sensitivity indicates a precision better than 3 %.

Residual sensitivities from redundant beam modulation measurements, which were not directly applied as Lagrange Multiplier constraints, provide cross validation for the accuracy of Lagrange Multiplier. The run averages of these redundant coils are listed in the last two columns of Table 5.2 and Table 5.3. Data in these two columns can be obtained from the text box in the last rows on the right panel of similar plots as Figure 5.7 and Figure 5.8.

A example of slug averaged measured sensitivity and residual sensitivity are shown in Figure 5.6. Coil 5 was excluded from Lagrange multiplier analysis in the first 60 slugs, where

both the central value and RMS of its residual sensitivities remain at a similar level with those of the rest of the run period. Note that in Figure 5.6, the "error bars" of data points at slug level in the residual sensitivity strip charts are the RMS of the residual sensitivity in the slug to illustrate the cyclewise fluctuation within the slug. The "error bars" should not be interpreted as the slug averaged uncertainties in this type of plot.

A similar comparison was also performed for regression with the same BPM set. The residual sensitivities evaluated with regression slopes are slightly worse than those from the Lagrange multiplier as expected. Both independent and correlated instrumental noises in the BPMs contribute to the fluctuation of regression's residual sensitivities. For a side-by-side comparison between regression and Lagrange multiplier, the residual sensitivities in redundant coils for regression are also calculated separately in columns titled with "Redundant Residual Sensitivity" in Table 5.3. Though the regression's residual sensitivity is not optimized by definition, the results in Table 5.3 are in a similar level with those from the Lagrange multiplier, therefore suggest regression as a reliable reference for estimating the systematic noise of the Lagrange multiplier method.

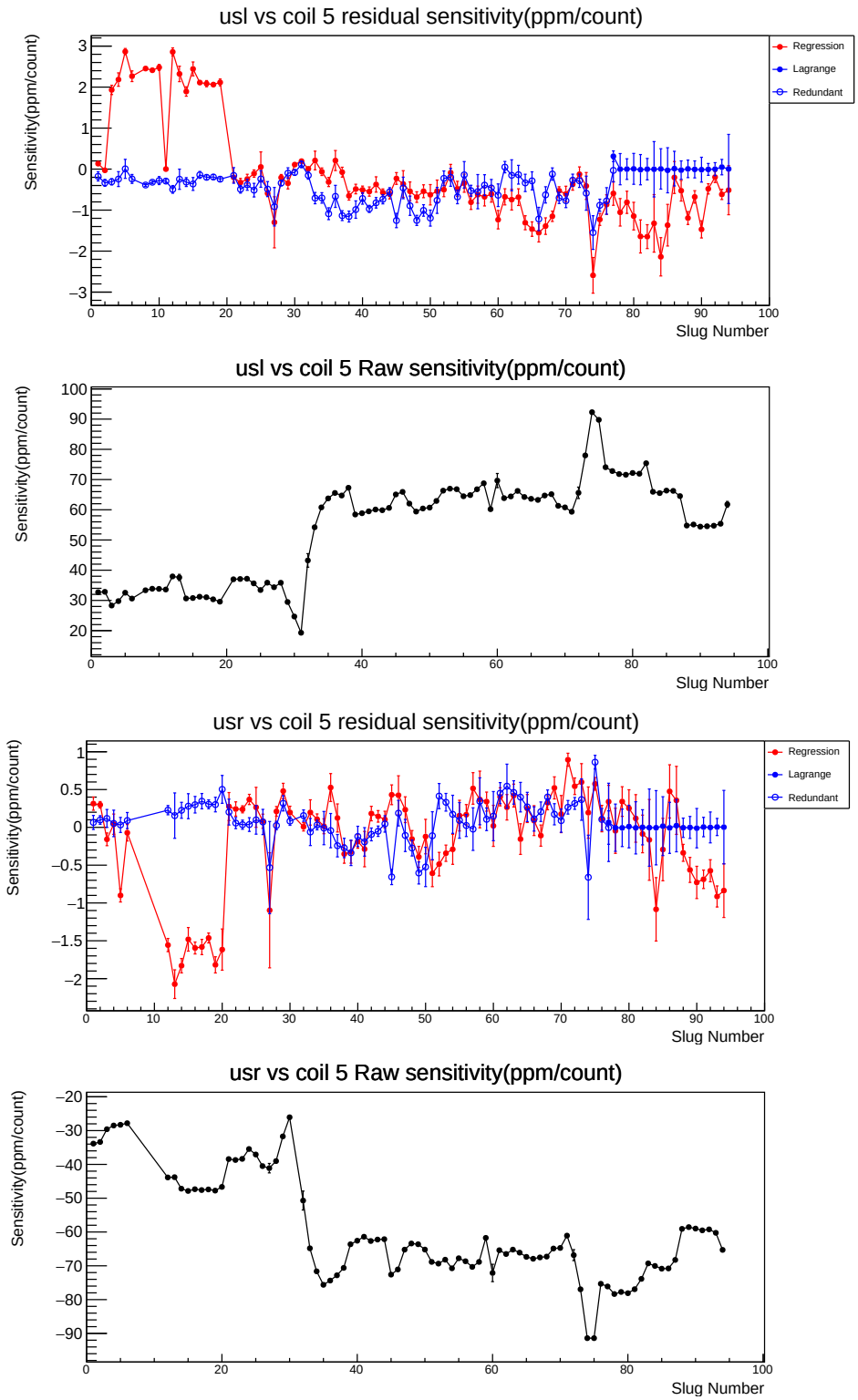

Figure 5.6: Slug summary of coil 5 residual sensitivity for the left and right main detectors. The "error bars" of data points at slug level in the residual sensitivity strip charts are the RMS of the residual sensitivity in the slug to illustrate the cyclewise fluctuation within the slug. The "error bars" should not be interpreted as the slug averaged uncertainties directly in this plot.

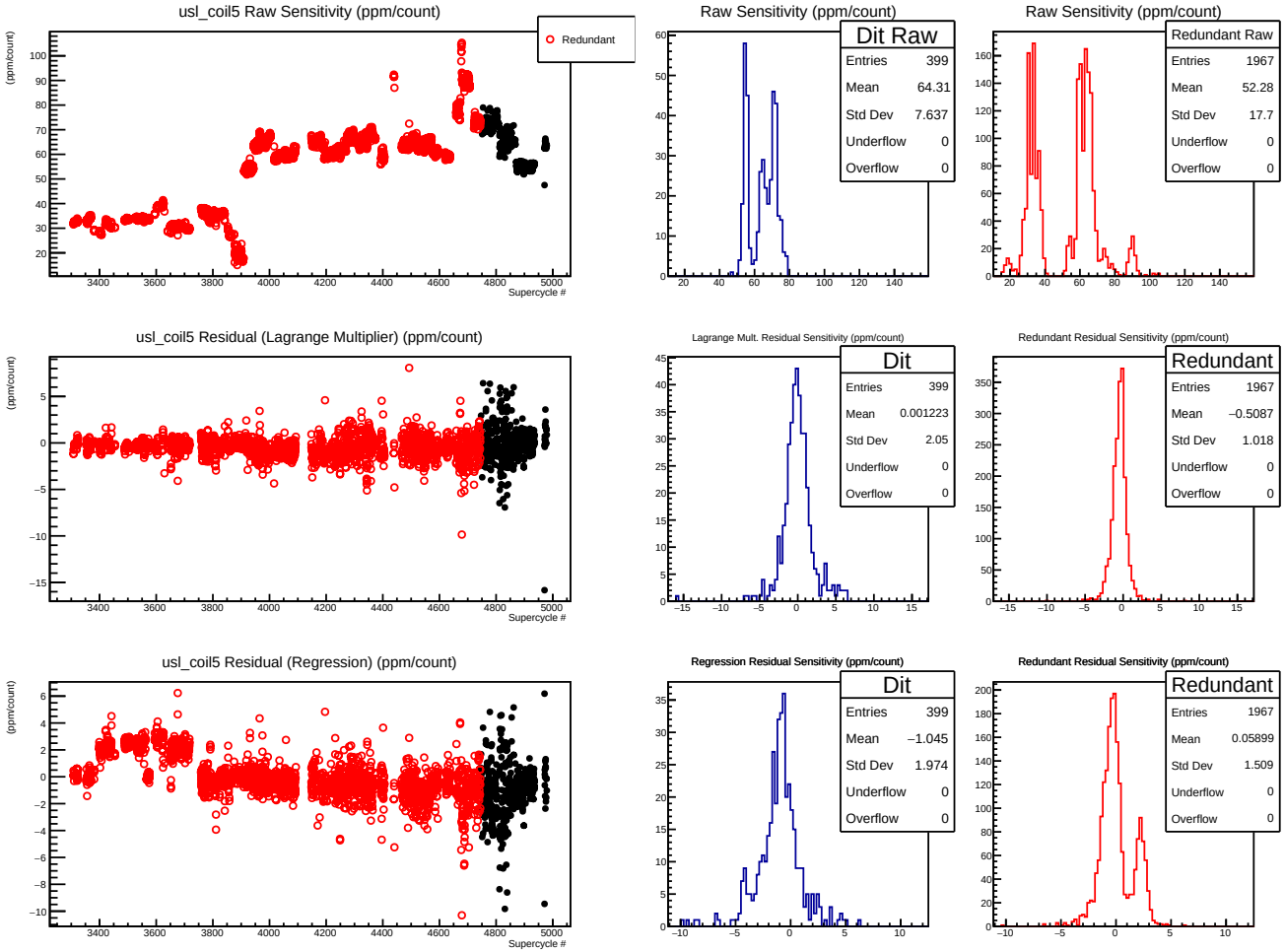

Figure 5.7: Cyclewise history for full PREX-2 run. From top to bottom: 1) Measured the left-arm detector's dithering sensitivity to coil 5. 2) The left-arm detector's residual sensitivity to coil 5 corrected by Lagrange Multiplier method. 3) The left-arm detector's residual sensitivity to coil 5 corrected by regression with all BPMs. See in the text for a full description of the plots.

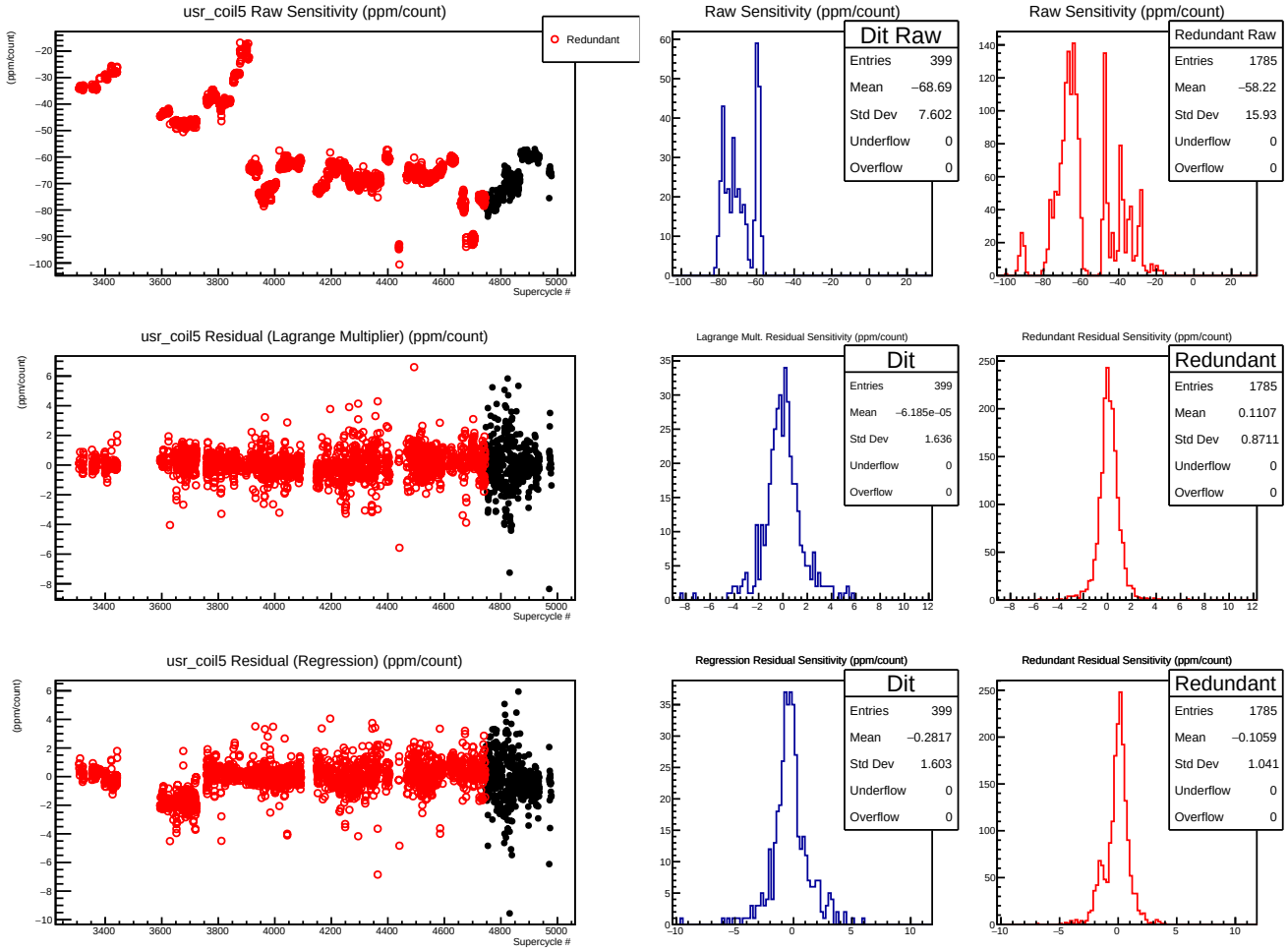

Figure 5.8: Cyclewise history for full PREX-2 run. From top to bottom: 1) Measured the right-arm detector's dithering sensitivity to coil 5. 2) The right-arm detector's residual sensitivity to coil 5 corrected by Lagrange Multiplier method. 3) The right-arm detector's residual sensitivity to coil 5 corrected by regression with all BPMs. See in the text for a full description of the plots.

	Measured Sensitivity Mean	Residual Sensitivity Mean	Residual Sensitivity RMS	Redundant Residual Sensitivity Mean	Redundant Residual Sensitivity RMS
usl vs coil 1	-44.48	7.7e-3	0.85	-3.2e-1	1.58
usl vs coil 2	-7.36	-1.2e-1	0.09	5.3e-2	0.28
usl vs coil 3	-13.96	2.0e-3	0.32	-	-
usl vs coil 4	-6.97	-1.8e-3	0.21	-	-
usl vs coil 5	64.31	1.2e-3	2.05	-5.1e-1	1.02
usl vs coil 6	8.34	-1.1e-2	0.36	1.6e-1	0.33
usl vs coil 7	53.48	7.9e-5	0.82	-	-
usr vs coil 1	49.41	-4.2e-3	0.71	2.0e-1	1.33
usr vs coil 2	-9.18	-3.6e-2	0.09	-2.7e-3	0.26
usr vs coil 3	15.13	-6.6e-5	0.26	-	-
usr vs coil 4	-5.75	-9.8e-4	0.21	-	-
usr vs coil 5	-68.69	-6.2e-5	1.64	1.1e-1	0.87
usr vs coil 6	8.48	3.1e-3	0.30	-1.4e-2	0.18
usr vs coil 7	32.87	2.9e-3	0.64	-	-
us avg vs coil 1	2.03	-7.2e-4	0.71	-6.3e-2	1.39
us avg vs coil 2	-8.27	-7.9e-2	0.08	2.8e-2	0.24
us avg vs coil 3	0.43	4.6e-4	0.27	-	-
us avg vs coil 4	-6.48	-1.5e-3	0.19	-	-
us avg vs coil 5	-2.19	5.8e-4	1.77	-2.0e-1	0.85
us avg vs coil 6	8.55	-5.0e-3	0.28	7.5e-2	0.22
us avg vs coil 7	43.89	1.6e-3	0.68	-	-
us dd vs coil 1	-47.50	3.6e-3	0.34	-2.6e-1	0.45
us dd vs coil 2	0.91	-4.4e-2	0.04	3.0e-2	0.14
us dd vs coil 3	-14.73	5.3e-4	0.13	-	-
us dd vs coil 4	-0.71	-5.4e-4	0.10	-	-
us dd vs coil 5	66.50	6.4e-4	0.57	-3.1e-1	0.43
us dd vs coil 6	0.03	-8.1e-3	0.18	9.0e-2	0.15
us dd vs coil 7	10.88	-1.3e-3	0.27	-	-

Table 5.2: Dithering residual sensitivities of Lagrange multipliers. unit: ppm/counts

	Measured Sensitivity Mean	Residual Sensitivity Mean	Residual Sensitivity RMS	Redundant Residual Sensitivity Mean	Redundant Residual Sensitivity RMS
usl vs coil 1	-44.48	-4.2e-1	1.28	7.4e-1	1.48
usl vs coil 2	-7.36	-3.9	0.82	-1.2	2.46
usl vs coil 3	-13.96	-4.6e-3	0.51	-	-
usl vs coil 4	-6.97	-9.7e-1	1.61	-	-
usl vs coil 5	64.31	-1.0	1.97	5.9e-2	1.51
usl vs coil 6	8.34	1.4	2.67	2.5	0.62
usl vs coil 7	53.48	3.0e-1	0.95	-	-
usr vs coil 1	49.41	2.1e-1	0.91	6.6e-1	1.16
usr vs coil 2	-9.18	-5.1	0.53	-1.7	2.42
usr vs coil 3	15.13	2.1e-3	0.45	-	-
usr vs coil 4	-5.75	-1.2	1.70	-	-
usr vs coil 5	-68.69	-2.8e-1	1.60	-1.1e-1	1.04
usr vs coil 6	8.48	1.9	2.64	3.1	0.43
usr vs coil 7	32.87	3.7e-1	0.77	-	-
us avg vs coil 1	2.03	-6.4e-2	0.76	7.0e-1	1.25
us avg vs coil 2	-8.27	-4.5	0.49	-1.5	2.37
us avg vs coil 3	0.43	1.5e-2	0.40	-	-
us avg vs coil 4	-6.48	-1.1	1.61	-	-
us avg vs coil 5	-2.19	-6.6e-1	1.71	-7.5e-2	0.81
us avg vs coil 6	8.55	1.7	2.58	2.8	0.49
us avg vs coil 7	43.89	3.2e-1	0.77	-	-
us dd vs coil 1	-47.50	-2.5e-1	0.75	3.8e-2	0.45
us dd vs coil 2	0.91	5.9e-1	0.49	2.4e-1	0.75
us dd vs coil 3	-14.73	1.6e-2	0.26	-	-
us dd vs coil 4	-0.71	7.4e-2	0.51	-	-
us dd vs coil 5	66.50	-3.8e-1	0.57	1.6e-2	0.91
us dd vs coil 6	0.03	-2.4e-1	0.83	-3.0e-1	0.21
us dd vs coil 7	10.88	-4.2e-2	0.39	-	-

Table 5.3: Dithering residual sensitivities of Regression. unit: ppm/counts

5.5 Eigenvector Analysis

As discussed in Section 5.2.4, direct comparison between regression with other beam correction techniques, e.g. beam modulation, can be overwhelmed by the effects of parameter correlation which over-estimates the errors. To get rid of the parameter correlation effect, it is convenient to diagonalize the BPMs covariance matrix by eigenvalue decomposition and compare regression with other techniques side-by-side on the basis of eigenvectors.

5.5.1 Basic Technique

Covariance between ΔM_μ and ΔM_ν in n helicity patterns is

$$\mathrm{cov}(\Delta M_\mu, \Delta M_\nu) = \sum_i^n \Delta M_\mu^{(i)} \Delta M_\nu^{(i)} = \vec{X}_\mu^T \cdot \vec{X}_\nu. \tag{5.99}$$

where ΔM_μ is the helicity-correlated BPM differences and $\vec{X}$ is the events vector

$$\vec{X}_\mu^T = \begin{pmatrix} \dots & \Delta M_\mu^{(i)} & \dots \end{pmatrix}_{1\times n}, \tag{5.100}$$

μ is the index of BPM and i is the event index.

The covariance matrix is a $M \times M$ symmetric matrix $\mathbf{S}$

$$\mathbf{S} = \begin{pmatrix} \ddots & & \\ & \mathrm{cov}(\Delta M_\mu, \Delta M_\nu) & \\ & & \ddots \end{pmatrix}_{m\times m} = \mathbf{X^T X} \tag{5.101}$$

where

$$\mathbf{X} = \begin{pmatrix} \vec{X}_1 & \dots & \vec{X}_m \end{pmatrix}_{n\times m}, \tag{5.102}$$

where m is the number of BPMs and n is the total number of events.

The orthogonal matrix $\mathbf{Q}$ obtained from the eigenvalue decomposition diagonalizes the covariance matrix $\mathbf{S}$ and constructs the orthogonal monitors:

$$\mathbf{Q^T S Q} = \mathbf{\Lambda} = \begin{pmatrix} \lambda_1 & 0 & \dots & 0 \\ 0 & \lambda_2 & \dots & 0 \\ \vdots & \vdots & \ddots & \vdots \\ 0 & 0 & \dots & \lambda_m \end{pmatrix}, \tag{5.103}$$

where $\sqrt{\lambda_\mu}$ is also the RMS of jitter in the orthogonal monitor M'_μ.

In general, the identity of an eigenvector is based on the ranking sorted by eigenvalues in descending order. Since the eigenvalue of a given eigenvector could change with the

accelerator beam optics and result in frequent changes in rank ordering and mixing identities in the same rank. In practice, the eigenvector set was calculated for each 5-minute data set and was identified with the best matching of the BPMs components from run to run. And the ranking of the identified eigenvectors was based on their grand averaged eigenvalues, equivalently the RMS jitter.

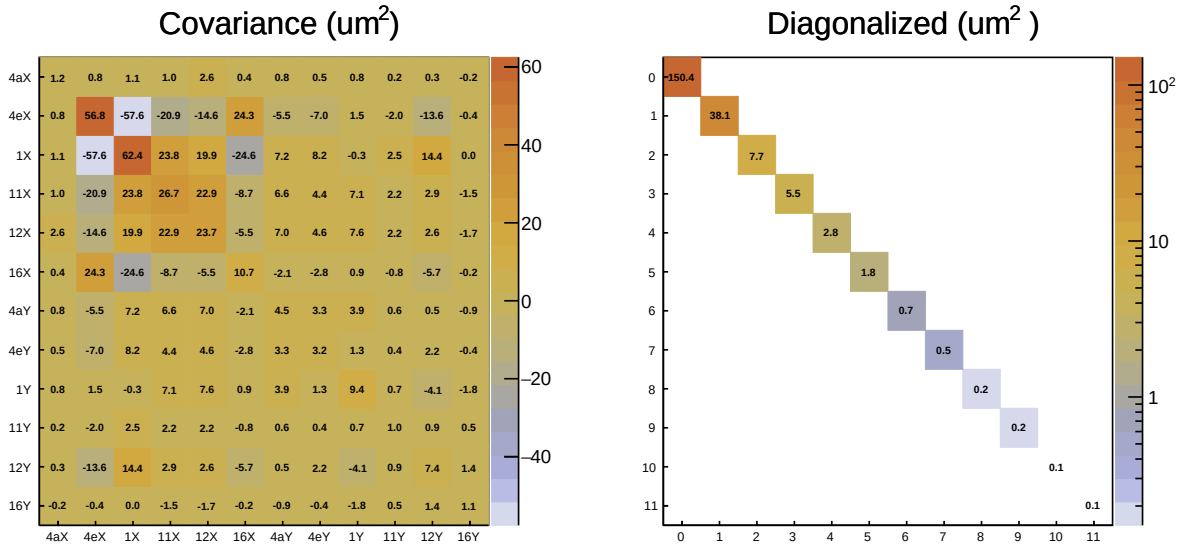

Figure 5.9: Example of matrix diagonalization with 12 BPMs channels using eigenvector decomposition. Values of covariance are indicated by the hue of color.

The matrix $\mathbf{Q}$ can be viewed as a collection of column vectors $\vec{Q}_\mu$

$$\mathbf{Q} = \left(\vec{Q}_1 \quad \dots \quad \vec{Q_m}\right)_{m\times m}, \quad \vec{Q}_\mu = \begin{pmatrix} \vdots \\ Q_{\nu\mu} \\ \vdots \end{pmatrix}_{m\times 1}, \tag{5.104}$$

which are essentially the eigenvectors of the covariance matrix $\mathbf{S}$

$$\mathbf{S}\vec{Q}_\mu = \lambda_\mu \vec{Q}_\mu. \tag{5.105}$$

The matrix $\mathbf{Q}$ projects the BPM's ΔM_μ to the orthogonal $\Delta M'_\mu$

$$\vec{X}'_\mu = \mathbf{X}\vec{Q}_\mu, \tag{5.106}$$

and ensures the correlation between orthogonal monitors are all zeros:

$$\mathrm{cov}(\Delta M'_\mu, \Delta M'_\nu) = \vec{X}'^{\,T}_\mu \cdot \vec{X}'_\nu = (\vec{Q}^T_\mu \mathbf{X}^T)(\mathbf{X}\vec{Q}_\nu) = \vec{Q}^T_\mu \mathbf{S}\vec{Q}_\nu = \lambda_\mu \delta_{\mu\nu}, \tag{5.107}$$

where $\delta_{\mu\nu}$ is the Kronecker delta.

Projection of correction slopes in the eigenvector basis β'_ν can be also derived from the derivative chain rule

$$\beta_\mu = \frac{\partial A}{\partial \Delta M_\mu} = \sum_\nu \frac{\partial A}{\partial \Delta M'_\nu}\frac{\partial \Delta M'_\nu}{\partial \Delta M_\mu} = \sum_\nu \beta'_\nu \frac{\partial \Delta M'_\nu}{\partial \Delta M_\mu} = \sum_\nu \beta'_\nu Q_{\nu\mu}, \tag{5.108}$$

so that

$$\beta'_\nu = \sum_\mu (Q^{-1})_{\nu\mu}\beta_\mu = \sum_\mu Q^T_{\nu\mu}\beta_\mu. \tag{5.109}$$

The last step in Equation (5.109) is valid only if $\mathbf{Q}$ is a normalized orthogonal matrix which is defined as:

$$\mathbf{Q^T Q} = \mathbf{I} \rightarrow \mathbf{Q}^{-1} = \mathbf{Q^T}. \tag{5.110}$$

5.5.2 Run History of Eigenvectors

The eigenvector construction is summarized in Table 5.4 of which each row is filled with grand averaged ortho-normal weighting factors from the 12 BPM x-y coordinates along the Hall A beamline.

An eigenvector can be interpreted by the geometrical relation and the BPM locations in the Hall A beamline. The relative locations of BPMs can be found in Figure 3.2. The top eigenvector, i.e. Eigenvector-0, has RMS jitter of 15 μm in the helicity-correlated differences and is basically the subtraction between BPM 4eX and BPM 1X indicating the beam angle fluctuations. Meanwhile BPM 4aY , BPM 4eY and BPM 1Y attribute to Eigenvector-1 with approximately equal weights and depict the vertical beam motion. BPM 12X and 11X at the high dispersion region together make the largest contribution to Eigenvector-2, which is believed to be sensitive to the beam energy fluctuation. Figure 5.10 shows the history of Eigenvector-2. Contributions from each BPM are consistent at 0.1 level over the entire run history. Jitters in y coordinates reflect the BPMs electronic noise mode. For all of the eigenvectors computed from 12 BPMs, the mini-run history of their components can be found in Appendix C.

Beam fluctuations in the eigenvector ranked from 5 to 11 are close to the BPM instrumental resolution (0.3 μm-0.5 μm) and the grand averaged central values are mostly consistent within their convergence radius. Therefore these low-ranked eigenvectors are more likely to be subjected to modes of the electronic noises. Meanwhile the top five eigenvectors are sensitive to the fluctuations in the full phase space.

Rank	4aX	4eX	1X	11X	12X	16X	4aY	4eY	1Y	11Y	12Y	16Y
0	0.1	0.7	-0.6	-0.2	-0.1	0.3	-0.1	-0.1	0.0	0.0	-0.1	0.0
1	0.1	0.2	0.0	-0.2	0.1	0.1	0.6	0.5	0.4	0.2	0.3	-0.1
2	-0.1	-0.2	0.1	-0.7	-0.7	-0.1	0.0	0.0	-0.1	0.0	0.1	0.0
3	0.0	-0.1	0.1	-0.1	-0.1	0.0	0.1	0.0	0.5	-0.2	-0.8	-0.2
4	-0.4	-0.2	-0.5	0.5	-0.5	-0.2	0.1	0.1	0.0	0.1	0.1	0.1
5	0.0	0.0	0.0	0.0	0.0	0.0	0.2	0.3	-0.5	-0.6	-0.1	-0.5
6	-0.3	-0.5	-0.4	-0.4	0.5	0.3	0.1	-0.2	0.0	0.0	0.1	0.0
7	0.1	0.0	0.0	0.0	-0.1	-0.1	-0.1	-0.4	0.3	-0.1	0.5	-0.7
8	-0.1	0.0	0.0	-0.1	0.1	0.0	-0.7	0.5	0.4	-0.3	0.2	0.1
9	-0.6	0.2	0.2	0.0	0.0	0.1	-0.2	0.2	-0.1	0.5	-0.1	-0.4
10	0.5	-0.3	-0.3	0.0	0.1	-0.2	-0.2	0.3	-0.1	0.5	-0.2	-0.3
11	0.2	-0.2	0.1	0.2	-0.3	0.9	-0.1	0.1	0.0	0.1	0.0	-0.1

Table 5.4: Components of eigenvectors with round-off to the first decimal point. The ranking was sorted by eigenvalues in descending order.

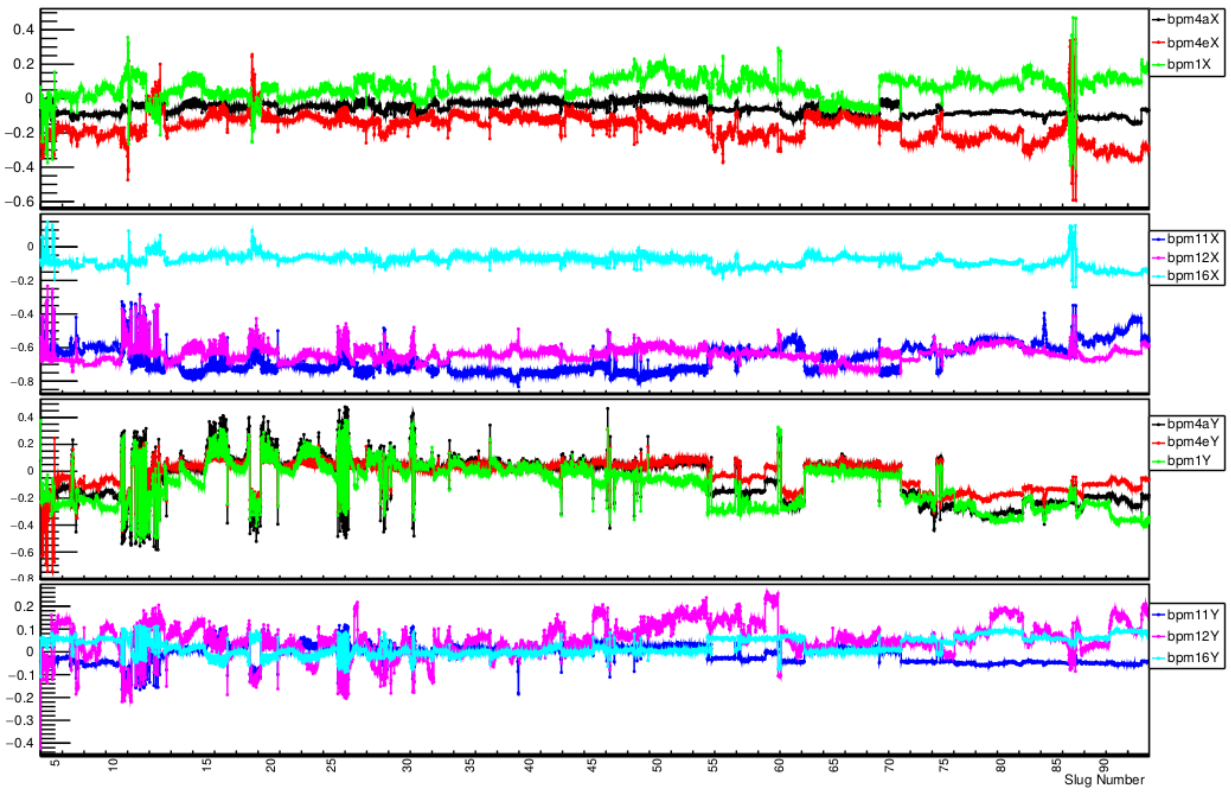

Figure 5.10: History of BPM contributions in Eigenvalues 2.

Rank	Mean (nm)	Std. Err. (nm)	RMS (um)	Nominal Slope (ppm/um)	Slope Diff. Mean (ppm/um)	Slope Diff. RMS (ppm/um)
0	-3.96	2.12	14.9	-2.70	0.08	0.40
1	2.31	1.38	9.60	9.50	-0.24	0.56
2	-1.83	1.01	7.05	36.29	-0.14	0.66
3	-1.61	0.46	3.33	3.95	-0.13	0.70
4	-1.01	0.38	2.66	-13.55	-0.45	1.19
5	0.16	0.2	1.39	-1.86	0.11	0.79
6	0.15	0.12	0.99	5.36	-0.20	1.82
7	0.02	0.11	0.76	10.91	-1.06	1.87
8	-0.08	0.07	0.48	-2.84	1.55	4.30
9	-0.02	0.06	0.38	4.67	-0.41	3.48
10	-0.04	0.05	0.36	4.96	-1.96	5.39
11	-0.01	0.04	0.31	-6.18	0.63	3.65

Table 5.5: Weighted grand averages of eigenvector helicity correlated differences. Weighting factor is based on beam corrected statistical error. The ranking was sorted by eigenvalues in descending order. The last two columns are grand averages of differences between regression and Lagrange multiplier slopes in eigenvector basis.

5.5.3 Regression vs Lagrange Multipliers

The main goal of eigenvector analysis is to isolate the effects of parameter correlation and cross validate beam corrections with different methods. The quantity to compare in this part is the slope, that is the sensitivity of detected asymmetry to the fluctuations in a given eigenvector. Fluctuation of the slope largely depends on the beam transport optics therefore is not relevant to the precision of a certain slope calibration technique. The run history of the slopes of the averaged detected asymmetry to Eigenvector 2 using regression and Lagrange multiplier are shown in the top panel of Figure 5.11. In the top panel of Figure 5.11, the mean value displayed in the box is the grand average of the nominal Lagrange multipliers correction slope. In the bottom panel, the mean and the "Std Dev" in the box are the grand average central value and RMS width of the difference in slope between Lagrange multipliers and regression. The same statistics summary for all eigenvectors are summarized in Table 5.5. All eigenvectors are computed from the same 12 BPM channels. The history of slopes for all eigenvectors can be found in Appendix D

Though regression potentially is susceptible to BPM's electronic noise, the beam modulation residuals analysis on the regression suggests that the regression with all 12 BPMs has little instrumental effect and is consistent with the beam modulation data to a certain degree. Therefore comparing Lagrange multiplier with regression by differentiation is a useful cross check of beam corrections. The run history and distribution of the differences of slope for Eigenvector 2 between regression and Lagrange multiplier are shown in the bottom panel of Figure 5.11, which is the largest slope in the averaged asymmetry of all eigenvectors. The standard deviation of the slope differences is 0.66 ppm/um, about 2 % of its nominal slope 38 ppm/um. The central offset is -0.14 ppm/um which is negligible relative to the random noise in the determination of this slope.

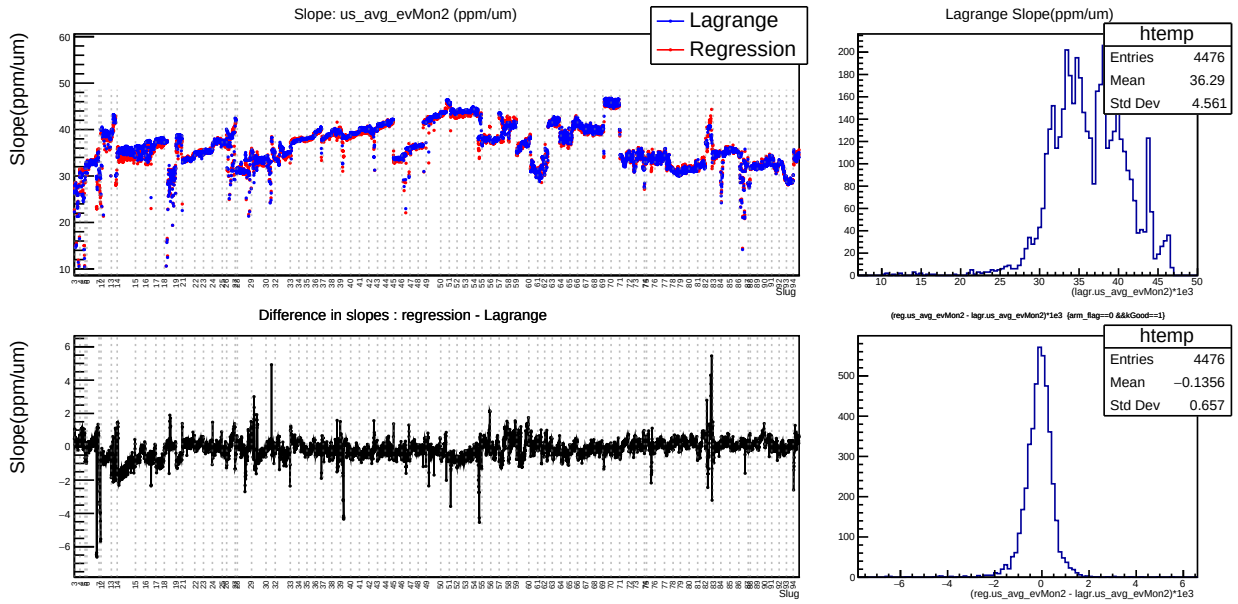

Figure 5.11: Slope History of Eigenvector 2. Top: History of regression and Lagrange multiplier slopes. Bottom: Difference of regression and Lagrange multiplier slopes.

Table 5.5 summarizes the differences in slopes between the regression and Lagrange multiplier method. The slope differences in the top five eigenvectors have standard deviation at a level of 0.6 ppm/um and negligible central values. Although the lower ranked eigenvectors have larger and noisier slope differences, the grand averaged helicity-correlated differences of these eigenvectors are tiny therefore its contribution to the systematic noise of beam correction is small. A detailed evaluation of beam correction uncertainty is discussed in the next section.

It is also worth pointing out that Eigenvector-2 contributes the largest slope and its 7 μm random fluctuation is apparent over the instrumental resolution ($\approx$ 0.4 μm) therefore

the calibration of this slope is known to be relatively precise. Also notice that all the lower ranked eigenvectors, i.e. Eigenvector-5 to Eigenvector-11, have negligible helicity-correlated central values in their grand averages and contribute with small correction slopes ($|\beta| \leq 10$ ppm/μm) thus have a tiny contribution in the systematic uncertainty. These two facts make it possible to assign a small systematic uncertainty for the beam correction in PREX-2. For other experiments with different beam conditions and optics, e.g. the energy-sensitive dimension has a large slope and a large helicity-correlated central value meanwhile its random fluctuation is suppressed and close to the monitor resolution level, the evaluation of the systematic uncertainty for beam correction may require further examinations.

5.6 Systematic Uncertainty

The PREX-2 beam correction result is the sum of beam position helicity-correlated differences multiplied by the slopes calculated from Lagrange multiplier method in eigenvector basis

$$A_{\text{corr}} = \sum_i w_i \Big[A^{(i)}_{\text{meas}} - \sum_\mu \beta^{(i)}_\mu \Delta M^{(i)}_\mu \Big], \tag{5.111}$$

where i is the index of data set and the weighting factor w_i is based on the statistical error of asymmetry measurements σ_i:

$$w_i = \frac{1}{\sigma_i^2} \Big/ \Big(\sum_k^N \frac{1}{\sigma_k^2} \Big). \tag{5.112}$$

The systematic uncertainty of grand averaged beam asymmetry correction is

$$\delta(A_{\text{beam}}) = \sum_i w_i \Big[\bigoplus_{\mu=1}^{12} \delta\beta_\mu \Delta M^{(i)}_\mu \Big], \tag{5.113}$$

where $\delta\beta_\mu$ is the precision of the slope calibration technique and is assumed to be universal and run independent. Discussed in Section 5.4 and Section 5.5, the precision of the slope calibration $(\delta\beta_\mu)/\beta_\mu$ is known better than 3 %. This conclusion is supported by the ratio of the RMS values of residual sensitivity over the nominal sensitivity in Table 5.2 and the ratio of the RMS values of the slopes difference between regression and Lagrange multiplier over the nominal Lagrange multipliers slope in Table 5.5.

Table 5.6 summarizes the corrections made by each eigenvector. The first two columns "Mean" and "Std. Err." are the grand averaged mean and standard error weighted by the statistical uncertainty in the Lagrange multiplier technique. The grand weighted standard

error $\langle\sigma_k\rangle$ for Eigenvector-k is calculated as follow:

$$\langle\sigma_k\rangle = \sqrt{\sum_i \frac{\sigma_k^2(i)}{\sigma_{\text{stat}}^4(i)}} \Big/ \Big(\sum_i \frac{1}{\sigma_{\text{stat}}^2(i)}\Big), \tag{5.114}$$

where $\sigma_{\text{stat}}(i)$ and $\sigma_k(i)$ is the statistical uncertainty in the Lagrange multiplier technique and the standard error in the correction attributed to Eigenvector-k for the i-th minirun. $\sigma_k(i)$ is calculated from fluctuations in each correction normalized by the number of patterns in each minirun, that is:

$$\sigma_k(i) = \frac{\text{RMS}_k(i)}{\sqrt{N_i}}, \tag{5.115}$$

where N_i is the number of patterns in the i-th minirun.

Rank	Mean (ppb)	Std. Err. (ppb)	RMS (ppm)
0	-22.334	16.46	191.61
1	22.500	10.5	88.89
2	-70.444	36.45	257.49
3	-2.842	4.46	36.02
4	9.697	5.7	40.81
5	1.267	0.95	7.16
6	-0.013	1.33	12.75
7	1.055	1.46	11.06
8	0.259	0.61	5.09
9	0.242	0.42	3.09
10	0.176	0.54	5.2
11	0.061	0.39	3.65
Total	-60.375		

Table 5.6: Weighted Averages of asymmetry correction from each eigenvector. The ranking was sorted by eigenvalues in descending order.

Assuming 3 % precision is universal for all eigenvector slopes calculation, the beam correction uncertainty can be calculated from the grand weighted averaged corrections from each eigenvector independently (the first column in Table 5.6),

$$\delta(A_{\text{beam}}) = \sqrt{\sum_\mu \langle\beta_\mu \Delta M_\mu\rangle^2 \cdot (0.03)^2} = 2.3 \text{ ppb}. \tag{5.116}$$

Taking significant figures of the final asymmetry result into account, the systematic uncertainty of beam correction was determined to be 2.5 ppb:

$$\boxed{A_{\text{beam}} = -60.4 \pm 2.5 \text{ ppb.}} \tag{5.117}$$

The following discussion is to justify the systematic uncertainty assigned to beam correction. To validate the systematic uncertainty, the difference in the corrected asymmetry between any two correction techniques are calculated and weighted by the fluctuation of the difference to obtain its grand average. Concretely, the corrected asymmetry difference between Method-I and Method-II in i-th minirun is:

$$\Delta A_i = A_i^I - A_i^{II}, \tag{5.118}$$

and the slug average $\langle \Delta A \rangle$ is calculated as the average over miniruns in this slug:

$$\langle \Delta A \rangle = \frac{1}{N} \sum_i^N \Delta A_i, \tag{5.119}$$

of which the standard error of $\langle \Delta A \rangle$ is characterized by the fluctuation of the differences

$$\sigma(\langle \Delta A \rangle) = \frac{\sqrt{\sum_i^N (A_i^I - A_i^{II})^2}}{N}. \tag{5.120}$$

Note that because of the weighting scheme, the value $\langle \Delta A \rangle$ is different from direct subtraction between grand averages by different techniques, i.e $\langle A^I \rangle - \langle A^{II} \rangle$.

	$\langle \Delta A \rangle$ (ppb)	σ(ΔA)(ppb)	χ^2/ndf	Prob.
dit vs reg_5bpm	-4.39	2.68	128.8/95	0.01
dit vs lagr_all	2.17	3.51	86.4/95	0.72
dit vs reg_all	-0.47	3.83	88.9/95	0.66
reg_5bpm vs reg_all	5.76	2.61	106.1/95	0.21
lagr_all vs reg_all	-1.03	1.21	91.2/95	0.59

Table 5.7: Summary of ΔAs between different beam correction techniques

Grand averages of comparisons among beam correction techniques are summarized in Table 5.7 and Figure 5.12. The grand averages for each comparison are weighted by $\sigma(\langle \Delta A \rangle)$ defined in Equation (5.120). The four techniques included are beam modulation with 5 BPM (dit), regression with 5 BPMs (reg_5bpm), regression with 12 BPMs (reg_all) and Lagrange multiplier with 12 BPMs (lagr_all). The significant difference, in terms of both central value

and standard error, between "dit" and "reg_5bpm" demonstrates the effect of correlated instrumental noise in regression with 5 BPMs. Meanwhile, phase space resolution of beam modulation analysis is limited by the number of available BPMs. The comparison between "dit" with "lagr_all" or "reg_all" confirms this limitation by showing relatively large $\sigma(\Delta A)$ of ≈ 3 ppb with $\langle \Delta A \rangle$ consistent within 1-σ. The difference between "reg_5bpm" and "reg_all" reveals BPM instrumental effects from both independent random noise and electronic cross-talk. The discrepancy between "lagr_all" and "reg_all" is consistent within 1-σ and places a lower bound on the systematic uncertainty of Lagrange multiplier method. In conclusion, the results in Table 5.7 validate the systematic uncertainty assigned to beam correction should be bounded within 2 ppb $\sim$ 3 ppb, which is comparable to the independent conclusion in Equation (5.116).

A relevant quantity to discuss is the event-to-event systematic noise left in the corrected detector asymmetry

$$\sigma_{\text{syst}} = \Big(\bigoplus_{\mu} \delta\beta_{\mu} \sigma_{\Delta M_{\mu}} \Big) \oplus \Big(\bigoplus_{\mu} \beta_{\mu} \delta_{\Delta M_{\mu}} \Big), \tag{5.121}$$

determined by the deviation of the calculated slope from the true value $\delta\beta_{\mu}$, the instrumental resolution of the BPM $\delta_{\Delta M}$ and beam fluctuation observed by it $\sigma_{\Delta M}$.

Instrumental uncorrelated resolution of BPM 0.3 um is quoted from the bottom ranked eigenvector. Based on Table 5.5, residual noise sourced from the BPM resolution can be calculated:

$$\sigma_{\text{BPM}} = \sqrt{\sum_{\mu} \beta_{\mu}^2 \cdot (0.3\ \mu\text{m})^2} = 13 \text{ ppm}, \tag{5.122}$$

where the unit of β_{μ} should be ppm/um.

And assume the calculated slope is apart from its true value by 3 %, the residual beam noise can be estimated from Table 5.5

$$\sigma_{\text{residual}} = \sqrt{\sum_{\mu} \langle \beta_{\mu} \sigma_{\Delta M_{\mu}} \rangle^2 \cdot (0.03)^2} = 10 \text{ ppm}. \tag{5.123}$$

Based on Equation (5.121), the estimated systematic noise σ_{syst} can be calculated by adding Equation 5.122 and Equation 5.123 in quadrature under a square root:

$$\sigma_{\text{syst}} = \sqrt{\sigma_{\text{BPM}}^2 + \sigma_{\text{residual}}^2} = 16 \text{ ppm}. \tag{5.124}$$

The random fluctuation in the PREX-2 corrected asymmetry is known to be 93 ppm and is dominated by counting statistics. The 'dilution' introduced by the estimated systematic noise σ_{syst} can be estimated as

$$\sqrt{\frac{93^2}{93^2 - 16^2}} - 1 = 1.5\ \%, \tag{5.125}$$

which is negligible. It should be pointed out that σ_{syst} is already included in the random fluctuation of the corrected asymmetry and does not represent an additional systematic uncertainty.

As a summary for the discussion in this section, a correction of -60.4 ppb for beam fluctuations is applied to the raw detected asymmetry. Based on the studies in Section 5.4.4 and Section 5.5.3 , the systematic uncertainty of this correction is assigned to be 2.5 ppb:

$$\boxed{A_{\text{beam}} = -60.4 \pm 2.5 \text{ ppb.}}$$

The comparison among different beam correction techniques provides a justification for the assigned systematic uncertainty. Effects of the BPM instrumental resolution and the uncertainties of the correction slopes are evaluated and turn out to be negligible for the corrected asymmetry.

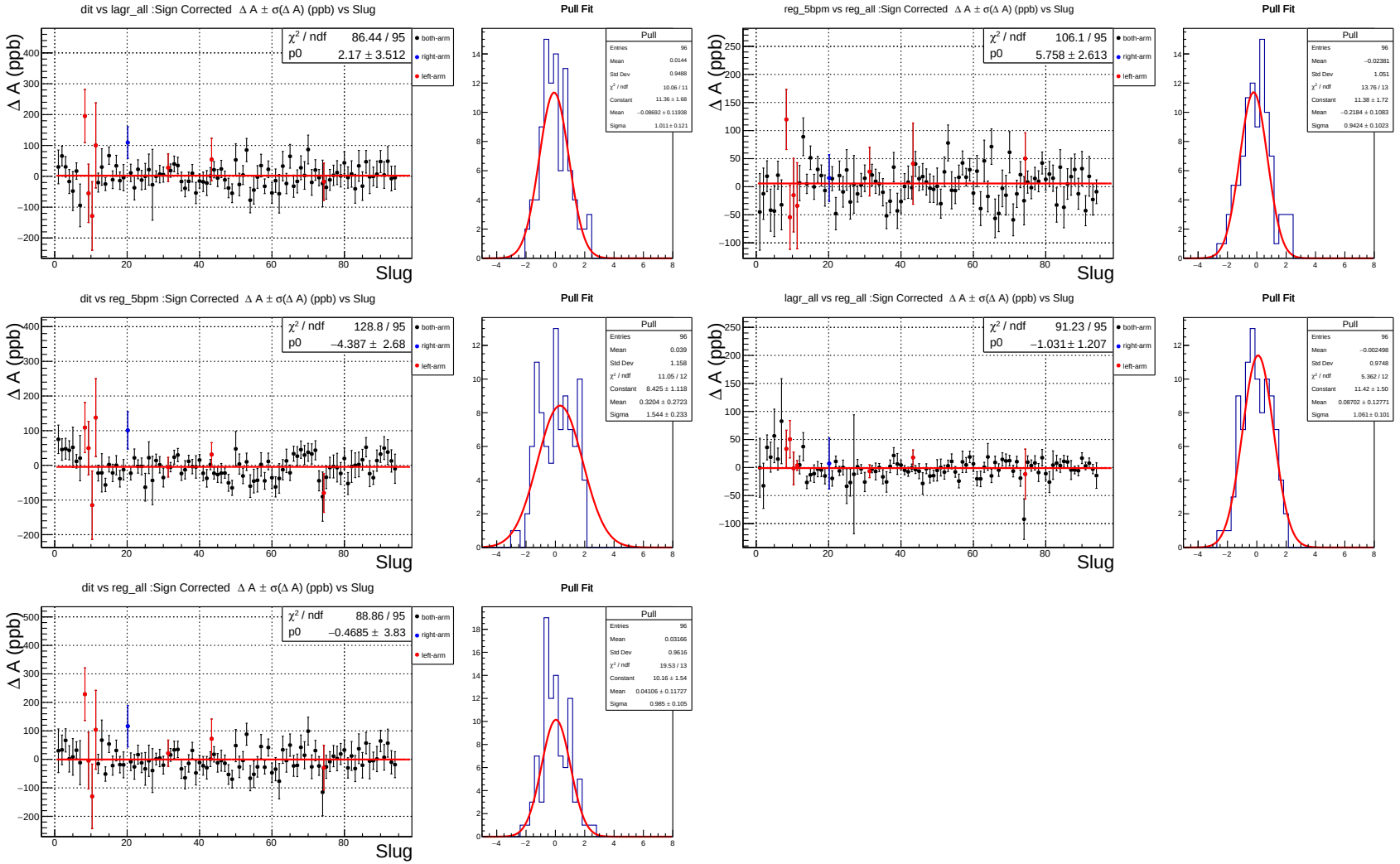

Figure 5.12: Slug averages of ΔAs between different beam correction techniques

Chapter 6

Physics Results

This chapter discusses the physics results and implications from the PREX-2 data. Corrections to the measured asymmetry for the beam polarization, backgrounds, e.g. from the diamond foils and inelastic scattering, the detector non-linearity and others are performed and their systematic uncertainties are summarized in Section 6.1. The weak charge radius and the neutron radius of ^{208}Pb, therefore the weak skin and the neutron skin, are deduced in Section 6.2 from the final parity-violating asymmetry result. The physics impacts and implications of the neutron skin thickness are discussed in Section 6.3.

6.1 Parity-Violating Asymmetry

Correction	Absolute [ppb]	Relative [%]
Beam asymmetry	-60.4 ± 3.0	11.0 ± 0.5
Charge correction	20.7 ± 0.2	3.8 ± 0.0
Beam polarization	56.8 ± 5.2	10.3 ± 1.0
Target diamond foils	0.7 ± 1.4	0.1 ± 0.3
Spectrometer rescattering	0.0 ± 0.1	0.0 ± 0.0
Inelastic contributions	0.0 ± 0.1	0.0 ± 0.0
Transverse asymmetry	0.0 ± 0.3	0.0 ± 0.1
Detector nonlinearity	0.0 ± 2.7	0.0 ± 0.5
Angle determination	0.0 ± 3.5	0.0 ± 0.6
Acceptance function	0.0 ± 2.9	0.0 ± 0.5
Total correction	17.7 ± **8.2**	3.2 ± 1.5
$A_{\mathrm{PV}}^{\mathrm{meas}}$	**550 ± 16**	100.0 ± 2.9

Table 6.1: Corrections and systematic uncertainties to extract $A_{\mathrm{PV}}^{\mathrm{meas}}$ listed on the bottom row with its statistical uncertainty. Reused from [37]

The detected asymmetry A_{raw} was corrected for the beam charge asymmetry $A_{\mathrm{BCM}} = 20.7 \pm 0.2$ ppb using the beam current monitor. The beam-induced false asymmetry in the normalized asymmetry was further corrected by the Lagrange multiplier regression as discussed in Chapter 5. Note that the 2.5 ppb uncertainty assigned for beam correction in Section 5.6 is further normalized by the 89.7 % beam polarization and turns into the 3.0 ppb uncertainty in the "beam asymmetry" row of Table 6.1.

After completion of analysis, data was unblinded by subtraction with the blinding term $A_{\mathrm{blind}} = -0.5313$ ppb. The correction for the detectors' non-linearity is zero by the construction of pedestals and assigned a systematic uncertainty of 0.5%. The corrected measured asymmetry is defined as below

$$A_{\mathrm{corr}} = A_{\mathrm{raw}} - A_{\mathrm{BCM}} - A_{\mathrm{beam}} - A_{\mathrm{blind}}. \tag{6.1}$$

The corrected asymmetry A_{corr} must be further corrected for the beam polarization P_b and the background dilutions f_i and asymmetries A_i to obtain A_{PV}

$$A_{\mathrm{PV}}^{\mathrm{meas}} = \frac{1}{P_b} \frac{A_{\mathrm{corr}} - P_b \sum_i f_i A_i}{1 - \sum_i f_i}. \tag{6.2}$$

The average beam polarization result P_b was (89.7 $\pm$ 0.8)%. The determination of the polarimeter target foil polarization was the largest contribution to the uncertainty (0.6%). The largest background dilution $f_C = 6.3 \pm 0.5$ % was due to the diamond foils. The effect of re-scattering from magnetized pole tips in the spectrometer was found to be negligible. The correction for the residual transverse electron beam polarization component is negligible and assigned a systematic uncertainty. Other background corrections are listed in Table 6.1. The final corrected parity-violating asymmetry is

$$A_{\rm PV}^{\rm meas} = 550 \pm 16 \text{ (stat)} \pm 8 \text{ (syst) ppb.} \tag{6.3}$$

6.2 Weak Charge, Neutron Radius and Neutron Skin

To predict the parity-violating asymmetry in ^{208}Pb theoretically, one has to make modest assumptions on the model to describe the weak charge density distribution $\rho_W(r)$. The model and its parameters are chosen to calculate the parity-violating asymmetry as a function of scattering angle $A(\theta)$, which includes the full Coulomb distortions [73] and reproduces the measured parity-violating asymmetry $A_{\rm PV}^{\rm meas}$.

The direct comparison of the measured parity-violating asymmetry to the theoretical predictions requires the spectrometer acceptance function $\epsilon(\theta)$ characterizing the probability for an electron to reach the integrating detector as a function of scattering angle θ. The modeled parity-violating asymmetry $A(\theta)$ is convoluted with the cross-section $\mathrm{d}\sigma/\mathrm{d}\Omega$ and the acceptance function $\epsilon(\theta)$, which was generated through a Monte Carlo simulation to match the observed distributions of the scattered momentum and angle. Explicitly, the convolution of $A(\theta)$ with $\epsilon(\theta)$ is shown below

$$\langle A \rangle = \frac{\int \mathrm{d}\theta \sin\theta A(\theta) \frac{\mathrm{d}\sigma}{\mathrm{d}\Omega} \epsilon(\theta)}{\int \mathrm{d}\theta \sin\theta \frac{\mathrm{d}\sigma}{\mathrm{d}\Omega} \epsilon(\theta)}. \tag{6.4}$$

Through Fourier transformation, the neutral weak charge form factor $F_W(q)$ was calculated from the weak charge density distribution $\rho_W(r)$ which reproduces $A_{\rm PV}^{\rm meas}$ in the theoretical calculation

$$F_W(q) = \frac{1}{Q_W} \int \mathrm{d}^3 r \frac{\sin qr}{qr} \rho_W(r), \tag{6.5}$$

where Q_W = -117.9 $\pm$ 0.3 incorporates one-loop radiative corrections including γ-Z box contributions as an overall constraint [74, 75, 76, 37].

The final result for F_W with the acceptance function $\epsilon(\theta)$ and the momentum transfer $\langle Q^2 \rangle = 0.00616$ GeV^2 is

$$F_W(\langle Q^2 \rangle) = 0.368 \pm 0.013 \text{ (exp)} \pm 0.001 \text{ (theo)}, \tag{6.6}$$

where the experimental uncertainty includes both statistical and systematic contributions.

To access the model uncertainty and the correlation between $A_{\rm PV}$ and the ^{208}Pb weak radius, the theoretical $\rho_W(r)$ predictions from a large variety of non-relativistic and relativistic density functional models were fitted to the two-parameter Fermi function $\rho_W(r,c,a)$ [77, 78]

$$\rho_W(r,c,a) = \rho_W^0 \frac{\sinh(c/a)}{\cosh(r/a)+\sinh(c/a)}, \tag{6.7}$$

$$\rho_W^0 = \frac{3Q_W}{4\pi c(c^2+\pi^2a^2)}, \tag{6.8}$$

where parameter c characterizes the nucleus size and parameter a is the surface thickness. The interior weak density ρ_W^0 is normalized by the total nucleus weak charge Q_W defined as

$$Q_W = \int {\rm d}r \rho_W(r) = -117.9 \pm 0.3. \tag{6.9}$$

Figure 6.1 shows the correlation between $A_{\rm PV}$ and the weak charge radius indicated by a sampling of theoretical calculations along with the vertical green band highlighting the PREX-2 $A_{\rm PV}^{\rm meas}$ with its 1-σ experimental uncertainty. The red solid curve was fitted as a polynomial function of $A_{\rm PV}$

$$R_W = 2.3462 \times 10^{-6} A_{\rm PV}^2 - 7.1705 \times 10^{-3} A_{\rm PV} + 9.02869. \tag{6.10}$$

Table 6.3 show the surface thickness extracted from each mean field models and suggests a range of uncertainty $a = 0.605 \pm 0.025$ fm which is reflected as red dash lines in Figure 6.1. The mean-square weak radius from Equation (6.7) is

$$R_W^2 = \frac{1}{Q_W}\int {\rm d}^3r^2 \rho_W(r) = \frac{3}{5}c^2 + \frac{7}{5}(\pi a)^2, \tag{6.11}$$

therefore the uncertainty of the surface thickness a is a small model uncertainty for R_W.

The weak radius R_W and its uncertainty were determined by projecting $A_{\rm PV}^{\rm meas}$ to R_w using Equation (6.10). The PREX-2 result for the weak radius is

$$R_W = 5.795 \pm 0.082\ ({\rm exp}) \pm 0.013\ ({\rm theo})\ {\rm fm}. \tag{6.12}$$

And the weak skin thickness, defined as the difference between the weak radius and the charge radius, can also be determined with the existing accurate charge radius $R_{\rm ch} = 5.503$ fm [79, 80]

$$R_W - R_{\rm ch} = 0.292 \pm 0.082\ ({\rm exp}) \pm 0.013\ ({\rm theo})\ {\rm fm}. \tag{6.13}$$

Figure 6.2 illustrates the inferred radial dependence of the ^{208}Pb charge, weak and total baryon densities along with the R_W and $R_{\rm ch}$ landmarks for the weak skin.

The neutron skin thickness is defined as the difference between the point neutron radius and the point proton radius. The point neutron mean-square radius can be calculated from the weak radius R_W

$$R_n^2 = \frac{Q_W}{q_W^n N} R_W^2 - \frac{q_W^p Z}{q_W^n N} R_{\rm ch}^2 - \langle r_p^2 \rangle - \frac{Z}{N}\langle r_n^2 \rangle + \frac{Z+N}{q_W^n N}\langle r_s^2 \rangle. \tag{6.14}$$

Recall that $\langle r_n^2 \rangle$ and $\langle r_p^2 \rangle$ are the mean-squared single neutron radius and the mean-squared point proton radius. The nucleon strangeness radius is constrained $\langle r_s^2 \rangle = 0.02 \pm 0.04$ fm^2 for $Q^2 < 0.11$ GeV^2 by experimental data [48, 49, 50, 51, 52, 53, 54, 55, 56, 57, 58, 59, 60, 61] and their global analysis [81, 82]. Meanwhile the electric charge radius relates with the point proton radius [83]

$$R_{\rm ch}^2 = R_p^2 + \langle r_p^2 \rangle + \frac{N}{Z}\langle r_n^2 \rangle + \frac{3}{4M^2} + \langle r^2 \rangle_{\rm so}, \tag{6.15}$$

where the Darwin contribution $3/(4M^2)$ and spin-orbit current $\langle r^2 \rangle_{\rm so}$ are small [47, 79].

Based on Equation (6.14) and (6.15), the neutron skin thickness can be approximately calculated from the weak skin thickness

$$R_n - R_p \approx (1 + \frac{Z q_W^p}{N q_W^n})(R_W - R_{\rm ch}) = 0.278 \pm 0.078\ ({\rm exp}) \pm 0.012\ ({\rm theo})\ {\rm fm}, \tag{6.16}$$

where the nucleon weak charges $q_W^n = -0.9878$ and $q_W^p = 0.0721$ include the radiative corrections [84, 85], .

The interior weak density ρ_W^0 in Equation (6.8) can be extracted [86]

$$\begin{aligned} \rho_W^0 &= \frac{27 Q_W}{4\pi(5R_W^2 - 4\pi^2 a^2)\sqrt{15R_W^2 - 21\pi^2 a^2}} \\ &= -0.0798 \pm 0.0038\ ({\rm exp}) \pm 0.0013\ ({\rm theo})\ {\rm fm}^{-3}. \end{aligned} \tag{6.17}$$

With the interior electric charge density $\rho_{\rm ch}^0 = 0.06246$ fm^{-3} inferred from $R_{\rm ch}$ [86], the interior baryon density ρ_b^0 determined from the PREX-2 data is

$$\begin{aligned} \rho_b^0 &= \rho_n^0 + \rho_p^0 \\ &= \frac{1}{q_n}(\rho_W^0 - q_p \rho_{\rm ch}^0) + \rho_{\rm ch}^0 \\ &= \frac{1}{q_n}\rho_W^0 + (1 - \frac{q_p}{q_n})\rho_{\rm ch}^0 \\ &= 0.1482 \pm 0.0040\ {\rm fm}^{-3}, \end{aligned} \tag{6.18}$$

which is pointed out as the baryon density at r=0 in Figure 6.2. The nuclear saturation density ρ^0 can be extrapolated from the interior baryon density using the extrapolation factor $f_{\rm ex}$ given by [86]

$$f_{\rm ex} = \frac{\rho^0}{\rho_b^0} = 1.02 \pm 0.03. \tag{6.19}$$

Following the calculation in [86] with the PREX-2 result, the extrapolated nuclear saturation density is updated:

$$\rho^0 = 0.1511 \pm 0.0041 \pm 0.0045 \text{ fm}^{-3}, \tag{6.20}$$

where the first error is due to the uncertainty of ρ_b^0 and the second error is due to the uncertainty of f_{ex}. The empirical value of the nuclear saturation density has been known as 0.17 ± 0.03 fm^{-3} [87] and can be obtained using the Droplet Model [88] and the Liquid Drop Model [89] of the nucleus. Notably the extrapolated saturation density is consistent with $\rho^0 = 0.151 \pm 0.001$ fm^{-3} predicted by a relativistic energy density functional [90].

The PREX-1 results can be found in [47]

$$R_W = 5.826 \pm 0.183 \text{ fm}, \tag{6.21}$$

$$R_n - R_p = 0.302 \pm 0.177 \text{ fm}, \tag{6.22}$$

which are consistent with the PREX-2 results. The combined PREX results are summarized in Table 6.2.

^{208}Pb Parameters	Values
Weak Radius (R_W)	5.800 ± 0.075 fm
Neutron skin ($R_n - R_p$)	0.283 ± 0.071 fm
Interior weak Density (ρ_W^0)	-0.0796 ± 0.0038 fm^{-3}
Interior baryon Density (ρ_b^0)	0.1480 ± 0.0038 fm^{-3}

Table 6.2: Combined results for ^{208}Pb from PREX-1 and PREX-2.

Model	a[^{208}Pb] (fm)
Big Apple [91]	0.6087
FSUgold [92]	0.6134
IUFSU [93]	0.6079
NL3 [94]	0.6096
SIII [95]	0.5792
SLY4 [96]	0.6040
TAMUc [97]	0.6351
TAMUb [97]	0.6210
TAMUa [97]	0.6125

Table 6.3: Surface thickness parameter a of the Fermi function fits to the weak charge densities of ^{208}Pb.

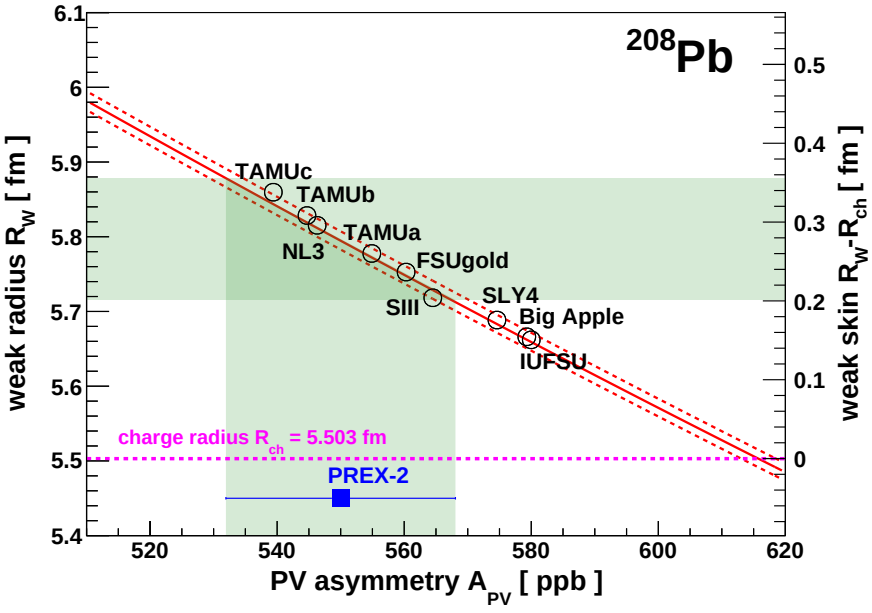

Figure 6.1: Extraction of the weak radius (left vertical axis) or neutron skin (right vertical axis) for the 208 Pb nucleus. $R_{\rm ch}$ [25] is shown for comparison.

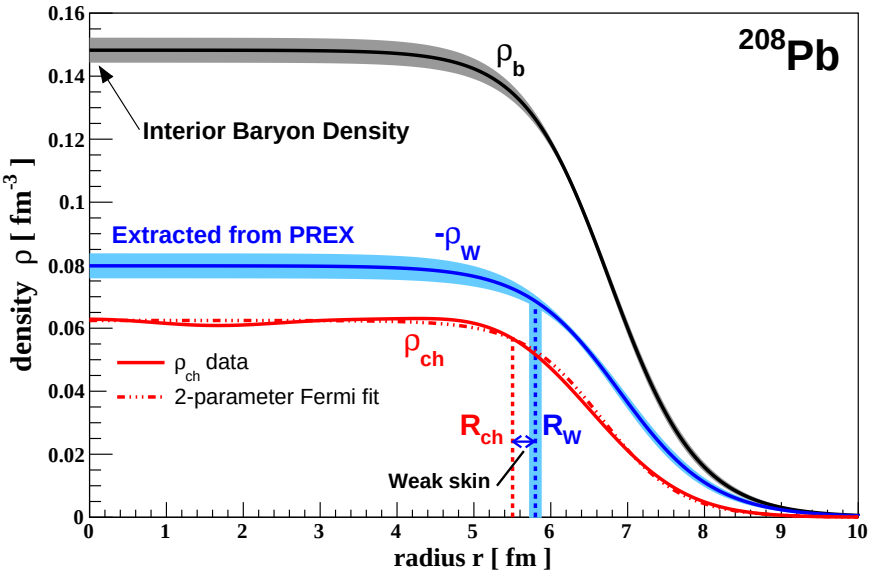

Figure 6.2: ^{208}Pb weak and baryon densities from the combined PREX datasets, with uncertainties shaded. The charge density [25] is also shown.

6.3 Implications of the Physics Result

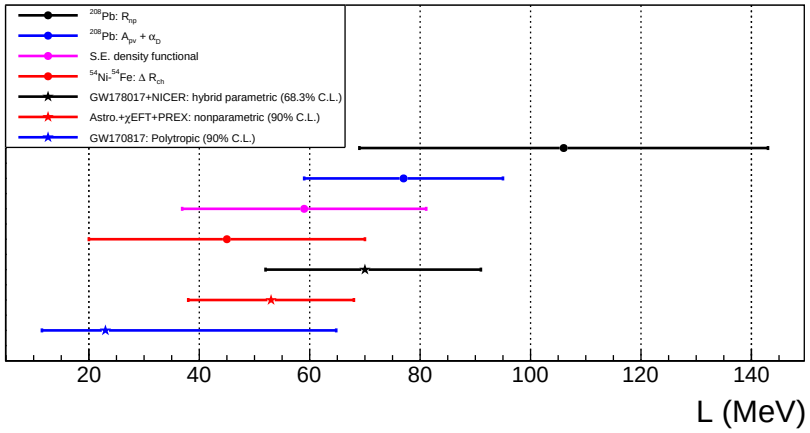

Figure 6.3: Constraints on L from different observables and analyses. From top to bottom: 1) ^{208}Pb neutron skin thickness [26]; 2) An EDF prediction constrained by the electric dipole polarizability (α_D) and the $A_{\rm PV}$ in ^{208}Pb [27]. 3) Symmetry energy density functional fitted to the PREX-2 result, HIC observables and others [28]; 4) Difference between the charge radii of ^{54}Ni and ^{54}Fe [29, 30]; 5) Joint Bayesian analysis of GW170817, PSR J0030+0451, and PSR J0740+6620 [31] ; 6) Combined analysis of astrophysical data with chiral effective field theory (χEFT) and PREX with a nonparametric EOS [32, 33]; 7) Neutron star tidal deformability of gravitational-wave event GW170817 [34, 35, 36].

Recently, the density dependency of the symmetry energy was deduced from the correlation between the neutron skin thickness of ^{208}Pb $R_{\rm skin}^{208}$ and L established by a set of 16 covariant energy density functionals [26]. The linear correlation presented in [26] is approximately

$$L = 521.5 \times R_{\rm skin}^{208} - 41.96. \tag{6.23}$$

And note that the 16 models used also predict the binding energy per nucleon B/A and the charge radius of ^{208}Pb in good agreement with the experimental values.

Based on the PREX combined result $R_n - R_p = (0.283 \pm 0.071)$ fm, the Gaussian probability of L was also obtained

$$L = (106 \pm 37)\ \text{MeV}, \tag{6.24}$$

along with the symmetry energy at nuclear saturation density

$$S_v = (38.1 \pm 4.7)\ \text{MeV}. \tag{6.25}$$

A purely electromagnetic method to constrain L has been introduced in [29] and proposed L can be constrained from $\Delta R_{\rm ch}$, the difference of the charge radii of mirror nuclei, e.g. ^{52}Cr and ^{52}Ni. The correlation between $\Delta R_{\rm ch}$ and $|N-Z| \times L$ can be shown from the Skyrme and CODF calculations in [29, 30]. And the 1-σ error band of the ^{54}Ni-^{54}Fe $\Delta R_{\rm ch}$ implies a value of L in the range of 20-70 MeV, which is barely consistent with the lower bound of Equation (6.24).

A systematic study on EDF models is carried out in [27] and calibrates several families of EDFs to a large set of ground observables, such as binding energies and charge radii. The result of [27] shows no single model is able to reproduce $A_{\rm PV}$ and α_D within the 1-σ experimental error bands simultaneously, which indicates a clear tension between the PREX-2 result and the electric dipole polarizability α_D in ^{208}Pb. An averaged prediction $L = (77 \pm 18)$ MeV is obtained from two calibrated EDFs constrained by $A_{\rm PV}$ and α_D in ^{208}Pb.

It is also pointed in [28] that most of the experimental observables probe the symmetry energy at densities far from saturation density ρ_0. For example, Pearson correlation analysis of [98] indicates that α_D constrains the symmetry energy most accurately at $\approx 0.31\rho_0$. The fit in [28] includes the PREX-2 result and the symmetry energy at $\approx 1.5\rho_0$ measured from pion emission in heavy ion collisions (HIC), as well as other observables sensitive at $0.2\rho_0 - 0.66\rho_0$, and yields a new symmetry energy functional suggesting $L = (59.6 \pm 22.1)$ MeV.

A 90% highest-posterior density interval (HPDI) $11.5 < L < 64.8$ MeV with a peak likelihood at $L = 23$ MeV [36] was inferred from the tidal deformability of gravitational-wave event GW170817 [34, 35]. Meanwhile a joint Bayesian analysis [31] of GW170817, PSR J0030+0451, and PSR J0740+6620 yields $L = 70^{+21}_{-18}$ MeV at 68.3% credible level. A combined analysis constrained with astrophysical data, chiral effective field theory (χEFT) and the PREX result yields $L = 53^{+13}_{-15}$ MeV at 90% credible level [32, 33].

These recent analyses of the density dependence of the symmetry energy are summarized in Figure 6.3. At the time of writing, the interpretation of the PREX-2 result and the explanation for the tension between the result in [26] with others are still under debate, partially due to the relatively larger uncertainty in (6.24).

Neutron stars are born with high temperatures in supernova explosions. Neutron stars then rapidly cooled down primarily by neutrino emission. The direct URCA processing is an enhanced-cooling mechanism in which the neutron beta decay is followed by the electron capture

$$\begin{aligned} n &\to p + e^- + \overline{\nu_e}, \\ p + e^- &\to n + \nu_e. \end{aligned} \tag{6.26}$$

The direct URCA threshold density is the density where the equality of Fermi momenta of neutrons, protons and electrons is satisfied

$$k_F^n = k_F^p + k_F^e, \tag{6.27}$$

and at the onset of this enhanced cooling, the proton fraction is $Y_P = Z/A \approx 1/9$. The proton fraction of nuclear matter in beta equilibrium is sensitive to the symmetry energy and its density dependence [99, 100]. A stiff symmetry energy imposes penalty for $N - Z$ imbalance and retains a large proton fraction therefore allows the onset of the direct URCA process at lower central densities. Using the 1-σ lower values of the neutron skin thickness $R_{\rm skin}^{208} = 0.212$ fm, the direct URCA threshold density and its corresponding mass can be obtained [26]

$$\begin{aligned} \rho_\star &\approx 0.42 \text{ fm}^{-3}, \\ M_\star &\approx 1.45\ M_\odot. \end{aligned} \tag{6.28}$$

If the central values $R_{\rm skin}^{208} = 0.283$ fm were used instead, the direct URCA thresholds are

$$\begin{aligned} \rho_\star &\approx 0.24 \text{ fm}^{-3}, \\ M_\star &\approx 0.85\ M_\odot, \end{aligned} \tag{6.29}$$

where the central density triggering the direct URCA cooling is slightly above the nuclear saturation density.

In the meantime, the strong correlation between the neutron skin thickness of ^{208}Pb and the tidal deformability of a 1.4 $M_\odot$ neutron star $\Lambda_\star^{1.4}$ shown in [26] makes it possible to compare the PREX-2 result directly with neutron star observables, such as PSR J0030+0451 reported by NICER [101, 102].

The PSR J0030+0451 result [101, 102] suggests an upper limit of $R_\star^{1.4} \leq 14.26$ km and is mapped to an upper limit of $R_{\rm skin}^{208} \leq 0.31$ fm [26]. Meanwhile, the 1-σ lower limit of $R_{\rm skin}^{208} \geq 0.21$ fm places a lower limit of $R_\star^{1.4} \geq 13.25$ km. The 1-σ confidence zone allowed by both $R_\star^{1.4}$ and $R_{\rm skin}^{208}$ sets limits on the tidal deformability of a 1.4 $M_\odot$ neutron star

$$642 \leq \Lambda_\star^{1.4} \leq 955, \tag{6.30}$$

which indicates some tension with revised limit of $\Lambda_\star^{1.4} = 190^{+390}_{-120} \leq 580$ for the GW170817 discovery [103].

In the near feature, the Mainz Radius EXperiment (MREX) at Mainz Energy Recovery Superconducting Accelerator (MESA) [104] proposed to measure the neutron radius in ^{208}Pb with 0.5 % experimental uncertainty ($\delta R_n/R_n \approx 0.5\%$), an improvement with a factor of

2 compared to PREX-2. Using the correlation in Equation (6.23), if MREX reproduces the central value of the PREX result ($L = 106$ MeV), the MREX result will constrain L with an experimental uncertainty of 15.6 MeV, which will exclude most of the observables independent from ^{208}Pb neutron skin in Figure 6.3. If the tension in Equation (6.30) is confirmed from the next generation of the laboratory measurements of the neutron skin by MREX and astronomical observations, e.g. from NICER and LIGO-Virgo-KAGRA, it may be suggesting a phase transition in the stellar core, where the EOS is soft at intermediate densities then is stiffened at high densities to support massive neutron matter.

Appendix A

Pitts Definition and Slugs Information

Pitt	Slug	IHWP	WIEN	HRS Arm
1	1	OUT	FLIP-RIGHT	Both-arm
1	2	IN	FLIP-RIGHT	Both-arm
1	3	OUT	FLIP-RIGHT	Both-arm
1	4	OUT	FLIP-RIGHT	Both-arm
1	5	OUT	FLIP-RIGHT	Both-arm
1	6	OUT	FLIP-RIGHT	Both-arm
2	7	IN	FLIP-RIGHT	Both-arm
2	8	IN	FLIP-RIGHT	Left-arm
2	9	OUT	FLIP-RIGHT	Left-arm
2	10	IN	FLIP-RIGHT	Left-arm
2	11	OUT	FLIP-RIGHT	Left-arm
3	12	IN	FLIP-RIGHT	Both-arm
3	13	OUT	FLIP-RIGHT	Both-arm
3	14	IN	FLIP-RIGHT	Both-arm
3	15	OUT	FLIP-RIGHT	Both-arm
4	16	IN	FLIP-RIGHT	Both-arm
4	17	OUT	FLIP-RIGHT	Both-arm
4	18	IN	FLIP-RIGHT	Both-arm
4	19	OUT	FLIP-RIGHT	Both-arm
4	20	OUT	FLIP-RIGHT	Right-arm
5	21	IN	FLIP-RIGHT	Both-arm
5	22	OUT	FLIP-RIGHT	Both-arm
5	23	IN	FLIP-RIGHT	Both-arm

5	24	OUT	FLIP-RIGHT	Both-arm
5	25	IN	FLIP-RIGHT	Both-arm
6	26	OUT	FLIP-LEFT	Both-arm
6	27	IN	FLIP-LEFT	Both-arm
6	28	OUT	FLIP-LEFT	Both-arm
6	29	IN	FLIP-LEFT	Both-arm
7	30	OUT	FLIP-LEFT	Both-arm
7	31	OUT	FLIP-LEFT	Left-arm
7	32	IN	FLIP-LEFT	Both-arm
7	33	OUT	FLIP-LEFT	Both-arm
7	34	IN	FLIP-LEFT	Both-arm
8	35	OUT	FLIP-LEFT	Both-arm
8	36	IN	FLIP-LEFT	Both-arm
8	37	OUT	FLIP-LEFT	Both-arm
8	38	IN	FLIP-LEFT	Both-arm
9	39	OUT	FLIP-LEFT	Both-arm
9	40	IN	FLIP-LEFT	Both-arm
9	41	OUT	FLIP-LEFT	Both-arm
9	42	IN	FLIP-LEFT	Both-arm
10	43	OUT	FLIP-LEFT	Both-arm
10	43	OUT	FLIP-LEFT	Left-arm
10	44	IN	FLIP-LEFT	Both-arm
11	45	IN	FLIP-RIGHT	Both-arm
11	46	OUT	FLIP-RIGHT	Both-arm
11	47	IN	FLIP-RIGHT	Both-arm
11	48	OUT	FLIP-RIGHT	Both-arm
12	49	IN	FLIP-RIGHT	Both-arm
12	50	OUT	FLIP-RIGHT	Both-arm
12	51	IN	FLIP-RIGHT	Both-arm
12	52	OUT	FLIP-RIGHT	Both-arm
13	53	IN	FLIP-RIGHT	Both-arm
13	54	OUT	FLIP-RIGHT	Both-arm
13	55	IN	FLIP-RIGHT	Both-arm
13	56	OUT	FLIP-RIGHT	Both-arm
14	57	IN	FLIP-RIGHT	Both-arm

14	58	OUT	FLIP-RIGHT	Both-arm
14	59	IN	FLIP-RIGHT	Both-arm
15	60	IN	FLIP-LEFT	Both-arm
15	61	OUT	FLIP-LEFT	Both-arm
15	62	IN	FLIP-LEFT	Both-arm
15	63	OUT	FLIP-LEFT	Both-arm
16	64	IN	FLIP-LEFT	Both-arm
16	65	OUT	FLIP-LEFT	Both-arm
16	66	IN	FLIP-LEFT	Both-arm
16	67	OUT	FLIP-LEFT	Both-arm
17	68	IN	FLIP-LEFT	Both-arm
17	69	OUT	FLIP-LEFT	Both-arm
17	70	IN	FLIP-LEFT	Both-arm
17	71	OUT	FLIP-LEFT	Both-arm
18	72	IN	FLIP-LEFT	Both-arm
18	73	OUT	FLIP-LEFT	Both-arm
18	74	IN	FLIP-LEFT	Both-arm
18	74	IN	FLIP-LEFT	Left-arm
18	75	OUT	FLIP-LEFT	Both-arm
19	76	IN	FLIP-LEFT	Both-arm
19	77	OUT	FLIP-LEFT	Both-arm
19	78	IN	FLIP-LEFT	Both-arm
19	79	OUT	FLIP-LEFT	Both-arm
20	80	IN	FLIP-LEFT	Both-arm
20	81	OUT	FLIP-LEFT	Both-arm
20	82	IN	FLIP-LEFT	Both-arm
20	83	OUT	FLIP-LEFT	Both-arm
21	84	IN	FLIP-LEFT	Both-arm
21	85	OUT	FLIP-LEFT	Both-arm
21	86	IN	FLIP-LEFT	Both-arm
21	87	OUT	FLIP-LEFT	Both-arm
21	88	OUT	FLIP-LEFT	Both-arm
22	89	IN	FLIP-LEFT	Both-arm
22	90	OUT	FLIP-LEFT	Both-arm
22	91	IN	FLIP-LEFT	Both-arm

22	92	OUT	FLIP-LEFT	Both-arm
23	93	IN	FLIP-LEFT	Both-arm
23	94	OUT	FLIP-LEFT	Both-arm

Table A.1: Pitts definition with slugs information.

Appendix B

Residual Sensitivities Supercycle History

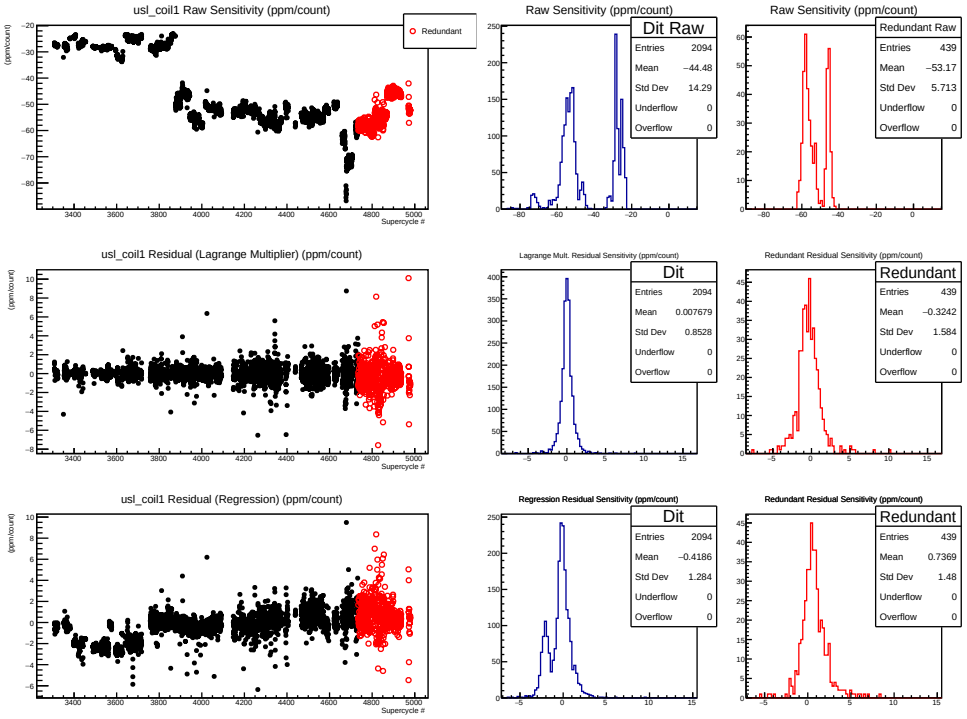

Figure B.1: History for the residual sensitivity of the left-arm main detector to Coil-1

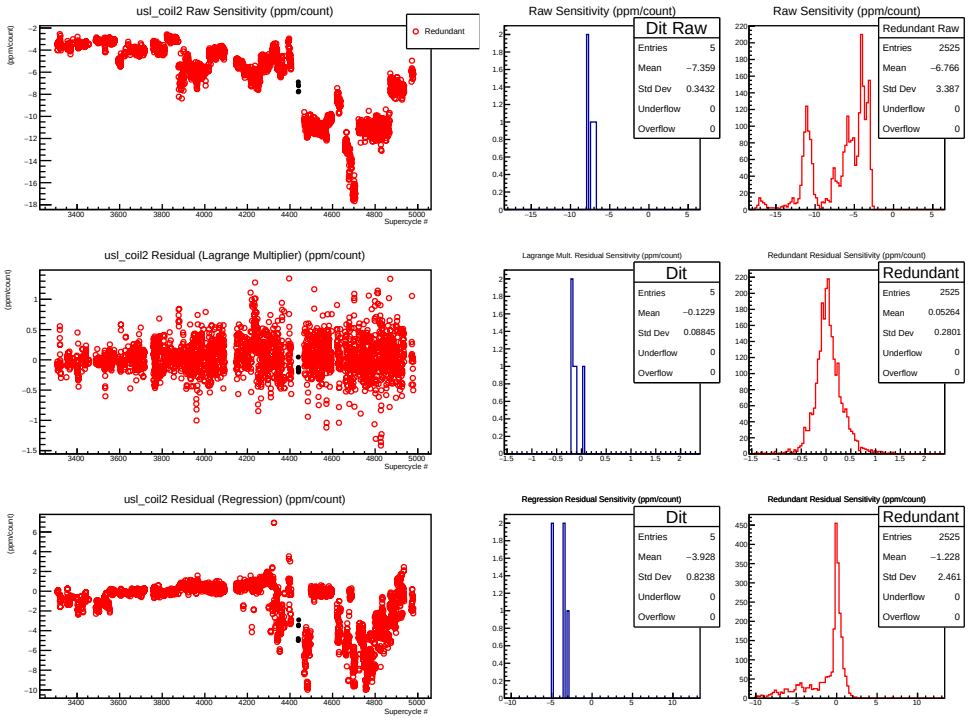

Figure B.2: History for the residual sensitivity of the left-arm main detector to Coil-2

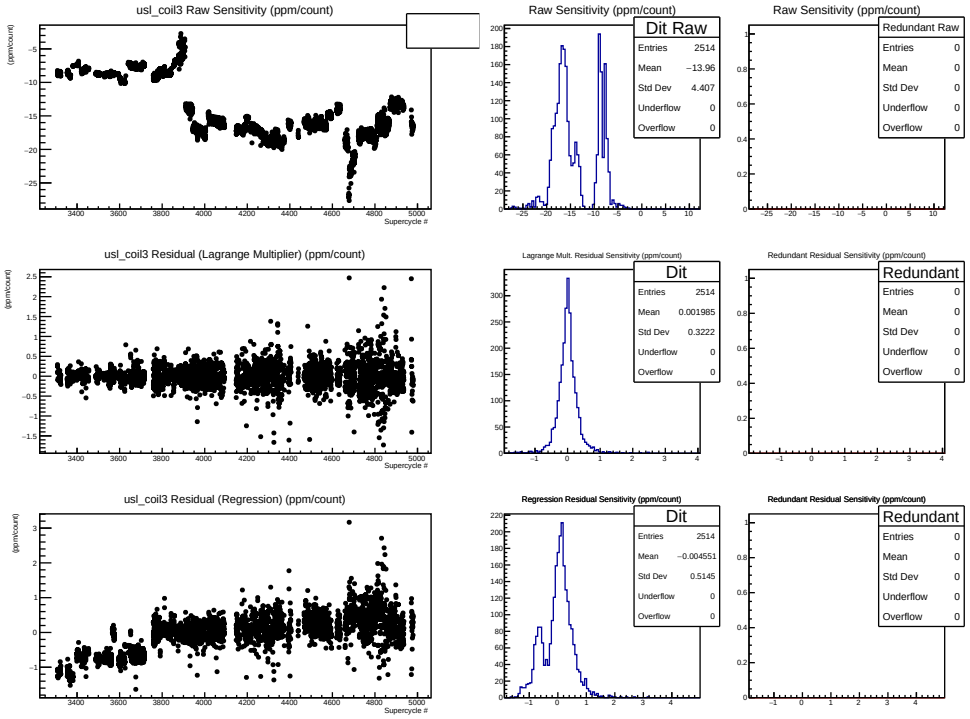

Figure B.3: History for the residual sensitivity of the left-arm main detector to Coil-3

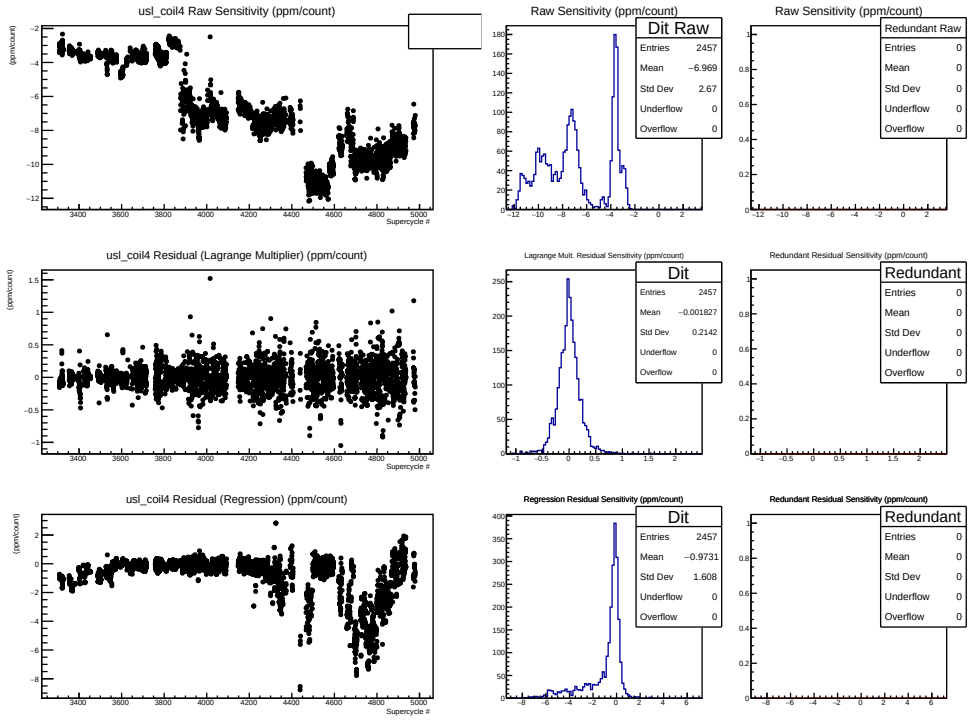

Figure B.4: History for the residual sensitivity of the left-arm main detector to Coil-4

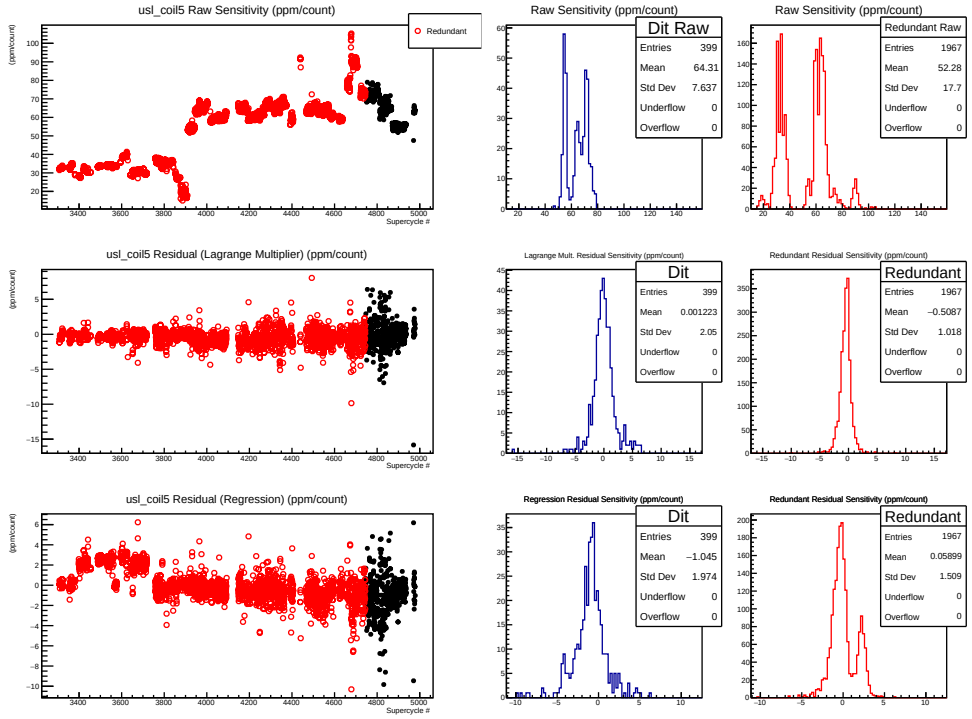

Figure B.5: History for the residual sensitivity of the left-arm main detector to Coil-5

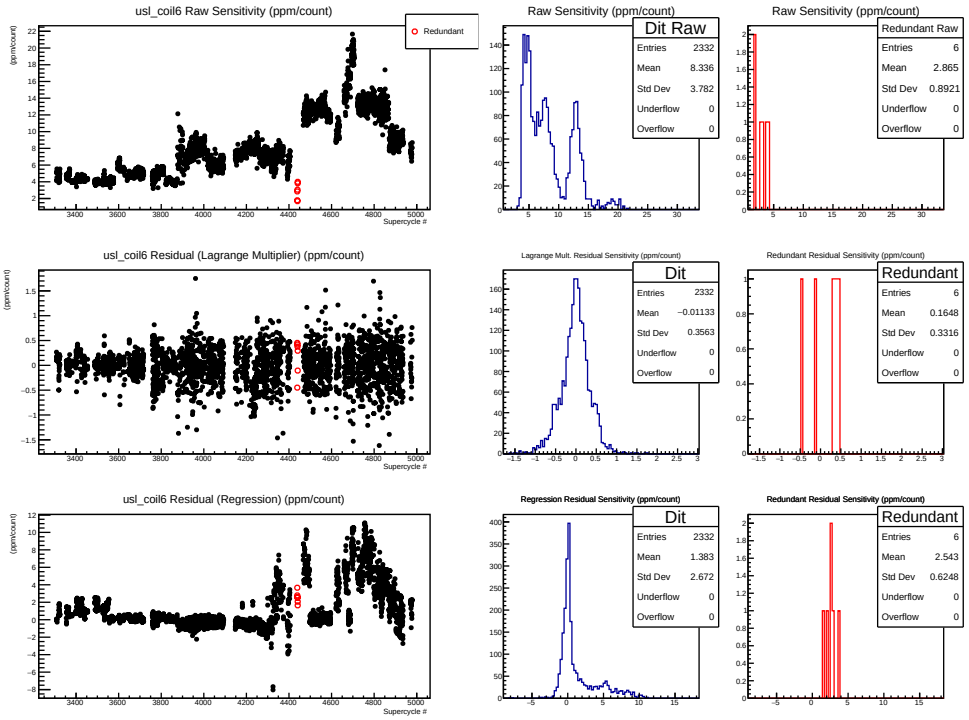

Figure B.6: History for the residual sensitivity of the left-arm main detector to Coil-6

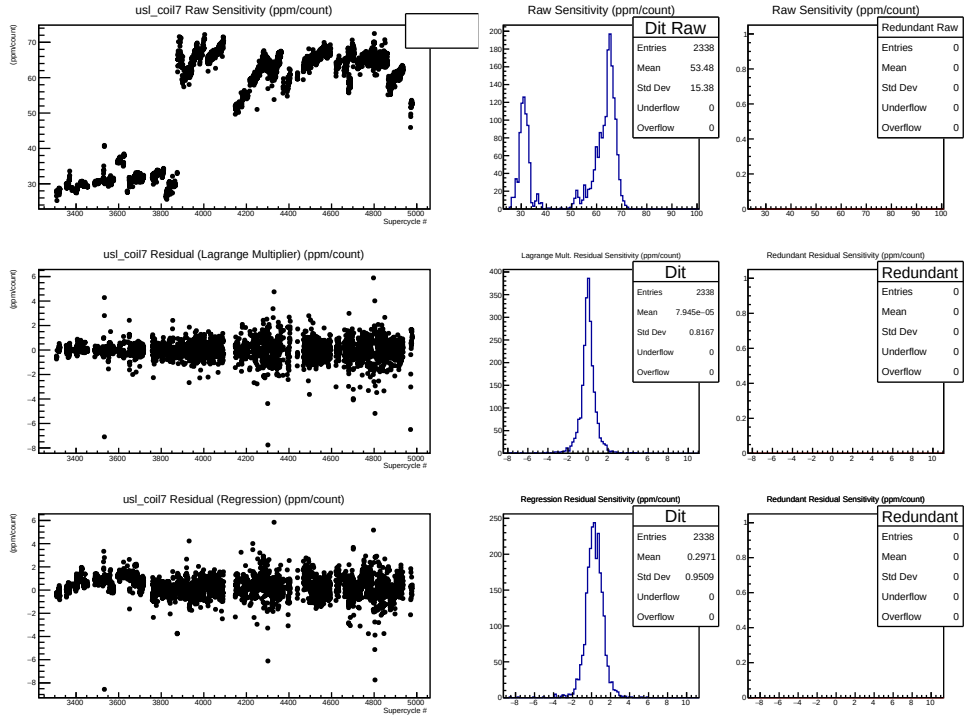

Figure B.7: History for the residual sensitivity of the left-arm main detector to Coil-7

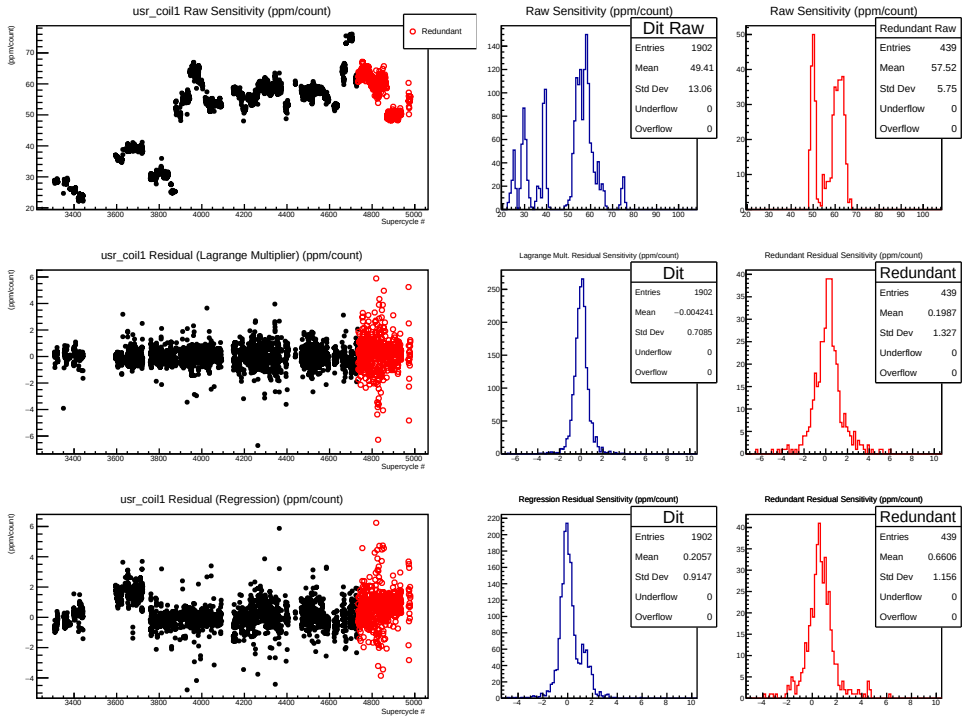

Figure B.8: History for the residual sensitivity of the right-arm main detector to Coil-1

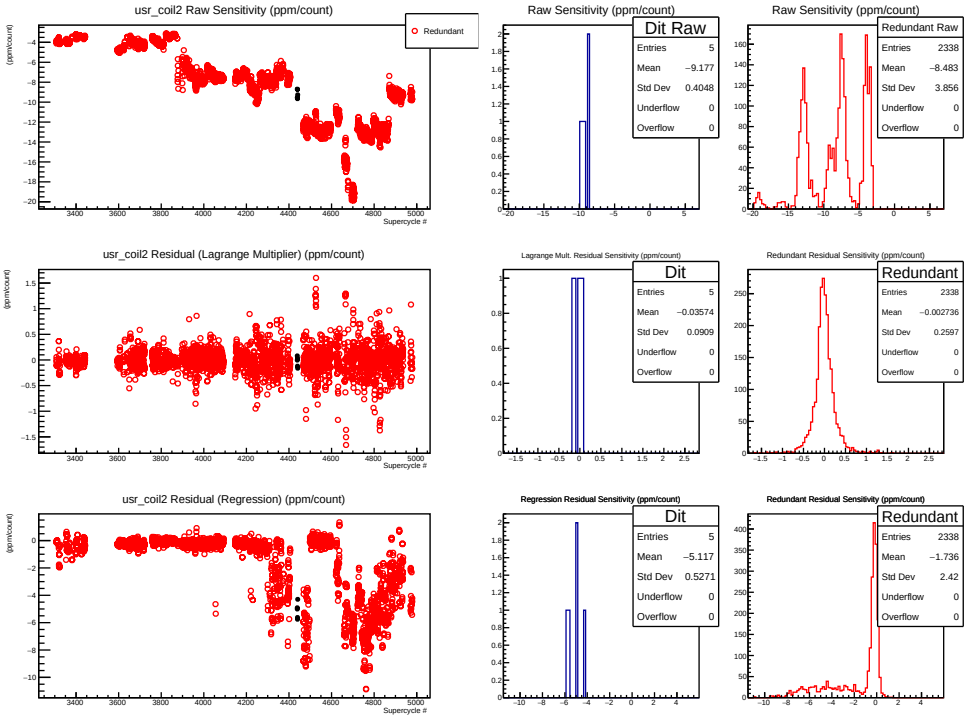

Figure B.9: History for the residual sensitivity of the right-arm main detector to Coil-2

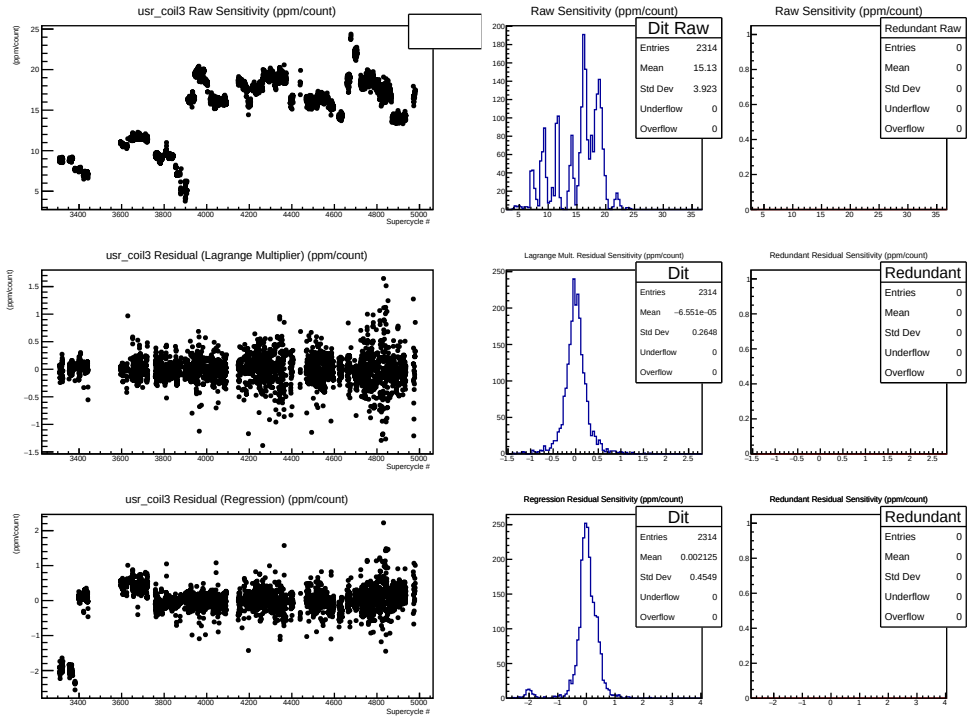

Figure B.10: History for the residual sensitivity of the right-arm main detector to Coil-3

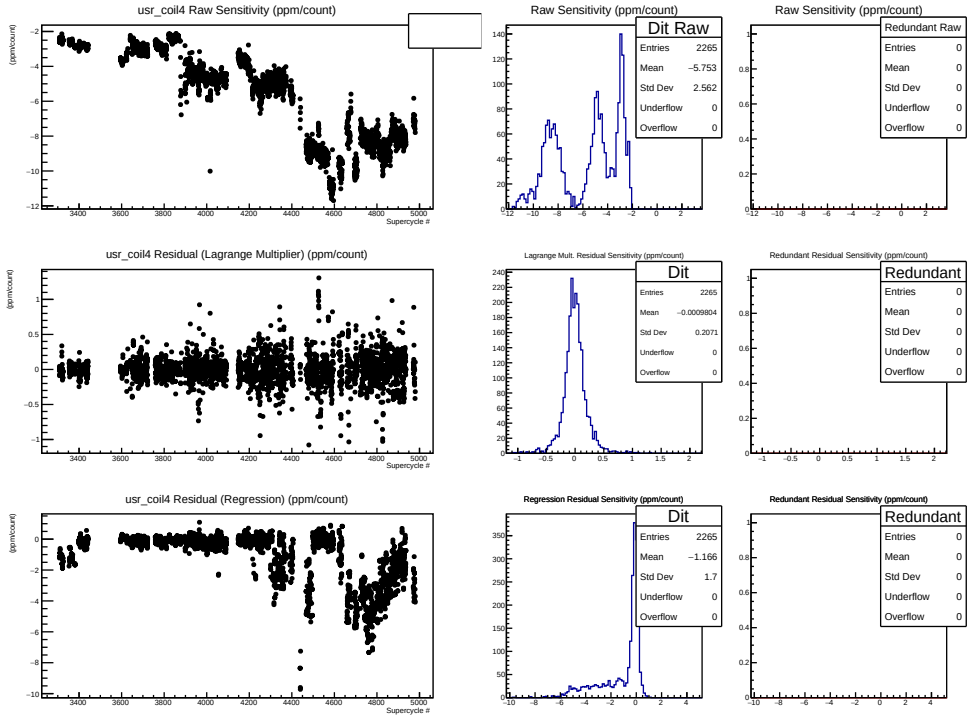

Figure B.11: History for the residual sensitivity of the right-arm main detector to Coil-4

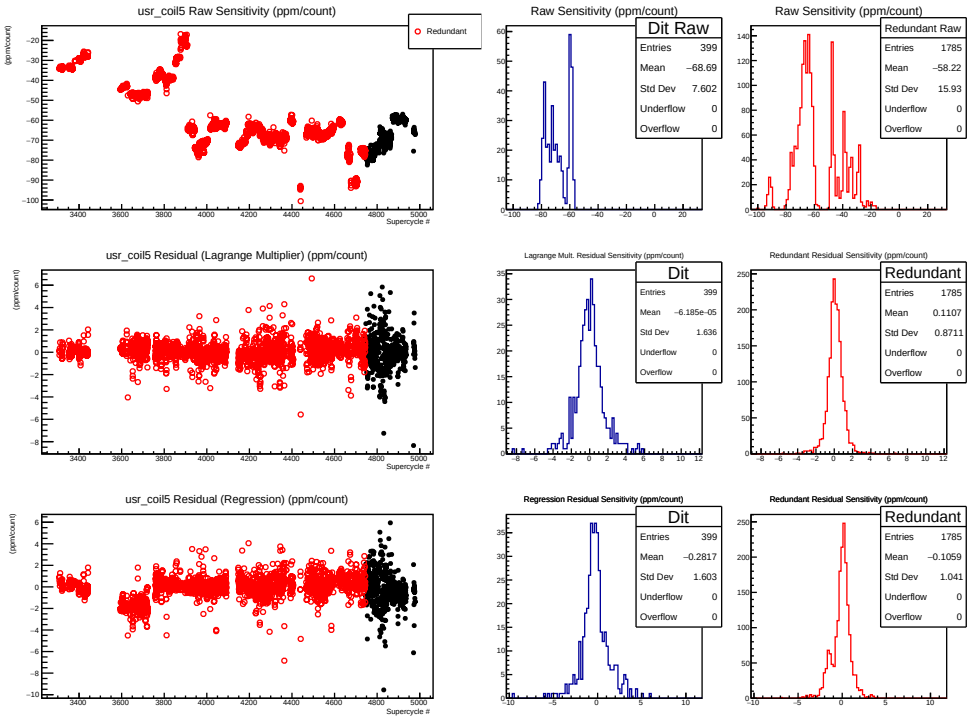

Figure B.12: History for the residual sensitivity of the right-arm main detector to Coil-5

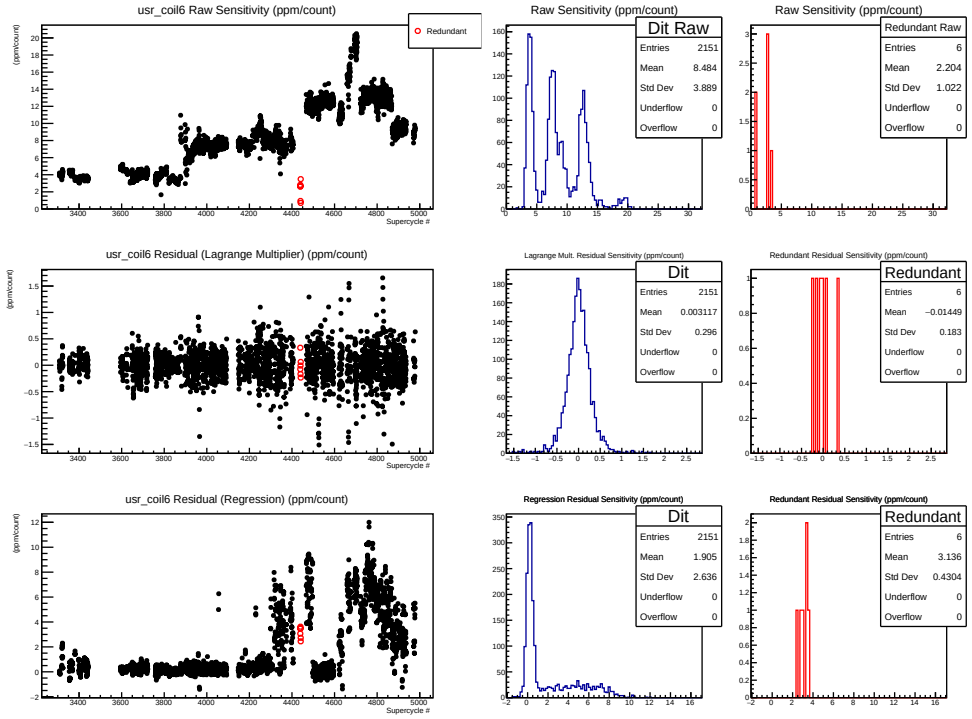

Figure B.13: History for the residual sensitivity of the right-arm main detector to Coil-6

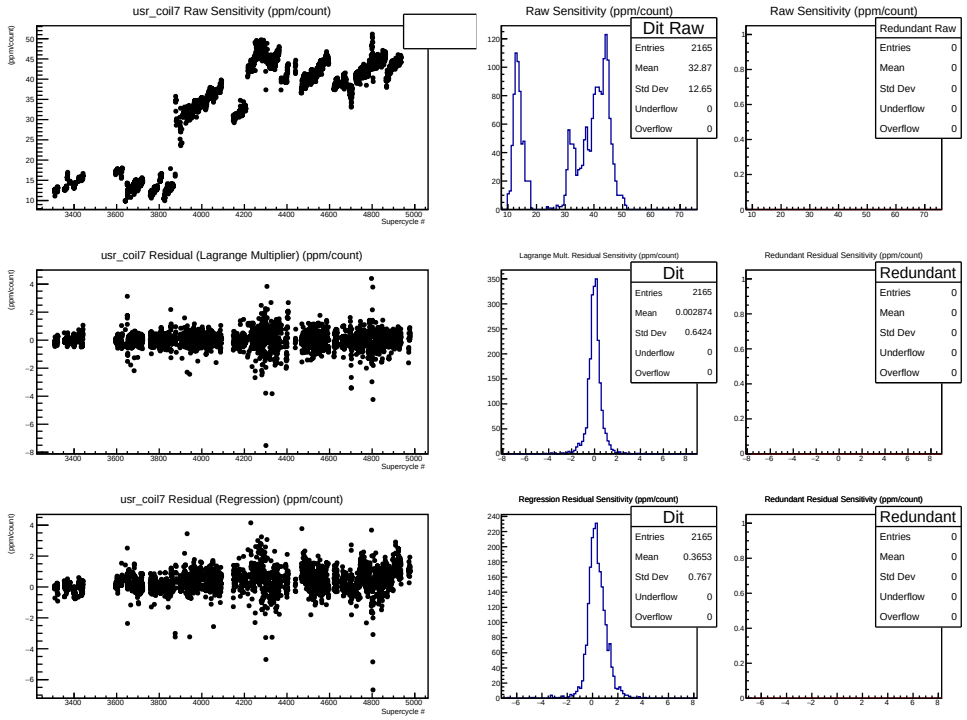

Figure B.14: History for the residual sensitivity of the right-arm main detector to Coil-7

Appendix C

Eigenvectors Run History

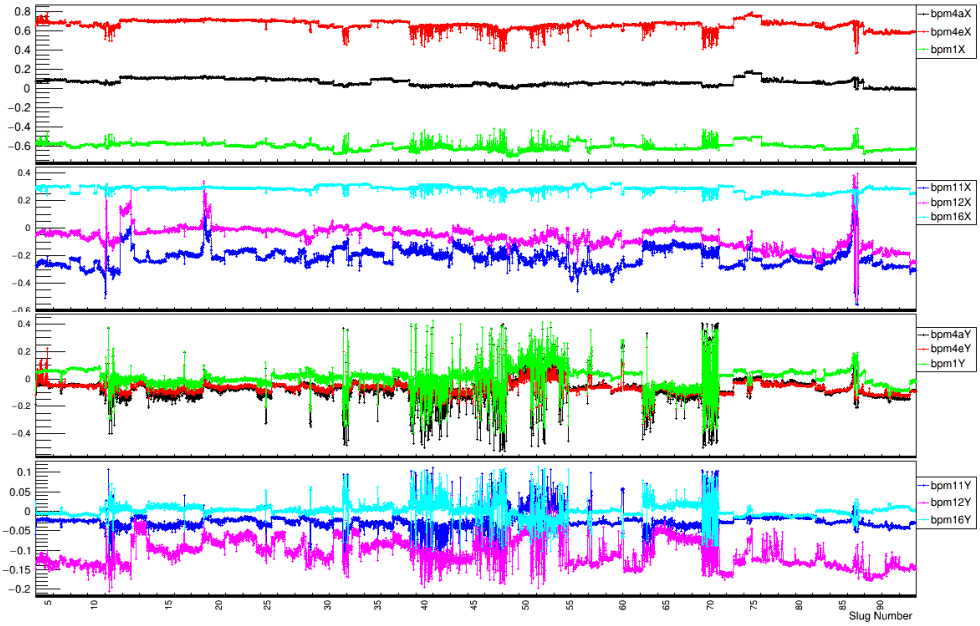

Figure C.1: History of the Eigenvector-0 components

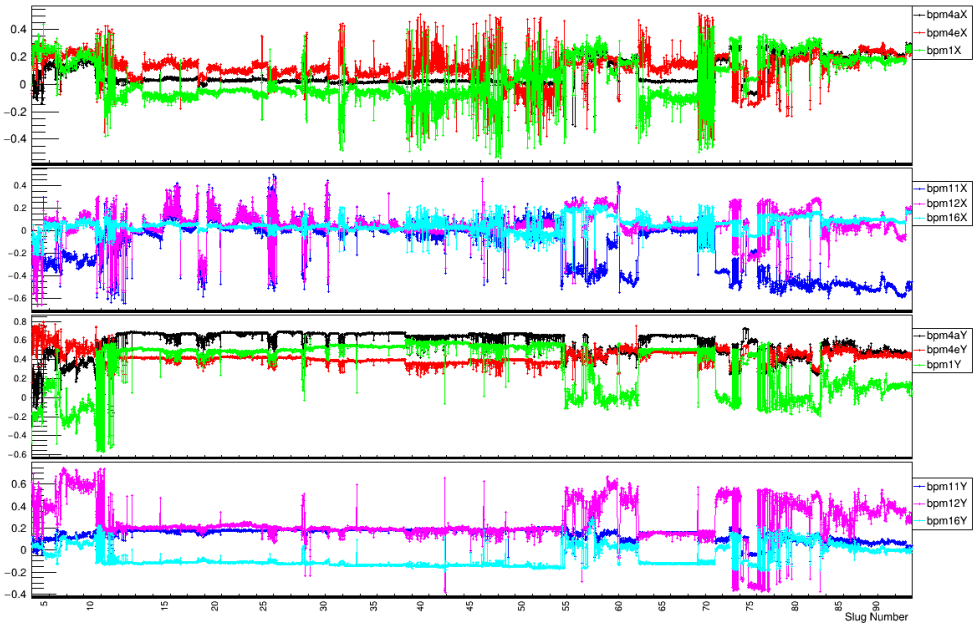

Figure C.2: History of the Eigenvector-1 components

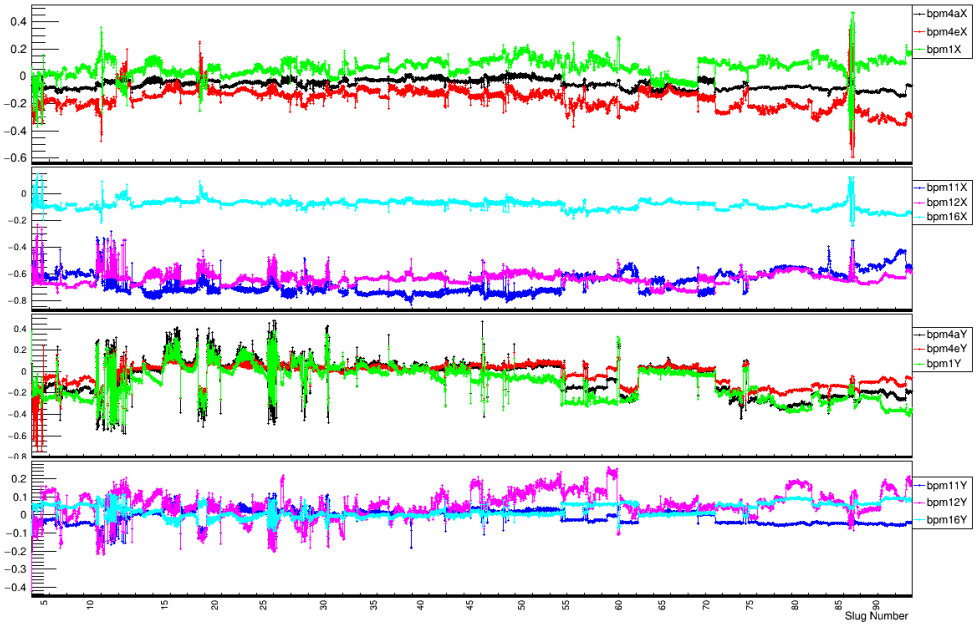

Figure C.3: History of the Eigenvector-2 components

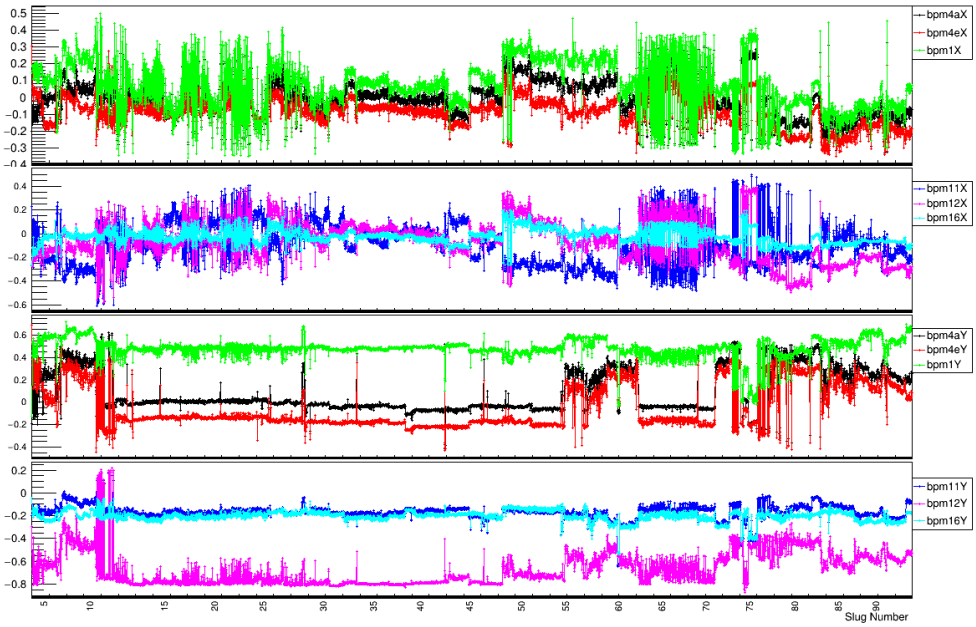

Figure C.4: History of the Eigenvector-3 components

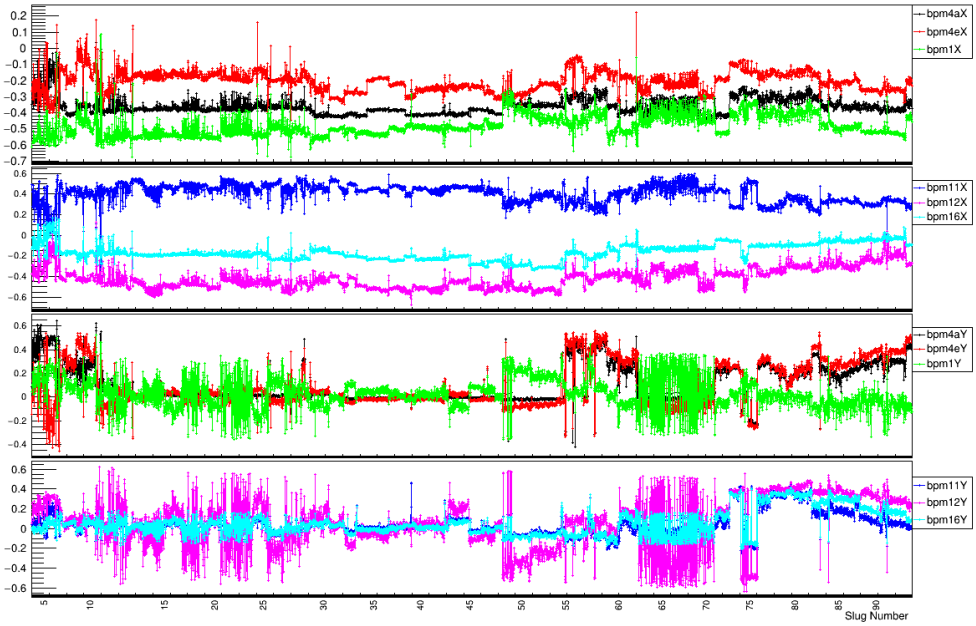

Figure C.5: History of the Eigenvector-4 components

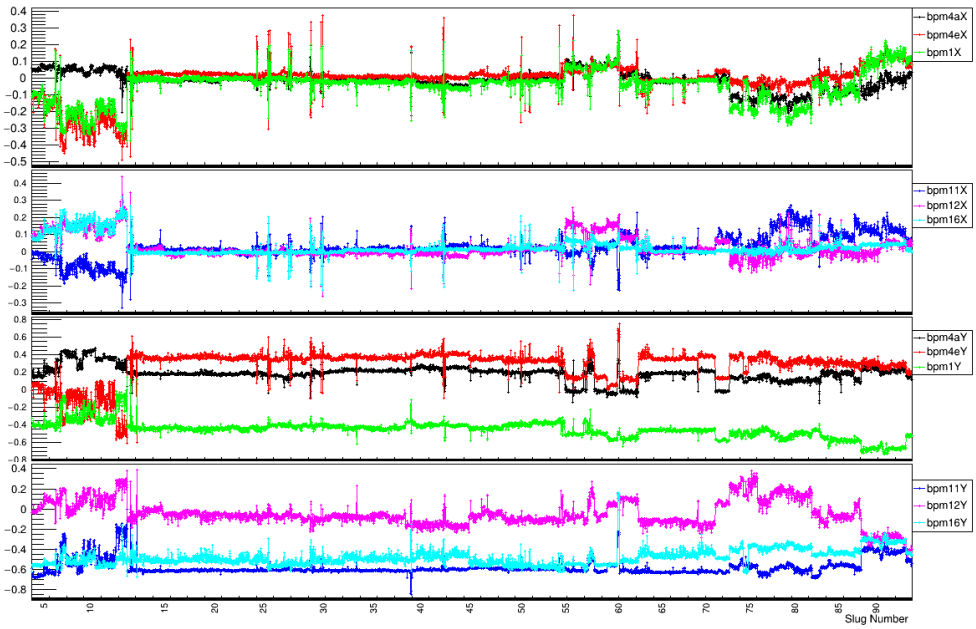

Figure C.6: History of the Eigenvector-5 components

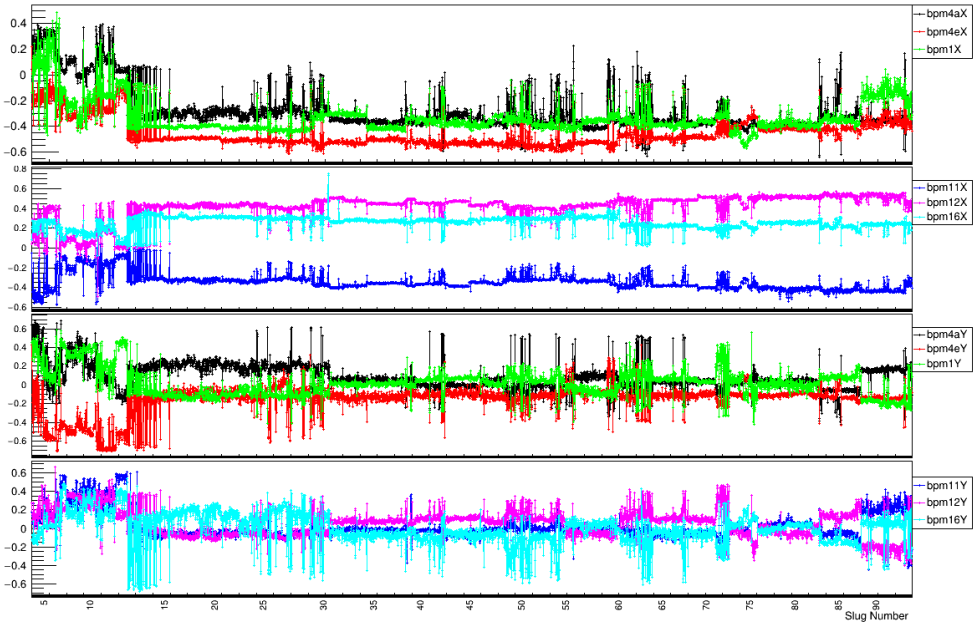

Figure C.7: History of the Eigenvector-6 components

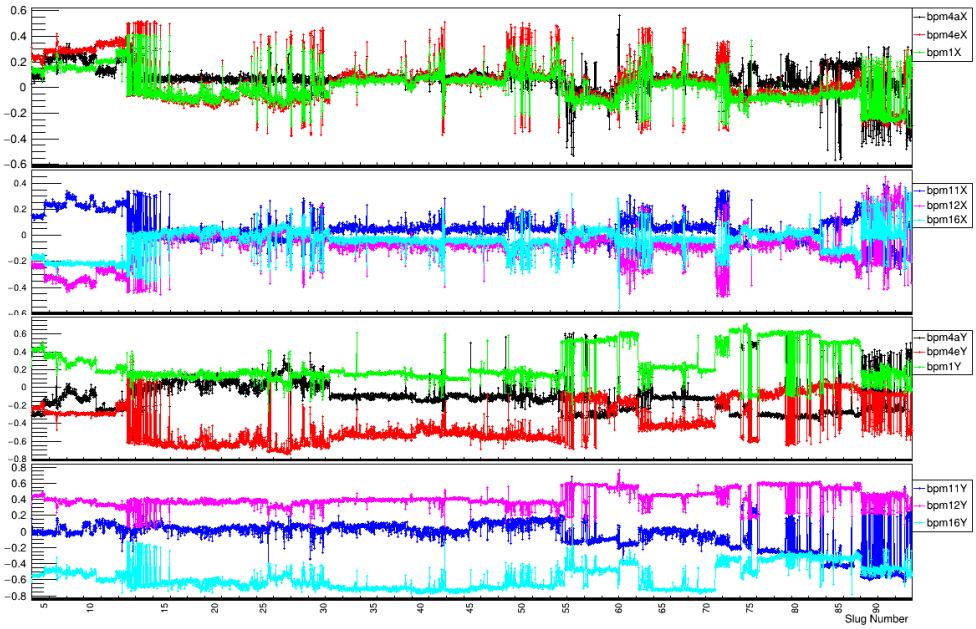

Figure C.8: History of the Eigenvector-7 components

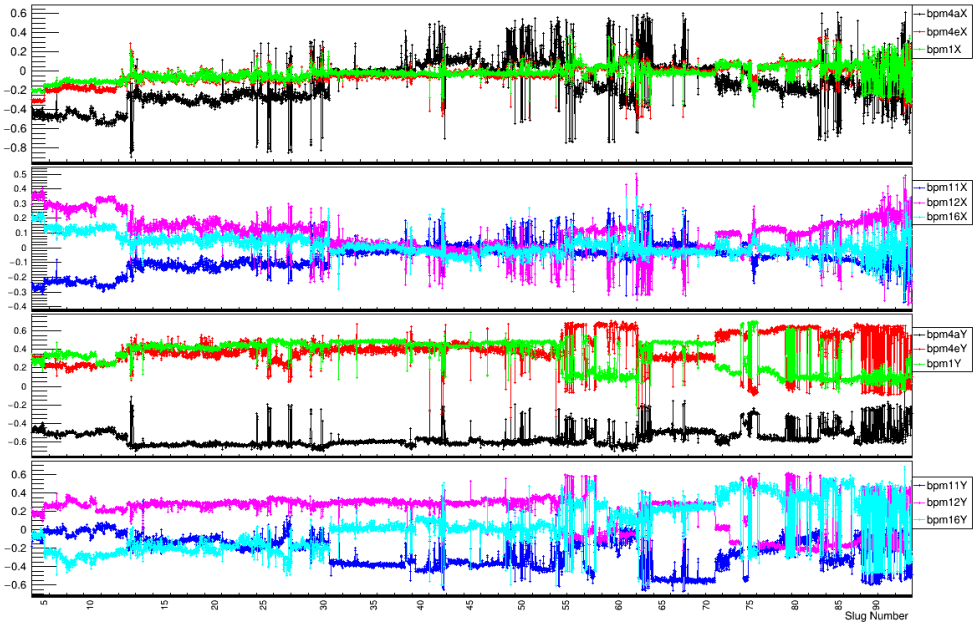

Figure C.9: History of the Eigenvector-8 components

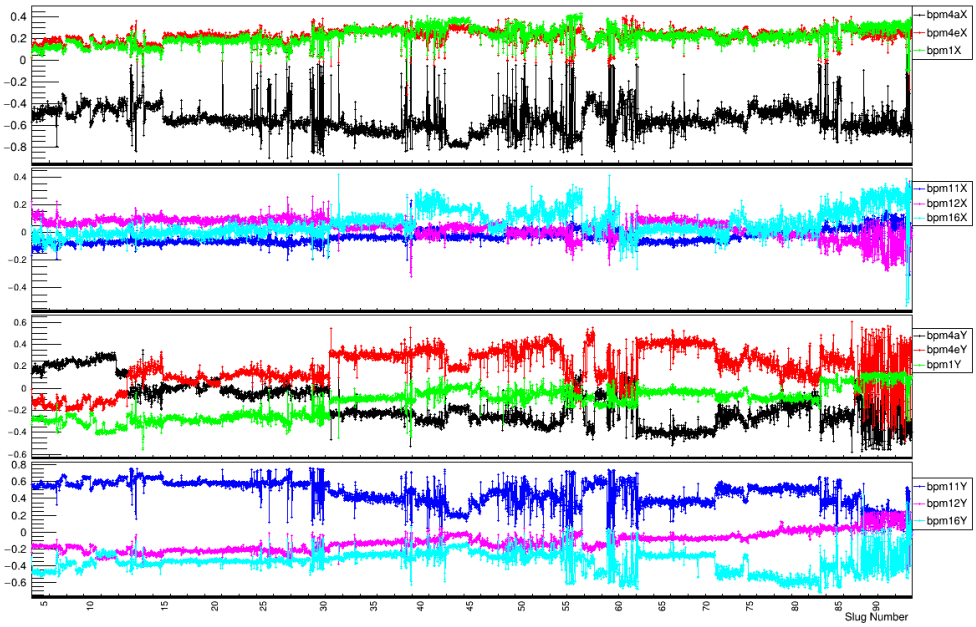

Figure C.10: History of the Eigenvector-9 components

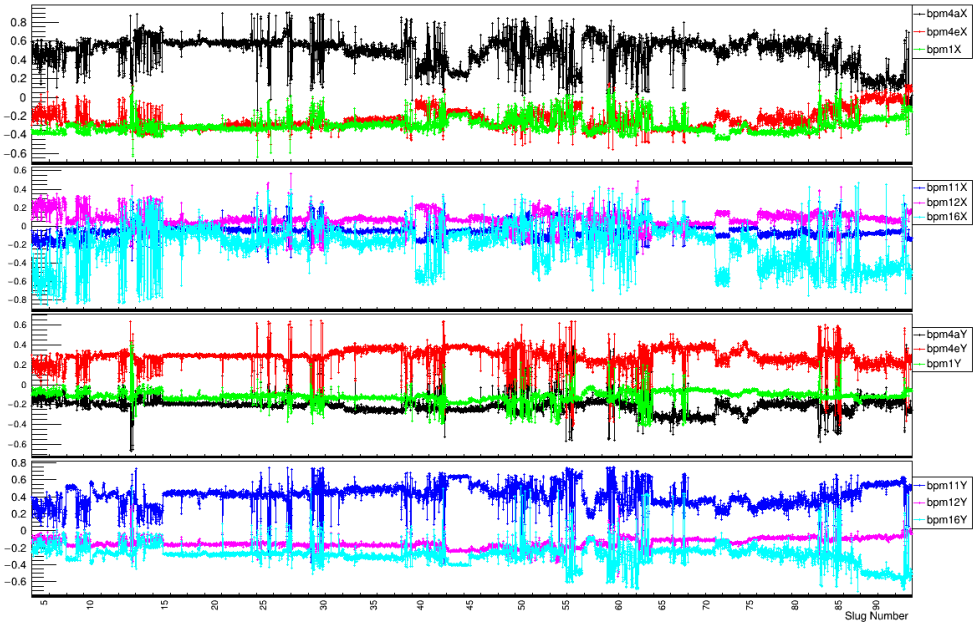

Figure C.11: History of the Eigenvector-10 components

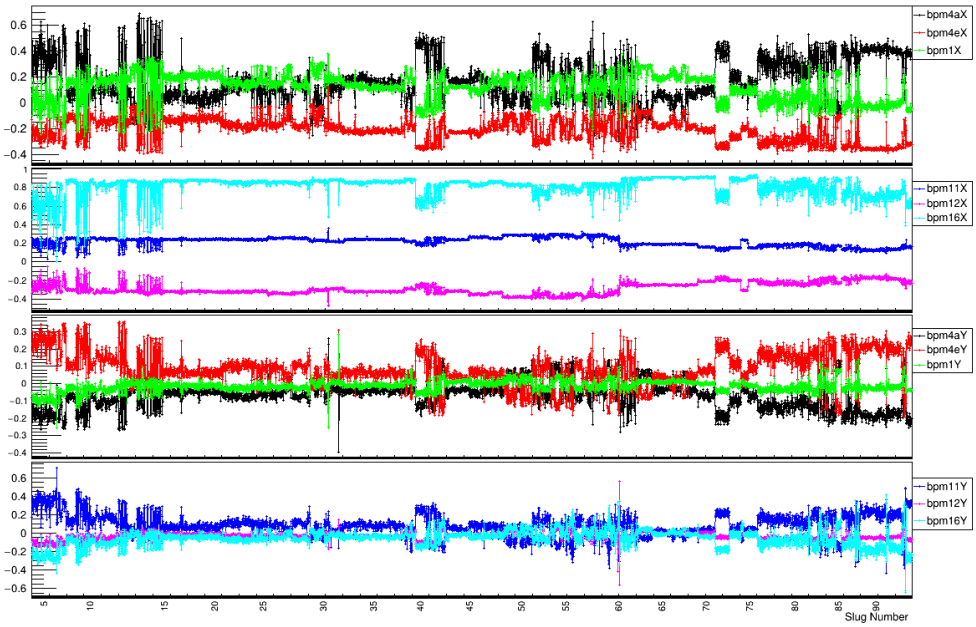

Figure C.12: History of the Eigenvector-11 components

Appendix D

Lagrange Multiplier and Regression Slopes Mini-run History

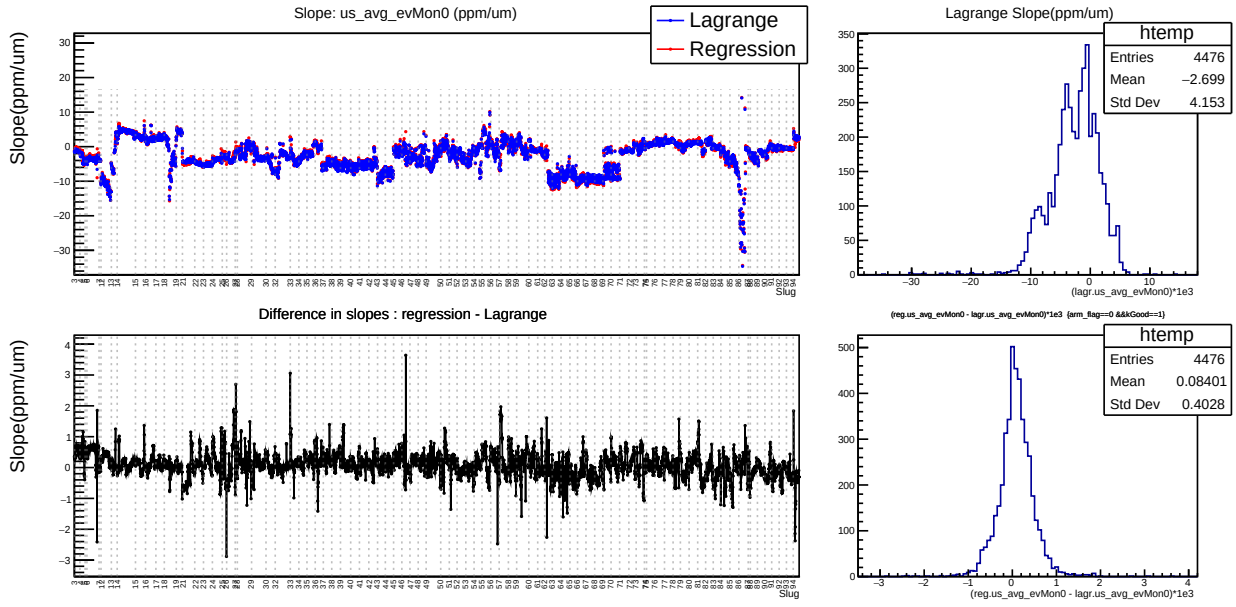

Figure D.1: History of the Lagrange Multiplier (Blue) and regression (Red) slope for the upstream averaged asymmetry v.s. Eigenvector-0.

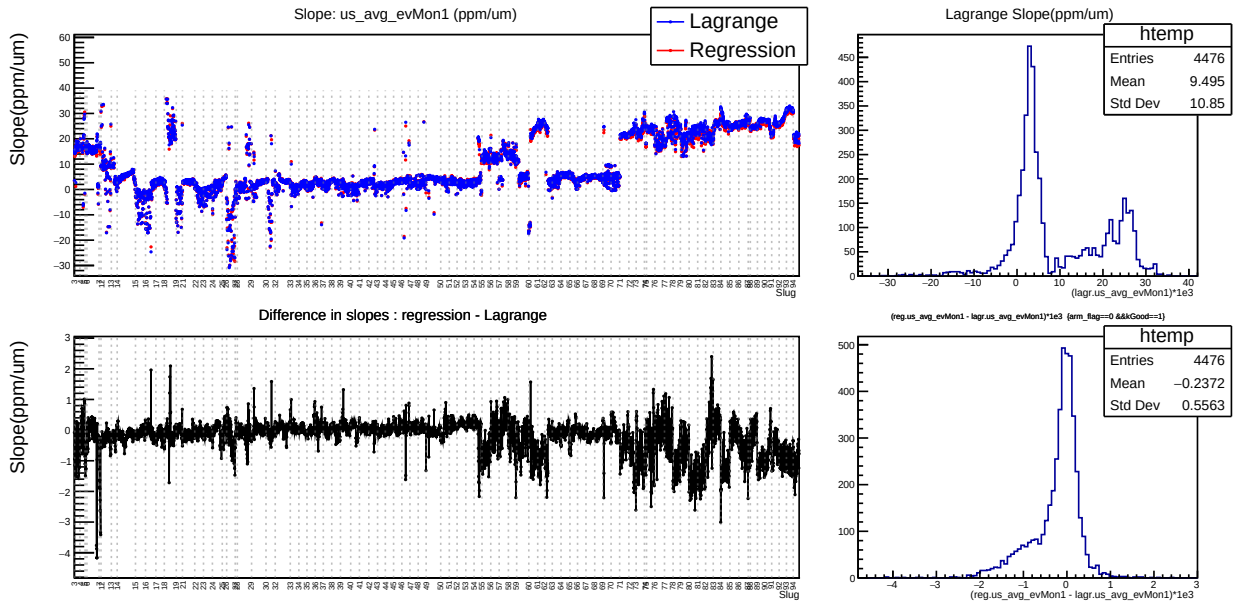

Figure D.2: History of the Lagrange Multiplier (Blue) and regression (Red) slope for the upstream averaged asymmetry v.s. Eigenvector-1.

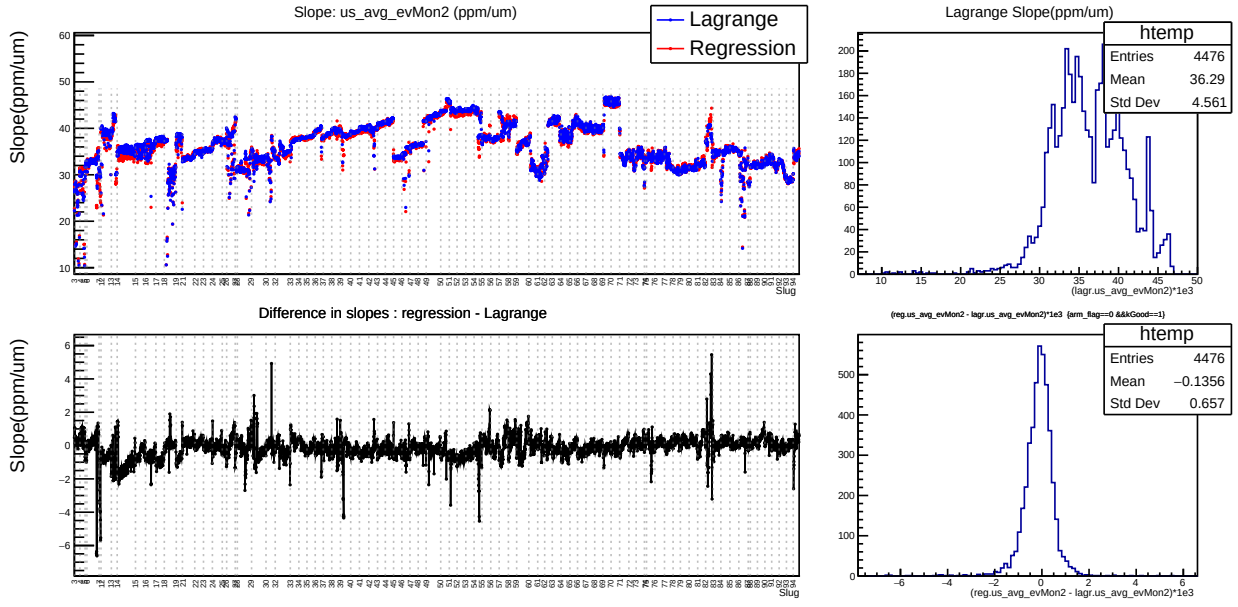

Figure D.3: History of the Lagrange Multiplier (Blue) and regression (Red) slope for the upstream averaged asymmetry v.s. Eigenvector-2.

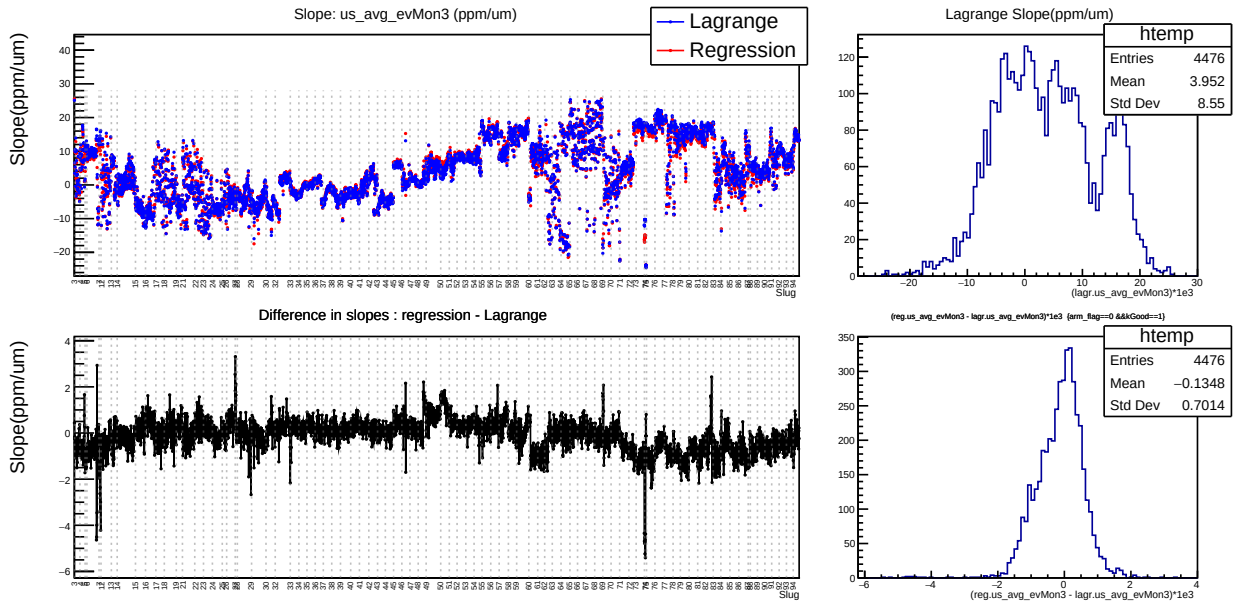

Figure D.4: History of the Lagrange Multiplier (Blue) and regression (Red) slope for the upstream averaged asymmetry v.s. Eigenvector-3.

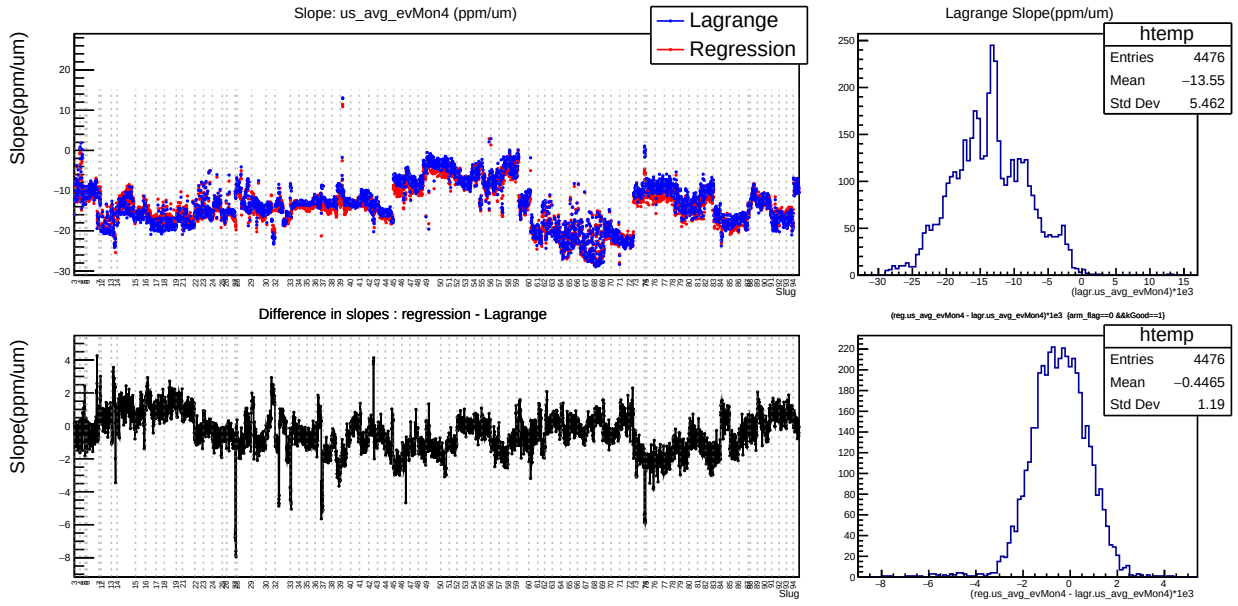

Figure D.5: History of the Lagrange Multiplier (Blue) and regression (Red) slope for the upstream averaged asymmetry v.s. Eigenvector-4.

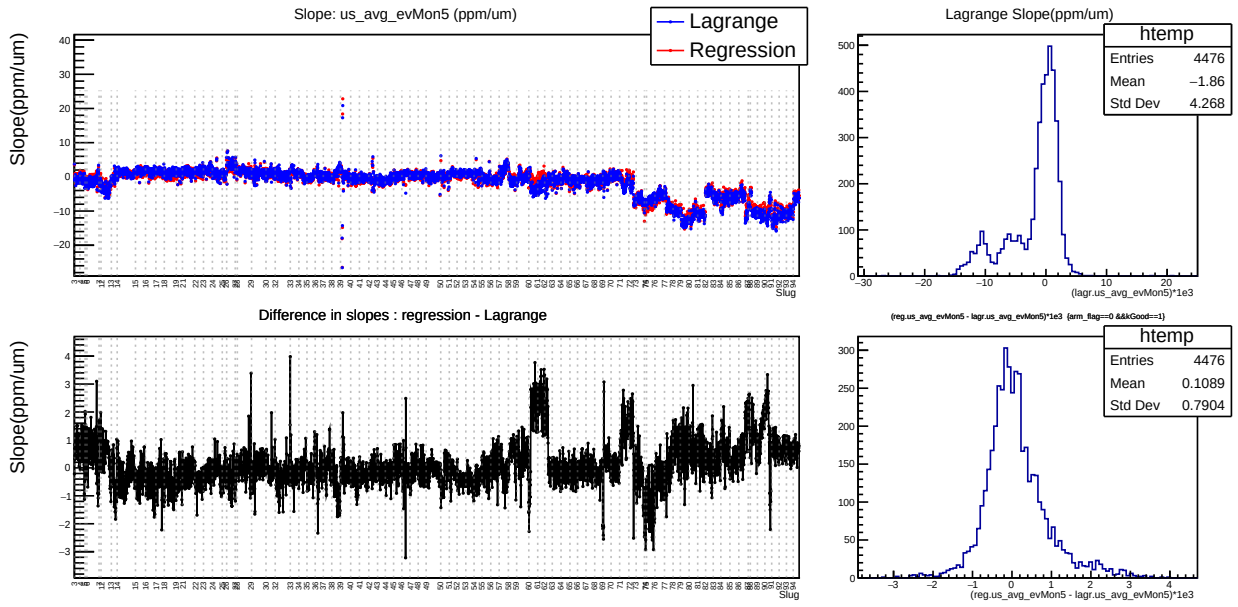

Figure D.6: History of the Lagrange Multiplier (Blue) and regression (Red) slope for the upstream averaged asymmetry v.s. Eigenvector-5.

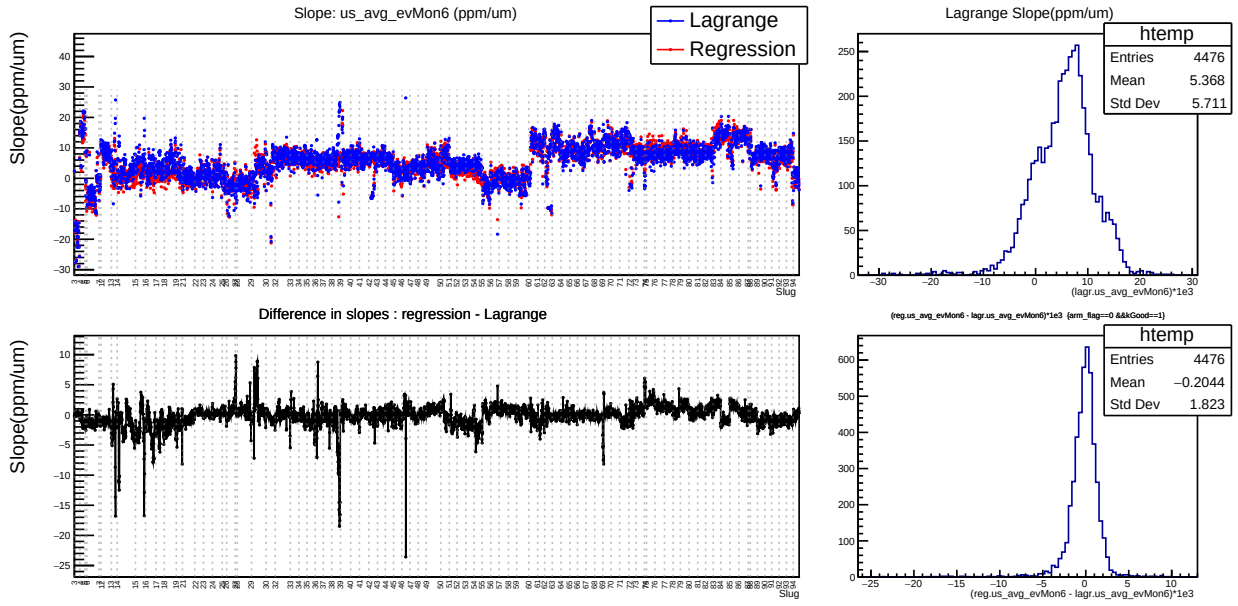

Figure D.7: History of the Lagrange Multiplier (Blue) and regression (Red) slope for the upstream averaged asymmetry v.s. Eigenvector-6.

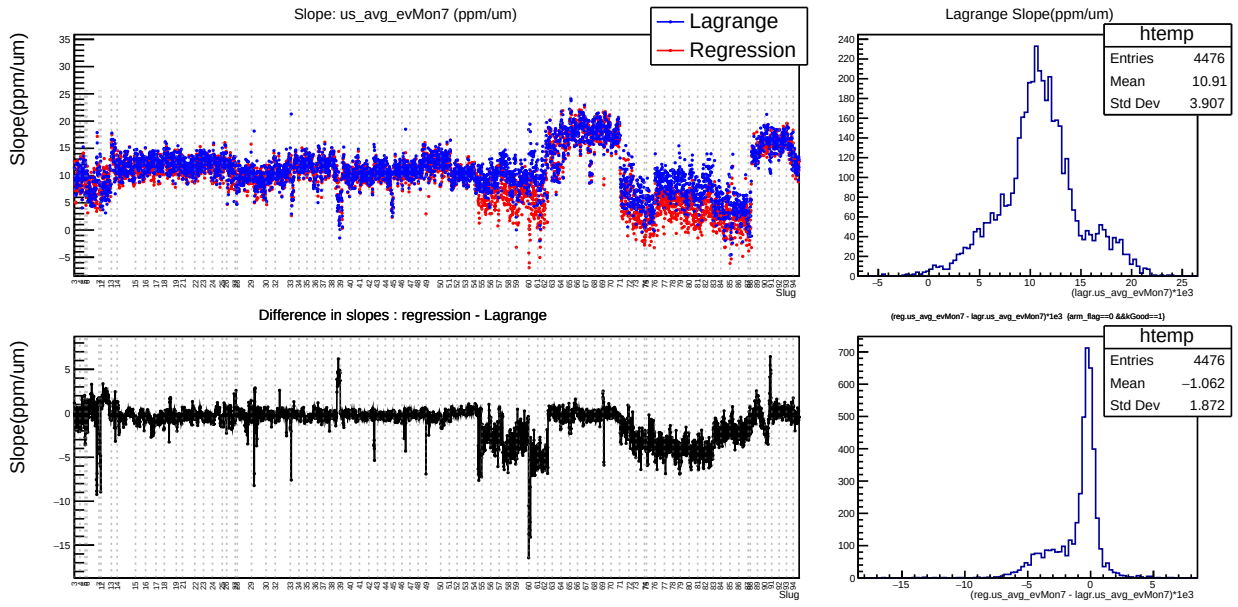

Figure D.8: History of the Lagrange Multiplier (Blue) and regression (Red) slope for the upstream averaged asymmetry v.s. Eigenvector-7.

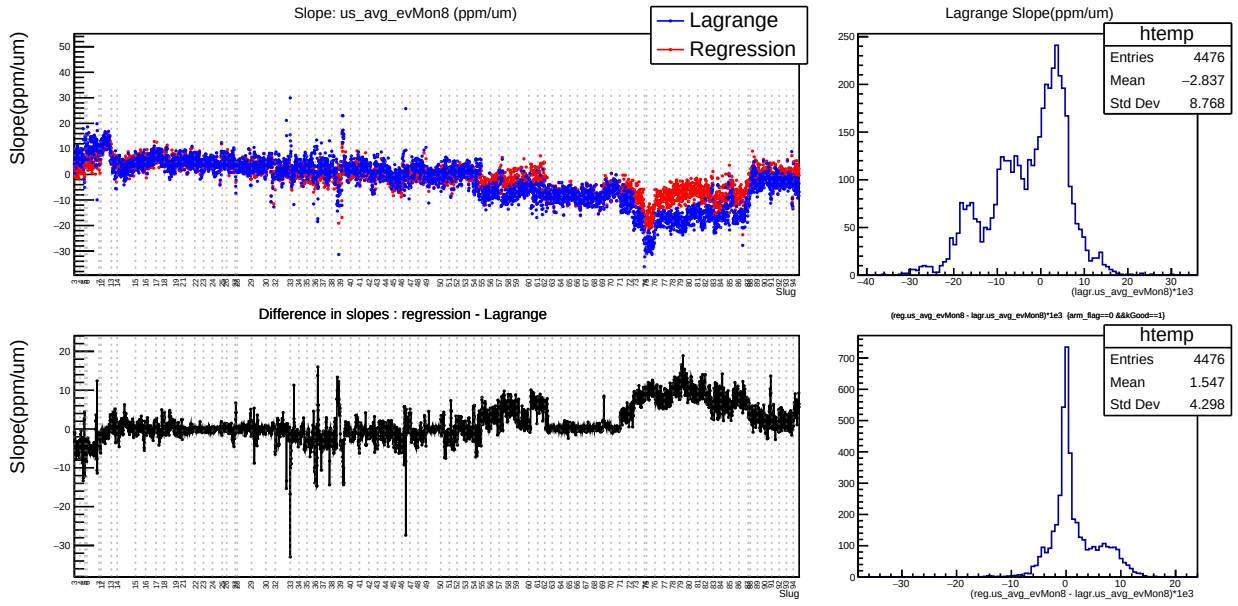

Figure D.9: History of the Lagrange Multiplier (Blue) and regression (Red) slope for the upstream averaged asymmetry v.s. Eigenvector-8.

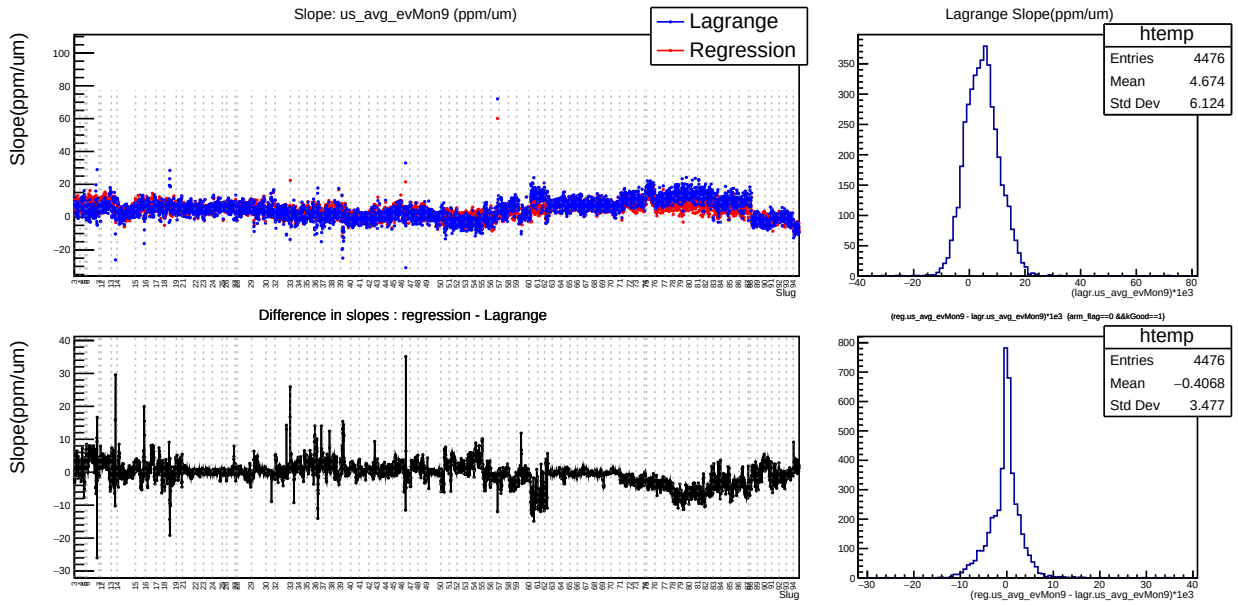

Figure D.10: History of the Lagrange Multiplier (Blue) and regression (Red) slope for the upstream averaged asymmetry v.s. Eigenvector-9.

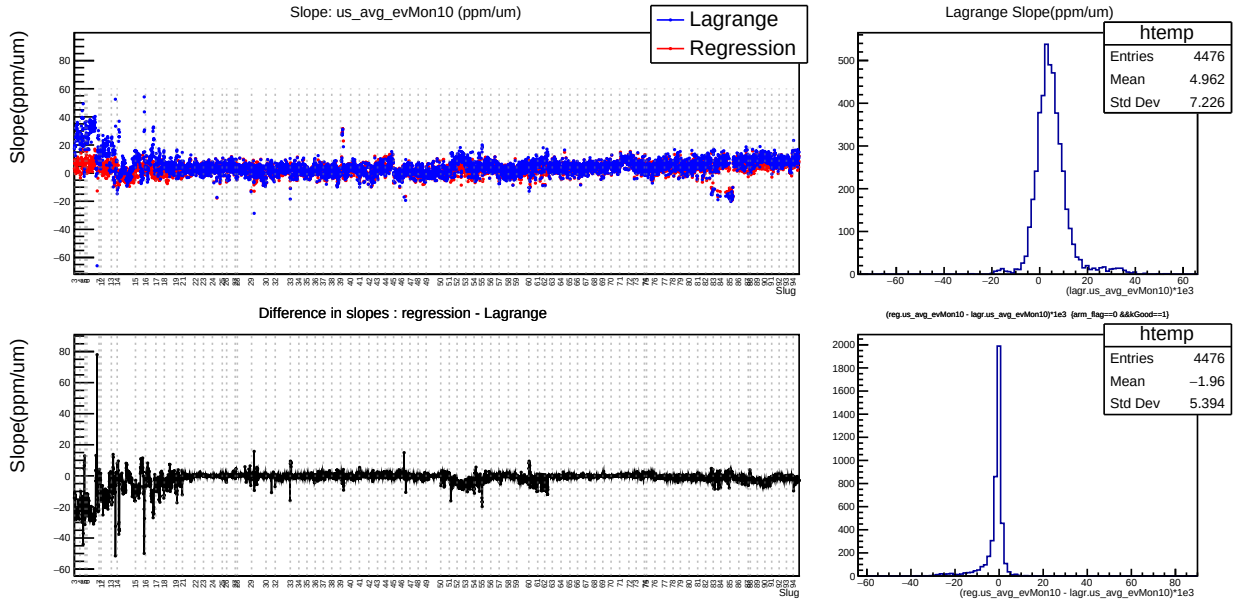

Figure D.11: History of the Lagrange Multiplier (Blue) and regression (Red) slope for the upstream averaged asymmetry v.s. Eigenvector-10.

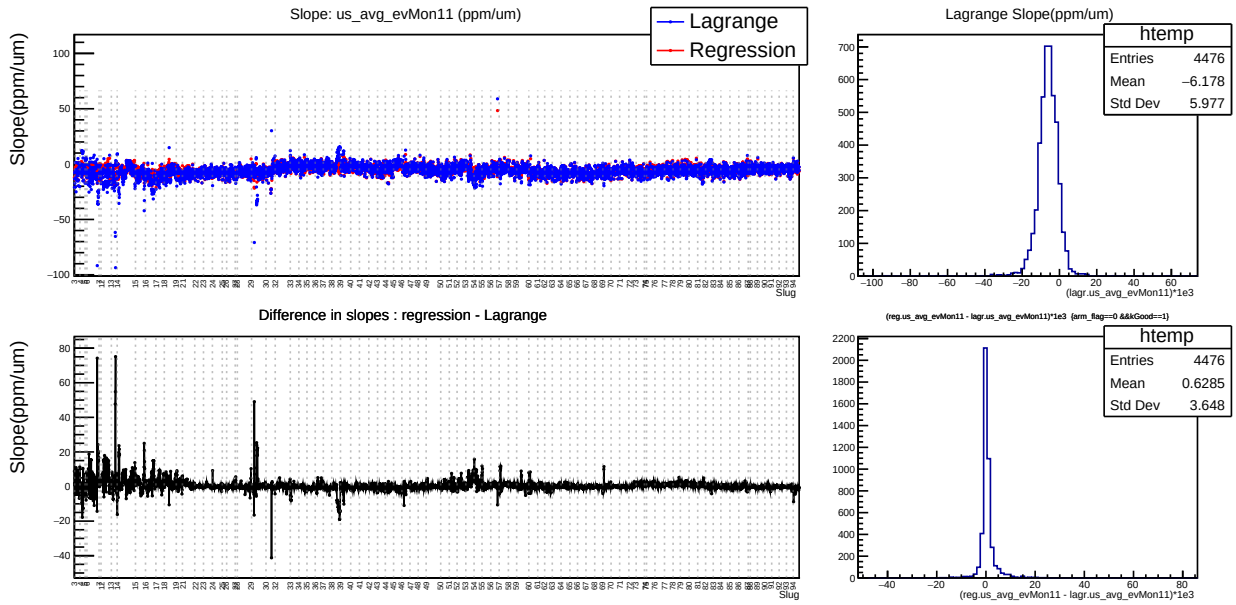

Figure D.12: History of the Lagrange Multiplier (Blue) and regression (Red) slope for the upstream averaged asymmetry v.s. Eigenvector-11.

Bibliography

[1] X. Roca-Maza, M. Centelles, X. Viñas, and M. Warda. Neutron Skin of ^{208}Pb, Nuclear Symmetry Energy, and the Parity Radius Experiment. *Phys. Rev. Lett.*, 106:252501, Jun 2011.

[2] James M Lattimer. The Nuclear Equation of State and Neutron Star Masses. *Annual Review of Nuclear and Particle Science*, 62:485–515, 2012.

[3] James M Lattimer and Andrew W Steiner. Constraints on the Symmetry Energy Using the Mass-Radius Relation of Neutron Stars. *The European Physical Journal A*, 50(2):1–24, 2014.

[4] C Drischler, RJ Furnstahl, JA Melendez, and DR Phillips. How Well Do We Know the Neutron-Matter Equation of State at the Densities Inside Neutron Stars? A Bayesian Approach with Correlated Uncertainties. *Physical Review Letters*, 125(20):202702, 2020.

[5] Markus Kortelainen, Thomas Lesinski, J Moré, W Nazarewicz, J Sarich, N Schunck, MV Stoitsov, and S Wild. Nuclear Energy Density Optimization. *Physical Review C*, 82(2):024313, 2010.

[6] Lie-Wen Chen, Che Ming Ko, Bao-An Li, and Jun Xu. Density Slope of the Nuclear Symmetry Energy from the Neutron Skin Thickness of Heavy Nuclei. *Physical Review C*, 82(2):024321, 2010.

[7] Luca Trippa, Gianluca Colò, and Enrico Vigezzi. Giant Dipole Resonance as a Quantitative Constraint on the Symmetry Energy. *Physical Review C*, 77(6):061304, 2008.

[8] MB Tsang, Yingxun Zhang, P Danielewicz, M Famiano, Zhuxia Li, WG Lynch, AW Steiner, et al. Constraints on the Density Dependence of the Symmetry Energy. *Physical Review Letters*, 102(12):122701, 2009.

[9] A Tamii, I Poltoratska, P von Neumann-Cosel, Y Fujita, T Adachi, CA Bertulani, J Carter, M Dozono, H Fujita, K Fujita, et al. Complete Electric Dipole Response and the Neutron Skin in Pb 208. *Physical review letters*, 107(6):062502, 2011.

[10] Xavier Roca-Maza, M Brenna, G Colo, M Centelles, X Vinas, BK Agrawal, Nils Paar, Dario Vretenar, and J Piekarewicz. Electric Dipole Polarizability in ^{208}Pb: Insights from the Droplet Model. *Physical Review C*, 88(2):024316, 2013.

[11] Sea Abrahamyan, Z Ahmed, H Albataineh, K Aniol, DS Armstrong, W Armstrong, T Averett, B Babineau, A Barbieri, V Bellini, et al. Measurement of the Neutron Radius of Pb-208 through Parity Violation in Electron Scattering. *Physical review letters*, 108(11):112502, 2012.

[12] CJ Horowitz, Steven J Pollock, Paul A Souder, and Robert Michaels. Parity Violating Measurements of Neutron Densities. *Physical Review C*, 63(2):025501, 2001.

[13] Shufang Ban, Charles J Horowitz, and R Michaels. Parity Violating Electron Scattering Measurements of Neutron Densities. *Journal of Physics G: Nuclear and Particle Physics*, 39(1):015104, 2011.

[14] D.W Higinbotham and T. Keppel. Hall A Standard Equipment Manual. https://hallaweb.jlab.org/github/halla-osp/version/Standard-Equipment-Manual.pdf, 2019.

[15] Bryan James Moffit. Elastic Scattering of Longitudinally Polarized Electrons from Helium-4: A Measurement of G_E^S at Q^2= 0.1 GeV/c^2. *PhD Thesis*, 2007.

[16] CR Carman and J-L Pellegrin. The Beam Positions of the SPEAR Storage Ring. *Nuclear Instruments and Methods*, 113(3):423–432, 1973.

[17] John Alcorn, BD Anderson, KA Aniol, JRM Annand, L Auerbach, J Arrington, T Averett, FT Baker, M Baylac, EJ Beise, et al. Basic Instrumentation for Hall A at Jefferson Lab. *Nuclear Instruments and Methods in Physics Research Section A: Accelerators, Spectrometers, Detectors and Associated Equipment*, 522(3):294–346, 2004.

[18] KG Fissum, William Bertozzi, JP Chen, Daniel Dale, HC Fenker, Juncai Gao, A Gavalya, Shalev Gilad, CR Leathers, Nilanga Liyanage, et al. Vertical Drift Chambers for the Hall A High-Resolution Spectrometers at Jefferson Lab. *Nuclear Instruments and Methods in Physics Research Section A: Accelerators, Spectrometers, Detectors and Associated Equipment*, 474(2):108–131, 2001.

[19] Devi Adhikari. Private Communication.

[20] Devi Adhikari, JLAB HALL A Collaboration, et al. Integrating Quartz Cerenkov Detectors for PREX-II/CREX. In *APS Division of Nuclear Physics Meeting Abstracts*, volume 2020, pages MK–008, 2020.

[21] JLab CODA Group. CEBAF Online Data Acquisition (CODA). https://coda.jlab.org.

[22] Lisa J Kaufman. Precision Measurement of the Proton Neutral Weak Form Factors at Squared Momentum Transfer $Q^2 \sim 0.1$ GeV^2. *PhD Thesis*, 2007.

[23] C Yan, J Beaufait, P Brindza, R Carlini, W Vulcan, and R Wines. Beam Raster System at CEBAF. In *Proceedings of International Conference on Particle Accelerators*, pages 3103–3105. IEEE, 1993.

[24] Silviu Covrig Dusa. The PREX2/CREX Target. https://hallaweb.jlab.org/index/safety-docs/current/TargetOperations.pdf, 2020.

[25] H De Vries, CW De Jager, and C De Vries. Nuclear Charge-Density-Distribution Parameters from Elastic Electron Scattering. *Atomic data and nuclear data tables*, 36(3):495–536, 1987.

[26] Brendan T Reed, Farrukh J Fattoyev, Charles J Horowitz, and Jorge Piekarewicz. Implications of PREX-2 on the Equation of State of Neutron-Rich Matter. *Physical Review Letters*, 126(17):172503, 2021.

[27] Paul-Gerhard Reinhard, Xavier Roca-Maza, and Witold Nazarewicz. Information Content of the Parity-Violating Asymmetry in ^{208}Pb. *arXiv preprint arXiv:2105.15050*, 2021.

[28] WG Lynch and MB Tsang. Decoding the Density Dependence of the Nuclear Symmetry Energy. *arXiv preprint arXiv:2106.10119*, 2021.

[29] B Alex Brown. Mirror Charge Radii and the Neutron Equation of State. *Physical review letters*, 119(12):122502, 2017.

[30] Skyy V Pineda, Kristian König, Dominic M Rossi, B Alex Brown, Anthony Incorvati, Jeremy Lantis, Kei Minamisono, Wilfried Nörtershäuser, Jorge Piekarewicz, Robert Powel, et al. Charge Radius of Neutron-deficient ^{54}Ni and Symmetry Energy Constraints Using the Difference in Mirror Pair Charge Radii. *arXiv preprint arXiv:2106.10378*, 2021.

[31] Shao-Peng Tang, Jin-Liang Jiang, Ming-Zhe Han, Yi-Zhong Fan, and Da-Ming Wei. Gw170817, PSR J0030+ 0451, and PSR J0740+ 6620: Constraints on Phase Transition and Nuclear Symmetry Energy Parameters. *arXiv preprint arXiv:2106.04204*, 2021.

[32] Reed Essick, Philippe Landry, Achim Schwenk, and Ingo Tews. A Detailed Examination of Astrophysical Constraints on the Symmetry Energy and the Neutron Skin of ^{208}Pb with Minimal Modeling Assumptions. *arXiv preprint arXiv:2107.05528*, 2021.

[33] Reed Essick, Ingo Tews, Philippe Landry, and Achim Schwenk. Astrophysical Constraints on the Symmetry Energy and the Neutron Skin of ^{208}Pb with Minimal Modeling Assumptions. *arXiv preprint arXiv:2102.10074*, 2021.

[34] Benjamin P Abbott, Rich Abbott, TD Abbott, Fausto Acernese, Kendall Ackley, Carl Adams, Thomas Adams, Paolo Addesso, RX Adhikari, VB Adya, et al. GW170817: Observation of Gravitational Waves from a Binary Neutron Star Inspiral. *Physical review letters*, 119(16):161101, 2017.

[35] BP Abbott, R Abbott, TD Abbott, F Acernese, K Ackley, C Adams, T Adams, P Addesso, RX Adhikari, VB Adya, et al. Properties of the Binary Neutron Star Merger GW170817. *Physical Review X*, 9(1):011001, 2019.

[36] Carolyn A Raithel and Feryal Özel. Measurement of the Nuclear Symmetry Energy Parameters from Gravitational-wave Events. *The Astrophysical Journal*, 885(2):121, 2019.

[37] D Adhikari, H Albataineh, D Androic, K Aniol, DS Armstrong, T Averett, C Ayerbe Gayoso, S Barcus, V Bellini, RS Beminiwattha, et al. Accurate Determination of the Neutron Skin Thickness of Pb 208 through Parity-Violation in Electron Scattering. *Physical Review Letters*, 126(17):172502, 2021.

[38] Gerald Dugan, S Childress, LM Lederman, LE Price, and T Sanford. Elastic Scattering of Low-Energy Pions and Muons from Lead. *Physical Review C*, 8(3):909, 1973.

[39] L Ray and GW Hoffmann. Relativistic and Nonrelativistic Impulse Approximation Descriptions of 300–1000 MeV Proton+Nucleus Elastic Scattering. *Physical Review C*, 31(2):538, 1985.

[40] L Ray. Neutron Isotopic Density Differences Deduced from 0.8 GeV Polarized Proton Elastic Scattering. *Physical Review C*, 19(5):1855, 1979.

[41] S Terashima, H Sakaguchi, H Takeda, T Ishikawa, M Itoh, T Kawabata, T Murakami, M Uchida, Y Yasuda, M Yosoi, et al. Proton Elastic Scattering from Tin Isotopes at 295 MeV and Systematic Change of Neutron Density Distributions. *Physical Review C*, 77(2):024317, 2008.

[42] A Krasznahorkay, A Balanda, JA Bordewijk, S Brandenburg, MN Harakeh, N Kalantar-Nayestanaki, BM Nyakó, J Timár, and A van der Woude. Excitation of the Isovector GDR by Inelastic α-Scattering as a Measure of the Neutron Skin of Nuclei. *Nuclear Physics A*, 567(3):521–540, 1994.

[43] A Krasznahorkay, M Fujiwara, P Van Aarle, H Akimune, I Daito, H Fujimura, Y Fujita, MN Harakeh, T Inomata, J Jänecke, et al. Excitation of Isovector Spin-Dipole Resonances and Neutron Skin of Nuclei. *Physical review letters*, 82(16):3216, 1999.

[44] A Trzcińska, J Jastrzebski, P Lubiński, FJ Hartmann, R Schmidt, T Von Egidy, and B Kłos. Neutron Density Distributions Deduced from Antiprotonic Atoms. *Physical review letters*, 87(8):082501, 2001.

[45] A Klimkiewicz, Nils Paar, P Adrich, M Fallot, K Boretzky, T Aumann, D Cortina-Gil, U Datta Pramanik, Th W Elze, H Emling, et al. Nuclear Symmetry Energy and Neutron Skins Derived from Pygmy Dipole Resonances. *Physical Review C*, 76(5):051603, 2007.

[46] James M Lattimer and Yeunhwan Lim. Constraining the Symmetry Parameters of the Nuclear Interaction. *The Astrophysical Journal*, 771(1):51, 2013.

[47] CJ Horowitz, Z Ahmed, C-M Jen, A Rakhman, PA Souder, MM Dalton, N Liyanage, KD Paschke, K Saenboonruang, R Silwal, et al. Weak Charge Form Factor and Radius of 208 Pb through Parity Violation in Electron Scattering. *Physical Review C*, 85(3):032501, 2012.

[48] RD McKeown. Sensitivity of Polarized Elastic Electron-Proton Scattering to the Anomalous Baryon Number Magnetic Moment. *Physics Letters B*, 219(2-3):140–142, 1989.

[49] DT Spayde, DH Beck, R Hasty, T Averett, D Barkhuff, G Dodson, K Dow, M Farkhondeh, W Franklin, E Tsentalovich, et al. The Strange Quark Contribution to the Proton's Magnetic Moment. *Physics Letters B*, 583(1-2):79–86, 2004.

[50] TM Ito, Todd Averett, David Barkhuff, Guillaume Batigne, DH Beck, EJ Beise, A Blake, Herbert Breuer, Robert Carr, Benjamin Clasie, et al. Parity-Violating Electron Deuteron Scattering and the Proton's Neutral Weak Axial Vector Form Factor. *Physical review letters*, 92(10):102003, 2004.

[51] KA Aniol, DS Armstrong, Todd Averett, Maud Baylac, Etienne Burtin, John Calarco, GD Cates, Christian Cavata, Zhengwei Chai, CC Chang, et al. New Measurement of Parity Violation in Elastic Electron–Proton Scattering and Implications for Strange Form Factors. *Physics Letters B*, 509(3-4):211–216, 2001.

[52] KA Aniol, DS Armstrong, Todd Averett, Hachemi Benaoum, PY Bertin, Etienne Burtin, Jason Cahoon, GD Cates, CC Chang, Y-C Chao, et al. Parity-Violating Electron Scattering from He-4 and the Strange Electric Form Factor of the Nucleon. *Physical review letters*, 96(2):022003, 2006.

[53] KA Aniol, DS Armstrong, T Averett, H Benaoum, PY Bertin, E Burtin, J Cahoon, GD Cates, CC Chang, Y-C Chao, et al. Constraints on the Nucleon Strange Form Factors at $Q^2 \sim 0.1$ GeV^2. *Physics Letters B*, 635(5-6):275–279, 2006.

[54] A Acha, KA Aniol, DS Armstrong, John Arrington, Todd Averett, SL Bailey, James Barber, Arie Beck, Hachemi Benaoum, Jay Benesch, et al. Precision Measurements of the Nucleon Strange Form Factors at $Q^2 \sim 0.1$ GeV^2. *Physical review letters*, 98(3):032301, 2007.

[55] Z Ahmed, K Allada, KA Aniol, DS Armstrong, J Arrington, P Baturin, V Bellini, J Benesch, R Beminiwattha, F Benmokhtar, et al. New Precision Limit on the Strange Vector Form Factors of the Proton. *Physical review letters*, 108(10):102001, 2012.

[56] DH Beck. Strange-Quark Vector Currents and Parity-Violating Electron Scattering from the Nucleon and from Nuclei. *Physical Review D*, 39(11):3248, 1989.

[57] DS Armstrong, J Arvieux, Razmik Asaturyan, Todd Averett, SL Bailey, Guillaume Batigne, DH Beck, EJ Beise, Jay Benesch, Louis Bimbot, et al. Strange-Quark Contributions to Parity-Violating Asymmetries in the Forward G0 Electron-Proton Scattering Experiment. *Physical review letters*, 95(9):092001, 2005.

[58] Darko Androić, DS Armstrong, J Arvieux, SL Bailey, DH Beck, EJ Beise, J Benesch, F Benmokhtar, L Bimbot, J Birchall, et al. Strange Quark Contributions to Parity-Violating Asymmetries in the Backward Angle G0 Electron Scattering Experiment. *Physical review letters*, 104(1):012001, 2010.

[59] FE Maas, P Achenbach, K Aulenbacher, S Baunack, L Capozza, J Diefenbach, K Grimm, Y Imai, T Hammel, D Von Harrach, et al. Measurement of Strange-Quark Contributions to the Nucleon's Form Factors at $Q^2 = 0.230$ $(GeV/c)^2$. *Physical review letters*, 93(2):022002, 2004.

[60] FE Maas, K Aulenbacher, S Baunack, L Capozza, J Diefenbach, B Gläser, T Hammel, D Von Harrach, Y Imai, E-M Kabuß, et al. Evidence for Strange-Quark Contributions to the Nucleon's Form Factors at $Q^2 = 0.108$ $(GeV/c)^2$. *Physical review letters*, 94(15):152001, 2005.

[61] S Baunack, K Aulenbacher, D Balaguer Rios, L Capozza, J Diefenbach, B Gläser, D Von Harrach, Y Imai, E-M Kabuß, R Kothe, et al. Measurement of Strange Quark Contributions to the Vector Form Factors of the Proton at $Q^2 = 0.22$ $(GeV/c)^2$. *Physical review letters*, 102(15):151803, 2009.

[62] Kenzo Nakamura. Review of Particle Physics. *Journal of Physics G: Nuclear and Particle Physics*, 37(7 A), 2010.

[63] Donald Jones. Moller Polarimetry for the Neutron Skin Experiments at Jefferson Lab. In *APS Division of Nuclear Physics Meeting Abstracts*, volume 2020, pages MN–006, 2020.

[64] Eric King. Private Communication.

[65] J-C Denard, A Saha, and G Laveissiere. High Accuracy Beam Current Monitor System for CEBAF's Experimental Hall A. In *PACS2001. Proceedings of the 2001 Particle Accelerator Conference (Cat. No. 01CH37268)*, volume 3, pages 2326–2328. IEEE, 2001.

[66] C Yan, N Sinkine, and R Wojcik. Linear Beam Raster for Cryogenic Targets. *Nuclear Instruments and Methods in Physics Research Section A: Accelerators, Spectrometers, Detectors and Associated Equipment*, 539(1-2):1–15, 2005.

[67] H Erik Swanson and Stephan Schlamminger. Removal of Zero-Point Drift from AB data and the Statistical Cost. *Measurement Science and Technology*, 21(11):115104, 2010.

[68] GA Krafft, JJ Bisognano, MT Crofford, JC Hovater, L Merminga, SN Simrock, SD Witherspoon, and K Kubo. Energy Vernier System for CEBAF. In *Proceedings of International Conference on Particle Accelerators*, pages 2364–2366. IEEE, 1993.

[69] the PREX Collaboration. Just Another Parity Analyzer (JAPAN). https://github.com/JeffersonLab/japan, 2019.

[70] the PREX Collaboration. The PREX-2 Prompt Analysis. https://github.com/JeffersonLab/prex-prompt, 2019.

[71] Tao Ye. Dithering Analysis and Correction Engine (DANCE). https://github.com/leafybillow/dance, 2020.

[72] Tao Ye. The PREX-2 Statistical Analysis Tool. https://github.com/leafybillow/prex-stat, 2020.

[73] CJ Horowitz. Parity Violating Elastic Electron Scattering and Coulomb Distortions. *Physical Review C*, 57(6):3430, 1998.

[74] Jens Erler and Shufang Su. The Weak Neutral Current. *Progress in Particle and Nuclear Physics*, 71:119–149, 2013.

[75] M Gorchtein and CJ Horowitz. Dispersion γ Z-Box Correction to the Weak Charge of the Proton. *Physical review letters*, 102(9):091806, 2009.

[76] Mikhail Gorchtein, CJ Horowitz, and Michael J Ramsey-Musolf. Model Dependence of the γ Z Dispersion Correction to the Parity-Violating Asymmetry in Elastic *ep* Scattering. *Physical Review C*, 84(1):015502, 2011.

[77] DWL Sprung and J Martorell. The Symmetrized Fermi Function and Its Transforms. *Journal of Physics A: Mathematical and General*, 30(18):6525, 1997.

[78] J Piekarewicz, AR Linero, P Giuliani, and E Chicken. Power of Two: Assessing the Impact of a Second Measurement of the Weak-Charge Form Factor of Pb 208. *Physical Review C*, 94(3):034316, 2016.

[79] B Frois, Jl B Bellicard, JM Cavedon, M Huet, Ph Leconte, P Ludeau, A Nakada, Phan Zuan Hô, and I Sick. High-Momentum-Transfer Electron Scattering from Pb 208. *Physical Review Letters*, 38(4):152, 1977.

[80] O Madelung, U Rössler, and M Schulz. Springer Materials—The Landolt-Börnstein Database. *see http://www. springermaterials. com*, 2010.

[81] Ross Daniel Young, Julie Roche, Roger D Carlini, and Anthony William Thomas. Extracting Nucleon Strange and Anapole Form Factors from World Data. *Physical review letters*, 97(10):102002, 2006.

[82] Jianglai Liu, Robert D McKeown, and Michael J Ramsey-Musolf. Global Analysis of Nucleon Strange Form Factors at low Q^2. *Physical Review C*, 76(2):025202, 2007.

[83] A Ong, JC Berengut, and VV Flambaum. Effect of Spin-Orbit Nuclear Charge Density Corrections due to the Anomalous Magnetic Moment on Halonuclei. *Physical Review C*, 82(1):014320, 2010.

[84] Jens Erler, Andriy Kurylov, and Michael J Ramsey-Musolf. Weak Charge of the Proton and New Physics. *Physical Review D*, 68(1):016006, 2003.

[85] Particle Data Group et al. Review of Particle Physics. *Progress of Theoretical and Experimental Physics*, 2020(8):1–2093, 2020.

[86] CJ Horowitz, J Piekarewicz, and Brendan Reed. Insights into Nuclear Saturation Density from Parity-Violating Electron Scattering. *Physical Review C*, 102(4):044321, 2020.

[87] P Haensel, M Proszynski, and M Kutschera. Uncertainty in the Saturation Density of Nuclear Matter and Neutron Star Models. *Astronomy and Astrophysics*, 102:299–302, 1981.

[88] William D Myers. Droplet Model of Atomic Nuclei. 1977.

[89] William D Myers and Wladyslaw J Swiatecki. Nuclear Masses and Deformations. *Nuclear Physics*, 81(1):1–60, 1966.

[90] Wei-Chia Chen and J Piekarewicz. Building Relativistic Mean Field Models for Finite Nuclei and Neutron Stars. *Physical Review C*, 90(4):044305, 2014.

[91] FJ Fattoyev, CJ Horowitz, J Piekarewicz, and Brendan Reed. GW190814: Impact of a 2.6 Solar Mass Neutron Star on the Nucleonic Equations of State. *Physical Review C*, 102(6):065805, 2020.

[92] BG Todd-Rutel and J Piekarewicz. Neutron-Rich Nuclei and Neutron Stars: A New Accurately Calibrated Interaction for the Study of Neutron-Rich Matter. *Physical review letters*, 95(12):122501, 2005.

[93] Farrukh J Fattoyev, Charles J Horowitz, Jorge Piekarewicz, and Gang Shen. Relativistic Effective Interaction for Nuclei, Giant Resonances, and Neutron Stars. *Physical Review C*, 82(5):055803, 2010.

[94] GA Lalazissis, J König, and P Ring. New Parametrization for the Lagrangian Density of Relativistic Mean Field Theory. *Physical Review C*, 55(1):540, 1997.

[95] M Beiner, H Flocard, Nguyen Van Giai, and Phu Quentin. Nuclear Ground-State Properties and Self-Consistent Calculations with the Skyrme Interaction:(I). Spherical Description. *Nuclear Physics A*, 238(1):29–69, 1975.

[96] E Chabanat, P Bonche, P Haensel, J Meyer, and R Schaeffer. A Skyrme Parametrization from Subnuclear to Neutron Star Densities Part II. Nuclei Far from Stabilities. *Nuclear Physics A*, 635(1-2):231–256, 1998.

[97] FJ Fattoyev and J Piekarewicz. Has a Thick Neutron Skin in Pb 208 Been Ruled Out? *Physical review letters*, 111(16):162501, 2013.

[98] Zhen Zhang and Lie-Wen Chen. Electric Dipole Polarizability in Pb208 as a Probe of the Symmetry Energy and Neutron Matter around ρ_0 /3. *Physical Review C*, 92(3):031301, 2015.

[99] James M Lattimer, CJ Pethick, Madappa Prakash, and Pawel Haensel. Direct URCA Process in Neutron Stars. *Physical review letters*, 66(21):2701, 1991.

[100] CJ Horowitz and J Piekarewicz. Constraining URCA Cooling of Neutron Stars from the Neutron Radius of ^{208}Pb. *Physical Review C*, 66(5):055803, 2002.

[101] Thomas E Riley, Anna L Watts, Slavko Bogdanov, Paul S Ray, Renee M Ludlam, Sebastien Guillot, Zaven Arzoumanian, Charles L Baker, Anna V Bilous, Deepto Chakrabarty, et al. A NICER View of PSR J0030+ 0451: Millisecond Pulsar Parameter Estimation. *The Astrophysical Journal Letters*, 887(1):L21, 2019.

[102] MC Miller, Frederick K Lamb, AJ Dittmann, Slavko Bogdanov, Zaven Arzoumanian, Keith C Gendreau, S Guillot, AK Harding, WCG Ho, JM Lattimer, et al. PSR J0030+ 0451 Mass and Radius from NICER Data and Implications for the Properties of Neutron Star Matter. *The Astrophysical Journal Letters*, 887(1):L24, 2019.

[103] Benjamin P Abbott, Richard Abbott, TD Abbott, F Acernese, K Ackley, C Adams, T Adams, P Addesso, Rana X Adhikari, Vaishali B Adya, et al. GW170817: Measurements of Neutron Star Radii and Equation of State. *Physical review letters*, 121(16):161101, 2018.

[104] Dominik Becker, Razvan Bucoveanu, Carsten Grzesik, Kathrin Imai, Ruth Kempf, Matthias Molitor, Alexey Tyukin, Marco Zimmermann, David Armstrong, Kurt Aulenbacher, et al. The P2 Experiment. *The European Physical Journal A*, 54(11):1–61, 2018.